Nanoscale segregation of claudin-10a, -10b and -15 enables paracellular ion permeability

Inaugural-Dissertation

to obtain the academic degree

Doctor rerum naturalium (Dr. rer. nat)

submitted to the Department of Biology, Chemistry, Pharmacy

of the Freie Universität Berlin

by

Hannes Gonschior

from Berlin, Germany

2021

Die vorliegende Arbeit wurde in der Zeit vom Oktober 2017 bis August 2021 unter Anleitung von Prof. Dr. Volker Haucke und Dr. Martin Lehmann am Leibniz-Forschungsinstitut für Molekulare Pharmakologie (FMP), Berlin-Buch durchgeführt.

1st Reviewer: Prof. Dr. Volker Haucke

2nd Reviewer: Dr. Francesca Bottanelli

Date of defense: 09/03/2022

Affidavit

I declare that my Ph.D. thesis entitled "Nanoscale segregation of claudin-10a, -10b and -15 enables paracellular ion permeability" has been written independently and with no other sources and aids than quoted.

“Don't count the days. Make the days count.”

Muhammad Ali (17th January 1942 - 3rd June 2016)

Acknowledgments

I would like to thank Prof. Dr. Volker Haucke for giving me the opportunity to work on this exciting project and for his guidance throughout my PhD. It was a pleasure to be part of his great group.

A special thanks goes to Dr. Martin Lehmann who hired me as his first PhD student (citation: “Clark Kent”). He was a great supervisor and motivator for me. I greatly profited from his enthusiasm in science and his exceptional knowledge in microscopy.

I am very grateful that I had the opportunity to work with Jenny Eichhorst. It was a great pleasure to have her always around and it is even a bigger pleasure for me that we both are going to leave the FMP at the same time. I think she will be missed not only by me but by all the members of the FMP. Of course, I also want to thank all the current and former members of the FMP Cellular Imaging Facility: Dima, Christopher, Thomas, Vini, Kerem and his taxi service and of course Rozemarijn, who brought within her first 9 months a lot of "fresh wind" into our research. It was very pleasant to work with all of you.

I also want to thank all the members and former members of the AGHaucke, AGMaritzen and AGKrauss for their kind support and the great scientific and friendly atmosphere. Especially I want to point out the great time I had with Tine-Biene, my Habibi Malek and Tania López-Hernandez as well as the joyful time I had with the former lab members and now friends Marine Gil, and Alex Körner.

Many thanks go to the scientists from the Clinical Physiology/Nutritional Medicine department at the Charité Campus Benjamin Franklin in Berlin. Especially Prof. Dr. Dorothee Günzel, Dr. Jörg Piontek, Prof. Dr. Jörg Schulzke, Dr. Susanne Krug, Anja Fromm and In-Fah Lee have been a great help with their exceptional knowledge in the TJ research field.

Most importantly I also want to thank the GRK2318 for funding my first three years and three months of my PhD and the Sonnenfeld-Stiftung that allowed me to continue my research for another year, giving me the opportunity to finish my PhD thesis and to work on my scientific publication.

Finally, the greatest thanks go to my family, my closest friends, the friends I made during my scientific studies and mi Clara who supported me over the last decade.

I Abstract

Located between the epithelium's and endothelium's outer cells, the tight junction (TJ) acts as a semi-permeable barrier in the paracellular cleft. It balances two crucial functions: the protection of the tissue from the outer environment (pathogens, toxins) and the maintenance of the organ homeostasis by providing paracellular ion and macromolecule permeability. The TJ connects adjacent epithelial cells as a meshwork-like structure consisting of multiple interconnected strands. The strands are formed by a specific group of tetra-span transmembrane proteins, the claudin (Cldn) family. Since the discovery of its first members in 1998, the claudin family has expanded rapidly to 26 members in mammals. The fundamental role of claudins is to provide sealing and specific channel properties to the TJ by forming paracellular contact interfaces with their extracellular loop (ECL) domains. Inherent claudin mutations, and pathogens that target specific claudins can cause changes in the TJ structure resulting in severe chronic diseases. The nanoscale organization of claudins that enables their specific function, and their rearrangement under pathological conditions has yet to be investigated. The greatly apical and axial localization, together with the highly complex multi-protein-based structure of the TJ, make nanoscale imaging of various proteins and dynamics a sophisticated and nearly impossible task. In recent years, a couple of studies indicated the great potential of super-resolution fluorescence microscopy in solving this problem without exhausting it thoroughly.

Here, we could show for the first time that stimulated emission depletion (STED) microscopy in combination with advanced labeling techniques can resolve the TJ meshwork structure. In this way we could provide novel insights into the specific nano-organization principles of claudins in *in vitro* overexpression and mammalian tissue. Automated computational comparison of the TJ-like meshwork forming properties of all 26 mammalian claudins revealed that claudins differ in their ability to form meshwork and can be grouped into three classes based on their meshwork structure. Co-overexpression of barrier-forming Cldn3 and channel-forming Cldn2 with other claudins uncovered five different nano-interaction patterns: intermixing, integration, induction, segregation, and exclusion. Focusing on the nano-segregation of the channel-forming claudins Cldn10a, Cldn10b, and Cldn15, we could verify this novel interaction pattern on an endogenous level for Cldn2 and Cldn10a in whole isolated kidney tubules, as well as for Cldn3 and Cldn15 in the duodenum.

By testing how different extrinsic (functional inhibition of the Cldn2 pore, depletion of cholesterol, and diminishing of the PDZ binding motif) and intrinsic factors (deletion of the claudin C-terminus and claudin chimeras) influenced segregation, we could determine that the segregation is conserved in the ECLs of the claudins. By reintroducing single channel- and barrier-forming claudins and segregating claudin pairs in a novel genetically modified epithelial cell line, which lacks the TJ meshwork due to a quintuple claudin knockout, we could show on a functional level the relevance of segregation as a novel indispensable requirement for the formation of ion-specific paracellular channels and its necessity for a constant ion diffusion over the TJ meshwork.

II Zusammenfassung

Die *tight junction* (TJ) agiert im parazellulären Raum zwischen den äußersten Zellen des Epitheliums und Endotheliums als semipermeable Diffusionsbarriere. Als dichte Verbindung zwischen benachbarten Epithel- und Endothelzellen übt die TJ zwei elementare Funktionen aus: den Schutz des Gewebes vor der äußeren Umgebung (Pathogene und Toxine) und die Aufrechterhaltung der Gewebe Homöostase durch ihre passive Permeabilität für Ionen, Wasser und Makromolekülen. Bestehend aus mehreren miteinander verbundenen Strängen bildet die TJ eine Netzwerk-artige Struktur aus, die sich entlang des gesamten Zell-Zell Kontakts zieht. Die einzelnen Stränge des Netzwerks werden von Trans-Membran Proteinen aus der Claudin (Cldn) Familie gebildet. Seit ihrer Entdeckung im Jahr 1998 ist die Familie auf eine Anzahl von 26 Claudinen in Säugetieren angewachsen. Claudine nehmen eine fundamentale Rolle in der Ausbildung und Funktion der TJ ein, indem sie die TJ mit Barriere und spezifischen Ion-Kanal bildenden Eigenschaften ausstatten. Ihre elementar wichtigen Funktionen sind auf die Interaktionen ihrer extrazellulären Domänen (EZDs) und die damit verbundene molekulare Anordnung im parazellulären Spalt zurückzuführen. Vererbbare Mutationen in Claudinen und durch Pathogene hervorgerufene Veränderungen der TJ-Struktur können zur Ausbildung schwerer chronischer Krankheiten führen. Die Nano-Organisation der Claudine, welche ihre spezifische Funktion ermöglicht und die dynamischen Veränderungen des TJ Netzwerkes unter pathologischen Konditionen sind bislang weitestgehend unbekannt und müssen untersucht werden. Die apikale und axial zur optischen Ebene gerichtete Lokalisation einer vollausgebildeten TJ sowie die sehr dichte und aus mehreren Proteinen geformte komplexe TJ-Struktur hat es bislang zu einem sehr anspruchsvollen, wenn nicht unmöglichen Unterfangen gemacht multiple Claudine in einem TJ-Netzwerk zu mikroskopieren und deren einzelne Dynamik zu definieren. In den letzten Jahren haben erste wissenschaftliche Studien mit hochauflösender Fluoreszenzmikroskopie eine mögliche Lösung des Problems aufgezeigt, dennoch wurde das dahinterstehende Potential nicht ansatzweise ausgeschöpft.

In der vorliegenden Arbeit konnten wir zum ersten Mal demonstrieren, dass *stimulated emission depletion* (STED) Mikroskopie in Kombination mit neuesten Protein Markierungstechniken, das TJ-Netzwerk auf Nanoebene auflösen kann und es ermöglicht neue Einblicke in die Organisationsprinzipien der Claudine in Überexpression und Gewebe zu

bekommen. Eine automatisierte Analyse der TJ-Netzwerk bildenden Eigenschaften aller in Säugetieren exprimierten Claudine enthüllte die unterschiedlichen Fähigkeiten der Claudine, Netzwerke auszubilden und erlaubte es zum ersten Mal die Gruppierung der Netzwerk-bildenden Claudine in drei unterschiedliche Klassen. Überexpression von Cldn3, ein Barriere-bildendes Claudin, und Cldn2, ein Kanal-bildendes Claudin, zusammen mit anderen Claudinen erlaubte es uns fünf neue Nano-Interaktionen zu beschreiben: *intermixing, integration, induction, segregation* und *exclusion*. Mit Fokus auf die zum ersten Mal beschriebene Nano-Segregation der Kanal-bildenden Claudine, Cldn10a, Cldn10b and Cldn15 konnten wir auf endogenem Level die Segregation von Cldn2 und Cldn10a in isolierten murinen Nierentubuli sowie Cldn3 und Cldn15 im murinen Duodenum auflösen. Eine mechanistische Aufklärung, die verschiedenen extrinsischen Faktoren (funktionale Inhibierung der Cldn2 Pore, Depletion von Cholesterol und Verlust der Claudin-ZO1 Bindung) und intrinsische Faktoren (Deletion des Claudin C-Terminus und Claudin Chimären) einbezog, ergab, dass die Segregation in den EZDs der Claudine konserviert ist. Re-Expression von einzelnen Kanal- und Barrier-bildenden Claudinen und den segregierenden Claudin Paaren in einer genetisch modifizierten Epithelzelllinie, eine Zelllinie deren endogene TJ-Netzwerk Bildung durch einen fünffach Claudin *knockout* nicht mehr vorhanden ist, konnte auf funktioneller Ebene bestätigen, dass die Claudin Nano-Segregation eine notwendige Bedingung für die Bildung von funktionierenden spezifischen Ionenkanälen für die TJ darstellt und so einen konstanten Strom an Ionen über die TJ ermöglicht.

III Table of content

1 Introduction

1.1 Epithelium and endothelium

In multicellular organisms, organs and tissue compartments are separated from each other and the outer environment by a protective cell layer, the epithelium (Figure 1). By lining the exterior surfaces and inner surfaces of mammalian organs (e.g., intestine, kidney, skin, lung, glands), the epithelium creates a physiological border to the outer and luminal side of different tissues. It protects the inner tissue from pathogens and keeps the organ integrity and its homeostasis. As a highly specialized epithelium, the endothelium, enwraps our blood and lymph vessels, forming a physical barrier between blood and tissue.

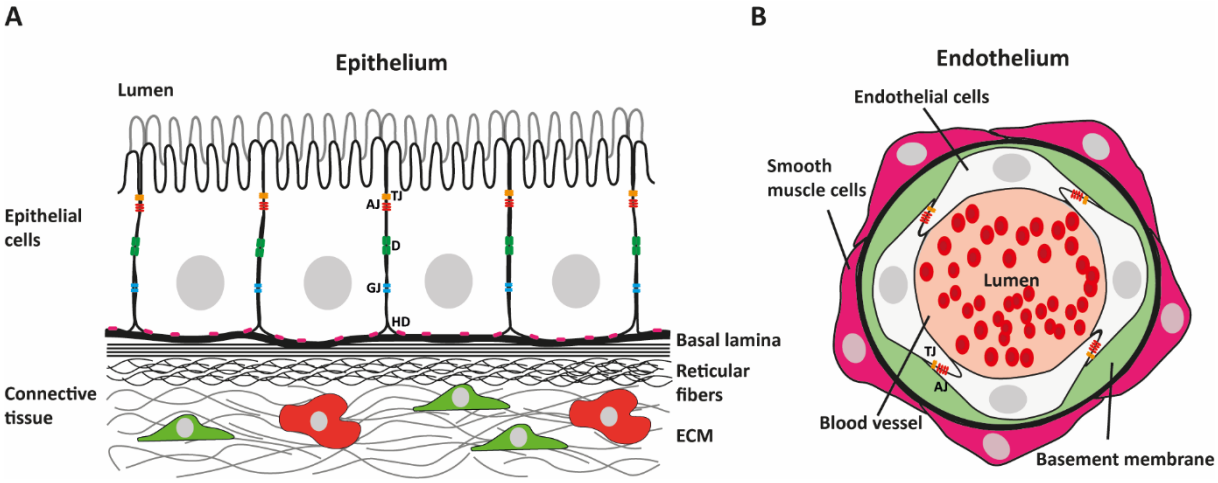

Figure 1 Illustration of a classic epithelium and endothelium. (A) Shown is a schematic illustration of a classic epithelium. Polarized epithelial cells face the luminal side with their apically increased cell surface area. Cell-cell junctions connect neighboring cells (here from apical to basal: tight junction (TJ) in yellow, adherens junction (AJ) in red, desmosomes (D) in green, gap junctions (GJ) in blue, hemidesmosomes (HD) in pink). The epithelial cell layer is connected on the basal side to the connective tissue formed by basal lamina, reticular fibers, and extracellular matrix (ECM). **(B)** Schematic illustration of an endothelium shown as a cross-section of a blood vessel. Endothelial cells enwrap the lumen of blood and lymph vessels. TJ (yellow) and AJ (red) are connecting the neighboring endothelial cells. The endothelial cells are encased by the basement membrane (green) and can be enclosed by different smooth muscle cells (red) depending on the tissue.

The epithelium is not only crucial for the protection against pathogenic, mechanical, and chemical harm, but also for the secretion of hormones in endocrine (e.g., insulin) and exocrine glands (e.g., digestive enzymes), the bidirectional transport of cargos, and the

absorption of nutrients (e.g., glucose uptake in the intestine). Similarly, the endothelium not only protects against the unwanted invasion of pathogens and their toxins from the blood (e.g., blood-brain barrier), but it also facilitates the exchange of solutes between blood and tissue (e.g., liver and bone marrow). Moreover, both cell layers must be highly flexible to resist the mechanical forces that occur during the widening and tightening of, e.g., the intestinal lumen or the blood vessels[1].

The selective transport of solutes and nutrients over the epithelium and endothelium is essential for the underlying tissue's function. There are two different ways of transport over the epi- and endothelial cell layer described: transcellular and paracellular. Transcellular transport allows the passage of solutes through the cells. This passage occurs along a gradient by passive channels, or by active channels, which use cell energy as a driving force. Another way of transcellular transport is transcytosis, a transport mechanism that starts by binding receptors on the cell membrane, followed by an endocytic uptake and transport through the cell. Paracellular transport describes the passive but selective passage of solutes and macromolecules through the paracellular cleft between neighboring epithelial and endothelial cells. It follows a bidirectional and electrochemical gradient and can be selective for charge and size. The primary regulator of the paracellular transport is a particular type of cell-cell junction, the tight junction (TJ)[1–3].

1.2 Tight junction

The TJ (lat. *zonula occludens)* is a vertebrate-specific cell-cell junction[3]. It forms in a Ca^{2+} dependent manner[4,5] together with the adherens junction (AJ) and desmosomes, the epithelial junctional complex in epithelial cells[1], and it connects, together with the AJ also neighboring endothelial cells[6,7]. It was first discovered in 1963 by Farquhar et al. and described in transmission electron microscopy (TEM) studies in different mammalian epithelia as a series of paracellular located “kissing points” (hemi fusions) between the apical-lateral membranes of two adjacent epithelial cells[8]. A few years later, Staehelin et al. (1969) and Goodenough et al. (1970) discovered with freeze-fracture electron microscopy (FFEM) that TJ spans along the whole epithelial contact site as a well-organized network (Figure 2A). The network is formed by ∼10 nm thick strands separated from each other by a distance of at least ∼8 nm[9–12]. Nowadays, it is known that the TJ is a multi-protein complex

consisting of different transmembrane proteins that connect neighboring cells with their extracellular domains. These transmembrane proteins are linked on the cytosolic side through adaptor proteins to the cytoskeleton and multiple signaling pathways (Figure 2B)[3]. Based on the protein composition of the TJ, it can take on several essential functions. Next to its protective and sealing function[13], it acts as a semi-permeable diffusion barrier for solutes[14] and as a fence for the specific sorting of lipids and proteins to the apical or basolateral membrane sides[15,16].

1.2.1 Semi-permeable diffusion barrier

The TJ forms a paracellular semi-permeable diffusion barrier for solutes (water and ions) and macromolecules[4,12,14,17] to maintain homeostasis in organs and tissue[2]. The semi-permeability of the TJ is passive but selective for charge and size. Its charge selectivity depends on the TJ protein composition, and the flow across the TJ is driven by an ion gradient and an electrochemical potential between the luminal and basal sides. In general, this ion gradient is created by active transcellular transport of solutes via transporters or ATP-regulated ion channels[2]. The TJ's paracellular ion permeability is described as a fast diffusion through ~4-8 Å sized pores[18,19]. The importance of the paracellular passive ion transport was shown by Wada et al. in 2013. In this study, the loss of the paracellular sodium transport back into the intestinal lumen leads to infant death due to insufficient glucose absorption by the sodium-glucose co-transport in mice[20]. The size-selective leaky pathway (exclusion limit ~30-60 Å)[21] facilitates diffusion of larger macromolecules over the TJ. The macromolecule diffusion is significantly slower than the paracellular ion permeability and might correlate more with the TJ's dynamic and structural remodeling processes[22–24]. However, the functional purpose is so far unclear.

1.2.2 Fence function

Another but not yet fully understood mechanism of the TJ is the fence function. The TJ has been described as an intramembranous barrier that allows the separation of membrane components and lipids between the apical and the basolateral side (e.g., Forssman antigen[25]). This separation creates a membrane environment needed for the polarization of epithelial cells and the formation of a functional epithelium[16,26,27]. It has been

shown that the diffusion of fluorescent lipids from the exoplasmic apical membranes of connected epithelial cells to the basolateral side is inhibited. In contrast, when applied to the cytoplasmic side, the diffusion of fluorescent lipids is not restricted. Disruption of the TJ by Ca^{2+} reduction unlocked this restriction. A transfer of applied fluorescent lipids from one cell to its neighboring cells has not been observed, speaking against a fusion of exoplasmic membranes as a potential mechanism behind the fence function[28]. One hypothesis is that the barrier and the fence function are most likely structurally related. It is assumed that the TJ transmembrane proteins and a specific lipid environment along their strands regulate the fence function together in a protein-lipid hybrid manner[3,29].

1.2.3 Structural organization

The TJ can be divided into two big compartments, the structural proteins, and the cytoplasmic plaque proteins. Together with the more basolateral located proteins of the AJ, it forms the so called apical junctional complex (AJC)[30] (Figure 2). The TJ-network structure, also called TJ meshwork (Figure 2A), is formed by different evolutionary conserved transmembrane proteins. The essential proteins involved in the TJ strand and meshwork formation belong to the 26 members strong (mammals; 25 members in humans), claudin (Cldn) family[3,31,32]. Additionally, the tetra-span transmembrane members of the TJ-associated MARVEL proteins (TAMP) family (occludin[33], tricellulin[34] and MARVELD3[35]) and junctional adhesion molecule (JAMs)[36] proteins are involved in the TJ formation (Figure 2B). The cytosolic adaptor proteins are essential for the initial TJ formation, TJ protein recycling, and the dynamic reaction to outer environment changes[3]. The key adaptor proteins are the zonula occludens proteins 1-3 (ZO1[37], ZO2[38,39], ZO3[40,41]), that act as a catalysator for claudin polymerization[42] and as a linker to the actin cytoskeleton. Other essential cytosolic adaptors belong to the multi-PDZ (PSD95, Dlg1, and ZO1) domain (MUPP-1)[43] proteins and the group of membrane-associated guanylate kinase inverted (MAGI1, 3) proteins[44,45]. Cingulin has been described as a microtubule, actin, and myosin II adaptor for the TJ that plays an essential role in recycling TJ proteins and fine-tuning the membrane tension at the apical membrane side[46–49]. Environmental influences can cause the localization of tight junctional located transcription factors, including ZONAB (ZO-1 associated nucleic acid binding protein) to the nucleus to regulate the expression of pro-proliferation genes[50], but ZONAB can also

interact at the TJ with kinases (e.g., CDK4)[51], GTP-binding proteins[52] and different post-transcriptional regulators[53]. Located in the most apical part above the TJ are the polarity signaling PAR (PAR3, PAR6, and aPKC) and Crumbs complex (Crumbs/Pals1/PATJ)[54,55].

For a long time, it was debated whether proteins form the TJ meshwork or whether the observed membrane attachments were formed by inverted cylindrical lipid micelles[3,16,56]. After discovering the TJ transmembrane proteins and the *in vitro* reconstitution of TJ strands by overexpression of claudins in a TJ-free fibroblast system[57], it is now widely accepted that proteins are mainly responsible for strand formation. In line with this assumption, recently published data demonstrated that claudin-free epithelial cells[58] do not form TJ strands anymore. Nevertheless, it is known that lipids or a specific lipid environment (lipid microdomains) are needed for the TJ integrity, its initial formation, and cell polarity. Some TJ transmembrane proteins require cholesterol-rich microdomains in the membrane to localize properly to the TJ. A reduction of the membrane-bound cholesterol drastically changes the properties of the epithelial TJ[59,60]. Shigetomi et al. demonstrated that the AJ seems to be involved in the interplay of cholesterol and TJ. A knockout (KO) of α-catenin led to a change in the plasma membrane's lipid composition and increased endocytosis of claudins. The addition of cholesterol fully restored the disrupted TJ[61] indicating that the TJ's lipid composition and cholesterol are connected to the AJ.

Based on calcium-switch experiments, it is proposed that first AJ proteins and ZOs form a connection between the neighboring cells, followed by recruitment of occludin and JAM-A, and finally, the strand formation by claudins and the specific localization of the PAR-complex[62,63]. Since the phosphorylation of claudins and other junctional molecules by aPKC leads to an increased apical junction localization, it is assumed that the phosphorylation of these proteins initiates the TJ strand assembly[64]. The gaps in between the TJ strands would then be filled with specific lipids. These lipids form, together with the transmembrane proteins, a continuous belt; the protein-lipid hybrid model. This co-arrangement of lipids and specific transmembrane proteins might also explain the observed different dynamic properties of different TJ proteins in TJ strands[65,66].

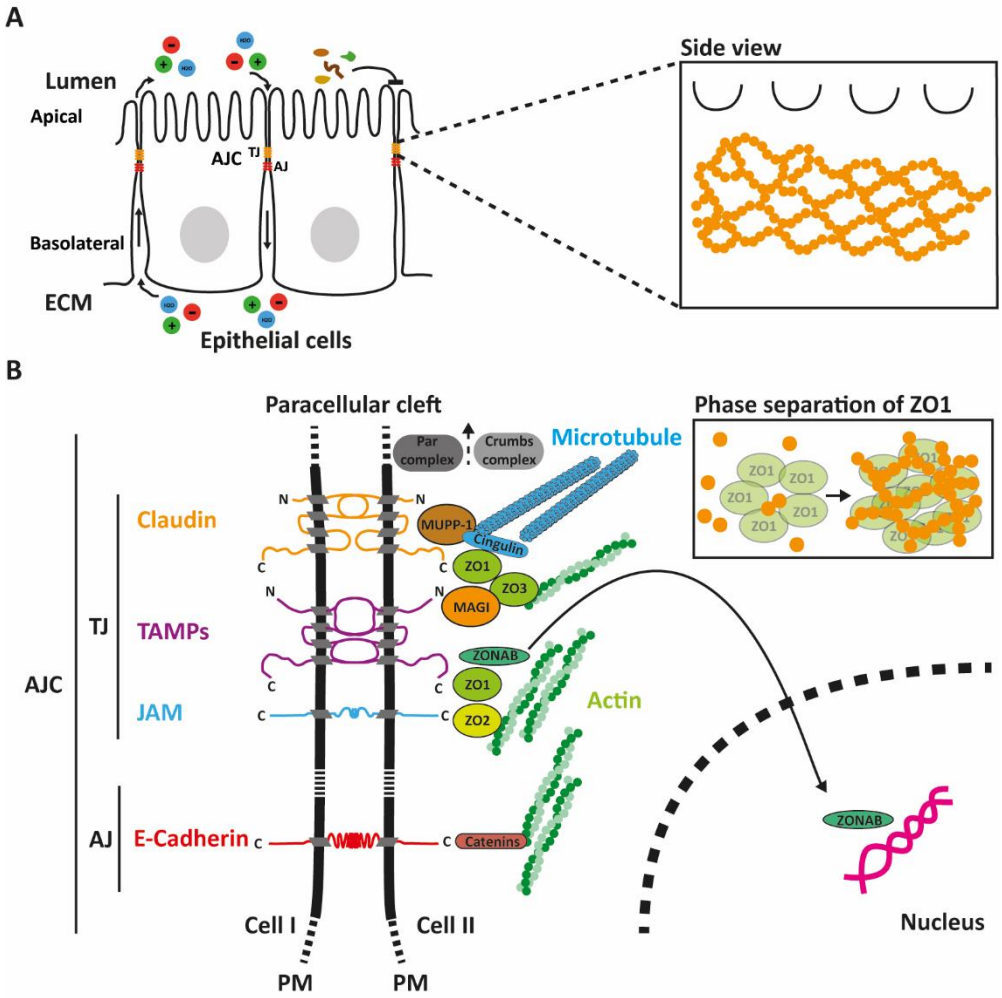

Figure 2 Schematic illustration of the apical junctional complex. (A) In epithelial cells, the tight junction (TJ) (yellow) is located above the adherens junction (AJ) (red) at the border between apical and lateral membranes of adjacent cells forming together the apical junctional complex (AJC). The TJ spans as a meshwork along the whole apical cell-cell contact side. Its function is to protect the underlying tissue from pathogens and to act as a semi-permeable barrier for solutes (dots: cations (green), anions (red), and water (blue)) through the paracellular cleft. **(B)** Overview of the main proteins of the AJC. The structural proteins of the TJ include the claudin family, TJ-associated MARVEL proteins (TAMPs: occludin, tricellulin, MARVELD3), and junctional adhesion molecules (JAM-A, B, C). These proteins consist of one to four transmembrane domains, extracellular domains for the interaction with proteins of the adjacent membrane, and cytosolic parts for the interaction with cytoplasmic plaque proteins. The key adaptor proteins on the cytosolic side are the zonula occludens proteins (ZO1-3). ZOs act as the major linker on the cytosolic site for the structure proteins, other adaptor proteins (e.g., cingulin, MUPP-1, MAGI), transcription factors (ZONAB), and cytoskeletal elements (actin and microtubules). A newly described function of ZO1 is the phase separation-based organization of claudin molecules in the lateral plasma membrane that initiate the claudin strand polymerization at the apical contact side. The AJ is located basolateral of the TJ, and it is mainly formed by *trans* interacting E-cadherin molecules. On the cytosolic side E-cadherin molecules are linked through α- and β-catenin to actin filaments. The two polarity complexes PAR and Crumbs are apically located of the TJ.

1.2.4 Tight junction related disease

Due to its essential function as a paracellular gatekeeper, the TJ is linked to many human diseases, usually of inherited nature, caused by mutations and polymorphisms in transmembrane proteins (claudins and TAMPs) but also in cytosolic TJ proteins (ZOs, ZONAB). Polymorphisms among claudin members are the most common cause for severe diseases, e.g., Cldn14 (non-syndromic deafness)[67,68], Cldn16 and Cldn19 (familial hypomagnesemia, hypercalciuria, nephrocalcinosis)[69], Cldn10b (HELIX-syndrome (HELIX: hypohidrosis, electrolyte imbalance, lacrimal gland dysfunction, ichthyosis, and xerostomia))[70], Cldn1 (neonatal ichthyosis)[71]. Moreover, claudins and TAMPs are also targets of multiple different pathogens, since these proteins can be hijacked and used as a virus entry site (e.g., Cldn1 and occludin for Hepatitis C)[72] or bound by bacterial toxins (Cldn3 and Cldn4 by *Clostridium perfringens* enterotoxin (CPE)[73,74], occludin by *Vibrio cholerae*[75]). Interference of the tight junction signaling pathways by pathogens can disrupt the TJ and lead to an inflammatory reaction (e.g., intestinal bowel disease)[76]. Several described diseases are linked to TJ disruption and a inflammatory response[77], but often, it remains unclear if the observed change in the TJ is the actual cause or a consequence of the infection. Therefore, it is essential to understand the pathology, causes, and consequences of disease-causing TJ disruptions.

1.3 Claudins

The TJ meshwork is formed by proteins from the claudin family (~20-24 kDa). Since their first discovery (Cldn1 and Cldn2 in the chicken liver) in 1998[31], the claudin family has expanded to a large protein family, including now 26 different claudins in mammals and, excluding Cldn13, 25 different claudins in humans[3,29,32,74,78]. Based on their sequence similarity, claudins can be divided into two large groups, the classic claudins (Cldn1-10, Cldn14, Cldn15, Cldn17, Cldn19) and the non-classic claudins (Cldn11-13, Cldn16, Cldn18, Cldn20 and Cldn22-27)[79,80]. In humans these two groups can be further divided into five different subgroups[80] (Figure 3) with an additionally different clustering of Cldn11, Cldn18 and Cldn20 to the in previous studies defined group of classic claudins. Cldn7, Cldn10, Cldn11, Cldn18, and Cldn19 are expressed in multiple spliced variants with different structural and functional properties. The expression of these isoforms is often restricted to

specific tissues or tissue parts[32]. Claudins are ubiquitously expressed at different expression levels in mammalian tissue, ranging from only two claudins in the kidney's proximal tubule (PT) to more than six different claudins in the more complex thick ascending limb (TAL) of the kidney tubule[81]. Claudins in the epithelial and endothelial TJ are involved in the semi-permeable paracellular barrier function of the TJ meshwork by providing sealing or specific ion channel properties[32]. Depletion of all endogenously expressed claudins causes a loss of the TJ meshwork and severe defects in the paracellular barrier in epithelial cells[58]. Nonetheless, already a loss of single claudins can have a severe impact on the TJ and organ homeostasis[20,82,83]. There is also evidence that claudins are involved in several epithelial signaling pathways and their deregulation is essential for cancer development and metastasis[84,85].

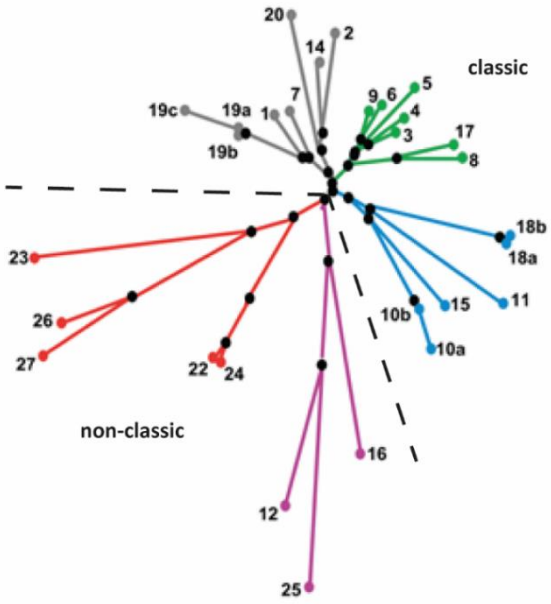

Figure 3 Phylogenetic tree of all human claudins. The different subgroups are labeled in five different colors: Subgroup A (Cldn1, Cldn2, Cldn7, Cldn14, Cldn19a-c, Cldn20) in grey, subgroup B (Cldn3, Cldn4, Cldn5, Cldn6, Cldn8, Cldn9, Cldn17) in green, subgroup C (Cldn10a-b, Cldn11, Cldn15, Cldn18a-b) in blue, subgroup D (Cldn12, Cldn16, Cldn25) in pink and subgroup E (Cldn22, Cldn23, Cldn24, Cldn26, Cldn27) in red. Cldn21 was erased out of the illustration since it has been confirmed that the discovered sequence is identical to Cldn24. The subgroups A-C are the classic claudins, D-E represent the non-classic claudins. In the present work, instead of human, murine Cldn14, Cldn18a-b, Cldn26 and Cldn27 were used (Figure S2). Adapted and modified from Günzel and Fromm et al. (2012)[80].

1.3.1 Structure

Almost all known claudins share the same structural features (Figure 4A). A single claudin molecule consists of four helical transmembrane domains, a short N-terminus (except Cldn5, Cldn16, and Cldn25), a short internal loop, and a longer C-terminus on the cytosolic side, as well as two extracellular loops (ECLs), a larger ECL1 (forming an anti-parallel β-sheet[86,87]) and a smaller ECL2, facing the extracellular space. So far, no relevant function has been described for the N-terminus nor for the internal loop of claudins. At the very end of the C-terminus, most claudins (except Cldn12 and Cldn24-27) contain a four amino acid long PDZ-binding motif[32]. The PDZ-binding motif allows claudins to interact with the PDZ1 domain of ZO proteins[88]. This interaction is essential for the barrier function and the initial formation of a fully functional TJ (see chapter 1.6.1). Additionally, the C-terminus contains several phosphorylation sites that are involved in claudin transport to and their localization at the TJ[64,89–93]. Palmitoylation sites are located at the transition from the C-terminus into the fourth transmembrane domain (TM_4) and in the intracellular loop (Figure 4A)[94]. The most studied structures of claudins are the two extracellular loops, ECL1 and ECL2. In general, the ECL1 is larger than the ECL2, and it contains the claudin-specific and well-conserved amino acid (AA) signature: W-GLW-C-C (W: tryptophan, G: glycine, L: leucine, C: cysteine)[32]. Moreover, it contains two very conserved cysteines that stabilize the anti-parallel β-sheet[95]. Together with the transmembrane domains, ECLs are involved in the interaction with neighboring claudin in the same membrane (*cis*-interaction)[96–98]. Next to the *cis*-interaction, ECLs are also critical for the interaction with claudins of adjacent cells in *trans*[87,96,98–100].

Depending on their AA composition in the ECL1, claudins provide a specific ion permeability to the TJ by forming ion-selective pores in the TJ strands[101–103]. According to the solved crystal structure of the cation channel-forming Cldn15[86], it is assumed that claudins are connected via specific interactions of adjacent extracellular domains that form anti-parallel orientated claudin tetramers. These tetramers form a β-barrel-like structure that defines an ion pore with an estimated diameter of 4-8 Å (Figure 4B)[18,81]. Depending on the AA in the center of these β-barrels, claudins equip the TJ with cation, anion, and water channels and/or with barrier properties. Further, it is proposed that two antiparallel strands align with each other to form the final functional intramembrane TJ strand[86,87]. This

particular arrangement of parallel double strands could be recently observed by Krystofiak et al.[104] in carbon replicas of TJ fibrils in Cldn11 overexpressing HEK cells.

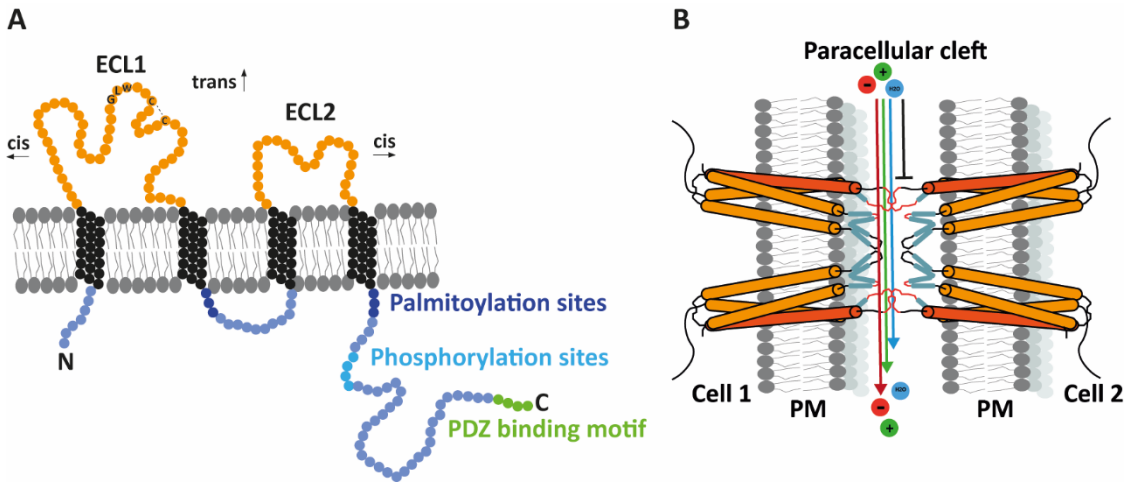

Figure 4 Single claudin domain structure and the claudin tetramer as a functional unit in the paracellular cleft. (A) An exemplary model of the structure of a claudin molecule in the plasma membrane. On the cytosolic side, it contains a short N-terminal part, a short intracellular loop, and a longer C-terminal part. Palmitoylation sites (dark blue) and phosphorylation sites (light blue) are located at the C-terminus and the intracellular loop. The last four amino acids (AAs) of the C-terminus form a PDZ-binding motif (green) that can interact with cytosolic adaptor proteins of the tight junctional cytoplasmic plaque. Claudins contain four transmembrane (TM) domains (black) and two extracellular loops, ECL1 and ECL2 (orange), that allow the interaction with other claudin molecules in the same membrane (*cis*) and claudin molecules of the adjacent neighboring membrane (*trans*). The ECLs play a crucial role in the formation of the functional tetrameric claudin unit. **(B)** Based on the resolved crystal structure of Cldn15[86], an antiparallel claudin tetramer was proposed as a polymerization model, introducing ion permeability and sealing function[87]. In this model, the AA composition of the variable region of the ECLs determines the functionality of claudins as a paracellular ion channel for anions (red dots and arrow), cations (green dots and arrow) or water (blue dots and arrow) or as a sealing component (black line).

1.3.2 Barrier-forming claudins

Among the 26-known mammalian claudins, only four claudins are described to form a specific paracellular ion channel on their own. So far, all the other 22 claudins are classified as predominantly barrier-forming claudins that show no ion specificity and mostly an increased transepithelial resistance (TER) compared to ion channel-forming claudins[32]. Two of the first discovered claudins, Cldn1[31] and Cldn3[74], are very well studied and known to contribute sealing properties to the TJ. Both claudins are expressed among various tissues

and different organs[32]. Especially the expression of Cldn1 in the mammalian stratified epidermis is of significant importance considering that constitutive KO of Cldn1 is lethal to mice (death < 1 day) due to an unlimited water loss from the epidermis[83]. *In vitro* studies demonstrated that Cldn3 acts as a sealing component by reducing the TJ's ion permeability[105]. Yet, a Cldn3 knockout did not lead to a significant phenotype in mice due to the presumable compensation of the loss by other barrier-forming claudins (Cldn1 and Cldn4)[106]. Several *in vitro* overexpression studies showed that barrier-forming claudins have a tendency to interact with each other[80,107] except for Cldn11[107]. Cldn11 is in contrast to Cldn1 and Cldn3 only expressed in three regions of the body: Sertoli cells in the testis, basal cells in the cochlea, and myelin-forming cells in the brain[32]. Cldn11 forms multiple parallel strands in these tissues and contributes to the generation of a physical paracellular barrier for spermatogenesis[108], functional hearing[109] and normal central nervous system (CNS) function[110].

1.3.3 Channel-forming claudins

The first evidence for a connection between claudins and the paracellular ion permeability was revealed by Simon et al. in 1999. Through their discovery of the necessity of Cldn16 (paracellin-1) for paracellular magnesium resorption, a new claudin function emerged[69]. The ion channel-forming claudins can be divided into two groups: cation channel-forming and anion channel-forming claudins. The cation channel-forming group includes Cldn2[111,112], Cldn10b[113,114], Cldn15[115] and the combination of Cldn16 and Cldn19[116], whereas Cldn10a[113,114], Cldn17[117,118] and the combination of Cldn4 and Cldn8[119] form the anion channel-forming group. A distinct permeability for water was described for Cldn2[120,121] and Cldn15[122].

Cldn2 was discovered together with Cldn1 by Furuse et al. in 1998[31], and it is by now the most investigated claudin channel. Cldn2 is like Cldn1 and Cldn3 expressed in several mammalian tissues and provides the TJ with permeability for monovalent ions and water[111,112,120]. Cldn2 cysteine mutational analysis and patch-clamp measurements showed that the ion permeability is based on charged residues in the ECL1, and demonstrated a dynamical gating of paracellular claudin channels[123,124]. Among the different epithelial cell lines, Cldn2 is highly expressed in MDCKII cells and significantly influences the leaky

properties and high sodium permeability of the TJ in this cell line[112,125]. In the small intestine of mammals Cldn2 is expressed together with another cation channel-forming claudin, Cldn15. Although Cldn2 and Cldn15 share the same ion specificity, they are differently expressed in the intestinal epithelium: Cldn2 is highly expressed in the intestinal crypts of mice whereas Cldn15 is expressed in a gradient fashion from the crypts to the villus[126]. A constitutive KO of Cldn2 in mice did not significantly change viability, only a decreased net absorption of sodium in the proximal tubule of the kidney could be observed[121,127]. A single KO of Cldn15 in mice led to a more severe phenotype including a mild glucose malabsorption over the intestinal epithelium[127]. Nevertheless, both the Cldn15 and Cldn2 single KO mice were vital. Interestingly, a double KO (DKO) of Cldn2 and Cldn15 led to the death of infant mice due to defective absorption of glucose and fatty acids over the intestinal epithelium. The DKO disturbed sodium flux from the blood into the lumen what is essential for the uptake of glucose via sodium-glucose cotransporter. The strong effect in the DKO mice, combined with the mild phenotype in the single KOs indicates a mutual compensation of the cation permeability by Cldn2 and Cldn15[20].

The two essential isoforms of Cldn10, Cldn10a and Cldn10b, differ in their first TM and the first ECL[113]. The differences that are present in these domains are sufficient to completely change the ion permeability properties[97]. Cldn10a forms channels for monovalent anions, and Cldn10b channels for monovalent cations[128]. This difference in their ion permeability is accompanied by a difference in their tissue expression pattern. Cldn10a expression is restricted to the kidney's PTs (PCT: proximal convoluted tubule; PST: proximal straight tubule). Cldn10b is widely expressed but greatly found in the nephron downstream of the proximal tubule (thin ascending and thick ascending limb (TAL)) and secretory glands (sweat glands)[81,113,128]. Noteworthy, Cldn10a and Cldn10b share high sequence homology with Cldn15 making up a supposed separate channel-forming group, that differs in certain regions of their amino acid (AA) sequence compared to other channel-forming claudins (Figure 3). A deletion of Cldn10b in the TAL leads to the development of hypermagnesemia and nephrocalcinosis[129]. A constitutive KO of Cldn10 has not yet been described. However, it is known that inherent polymorphism and mutations of Cldn10b can cause a loss of function due to junctional mis localization resulting in severe claudinopathies. One of the more recent discovered disease caused by Cldn10b mutations is the HELIX-syndrome (e.g., autosomal recessive mutation: Cldn10b^{N48K})[70,82]. The HELIX-syndrome includes several symptoms from

hypohidrosis, hypokalemia and ichthyosis as consequence of a decreased NaCl absorption in the TAL of the kidney.

The anion permeability of Cldn17 was shown in overexpression studies in MDCKC7, a epithelial cell line that forms a sealing tight junction[117,118]. Cldn17 expression causes a slight increase in permeability for chloride. Whether Cldn17 also plays a role in ion permeability *in vivo* and not only *in vitro* must be further investigated.

Not only single claudins can form specific ion channels but also combinations of different claudins can do so. Cldn4 and Cldn8, two as barrier-forming described claudins, can form a monovalent anion channel (e.g., Cl^-)[119]. This observation is still under debate, and its specificity must be further validated. However, it is widely accepted that Cldn16 and Cldn19 can from a channel for divalent cations (e.g., Mg^{2+})[69,116,130,131]. Cldn16 and Cldn19 polymorphisms cause the inability to form Mg^{2+}-channels in the TAL of the mouse kidney and are linked to human diseases based on disbalances in the ion homeostasis[116,132,133].

The involvement of other transmembrane proteins in the claudin pore formation or their effect on paracellular ion or macromolecule permeability was intensively studied. The discovered key players belong to the TAMPs and JAMs on the transmembrane protein side, whereas on the cytosolic side, ZO proteins act as the major scaffolding adaptor protein.

1.4 TJ-associated MARVEL proteins

The TJ-associated MARVEL (MAL and related proteins for vesicle trafficking and membrane link) protein (TAMP) family is well conserved among mammalians and consists of three tetra-span transmembrane proteins: occludin[33] (~65 kDa), tricellulin[34] (~63 kDa), and MARVELD3[35] (~44 kDa). All TAMPs are expressed in most of the mammalian epithelial tissues but differ in their expression levels and localization specificities[33–35,134]. Their general structure is comparable to the claudins: cytosolic N-terminus, an intracellular loop between TM_2 and TM_3, a long C-terminus with multiple interaction sites for adaptor proteins, and two ECLs facing the TJ proteins of the neighboring cell. The N- and the C-terminus of the TAMPs are longer compared to claudins resulting in molecules that are almost three times the size of claudin molecules. One key property that all MARVEL proteins share is their association to cholesterol-rich membrane microdomains[135]. Association between the TAMP proteins with

specific lipid microdomains could explain TJ's fence function and the TJ rupture upon cholesterol depletion, however, these involvements are still unclear and must be investigated.

Among the TAMPs, occludin shows the most substantial connection to and interaction with claudins. Occludin was the first tight junctional transmembrane protein that was discovered and described[33]. *In vitro* KO of occludin is characterized by a decrease in the TER and an increase of macromolecular flux[136,137] whereas a KO in mice leads to different more complex phenotypes (growth retardation, deafness, brain calcification)[138–140]. Inherent mutations of occludin in humans are linked to limited development, brain calcification, seizures, and renal dysfunction[141–145]. It has been shown that occludin's ECLs and TMs play a role in protein recruitment towards the stability of the TJ. To what extent occludin can interact with the ECLs of claudin molecules and whether it can be incorporated in claudin strands is still unknown. There is evidence for a possible direct interaction of occludin with claudins[57,66]. However, the highly dynamic properties of occludin observed in FRAP experiments[65] speaks on the other hand, against it.

Tricellulin localizes primarily to the complex tricellular tight junctions (tTJ), the contacts where three different epithelial cells meet[34]. The tTJ evolves out of a bicellular junction and forms an extension of the TJ meshwork into more basolateral regions, called the central tube[10,146,147]. It is known that claudins and occludin localize at the tTJ, however, there is no indication that they have a specific preference for or specific function in it. In 2019 the group around Mikio Furuse showed in a KO study that angulin-1, another tTJ protein, and not tricellulin is responsible for the formation of tTJs. The resulting impaired barrier function indicates a possible minor role of tricellulin but a significant role for angulin-1 in the tTJ formation[148]. Visual separation of different tTJ proteins with fluorescence microscopy techniques was due to the difficulties that it presents not successful yet. FFEM of claudin and tricellulin double-transfected HEK293 cells revealed that tricellulin can interact with claudin-based TJ strands and alter their morphology from a rounded shape to more rectangular meshes[66,149]. Yet, a direct interaction of tricellulin with claudins could not be observed, and the exact mechanism of how the tTJ is formed must be still described.

MARVELD3 was identified as the last of the TAMP proteins[35], and very little is known about its functional purpose and impact on the TJ. There are two isoforms known, and both

tend to localize at the bicellular TJ. In MARVELD3 knockdown (KD) experiments, a slight increase of the TER could be observed[35]. A potential direct interaction of MARVELD3 with claudins was observed by Cording et al. in 2013 in co-expression with Cldn1 as well as with the other described TAMPs tricellulin and occludin[66]. But the exact location of MARVELD3 within a TJ meshwork is still unknown.

1.5 Junctional adhesion molecules

Next to the tetra-span transmembrane proteins, members of the immunoglobulin (Ig) superfamily, the junctional adhesion molecules (JAMs; JAM-A, -B, and -C) localize at the TJ[36] and got increasing attention in recent studies. JAMs, especially JAM-A, are expressed by various leukocytes and platelets[150,151] and also by epithelial and endothelial cells. JAMs localize via their single transmembrane domain at the TJ, interacting with their two extracellular Ig-domains with the JAMs of the neighboring plasma membrane[152]. The cytosolic part of JAM-A seems to interact with cytosolic proteins, including ZO1. In 2019 Otani et al. introduced a novel MDCKII quintuple claudin KO (QKO) cell line[58]. The KO of five claudins these cells express the most, leads to a complete loss of TJ strands. However, with FFEM detected single membrane appositions seemed to be sufficient for maintaining a barrier to macromolecules (≥4 kDa). Interestingly the epithelial polarity was fully developed in MDCKII QKO cells whereas an additional KO of JAM-A demonstrated a complete loss of the TJ barrier for macromolecules and an impaired polarity of the cells, indicating a cofunction of JAM-A with claudins in barrier formation and cell polarity[58].

1.6 Cytoplasmic plaque of TJ

On the cytosolic side of the TJ, multiple different proteins form the cytoplasmic plaque. These proteins form an interface between membrane proteins, the cytoskeleton and several signaling proteins (kinases and phosphatases), allowing the TJ to react rapidly to environmental changes. The central scaffolding proteins contain multiple interaction motifs. Among them, ZO proteins take a leading role.

1.6.1 Zonula occludens proteins

There are three different zonula occludens (ZO1, -2, -3) proteins described. All of them act as scaffolding proteins by bringing TJ membrane proteins close together. Whereas ZO3 seems to have minor effects on the TJ[153], especially ZO1 and partially ZO2 affect the TJ formation and dynamic[37–41]. ZO1 is a large protein (~220 kDa) with several different protein-protein interaction domains (Figure 5)[37]. It consists of three N-terminal located PDZ-domains (PDZ1-3), a short SH3 (SRC homology 3) domain, and a GUK (yeast guanylate kinase homology) domain. In the C-terminal half, it contains a large actin-binding region (ABR) to bind F-actin[154]. The three PDZ domains are essential for the interaction with the C-terminal ends of TJ membrane proteins. Claudins bind to the PDZ1 domain of ZO1, JAMs bind to the PDZ3, and interaction with ZO2 and oligomerization are provided by the PDZ2. The large GUK domain serves as an interaction site for occludin and the SH3 domain to the signaling protein ZONAB[155,156]. Within the ZO1 protein, an intramolecular interaction of GUK and a unique-6 motif (U6) can lead to a closed formation and a self-inhibition of ZO1[42]. The single constitutive KO of ZO1 or ZO2 was revealed as embryonic lethal[157,158]. In 2019 Otani et al. could show that ZO1 and ZO2 are essential for forming TJ strands and meshworks[58]. These findings go in line with Beutel et al. in 2019 that suggested that ZO proteins can recruit multiple different TJ proteins including claudins to the PM via phase separation and oligomerization. Nevertheless, although the phase separation of ZOs is regulated by self-inhibition and phosphorylation, it is still unclear how ZO proteins precisely controls the multi-step junction assembly[42].

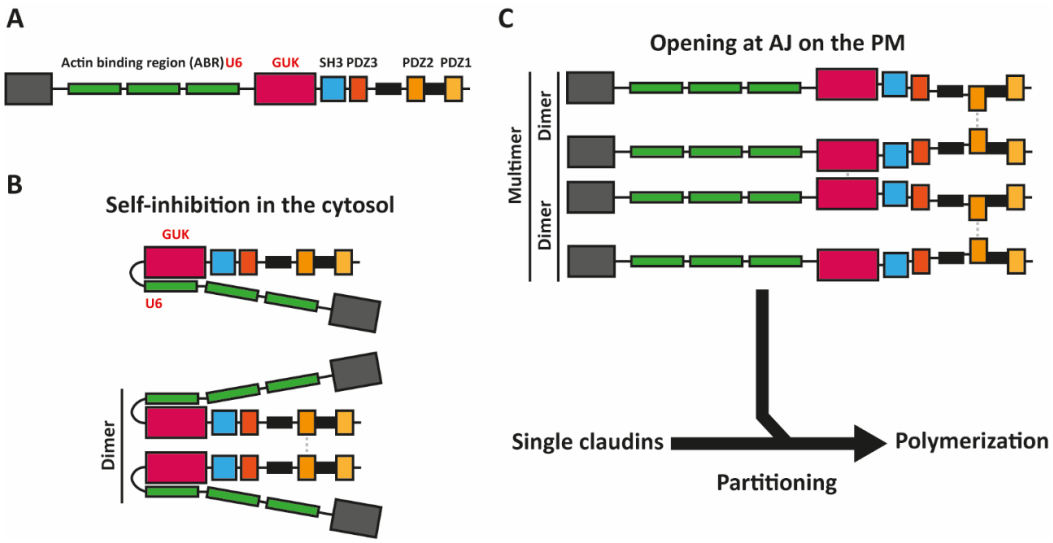

Figure 5 Domain structure of ZO1. (A) Domain structure of the open zonula occludens protein 1 (ZO1). The actin-binding region (ABR), the unique-6 motif (U6), the GUK (yeast guanylate kinase homology) domain, the SH3 (SRC homology 3), and the PDZ1-3 (PSD95, Dlg1, ZO1 homology) domains are annotated. **(B)** Self-inhibition of ZO1 due to an interaction between the U6 and GUK domain and the formation of dimers via the PDZ2 domain. **(C)** Back folding of the U6 domain and oligomerization of ZO1 leads to phase separation and recruitment of claudins and their polymerization into claudin strands at the apical side of the plasma membrane.

1.6.2 Actin

The connection of actin to the TJ complex and its impact on the TJ function was mainly described under inflammatory conditions. It has been shown that actomyosin rearrangements led to an increased permeability for macromolecules over the TJ due to transient breakages of TJ strands[159–161]. ZO1 is described to link the TJ transmembrane proteins to the actin cytoskeleton. Studies in zebrafish embryos revealed that ZO1 is transported along the lateral membrane to the apical side in association with the actomyosin retrograde flow. Whether the connection of the TJ with actin is of a more dynamic nature[162] and how the various actin-linked signaling proteins regulate the described tension at the cytosolic side is unknown[3,163]. Nevertheless, recent discoveries showed that the linkage of ZO1 to actin seems to be of transient nature. Changes in the mechanical force on the TJ and in ZO1 phase separation leads to a self-inhibition of ZO1[42,164,165]. However, it was also shown that the junctional actomyosin belt assembly is augmented when TJs are disorganized[166–168] and that Rho-dependent actomyosin contraction can repair small breaks in TJs[169].

1.7 Tight junctional nanostructure

One of the critical elements in understanding TJ's properties, organization, and underlying dynamics is the visualization of the TJ nano-organization. Over the last eight decades, various microscopy techniques provided novel insights into the TJ protein arrangement, deciphering step by step the underlying complex mechanism and interactions that regulate the properties of the TJ.

1.7.1 Transmission- and freeze-fracture electron microscopy reveal the TJ meshwork nanostructure

The initial discovery of the TJ and the first description of its nanostructure were based on electron microscopy (EM) techniques. The classic description of the TJ as a series of kissing points in the apical region of the cell is founded in transmission electron microscopy (TEM) of different epithelia in tissue samples[8] (Figure 6A). TEM revealed the localization of the different junction types (TJ, AJ, GJ, D) along the epithelial contact side and the localization of the dense actin-rich cytoplasmic plaque. TEM is still used as an essential technique for studying changes of the TJ contacts. But conventional TEM has its limitation in resolving the TJ meshwork between two connected cells with its interconnected strands, formed meshes and the electron dense cytoplasmic plaque.

In freeze-fracture electron microscopy (FFEM) this problem is solved by physically breaking up the previously fixed cellular plasma membrane along the lipid bilayer's hydrophobic plane in a snap freezing step[170]. The previously hidden structural details are now exposed on a platinum-carbon-covered fractured plane and can be visualized with TEM. As a result, it provides planar views of the internal organization of membranes and the TJ meshwork[9]. The TJ strands are visible either on the protoplasmic (P) fracture face (Figure 6B)[9] or the complementary exoplasmic (E) fracture face. The complementary side contains the pattern of the strands as empty grooves. One huge advantage of FFEM is the preservation of the lipid environment by its rapid freezing down to -120 °C, which immobilizes the membrane lipids[170]. FFEM is by now still one of the most valuable techniques in providing access to the ultrastructure of the TJ meshwork. In combination with other biochemical and microscopical techniques, it can demonstrate the total impact of different TJ components on the TJ ultra-structure[31,57].

The unquestionable limitation of FFEM is that the determination of the exact localization of multiple different proteins within the TJ is not possible. Multi-labeling by using differently sized gold-labeled antibodies allows discriminatory labeling of proteins in the TJ meshwork. Still, the very weak labeling density does not allow the exact spatial determination of the labeled proteins. Moreover, FFEM can only be used for fixed samples and does not provide any information about the dynamics in the TJ[57]. Also, it cannot be excluded that the harsh fixation of the TJ leads to some crucial structural changes and the

creation of structural artifacts[171]. Finally, FFEM is characterized by a very low sample rate due to long preparation and acquisition time, making high-throughput analysis of the TJ nanostructure very difficult to achieve.

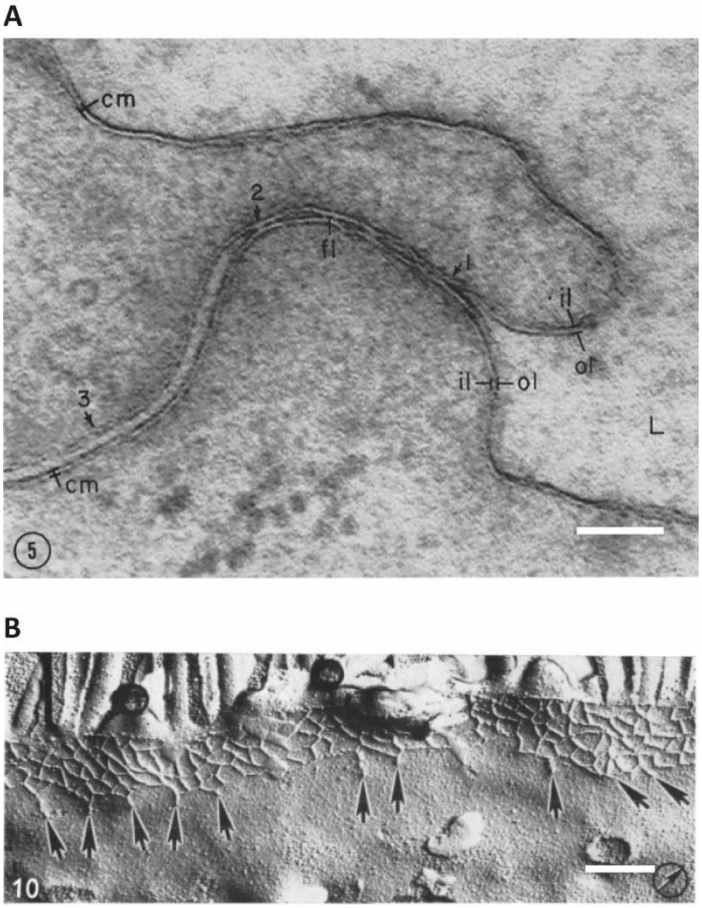

Figure 6 Transmission- and freeze-fracture electron microscopy of the TJ. (A) Transmission electron microscopy (TEM) image of an endogenous TJ in rat gastric epithelial tissue. The black arrows (labeled: 2, fl, l) point at the well-described hemi fusions between the two neighboring membranes (adapted and modified from Farquahr et al. (1963))[8]. **(B)** Freeze fracture electron microscopy (FFEM) image of the TJ meshwork at the apical contact side between two rat intestinal epithelial cells. Multiple claudin-based meshes and loose strands at the basolateral side are visible and pointed out by the black arrows (adapted and modified from Staehelin et al. (1973))[10]. Scale bars: 50 nm (A), 200 nm (B).

1.7.2 Confocal and basic fluorescence microscopy uncovered specific interactions between the transmembrane proteins of the TJ

Different fluorescence microscopy-based techniques (e.g., Förster resonance energy transfer (FRET), fluorescence recovery after photobleaching (FRAP)) were used to study tight

junctional protein interactions and their localization in the endogenously and by claudin overexpression formed TJ.

Confocal imaging of TJ in epithelial cell layers or tissue sections revealed several general localization patterns of TJ proteins, including the discovery of the different localization of the TAMPs[33,34] along the TJ (e.g., bicellular localization of occludin and tricellular localization of tricellulin), the more lateral localization of specific claudins (e.g., Cldn7) compared to other claudins[172] as well as the higher dynamics of TAMPs compared to claudins shown in FRAP experiments[65,66]. Furuse et al. discovered in 1998, with confocal microscopy, that the overexpression of claudins in TJ-free fibroblasts led to the formation of a TJ-like meshwork with multiple interconnected claudin strands[57]. The first main advantages of this system compared to a common epithelial cell line is the possibility to study the interaction behavior of TJ structure proteins and their influence on each other without any influence by endogenously expressed TJ structure proteins. The second big advantage is the conversion of the TJ from an axial direction into a lateral direction, enabling imaging of the TJ at a higher resolution (Figure 7). This system was used several times to study the interactions between claudins, TAMPs, JAMs, and ZO1[23,66,173]. To uncover their abilities to interact with each other, mainly two different techniques were used. Interactions in *cis* were verified by FRET and interactions in *trans* by co-culture experiments. Those observations were often expanded with yeast-to-hybrid interaction studies[119,130] and FFEM[31,66,96–98,174–176] images. Together, these techniques provided novel insights, revealing the interesting observation that Cldn2 as pore-forming claudin can interact with barrier-forming Cldn3 and Cldn1, in *trans* and *cis* respectively. Moreover, it was shown that TAMPs can interact with claudins[66] and that observed tissue phenotypes can be explained partially with those *in vitro* interaction studies. For instance, the description of the different heterophilic interactions between Cldn10b, Cldn16, and Cldn19[130] that goes in line with their mosaic expression in the thick ascending limb of kidney tubules[133]. Nevertheless, the nano-localization of specific proteins stayed unclear and could not be resolved with diffraction-limited confocal microscopy, neither in polarized epithelial cells nor in planar-grown fibroblasts. Live imaging of single claudin strands and their dynamics could be performed in overexpression of EGFP-tagged Cldn2 in fibroblasts[22]. Still, only isolated strands in the TJ-like meshwork's peripheral area could be resolved, leaving a huge gap open for improvement.

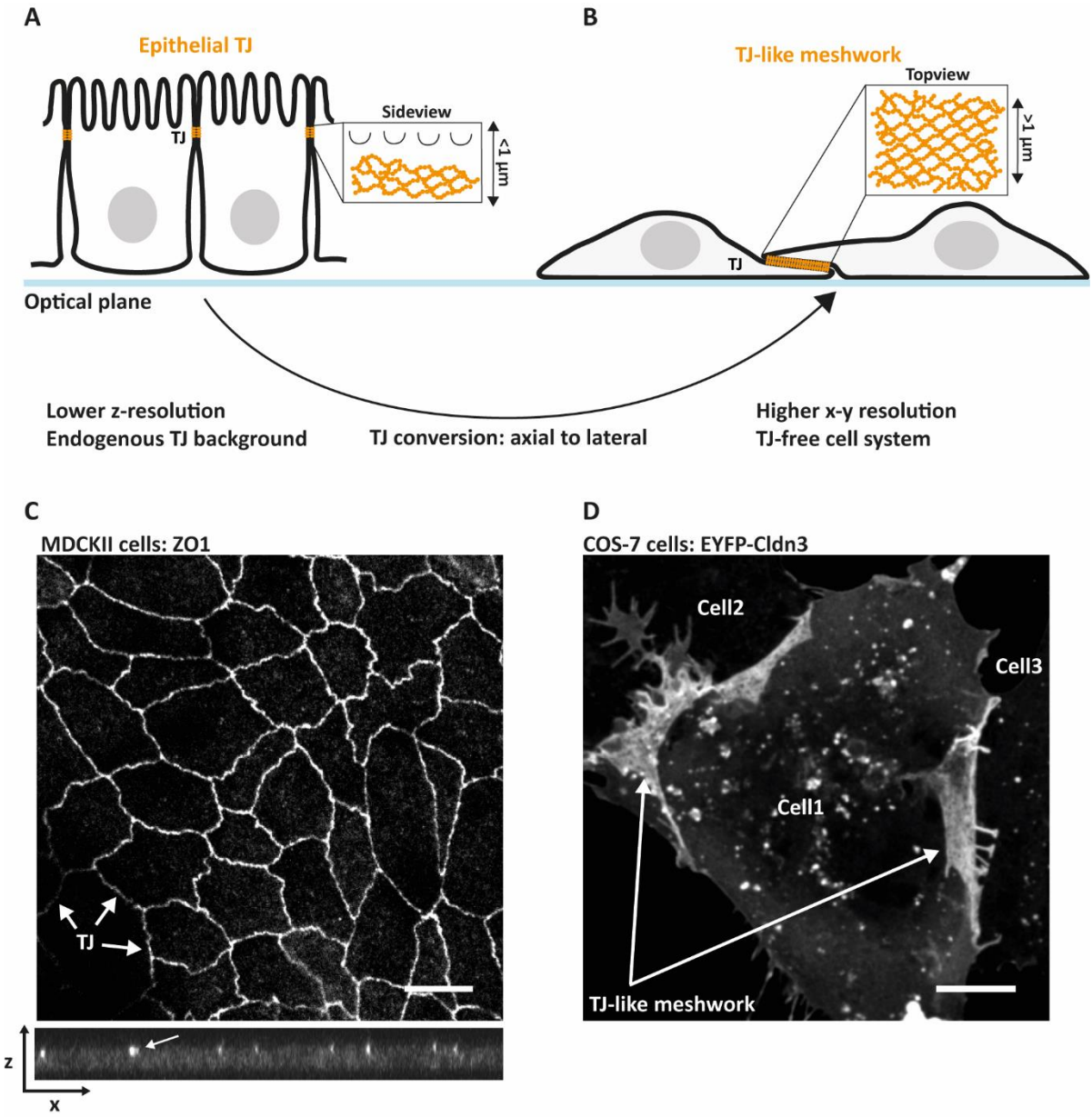

Figure 7 Endogenously formed TJ compared to the TJ-like meshwork in fibroblasts. (A) Schematic illustration of the endogenous TJ between neighboring epithelial cells (MDCKII) at the apical contact side. Due to its axial direction to the optical plane, the TJ appears as a line between the cell contacts in x-y projection (big white arrows in (C)) or as an apical spot in z-projection (small white arrow in (C)). The TJ's nano-organization cannot be resolved by confocal light microscopy due to the diffraction limit of the light and the limited z-resolution. **(B)** Schematic illustration of a TJ-like meshwork (white arrows in (D)) formed by overexpressed claudins in TJ-free fibroblasts. The TJ-like meshwork formation occurs in the overlap of two claudin expressing cells and can be formed in the whole overlap. The direction of the TJ is turned from the axial direction in epithelial cells to a more lateral direction in fibroblasts. It allows imaging the TJ in a higher resolution and studying claudins in an environment without a TJ background. **(C)** Representative image of the epithelial TJ (labeled for ZO1) in polarized MDCKII cells in xy-projection (bigger white arrows) and z-projection (smaller white arrow). **(D)** Representative image of the TJ-like meshwork between the overlaps of EYFP-Cldn3 overexpressing COS-7 fibroblasts indicated by the substantial signal increase in these areas (white arrows). Scale bars: 10 µm (C, D).

1.7.3 Super-resolution microscopy imaging uncovers the TJ nano-organization

In recent years, novel super-resolution microscopy (SRM) techniques offer different ways to overcome the biggest limitation in fluorescence light microscopy, the diffraction limit of the light. By "combining" the resolution advantage of EM with the multi-protein labeling and the higher throughput of confocal microscopy, SRM provides the possibility to resolve multiple structures at the nanoscale level. Right now, three main SRM techniques offer standardized approaches in imaging at high resolution: SIM (structured illumination microscopy), gSTED (gated stimulated emission depletion), and SMLM (single-molecule localization microscopy) (Figure 8)[177,178].

A

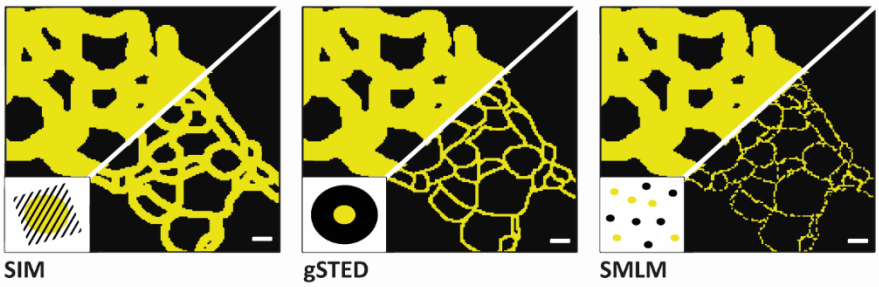

B

	SIM	gSTED	SMLM
Resolution limit	100 nm (lateral) 250 nm (axial)	40 nm (lateral) 70 nm (axial)	20 nm (lateral) 50 nm (axial)
Multi-color	4 colors	2 - 4 colors	2 - 4 colors
Sample preparation	Standard	Standard	Standard
Live imaging	Yes	Yes	Yes
Imaging speed	10 ms - 10 s	10 s - 5 min	10 min
Illumination power	10-100 W/cm^2	1-100 kW/cm^2	1-100 kW/cm^2

Figure 8 Schematic illustration and technical details of the three SRM techniques: SIM, gSTED, and SMLM. **(A)** Schematic illustration of a TJ-like meshwork resolved with structured illumination microscopy (SIM), gated stimulated emission depletion (gSTED), and single-molecule localization microscopy (SMLM) compared to confocal microscopy (upper left corner). A finer resolved TJ structure depicts the resolution increase from SIM over gSTED to SMLM. One of the main disadvantages of SMLM, the weak labeling density by antibodies, is pointed out by a dot-wise pattern of the TJ strands. The scale bar is set to 0.2 µm. **(B)** Summary of the technical facts of SIM, gSTED, and SMLM. Adapted and modified from Gonschior et al. (2020)[178].

In the TJ research field, the power of these techniques was tested, but it is still far away from being mastered[178]. The first SRM based study of a TJ-like meshwork was

performed in 2012 by Kaufmann et al., comparing the nanostructure of overexpressed EYFP-tagged murine Cldn3 and Cldn5 in HEK cells using SMLM. In this study, it was shown for the first time with light microscopy that different claudins can form different TJ-like meshworks and that SRM can be an key tool for understanding the single claudin properties in TJ meshworks[179]. Van Itallie et al. analyzed in 2016 TJ-like meshworks formed by Cldn2 with SIM. The group could visualize the dynamics of single claudin strands and whole TJ-like meshworks in live imaging. Also, they could observe the change from a static meshwork to a more dynamic meshwork when diminishing the connection to ZO1 upon elimination of the claudin PDZ-binding motif. The same study showed for the first time on nanoscale level that occludin can localize at single Cldn2 strands[23]. On an endogenous level, Schlingmann et al. were able to visualize the different localization of ZO1 and Cldn5 in alveolar endothelial cells and their change under ethanol (EtOH) influence[180]. These images showed very punctuated labeling, raising the question if this pattern could be a result of a weak antibody labeling. A recently published study from Maraspini et al. indicated the huge potential of STED microscopy for multi-color imaging of the endogenous junctions in MDCKII cell-formed cysts[181]. The cyst system is an elegant way to enable lateral imaging of the TJ at high resolution due to its unique architecture.

Nonetheless, no one so far was able to show the nano-localization of multiple claudins and their arrangement to each other in TJ. Such technique not only in fixed but also in live imaging could provide novel insights and a better understanding of the connection between nano-organization and function.

1.8 Organization of claudins and TAMPs in the tight junctional meshwork

Although the nano-organization in the TJ meshwork is unknown, some general interaction patterns and behaviors of claudins and TAMPs in and at the TJ could be already observed.

For the TJ's initial formation, it is assumed that ZO1 proteins bring claudin molecules in the plasma membrane in a certain proximity[42] allowing them to start their strand polymerization at the apical cell-cell contact side. The very slow turnover of claudins was several times described with FRAP experiments representing the claudin-based TJ meshwork

as a more static structure[23,65]. Pulse-chase-pulse experiments using SNAP-tagged claudins uncovered that the new addition of claudins to the TJ occurs at the basolateral side and the TJ periphery. In contrast, the most apical part of the TJ remained longer in a stable condition[182]. The kind of dynamic that underlies this addition and the subsequent claudin arrangement towards the more apical side is not fully clarified yet.

Very little is known about how different claudins arrange themselves in the dense and crowded TJ especially while maintaining their barrier-forming and channel-forming properties. Based on FRET and co-culture studies of different claudin combinations, it was suggested that claudins might interact, fully or at least partially, with specific other claudins or TAMPs[57,66]. It was shown that most of the as barrier-forming described claudins could interact in *cis* and *trans*[107]. The proposed interaction of the channel-forming Cldn2 with Cldn1 and Cldn3 is controversial debated however, it indicates that channel-forming claudins might have different interaction patterns than barrier-forming claudins[173]. That claudins can be excluded from other claudins was shown already in a handful of studies. For example, it could be observed on FFEM level that different claudins localize in different areas of the TJ meshwork between sensory and non-sensory cells in the rodent's inner ear. There it seems that Cldn6 and Cldn9 form TJ strands separated from Cldn14 in the more basolateral facing region, whereas Cldn14 forms its own parallel strands in the more apical part of the meshwork[183]. On tissue level, Milatz et al. observed that Cldn3, Cldn10b, Cldn16, and Cldn19 are expressed in a mosaic manner in the TAL of the kidney. Further studies confirmed that Cldn16 and Cldn19 form together a channel for divalent cations (Mg^{2+}), whereas Cldn10b is described as a channel for monovalent cations (Na^{+})[130,133].

It remains to be clarified how different claudins and other TJ transmembrane proteins orchestrate the TJ structure and function. It is especially interesting how the described channel-forming claudins fit in, as they are essential for paracellular ion permeability (Figure 9). For this purpose, the right SRM microscopy along with multi-labeling of different TJ proteins should provide novel insight into the organization and functional TJ principles and answer how the different transmembrane proteins and the associated tight junctional cytoplasmic plaque assemble the TJ.

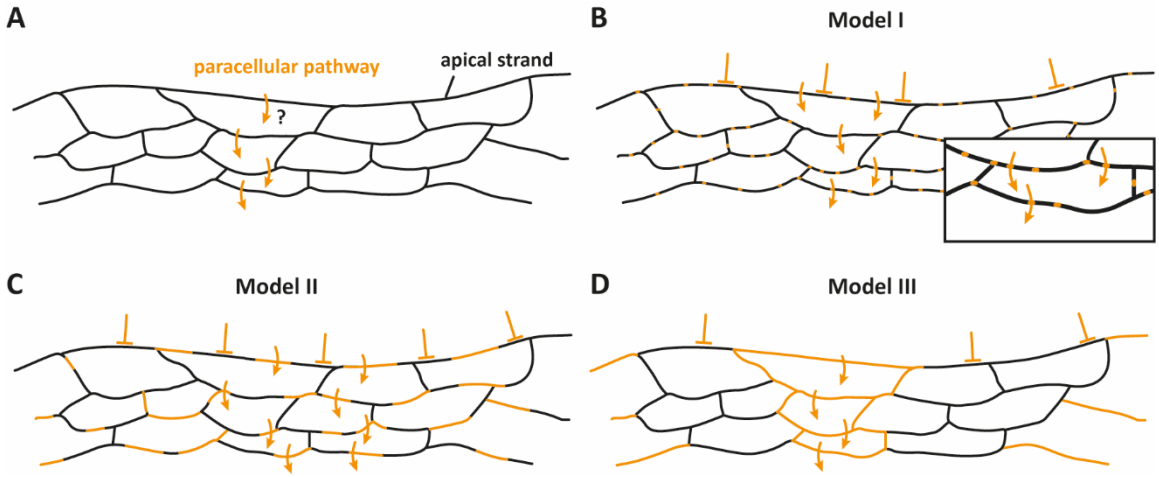

Figure 9 Schematic illustration of different models for the paracellular ion permeability over the TJ meshwork. (A) The assumption is that channel-forming claudins provide the TJ meshwork with a paracellular permeability for specific ions. How this channel formation and incorporation occurs on nanoscale level is unknown. **(B)** Model I: Channel-forming claudins form small oligomers that are incorporated in the TJ meshwork facilitating the ion flux. **(C)** Model II: Channel-forming claudins form longer strand parts separated from the other channel-forming or barrier-forming claudins. **(D)** Model III: Channel-forming claudins form large, connected meshwork parts that enable ion flux over bigger meshwork parts. Adapted and modified from Claude et al. (1973)[12].

2 Aim of the study

The study aimed to resolve the tight junctional meshwork with super-resolution microscopy by overcoming the fundamental limitations of electron microscopy and conventional confocal light microscopy (multi-protein labeling, label density, and diffraction limited resolution). Ideally, the combination of STED microscopy and new advanced labeling techniques provides new insights into the TJ meshwork organization in fixed and living samples and delivers an answer on how the structural proteins of the big claudin family arrange themselves in the multi-protein orchestra of the TJ without losing their essential and unique properties regarding the semi-permeable barrier function and paracellular ion permeability.

3 Material and Methods

3.1 Material

3.1.1 Chemicals, media, and disposables

Table 1 Chemicals and media used in this study.

Chemicals, media	Cat#	Source
(3-Aminopropyl)-triethoxysilane	A3648	Sigma Aldrich
Acetonitrile	T195.2	Carl Roth
Ampicillin sodium salt	HP62.1	Carl Roth
Argon gas	-	Internal supply from institute
Bioethanol (99%)	2211-5L	Chemsolute
Bovine serum albumin (BSA)	8076.1	Carl Roth
Bromophenol blue	B0126-25G	Sigma Aldrich
Butane/Propane gas (C 206 GLS)	0191.2	Carl Roth
Calcium chloride dihydrate ($CaCl_2$*$2H_20$)	5239.1	Carl Roth
Carl Zeiss Immersol Oil 518F	10539438	Thermo Fisher Scientific
Collagenase II	LS0004174	Pan biotech
cOmplete EDTA-free protease inhibitor cocktail (PIC)	5056489001	Sigma Aldrich, MERCK
Coomassie brillant blue G250	1154440025	Sigma Aldrich
Dimethylsulfoxid (DMSO)	D2650	Sigma Aldrich
Disodium hydrogen phosphate dihydrate (Na_2HPO_4*$2H_2O$)	4984.3	Carl Roth
Dithiothreitol (DTT)	6908.2	Carl Roth
D-mannitol	M4125	Sigma Aldrich
Dulbecco's modified Eagle's medium (DMEM) (1x), high glucose	41965062	Thermo Fisher Scientific, Gibco
Dulbecco's phosphate-buffered saline (DPBS) (1x), no $CaCl_2$, no $MgCl_2$	14190144	Thermo Fisher Scientific, Gibco
EDTA	EG-500G	Sigma Aldrich
Ethanol absolute (EtOH)	20821.296	VWR
Ethidium bromide (EtBr) (1%)	2218.3	Carl Roth
FastDigest Buffer Green	72B	Thermo Fisher Scientific
Fetal bovine serum (FBS)	10270106	Thermo Fisher Scientific, Gibco

Fluorescein	119241000	Fisher Scientific, Acros Organics
FluoroBrite DMEM (1x)	A1896701	Thermo Fisher Scientific, Gibco
G418, Geneticin	ant-gn-1	Invivogen
Glacial acetic acid (GAA)	A6283	Sigma Aldrich
Glucose	HN06.3	Carl Roth
Glutaraldehyde (GA) (25%)	3778.1	Carl Roth
Glycerin	3783.2	Carl Roth
Glycine	3908.3	Carl Roth
HEPES	HN78.3	Carl Roth
Intercept (PBS) Blocking Buffer	927-70001	LI-COR
Iso-Propanol	109634	Merck
JetPrime	114-75	VWR
Kanamycin sulfate	T832.4	Carl Roth
LB-Agar (Lennox)	X965.3	Carl Roth
L-glutamine (200 mM)	25030081	Thermo Fisher Scientific, Gibco
Lipofectamine 2000	11668019	Thermo Fisher Scientific, Invitrogen
Lipofectamine 3000	L3000015	Thermo Fisher Scientific, Invitrogen
Live cell imaging solution	A14291DJ	Thermo Fisher Scientific, Invitrogen
Magnesium chloride hexa-hydrate ($MgCl_2$*$6H_20$)	2189.3	Carl Roth
Matrigel	11553620	Fisher Scientific, Corning
MEM non-essential amino acids solution (100x)	11140035	Thermo Fisher Scientific, Gibco
Methanol (MeOH)	8388.1	Carl Roth
Methyl-β-cyclodextrin (MβCD)	C4555-1G	Sigma Aldrich
Mevastatin	474705-5MG	Sigma Aldrich
Minimal essential medium (MEM) (1x), low glucose	11095080	Thermo Fisher Scientific, Gibco
MTSES	91020	Biotium
MTSET	91021	Biotium
Nikon type N immersion oil	-	Nikon Instruments Europe BV
Normal goat serum (NGS)	16210072	Thermo Fisher Scientific, Gibco
Nuclease-free water, sterile	T143.5	Carl Roth
Opti-MEM (1x)	31985070	Thermo Fisher Scientific, Gibco

OrangeG	O3756-25G	Sigma Aldrich
Ortho-phosphoric acid (H_3PO_4)	6366.1	Carl Roth
Paraformaldehyde (PFA)	0335.1	Carl Roth
Penicillin/streptomycin (P/S) (10,000 U/mL)	15140-122	Thermo Fisher Scientific, Gibco
Pentobarbital	P-010-1ML	Merck, Supelco
Phosphate buffered saline (PBS) (1x), powder	L 182-50	Merck, Bio&Sell
Pierce ECL Western Blotting substrate	32106	Thermo Fisher Scientific
Ponceau S	5938.2	Carl Roth
Potassium chloride (KCl)	6781.1	Carl Roth
Pr_2Net (Diisopropylethylamine)	2474.1	Carl Roth
ProLong Gold Antifade mountant	P36934	Thermo Fisher Scientific
Puromycin	ant-pr-1	Invivogen
Rotiphorese gel 30	3029.1	Carl Roth
Rotiphorese TAE buffer (50x)	CL86.2	Carl Roth
Shandon Immu-Mount	9990402	Fisher scientific
Simvastatin	567022-5MG	Sigma Aldrich
Sodium azide (NaN_3)	S2002-100G	Sigma Aldrich
Sodium chloride (NaCl)	9265.1	Carl Roth
Sodium dodecyl sulfate (SDS) (99%), pellets	CN30.4	Carl Roth
Sodium fluoride (NaF)	201154	Sigma Aldrich
Sodium hydrogen carbonate ($NaHCO_3$)	HN01.1	Carl Roth
Sucrose	S7903-5KG	Sigma Aldrich
TEMED	2367.3	Carl Roth
Tissue-Tek O.C.T. compound	12351753	Fisher Scientific, Sakura Finetek,
Trifluoroacetic acid	P088.3	Carl Roth
TRIS	0188.3	Carl Roth
Tris buffered saline (TBS), (1x), powder	T6664-10PAK	Sigma Aldrich
Tris-HCl	9090.3	Carl Roth
Triton X-100	11332481001	Sigma Aldrich
TriTrack DNA loading dye (6x)	R1161	Thermo Fisher Scientific
TrypL express enzyme (1x), phenol	12605010	Thermo Fisher Scientific, Gibco

red		
Tryptone	T7293	Merck Millipore
Tween 20	P1379	Sigma Aldrich
Universal agarose	BS20.46.100	Bio&SELL
Water-free DMSO	D2650-2	Carl Roth
Yeast extract	2363.5	Carl Roth
β-mercaptoethanol	4227.1	Carl Roth

Table 2 Disposables used in this study.

Disposables	**Cat#**	**Source**
µ-Slide 8-well glass bottom chamber (#1.5H)	80827	Ibidi
Ø18 mm coverslips	15787572	Fisher Scientific
Ø25 mm coverslips (#1.5)	10593054	Fisher Scientific
Ø25 mm coverslips (#1.5H)	CG15XH1	Thorlabs
Ø5 mm coverslips	0111450	Superior Marienfeld
10 cm petri dish	82.1472	Sarstedt
10-well glass bottom plate	543079	Greiner Bio-one
12-well plate TC-treated	3513	Corning
24*50 mm coverslips	1871	Carl Roth
24-well plate TC-treated	3524	Corning
6-well plate TC-treated	3516	Corning
96-well micro test plate	82.1582	Sarstedt
96-well micro test plate	82.1582	Sarstedt
96-well glass bottom plate	P96-1.5H-N	Cellvis
96-well plate for colony PCR	83.3925	Sarstedt
96-well plate TC-treated	83.3924	Sarstedt
96-well plate TC-treated	83.3924	Sarstedt
Amicon Ultra-15, PLHK Ultracell-PL Membran, 100 kDa	UFC910024	MERCK
Biosphere SafeSeal tube, 1.5 ml	75.706.200	Sarstedt
Cell culture dish 10 cm, TC-treated	83.3902	Sarstedt
Cell culture dish 15 cm, TC-treated	83.3903	Sarstedt
Cell culture dish 6 cm, TC-treated	83.3901	Sarstedt
Cell scraper (25 cm)	734-2602	VWR
Combi tips advanced (10 ml)	0030089820	Eppendorf

Combi tips advanced (5 ml)	0030089669	Eppendorf
Corning polyester (PET) transwell-clear inserts (1.12 cm^2, 0.4 µm)	3460	Corning
Corning polyester (PET) transwell-clear inserts (4.67 cm^2, 0.4 µm)	3450	Corning
Cryomold intermediate	4566	Sakura
CryoPure tube (1.5 ml)	72.380.992	Sarstedt
Filter tips (Biosphere Plus) (10, 20, 200 and 1000 µl)	70.1130.215, 70.760.219, 70.760.216, 70.762.216	Sarstedt
Filter Upper Cup (0.2 µm)	10040-448	VWR
Filtropur filter (0.2 µm)	83.1826.001	Sarstedt
Inoculation tube (13 ml)	62.515.028	Sarstedt
Macro cuvette	634-0675	VWR
Millipore Millicell insets (0.6 cm^2, 0.4 µm pore size)	10126240	Fisher Scientific
Nitrocellulose blotting membrane (0.2 µm)	GE10600004	Merck, Amersham Protran
Parafilm	3-1012	NeoLab
Pasteur pipettes	4522	Carl Roth
Rotilabo-filter (0.45 µm)	P667.1	Carl Roth
Sample vials (brown glass) (1.5 ml)	XC65.1	Carl Roth
Scalpel (#10)	5518059	B. Braun
Serological pipettes (2, 5, 10, 25 ml)	CLS4021-1000EA, CLS4487-200EA, CLS4488-200EA, CLS4251-200EA	Merck, Corning Costar
Superfrost plus object slides	10149870	Thermo Fisher Scientific
Surgical blades	11-0150	Schreiber Instruments
Syringe (20 ml, Norm-Ject)	4200.X00V0	Henke-Sass-Wolf
Syringe (20 ml, Norm-Ject)	4200.X00V0	Henke-Sass-Wolf
Syringe (50 ml, Henke-Ject)	4850003000	Henke-Sass-Wolf
Tips (stack pack) (10 µl)	70.1130.46	Sarstedt
Tips (stack pack) (1250 µl)	VT0173	Biozym
Tips (stack pack) (200 µl)	70.760.45	Sarstedt
Transfection tubes	55.476.013	Sarstedt
Tubes (15 ml)	352099	Corning, Falcon
Tubes (50 ml)	352070	Corning, Falcon
Whatman gel blotting paper	10426994	GE Healthcare Life Sciences

3.1.2 Buffers, solutions, and media

For the preparation of all solutions, ultrapure water (18.2 MΩ, double-distilled water (ddH_2O)) was used. The pH of each solution was adjusted by using 1-3 M NaOH and or 1-5 M HCl unless otherwise specified. Buffers for certain methods or applications are further specified in detail in the method section.

Table 3 Media and solutions used for cell biological experiments.

Buffer, solutions, and media	Composition
$CaCl_2$ solution (2 M)	29.404 g $CaCl_2*2H_2O$ add 100 ml H_2O sterile filtered (0.2 µm pore size)
Cell culture medium (Caco-2 cells)	DMEM additives: 15% (v/v) FBS (heat-inactivated) 1% (v/v) non-essential amino acids (NEAA) 100 U/ml penicillin 0.1 mg/ml streptomycin
Cell culture medium (COS-7, HEK293, HEK293T, MDCKII, MDCKII QKO, MDCKC7 cells)	DMEM additives: 10% (v/v) FBS (heat-inactivated) 100 U/ml penicillin 0.1 mg/ml streptomycin
Cryo-protectant solution	50% (v/v) DMEM 40% (v/v) FBS (heat-inactivated) 10% (v/v) DMSO
FluoroBrite DMEM (1x) (for live imaging under CO_2 conditions)	FluoroBrite DMEM additives: 10% (v/v) FBS (heat-inactivated)
HEPES buffered saline (HBS) (2x)	50 mM HEPES 280 mM NaCl 1.5 mM Na_2HPO_4 adjusted to pH 7.05 in H_2O sterile filtered (0.2 µm pore size)
Live cell imaging solution (1x)	additives: 5 mM glucose sterile filtered (0.2 µm pore size)

Low chloride live imaging solution (1x)	5 mM NaCl 2.5 mM KCl 1.5 mM $CaCl_2$ 1 mM $MgCl_2$ 20 mM HEPES 270 mM mannitol adjusted to pH 7.4 in H_2O sterile filtered (0.2 µm pore size)
Matrigel working solution	2% (v/v) Matrigel stock solution 98% (v/v) DMEM additives: 10% (v/v) FBS (heat-inactivated) 100 U/ml penicillin 0.1 mg/ml streptomycin
SDS solution (2% (v/v))	diluted from a 10% SDS stock dilution with H_2O
Tris-EDTA (TE) (1x)	10 mM Tris 2 mM EDTA adjusted to pH 8.0 in H_2O sterile filtered (0.2 µm pore size)

Table 4 Buffers and solutions used for molecular biological experiments.

Buffer and solutions	**Composition**
Ampicillin stock (1000x)	100 mg/ml ampicillin sodium salt in H_2O sterile filtered (0.2 µm pore size)
Kanamycin stock (1000x)	50 mg/ml kanamycin sulfate in H_2O sterile filtered (0.2 µm pore size)
LB medium	1% (w/v) yeast extract 0.5% (w/v) NaCl 0.5% (w/v) Tryptone adjusted to pH 7.4 in H_2O autoclaved

LB plates	LB medium 15 g/l LB-agar autoclaved additives: 100 µg/ml ampicillin or 50 µg/ml kanamycin
OrangeG loading dye (10x)	spatula tip of OrangeG 70% (v/v) glycerol in H_2O
Tris-Acetate-EDTA (TAE) (50x)	200 mM Tris 100 mM glacial acetic acid 50 mM EDTA adjusted to pH 8.2-8.4 in H_2O

Table 5 Buffers and solutions used for biochemical experiments.

Buffer and solutions	**Composition**
Antibody blocking solution	1x PBST 3% (w/v) BSA
Antibody dilution solution	1x PBST 3% (w/v) BSA 0.03% (w/v) NaN_3 sterile filtered (0.2 µm pore size)
Bradford reagent (2x)	200 ml (85%) H_3PO_4 100 ml ethanol 140 g/l Coomassie G250 in H_2O
Lysis buffer	1% (v/v) Triton X-100 20 mM HEPES (pH 7.4) 130 mM NaCl 10 mM NaF 0.03% (v/v) PIC in H_2O
PBST (1x)	1x PBS 0.05% (v/v) Tween 20 (pH 7.4)

Phosphate-buffered saline (PBS) (10x)	1.37 M NaCl 43 mM Na_2HPO_4 14 mM NaH_2PO_4 27 mM KCl pH 7.4 in H_2O
Ponceau destaining solution	1% (v/v) acetic acid in H_2O
Ponceau staining solution	0.3% (w/v) Ponceau S 1% (v/v) acetic acid in H_2O
SDS running buffer (10x)	250 mM Tris 1% (w/v) SDS 1.92 M glycine in H_2O
SDS sample buffer (6x)	100 mM Tris-Cl (pH 6.8) 4% (w/v) SDS 0.2% (w/v) Bromophenol blue 200 mM DTT in H_2O
SDS separating gel buffer (4x)	0.4% (w/v) SDS 1.5 M Tris adjusted to pH 8.8 in H_2O
SDS stacking gel buffer (4x)	0.4% (w/v) SDS 0.5 M Tris adjusted to pH 6.8 in H_2O
Stripping buffer	2% (w/v) SDS 50 mM Tris-Cl (pH 6.8) in H_2O add fresh 0.78% (v/v) β-mercaptoethanol
TBS (10x)	0.2 M Tris (pH 7.6) 1.4 M NaCl in H_2O

Transfer buffer	25 mM Tris 192 mM glycine 20% (v/v) MeOH in H_2O

Table 6 Buffers and solutions for immunocytochemistry (ICC) experiments.

Buffer and solutions	**Composition**
Blocking solution	6% (v/v) NGS 1% (w/v) BSA 0.05% (v/v) Tween 20 in 1x PBS^{++}
Formaldehyde fixative	1% or 4% (w/v) PFA 4% (w/v) sucrose in 1x PBS adjusted to pH 7.4
Formaldehyde/Glutaraldehyde (GA) fixative	0.1% or 0.5% (v/v) GA 4% (w/v) PFA 4% (w/v) sucrose in 1x PBS adjusted to pH 7.4
PBS^{++} (1x), supplemented with $CaCl_2$ and $MgCl_2$	1x PBS 1 mM $CaCl_2*2H_2O$ 0.5 mM $MgCl_2*6H_2O$
Permeabilization buffer	0.2% TritonX-100 in 1x PBS^{++}
PFA quenching solution	0.1 M glycine in H_2O

Table 7 Buffers and solutions for electrophysiological measurements.

Buffer and solutions	Composition
Mannitol solution	238 mM mannitol 59.5 mM NaCl 21 mM $NaHCO_3$ 5.4 mM KCl 1 mM $MgCl_2$ 1.2 mM $CaCl_2$ 3 mM HEPES 10 mM glucose in H_2O adjusted to pH 7.4
Ringer solution	119 mM NaCl 21 mM $NaHCO_3$ 5.4 mM KCl 1 mM $MgCl_2$ 1.2 mM $CaCl_2$ 3 mM HEPES 10 mM glucose in H_2O adjusted to pH 7.4
Ussing chamber storage solution	1.8% (v/v) NaCl in H_2O

Table 8 Buffers and solutions for immunohistochemistry (IHC) experiments.

Buffer and solutions	Composition
Ringer solution	119 mM NaCl 21 mM $NaHCO_3$ 5.4 mM KCl 1 mM $MgCl_2$ 1.2 mM $CaCl_2$ in H_2O
Sucrose solution	10%, 20% or 30% (w/v) sucrose in H_2O

Trypsin-inhibited incubation solution for mouse kidney preparation	140 mM NaCl 0.4 mM KH_2PO_4 1.6 mM K_2HPO_4 1 mM $MgSO_4$ 10 mM sodium acetate 1 mM α-ketoglutarate 1.3 mM calcium gluconate 5 mM glycine in H_2O <u>additives:</u> 48 mg/l trypsin inhibitor 25 mg/l DNase I (pH 7.4) 2 mg/ml collagenase II

3.1.3 Enzymes and molecular biology kits

Fast digest restriction enzymes from Thermo Fisher Scientific were used for plasmid cloning (Table 9). All digests were performed in the presence of the FastDigest Buffer Green (10x) (Thermo Fisher Scientific) following the manufacturer's instructions.

Table 9 Restriction enzymes.

Restriction enzymes	Cat#	Company
BamHI	FD0055	Thermo Fisher Scientific
BshTI (AgeI)	FD1464	Thermo Fisher Scientific
Bsp1407I (BsrGI)	FD0933	Thermo Fisher Scientific
DpnI	FD1704	Thermo Fisher Scientific
Eco32I (EcoRV)	FD0304	Thermo Fisher Scientific
EcoRI	FD0275	Thermo Fisher Scientific
HindIII	FD0504	Thermo Fisher Scientific
KpnI	FD0524	Thermo Fisher Scientific
NotI	FD0593	Thermo Fisher Scientific
SalI	FD0644	Thermo Fisher Scientific
XhoI	FD0695	Thermo Fisher Scientific

Enzymes and molecular biology kits listed in Table 10 were used according to the manufacturer's instructions. Modifications are described in more detail in the method section.

Table 10 Enzymes and molecular biology kits.

Enzymes and kits	Application	Cat#	Company
NEBuilder HiFi DNA assembly cloning kit	Assembly of two linear overlapping DNA oligonucleotide fragments	E5520S	New England Biolabs
NucleoBond Xtra Midi EF kit	Large-scale endotoxin-free plasmid DNA isolation (Midi) from *E. coli*	740422.50	Macherey-Nagel
NucleoSpin gel and PCR clean-up kit	Purification of DNA from agarose gels and PCR reactions	740609.50	Macherey-Nagel
NucleoSpin plasmid kit	Small-scale preparation (Mini) of plasmid DNA from *E. coli*	740588.50	Macherey-Nagel
Phusion high-fidelity polymerase	Amplification of linear DNA fragments via polymerase chain reaction (PCR)	F530L	Thermo Fisher Scientific
T4 ligase kit	Ligation of linear DNA oligonucleotides to form DNA plasmids	15224041	Thermo Fisher Scientific
T4 polynucleotide kinase kit	5'phosphorylation of non-phosphorylated linear DNA oligonucleotides	EK0031	Thermo Fisher Scientific
Taq-polymerase	Amplification of linear DNA fragments via polymerase chain reaction (PCR)	10342020	Thermo Fisher Scientific, Invitrogen

3.1.4 Molecular weight standards and loading dyes

Table 11 Molecular weight standards and loading dyes.

Marker	Band pattern	Cat#	Source
6x TriTrack DNA loading dye	-	R1161	Thermo Fisher Scientific
Generuler 1 kb DNA Ladder	kb marker band: 10, 8, 6, 5, 4, 3.5, 3, 2.5, 2, 1.5, 1, 0.75, 0.5, 0.25	SM0311	Thermo Fisher Scientific
PageRuler Prestained Protein Ladder	kDa marker bands: 170, 130, 100, 70, 55, 40, 35, 25, 15, 10	26616	Thermo Fisher Scientific
PageRuler Prestained Plus Protein Ladder	kDa marker bands: 250, 130, 100, 70, 55, 35, 25, 15, 10	26620	Thermo Fisher Scientific

3.1.5 DNA oligonucleotides

All DNA oligonucleotides used as primers for polymerase chain reaction (PCR), sequencing or subcloning were purchased from BioTeZ Berlin GmbH. The lyophilized DNA oligonucleotides were dissolved in sterile ultrapure RNAse-free water to obtain a 100 µM stock concentration. 10 µM dilution was used as working solution. Dissolved primers were stored at -20°C. All primers are listed in Table 12.

Table 12 Primer sequences used for cloning and sequencing.

The name of the primer contains the targeted coding sequence, restriction enzyme (if used), and direction of the primer either FW (forward) or RV (reverse); capital letters indicate sequences overlapping with template sequence; italic letters indicate the restriction enzyme binding site and additional base pairs used as overhang; some primers contain four additional nucleotides (nts) (*TATA*) at 5' end in front of restriction sites and for primer stabilization; bold letters indicate the 5' end; Cldn – claudin; Puro – puromycin; EYFP – enhanced yellow fluorescent protein; EGFP – enhanced green fluorescent protein; HA – hemagglutinin; ECL – extracellular loop.

Primer	Sequence 5'-3'	Application
AgeI_EYFP_Cldn10a_pLIB_FW	***T****ATAACCGGT*ATGGTGAGCAAGGGCGAGGAGC TG	Insertion of EYFP-Cldn10a into pLIB-CMV-EGFP-Puro to create pLIB-CMV-EYFP-Cldn10a-Puro
NotI_Cldn10a_pLIB_ RV	***TA****TAGCGGCCGC*TTAGACATAAGCATTTTTATC AAACTGTTTTGAAGGG	
AgeI_EYFP_Cldn15_FW	***T****ATAACCGGT*ATGGTGAGCAAGGGCGAGGAGC TG	Insertion of EYFP-Cldn15 into pLIB-CMV-EGFP-Puro to create pLIB-CMV-EYFP-Cldn15-Puro
NotI_Cldn15_pLIB_RV	***TA****TAGCGGCCGC*CTACACGTAGGCGTTTCTGC	
AgeI_FLAG_Cldn10a_FW	***T****ATAACCGGT*ATGGATTACAAGGATGACGACG ATAAGCTGTACAAAAGCTTGGTACCGAGCTCG GATCCAATGTCC	Insertion of FLAG-Cldn10a into pLIB-CMV-EGFP-Puro to create pLIB-CMV-FLAG-Cldn10a-Puro
NotI_Cldn10a_pLIB _RV	***TA****TAGCGGCCGC*TTAGACATAAGCATTTTTATC AAACTGTTTTGAAGGG	
AgeI_FLAG_Cldn15_AgeI_FW	***T****ATAACCGGT*ATGGATTACAAGGATGACGACG ATAAGCTGTACAAAAGCTTGGTACCGAGCTCG GATCCAATGTCGATGGCTGTG	Insertion of FLAG-Cldn15 into pLIB-CMV-EGFP-Puro to create pLIB-CMV-FLAG-Cldn15-Puro
NotI_Cldn15_pLIB _RV	***TA****TAGCGGCCGC*CTACACGTAGGCGTTTCTGC	
AgeI_FLAG_Cldn2_FW	***T****ATAACCGGT*ATGGATTACAAGGATGACGACG ATAAGCTGTACAAAAGCTTGGTACCGAGCTCG GATCCAATGGCCTCTCTTGG	Insertion of FLAG-Cldn2 or FLAG-Cldn2$_{ECL10a}$ into pLIB-CMV-EGFP-Puro to create pLIB-CMV-FLAG-Cldn2-Puro and pLIB-CMV-FLAG-Cldn2$_{ECL10a}$-Puro
NotI_Cldn2_pLIB_RV	***TA****TAGCGGCCGC*TCACACATACCCTGTCAGG	

AgeI_HA_Cldn10a_FW NotI_Cldn10a_pLIB_RV	***T****ATAACCGGT*ATGGCGTACCCATACGACGTCCC AGACTACGCGCTGTACAAAAGCTTGGTACCGA GCTCGGATCCAATGTCCAGG ***TATAGCGGCCGC***TTAGACATAAGCATTTTTATC AAACTGTTTTGAAGGG	Insertion of HA-Cldn10a into pLIB-CMV-EGFP-Puro to create pLIB-CMV-HA-Cldn10a-Puro
AgeI_HA_Cldn15_FW NotI_Cldn15_pLIB_RV	***T****ATAACCGGT*ATGGCGTACCCATACGACGTCCC AGACTACGCGCTGTACAAAAGCTTGGTACCGA GCTCGGATCCAATGTCGATGGCTG ***TATAGCGGCCGC***CTACACGTAGGCGTTTCTGC	Insertion of HA-Cldn15 into pLIB-CMV-EGFP-Puro to create pLIB-CMV-HA-Cldn15-Puro
AgeI_HA_Cldn2_pLIB_FW NotI_Cldn2_pLIB_RV	***T****ATAACCGGT*ATGGCGTACCCATACGACGTCCC AGACTACGCGCTGTACAAAAGCTTGGTACCGA GCTCGGATCCAATGGCCTCTCTTG ***TATAGCGGCCGC***TCACACATACCCTGTCAGG	Insertion of HA-Cldn2 or HA-Cldn2$_{ECL10a}$ into pLIB-CMV-EGFP-Puro to create pLIB-CMV-HA-Cldn2-Puro and pLIB-CMV-HA Cldn2$_{ECL10a}$-Puro
AgeI_Halo-C1_FW BsrGI_Halo_RV	***T****ATAACCGGTCGCCACC*ATGGCAGAAATCGGTA CTGGCTTTCC ***T****ATATGTACA*GGCCGGAAATCTCGAGCGTGG	Insertion of Halo into C1-vector to create pHalo-C1
AgeI_Halo-N1-FW NotI_Halo-N1_RV	***T****ATAACCGGT*CACCGAAATCGGTACTGGCTTTC C ***TATAGCGGCCGC***TTTAGCCGGAAATCTCGAGC	Insertion of Halo into N1-vector to create pHalo-N1
AgeI_SNAP_Cldn2_pLIB_FW NotI_Cldn2_pLIB_RV	***T****ATAACCGGT*ATGGACAAAGACTGCGAAATGA AGCGCACCAC ***TATAGCGGCCGC***TCACACATACCCTGTCAGG	Insertion of SNAP-Cldn2 or SNAP-Cldn2$_{ECL10a}$ into pLIB-CMV-EGFP-Puro to create pLIB-CMV-SNAP-Cldn2-Puro and pLIB-CMV-SNAP-Cldn2$_{ECL10a}$-Puro
AgeI_SNAPf_FW BsrGI_SNAPf_RV	***T****ATAACCGGTCGCCACC*ATGGACAAAGACTG ***T****ATATGTACA*GACCCAGCCCAGGCTTGC	Insertion of SNAP into C1-vector to create pSNAP-C1
AgeI_SNAP-N1_FW NotI_SNAP-N1_RV	***T****ATAACCGGTCACC*ATGGACAAAGACTGCG ***TATAGCGGCCGCT***TTAACCCAGCCCAGGC	Insertion of SNAP into N1-vector to create pSNAP-N1

BsrGI_Cldns_FW SalI_Cldns_RV	***T****ATATGTAC*AAAAGCTTGGTACCGAGCTCGGATCC ***T****ATA*AGAAGCAGCGTCGACCGGCCGCCAGTGTGATG	Insertion of Cldns into SNAP-C1 or Halo-C1 to create pSNAP-Cldns and pHalo-Cldns
BsrGI_huCldns_FW EcoRV_Cldn2_cterm_stop_RV	***T****ATATGTAC*AAAAGCTTGGTACCGAGCTCGGATCC ***T****ATAGATATC*TCATGAGCAGGAAAAGCAGAGGATGATTCC	Insertion of Cldn2 without C-terminus into pSNAP-C1 to create pSNAP-Cldn2$^{\Delta CT}$
BsrGI_huCldns_FW EcoRV_Cldn3_cterm_stop_RV	***T****ATATGTAC*AAAAGCTTGGTACCGAGCTCGGATCC ***T****ATAGATATC*TTACGAGCAGCAGAGCAGCGCGCC	Insertion of Cldn3 without C-terminus into pSNAP-C1 to create pSNAP-Cldn3$^{\Delta CT}$
BsrGI_huCldns_FW EcoRV_Cldn10a_cterm_stop_RV	***T****ATATGTAC*AAAAGCTTGGTACCGAGCTCGGATCC ***T****ATAGATATC*TTAAGATATTGAAAAGCAAAATATGACACCACCAATTATGCACAGTGAG	Insertion of Cldn10a without C-terminus into pSNAP-C1 to create pSNAP-Cldn10a$^{\Delta CT}$
BsrGI_huCldns_FW_long EcoRV_Cldn15_cterm_stop_RV	***T****ATATGTAC*AAAAGCTTGGTACCGAGCTCGGATCC ***T****ATAGATATC*CTAGCAGCAGCAGGCGGAGCAG	Insertion of Cldn15 without C-terminus into pSNAP-C1 to create pSNAP-Cldn15$^{\Delta CT}$
BsrGI_TOPO_Cldn6_FW EcoRV_TOPO_Cldns_RV	***T****ATAGCTGTA*CAAAAGCTTGGTACCGAGCTCGGATCCAATGGCCTCTGCCGGAATGCAGATCCTGGG ***T****ATAGATATC*CTAGTAACGGCCGCCAGTGTGCTGGAATTCGC	Insertion of Cldn6 into pEYFP-pcDNA3.1 to create pEYFP-Cldn6
BsrGI_TOPO_Cldn9_FW EcoRV_TOPO_Cldns_RV	***T****ATAGCTGTA*CAAAAGCTTGGTACCGAGCTCGGATCCAATGGCTTCGACCGGCTTAGAACTGCTGGG ***T****ATAGATATC*CTAGTAACGGCCGCCAGTGTGCTGGAATTCGC	Insertion of Cldn9 into pEYFP-pcDNA3.1 to create pEYFP-Cldn9
Cldn2_ECL1Cldn10a_FW Cldn2_ECL1_Cldn10a_RV Cldn2_backbone_ECL1_FW Cldn2_backbone_ECL1_RV	**T**GGGCACACTGGTTGCCACCACGTCCAATGAGTGGAAAGTGAC **G**CCTGGATGTCACCATCATTCCTCTACATGCCTGTATATAACCTGCTACTTTG **A**TGATGGTGACATCCAGTGCAATC **G**GCAACCAGTGTGCCCAAAAGC	Two separated 2-step PCRs were performed to create the ECL1 of Cldn10a and the SNAP-Cldn2 full plasmid lacking the ECL1 to create pSNAP-Cldn2$_{ECL1Cldn10a}$ using HIFI-Assembly

Cldn2_ECL2_Cldn10a_FW Cldn2_ECL2_Cldn10a_RV Cldn2_backbone_ECL2_FW Cldn2_backbone_ECL2_RV	**G**GGATTCATTCCTGTTGCCCTATATGCAAACAA AATCACAACGG **T**AATGCCCAAGTAAAGAGCGGCTCCTAATTCAT ACTTTTGCTCAAC **G**CTCTTTACTTGGGCATTATTTCTTCC **G**GCAACAGGAATGAATCCCAGG	Two separated 2-step PCRs were performed to create the ECL2 of Cldn10a and the SNAP-$Cldn2_{ECL1Cldn10a}$ full plasmid lacking the ECL2 to create pSNAP-$Cldn2_{ECL10a}$ using HIFI-Assembly
CMV_FW	**C**GC AAA TGG GCG GTA GGC GTG	Sequencing and PCR
EcoRI_FLAG_Cldn3_FW SalI_Cldn3_pLIB_RV	***T****ATAGAATTC*ATGGATTACAAGGATGACGACG ATAAGCTGTACAAAAGCTTGGTACCGAGCTCG GATCCAATGTCCATGG ***T****ATAGTCGAC*TTAGACGTAGTCCTTGCGGTCGT AGCC	Insertion of FLAG-Cldn3 into pLIB-CMV-MCS2-Puro to create pLIB-CMV-FLAG-Cldn3-Puro
EcoRI_HA_Cldn3_FW SalI_Cldn3_pLIB_RV	***T****ATAGAATTC*ATGGCGTACCCATACGACGTCCC AGACTACGCGCTGTACAAAAGCTTGGTACCGA GCTCGGATCCAATGTCCATGG ***T****ATAGTCGA*CTTAGACGTAGTCCTTGCGGTCGT AGCC	Insertion of HA-Cldn3 into pLIB-CMV-MCS2-Puro to create pLIB-CMV-HA-Cldn3-Puro
EcoRI_SNAP_Cldn3_FW SalI_Cldn3_pLIB _RV	***T****ATAGAATTC*ATGGACAAAGACTGCGAAATGA AGCGCACCAC ***T****ATAGTCGAC*TTAGACGTAGTCCTTGCGGTCGT AGCC	Insertion of SNAP-Cldn3 into pLIB-CMV-MCS2-Puro to create pLIB-CMV-SNAP-Cldn3-Puro
EGFP-C1_RV	**G**TT CAG GGG GAG GTG TG	Sequencing and PCR
Halo-C1_FW	***T****ATA*ACGCTCGAGATTTCCGGC	Sequencing
HindIII_Cldns_FW SalI_Cldns_RV	***T****ATAAAGCTT*GGGTACCGAGCTCGGATCC ***T****ATAAGAAGCAGCGTCGAC*CGGCCGCCAGTGT GATG	Insertion of Cldns into pHA-C1 or pnoGFP-C1 to create pHA-Cldns and pnoGFP-Cldns
PDZ_deletion_Cldn10a_FW PDZ_deletion_Cldn10a_RV	**T**AAGATATCCATCACACTGGCGGCCGGTC **A**TTTTTATCAAACTGTTTTGAAGGGTTTGTTGTT TTAAAATCTTCTCCAC	pSNAP-$Cldn10a^{\Delta PDZ}$ by site-directed mutagenesis
PDZ_deletion_Cldn15_FW PDZ_deletion_Cldn15_RV	**T**AGGATATCCATCACACTGGCGGCCGG **G**TTTCTGCCGTATTTGCCAAAGCTGCTG	pSNAP-$Cldn15^{\Delta PDZ}$ by site-directed mutagenesis
PDZ_deletion_Cldn2_FW PDZ_deletion_Cldn2_RV	**T**GAGATATCCATCACACTGGCGGCCGGTC **T**GTCAGGCTGTAGGAATTGAACTCACTCTTGAC TTTGG	Creating pSNAP-$Cldn2^{\Delta PDZ}$ by site-directed mutagenesis

PDZ_deletion_Cldn3_FW PDZ_deletion_Cldn3_RV	**T**AAGGATCCACTAGTAACGGCCGCCAG **C**TTGCGGTCGTAGCCTGTGCCC	Creating pSNAP-Cldn3$^{\Delta PDZ}$ by site-directed mutagenesis
SNAP-C1_FW	***TATA***GGCAAGCCTGGGCTGGGT	Sequencing and PCR

3.1.6 Plasmid vectors

All expression vectors used in this study were stored at -20°C. Sequencing of introduced sequences in plasmids was performed by LGC Genomics (LGC, Biosearch Technologies, Berlin).

Table 13 Vector backbones used for cloning and protein overexpression.

EYFP – enhanced yellow fluorescent protein; HA – hemagglutinin; C – C-terminal tag; N – N-terminal tag; MCS – multiple cloning site; Puro – puromycin resistance; Neo – neomycin resistance.

Plasmid backbone	Properties	Source
pcDNA3.1	Mammalian expression vector; human cytomegalovirus (CMV) promoter; ampicillin resistance	Thermo Fisher Scientific
pEYFP-N1	Mammalian expression vector for fusion proteins with C-terminally tagged EYFP; CMV promoter; kanamycin/neomycin resistance	Obtained from Dr. Martin Lehmann (FMP, Berlin)
pHA-C1	Mammalian expression vector for fusion proteins with N-terminally tagged HA; CMV promoter; kanamycin/neomycin resistance	Obtained from Dr. Martin Lehmann (FMP, Berlin)
pHalo-C1 (pHTN1)	Mammalian expression vector for fusion proteins with N-terminally tagged Halo; CMV and T7 promoter; ampicillin/neomycin resistance	Promega
pHalo-N1 (pHTC1)	Mammalian expression vector for fusion proteins with C-terminally tagged Halo; CMV and T7 promoter; ampicillin/neomycin resistance	Promega

pLIB-CMV-EGFP-N1-Puro	Mammalian expression vector for fusion proteins with C-terminally tagged EGFP; CMV promoter; internal ribosome entry site (IRES); ampicillin/puromycin resistance	Obtained from Fabian Lukas (FMP, Berlin)
pLIB-CMV-MCS2-Puro	Mammalian expression vector; CMV promoter; IRES; ampicillin/puromycin resistance	Obtained from R. Kofler (Innsbruck)
pLIB-MCS2-Neo	Mammalian expression vector; CMV promoter; IRES; ampicillin/neomycin resistance	Obtained from Dr. Martin Lehmann (FMP, Berlin)
pmCherry-C1	Mammalian expression vector for fusion proteins with N-terminally tagged mCherry; CMV promoter; kanamycin/neomycin resistance	Obtained from Dr. Martin Lehmann (FMP, Berlin)
pnoGFP-C1	Mammalian expression vector for fusion proteins with no tag; CMV promoter; kanamycin/neomycin resistance	Obtained from Dr. Martin Lehmann (FMP, Berlin)
pSNAPf	Mammalian expression vector; CMV promoter; ampicillin/neomycin resistance	New England Biolabs
pTUBB-Halo	Mammalian expression vector with c-terminally tagged tubulin; CMV promoter; kanamycin/neomycin resistance	Addgene

Table 14 Plasmid DNA constructs used for transient recombinant protein expression.

m – murine; hu – human; Trq2 – Turquoise2; HA – hemagglutinin; ΔPDZ – PDZ binding motif deletion; ΔCT – C-terminus deletion; I66C – exchange of isoleucine (I) by a cysteine (C); S68C – exchange of serine (S) by a cysteine (C); C-term – C-terminal tag; N-term – N-terminal tag; ECL – extracellular loop; Cldn – claudin; EYFP – enhanced yellow fluorescent protein; EGFP – enhanced green fluorescent protein; N48K – exchange of asparagine (N) with lysine (K).

Constructs	**Species**	**Tag**	**Backbone**	**Source**
pECFP-huCldn17	human	ECFP (N-term)	pcDNA3.1	Obtained from Lorena Suarez Artiles (MDC, Berlin)

pEGFP-huCldn2^{I66C}	human	EGFP (N-term)	pEGFP-C1	Synthesized by Absea Biotechnology.
pEGFP-huCldn2^{S68C}	human	EGFP (N-term)	pEGFP-C1	Synthesized by Absea Biotechnology
pEGFP-mCldn26, 27	murine	EGFP (N-term)	pEGFP-C1	Synthesized by Absea Biotechnology
pEYFP-huCldn1, 2, 3, 4, 8, 10a, 10b, 11, 11b, 12, 15, 16, 19a, 19b, 20, 22, 23	human	EYFP (N-term)	pcDNA3.1	Obtained from Jörg Piontek and Dorothee Günzel (CBF, Berlin)
pEYFP-huCldn10a$^{\Delta CT}$, 15$^{\Delta CT}$	human	SNAP (N-term)	pcDNA3.1	This study
pEYFP-huCldn10a$^{\Delta PDZ}$, 15$^{\Delta PDZ}$	human	SNAP (N-term)	pcDNA3.1	This study
pEYFP-huCldn10b^{N48K}	human	EYFP (N-term)	pcDNA3.1	Obtained from Jörg Piontek (CBF, Berlin)
pEYFP-huCldn17	human	EYFP (N-term)	pcDNA3.1	This study
pEYFP-huCldn5, 7, 12, 20, 24, 25	human	EYFP (N-term)	pcDNA3.1	Obtained from Lorena Suarez Artiles (MDC, Berlin)
pEYFP-mCldn13, 14, 18a, 18b	murine	EYFP (N-term)	pcDNA3.1	Obtained from Lorena Suarez Artiles (MDC, Berlin)
pHA-huCldn2, 3, 10a, 15	human	HA	pHA-C1	This study
pHalo-C1	bacteria	Halo	pmCherry-C1	This study
pHalo-huCldn10a, 15	human	Halo (N-term)	pHalo-C1	This study
pHalo-N1	bacteria	Halo	pEYFP-N1	This study
phuCldn1, 3-EYFP	human	EYFP (C-term)	pEYFP-N1	Obtained from Dorothee Günzel (CBF, Berlin)
pmCldn1, 3-EYFP	murine	EYFP (C-term)	pEYFP-N1	Obtained from Jörg Piontek (CBF, Berlin)
pnoGFP-huCldn3, 15	human	-	pnoGFP-C1	This study

pSNAP-C1	human	SNAP	pmCherry-C1	This study
pSNAP-Cldn2$_{ECL1Cldn10a}$	human	SNAP(N-term)	p-SNAP-C1	This study
pSNAP-huCldn1, 2, 3, 4, 10a, 10b, 15, 19a	human	SNAP (N-term)	pSNAP-C1	This study
pSNAP-huCldn2$_{ECL10a}$	human	SNAP (N-term)	pSNAP-C1	This study
pSNAP-huCldn2$^{\Delta CT}$, 3$^{\Delta CT}$, 10a$^{\Delta CT}$, 15$^{\Delta CT}$	human	SNAP (N-term)	pSNAP-C1	This study
pSNAP-huCldn2$^{\Delta PDZ}$, 3$^{\Delta PDZ}$, 10a$^{\Delta PDZ}$, 15$^{\Delta PDZ}$	human	SNAP (N-term)	pSNAP-C1	This study
pSNAP-N1	human	SNAP	pEYFP-N1	This study
pTrq2-huCldn2, 3	human	Trq2 (N-term)	pTrq2-C1	This study
pTrq2-huCldn2$_{ECL10a}$	human	Trq2 (N-term)	pTrq2-C1	This study

Table 15 Plasmid DNA constructs used for stable protein expression.

Puro – puromycin resistance; Neo – neomycin resistance; MCS2 – multiple cloning site; EYFP – enhanced yellow fluorescent protein; EGFP – enhanced green fluorescent protein; HA – hemagglutinin; ECL – extracellular loop; Cldn – claudin.

Constructs	**Species**	**Tag**	**Backbone**
pLIB-CMV-EGFP-N1-Neo	jellyfish	EGFP (C-term)	pLIB-CMV-MCS2-Neo
pLIB-CMV-EGFP-N1-Puro	jellyfish	EGFP (C-term)	pLIB-CMV-MCS2-Puro
pLIB-CMV-EYFP-Cldn10a, 15 -Puro	human	EYFP (N-term)	pLIB-CMV-EGFP-N1-Puro
pLIB-CMV-EYFP-Cldn10a, 15-Neo	human	EYFP (N-term)	pLIB-CMV-EGFP-N1-Neo
pLIB-CMV-FLAG-Cldn2, 10a, 15-Neo	human	FLAG (N-term)	pLIB-CMV-EGFP-N1-Neo
pLIB-CMV-FLAG-Cldn2, 2$_{ECL10a}$, 10a, 15-Puro	human	FLAG (N-term)	pLIB-CMV-EGFP-N1-Puro
pLIB-CMV-FLAG-Cldn3-Neo	human	FLAG (N-term)	pLIB-CMV-MCS2-Neo
pLIB-CMV-FLAG-Cldn3-Puro	human	FLAG (N-term)	pLIB-CMV-MCS2-Puro
pLIB-CMV-HA-Cldn2, 2$_{ECL10a}$, 10a, 15-Puro	human	HA (N-term)	pLIB-CMV-EGFP-N1-Puro
pLIB-CMV-HA-Cldn3-Puro	human	HA (N-term)	pLIB-CMV-MCS2-Puro
pLIB-CMV-MCS2-Neo	X	X	pLIB-MCS2-Neo
pLIB-CMV-SNAP-Cldn2, 2$_{ECL10a}$-Puro	human	SNAP (N-term)	pLIB-CMV-EGFP-N1-Puro
pLIB-CMV-SNAP-Cldn2-Neo	human	SNAP (N-term)	pLIB-CMV-EGFP-N1-Neo
pLIB-CMV-SNAP-Cldn3-Neo	human	SNAP (N-term)	pLIB-CMV-MCS2-Neo
pLIB-CMV-SNAP-Cldn3-Puro	human	SNAP (N-term)	pLIB-CMV-MCS2-Puro

3.1.7 Antibodies

Table 16 Primary antibodies used in this study.

IgG/Y – immunoglobulin G/Y; ICC – immunohistochemistry; IHC – immunocytochemistry; WB – Western Blot; HSP70 – heat shock 70 kDa protein; ZO – zonula occludens; HA – hemagglutinin.

Antigen	Host/Isotype	Source	Clone	Cat#	Dilution
Claudin-1	rabbit/IgG	Thermo Fisher Scientific	polyclonal	51-9000	ICC 1:100 IHC 1:100
Claudin-2	mouse/IgG2b	Thermo Fisher Scientific	12H12	32-5600	ICC 1:100 IHC 1:100 WB 1:200
Claudin-2	rabbit/IgG	Thermo Fisher Scientific	polyclonal	51-6100	ICC 1:100 WB 1:200
Claudin-3	rabbit/IgG	Thermo Fisher Scientific	polyclonal	34-1700	ICC 1:100 IHC 1:100 WB 1:200
Claudin-3	rabbit/IgG	Aviva System, Biology	polyclonal	OAAB18340	ICC 1:100 IHC 1:100
Claudin-4	rabbit/IgG	Thermo Fisher Scientific	polyclonal	36-4800	ICC 1:100
Claudin-7	rabbit/IgG	Thermo Fisher Scientific	polyclonal	34-9100	ICC 1:100
Claudin-10	rabbit/IgG	antibodies-online.de	polyclonal	ABIN3183935	ICC 1:100 WB 1:200
Claudin-10	mouse/IgG	Thermo Fisher Scientific	monoclonal	41-5100	IHC 1:100
Claudin-15	rabbit/IgG	Thermo Fisher Scientific	polyclonal	38-9200	ICC 1:100 IHC 1:100 WB 1:200
FLAG	mouse/IgG1	Sigma Aldrich	M2	F3165	ICC 1:500
FLAG	rabbit/IgG	Sigma Aldrich	polyclonal	F7425	ICC 1:500
GFP	mouse/IgG2a	Thermo Fisher Scientific	3E6	A-11120	ICC 1:500 WB 1:1000
GFP	chicken/IgY	Abcam	polyclonal	ab13970	ICC 1:1000
HA	mouse	Abcam	16B12	ab130275	ICC 1:500
HA	rabbit	Cayman	polyclonal	162200	ICC 1:200
Halo-tag	mouse	Promega	monoclonal	G921A	WB 1:1000
HSP-70	mouse/IgG1	Thermo Fisher Scientific	3A3	MA3006	WB 1:2000
Occludin	mouse/IgG	Thermo Fisher Scientific	OC-3F10	33-1500	WB 1:500
SNAP-tag	rabbit	New England Biolabs	polyclonal	P9310s	WB 1:1000
Tubulin	mouse/IgG1	Sigma Aldrich	B5-1-2	T5168	ICC 1:500

Vinculin	rabbit/IgG	Abcam	polyclonal	ab73412	WB 1:500
ZO1	mouse/IgG1	Thermo Fisher Scientific	ZO1-1A12	33-9100	ICC 1:100
ZO1	rabbit/IgG	Thermo Fisher Scientific	polyclonal	61-7300	ICC 1:100 IHC 1:100 WB 1:200
β-actin	mouse/IgG1	Sigma Aldrich	ac-15	A5441	WB 1:5000

Table 17 Nanobodies and directly labeled primary antibodies used in this study.

V_HH – single variable domain on a heavy chain; IgG/Y – immunoglobulin G/Y; GFP – green fluorescent protein.

Antigen	Host/Isotype	Conjugate	Source	Cat#	Dilution
Claudin-3	rabbit/IgG	Atto590	IgG from Thermo scientific Fisher NHS-Ester from Sigma Aldrich	34-1700 79636	ICC 1:50 IHC 1:50
GFP	alpaca/V_HH	Atto647N	Chromotek	gba647n-100	ICC 1:200
GFP	alpaca/V_HH	Atto594	Chromotek	gba594-100	ICC 1:200
GFP	alpaca/V_HH	Alexa Fluor 488	Chromotek	gba488-100	ICC 1:200

Table 18 Secondary antibodies used in this study.

IgG (H+L) – immunoglobulin G (IgG) with heavy (H) and light chain (L); HRP – horseradish peroxidase.

Antigen	Host/Isotype	Conjugate	Source	Cat#	Dilution
mouse	goat/IgG(H+L)	Alexa Fluor 488	Thermo Fisher Scientific	A11001	ICC 1:200 IHC 1:200
mouse	goat/IgG(H+L)	Alexa Fluor 594 F(ab')2	Thermo Fisher Scientific	A-11020	ICC 1:200 IHC 1:200
mouse	goat/IgG(H+L)	Alexa Fluor 594 Plus	Thermo Fisher Scientific	A32744	ICC 1:200 IHC 1:200
mouse	donkey/IgG(H+L)	Atto542	NHS-Ester from ATTOTEC IgG from Jackson Immuno Research Ltd.	AD542-31 715-005-151	ICC 1:200
mouse	goat/IgG(H+L)	Atto647N	Active Motif	15058	ICC 1:200 IHC 1:200

mouse	donkey/IgG(H+L)	Atto647N	NHS-Ester from ATTOTEC IgG from Jackson Immuno Research Ltd.	AD 647N-31 715-005-151	ICC 1:200 IHC 1:200
mouse	goat/IgG(H+L)	HRP	Jackson Immuno Research Ltd.	115-035-003	WB 1:2000
mouse	donkey/IgG(H+L)	800CW	LI-COR	926-32212	WB 1:10000
rabbit	donkey/IgG(H+L)	800CW	LI-COR	926-32213	WB 1:10000
rabbit	goat/IgG(H+L)	Alexa Fluor 488	Thermo Fisher Scientific	A11008	ICC 1:200 IHC 1:200
rabbit	goat/IgG(H+L)	Alexa Fluor 594 F(ab')2	Thermo Fisher Scientific	A-11072	ICC 1:200 IHC 1:200
rabbit	goat/IgG(H+L)	Alexa Fluor 594 Plus	Thermo Fisher Scientific	A32740	ICC 1:200 IHC 1:200
rabbit	donkey/IgG(H+L)	Atto542	NHS-Ester from ATTOTEC IgG from Jackson Immuno Research Ltd.	AD542-31 711-005-151	ICC 1:200
rabbit	goat/IgG(H+L)	Atto647N	Active Motif	15048	ICC 1:200 IHC 1:200
rabbit	donkey/IgG(H+L)	Atto647N	NHS-Ester from ATTOTEC IgG from Jackson Immuno Research Ltd.	AD 647N-31 711-005-151	ICC 1:200 IHC 1:200
rabbit	goat/IgG(H+L)	HRP	Jackson Immuno Research Ltd.	111-035-003	WB 1:2000

3.1.8 Fluorophores and SNAP- and Halo-tag ligands

Table 19 SNAP- and Halo-tag ligands.

JF – Janelia Fluor; BG – O^6-benzylguanine; CA – O^6-chloralkane.

Fluorophore conjugated ligand	Tag system	Source	Cat#	Stock and final concentration
Atto590-BG	SNAP-tag	NHS-Ester from Sigma Aldrich Substrate from New England Biolabs	79636 S9148S	Stock: 1 mM Final: 2 µM
Atto590-CA	Halo-tag	NHS-Ester from Sigma Aldrich Substrate from Promega	79636 P6711	Stock: 1 mM Final: 1 µM
JF646-BG	SNAP-tag	NHS-Ester from Tocris Substrate from New England Biolabs	6148 S9148S	Stock: 1 mM Final: 2 µM
JF646-CA	Halo-tag	NHS-Ester from Tocris Substrate from Promega	6148 P6711	Stock: 1 mM Final: 1 µM

Table 20 Fluorescent cell and cell organelle marker.

siR – silicon rhodamine; DAPI – 4',6-diamidino-2-phenylindole.

Name	Source	Cat#	Stock and final concentration
CellMask	Thermo Fisher Scientific, Invitrogen	C10046	Stock: 5 mg/ml Final: 5 µg/ml
DAPI	Merck, Millipore	5087410001	Stock: 5 mg/ml Final: 1 µg/ml
Filipin III (*Streptomyces filipinensis*)	Sigma Aldrich	F4767	Stock: 1 mg/ml Final: 25 µg/ml
Lipilight580	Idylle Labs	-	Stock: 1 mM Final: 200 nM
Phalloidin Alexa Fluor 488	Thermo Fisher Scientific	A12379	Stock: 400x (66 µM) Final: 1x (165 nM)

Phalloidin Alexa Fluor 594	Thermo Fisher Scientific	A12381	Stock: 400x (66 µM) Final: 1x (165 nM)
siR-actin	Spirochrome	SC001	Stock: 1 mM Final: 1 µM
siR-tubulin	Spirochrome	SC002	Stock: 1 mM Final: 1 µM

3.1.9 Bacterial strains

For standard cloning and propagation of plasmid DNA chemically competent *E. coli* TOP10 strain (Life technologies) or 5-alpha competent *E. coli* (New England Biolabs) were used. For cloning and propagation of lentiviral plasmid vectors, the HB101 competent *E. coli* were used. HB101 cells are recA negative bacteria, which drastically reduces internal DNA recombination.

3.1.10 Eukaryotic cell lines

All cultured cells were regularly tested for mycoplasma with a PCR-based Mycoplasma test kit (PromoCell, #PK-CA91-1024).

Table 21 Eukaryotic cell lines.

sT – stably expressing; MDCK – Madin-Darby canine kidney; COS – *Cercopithecus aethiops*; HeLa – Henrietta Lacks; HEK293T – human embryonic kidney; MDCKC7 – Madin-Darby canine kidney clone 7; QKO – quintuple knockout; Cldn – claudin; EYFP – enhanced yellow fluorescent protein; HA – hemagglutinin; all stable cell lines were created by lentiviral transduction.

Cell lines	Origin and cell type	Source	Modification
Caco-2	*Homo sapiens*, adenocarcinoma, epithelial-like, adherent	ATCC HTB-37	-
COS-7	*Cercopithecus aethiops*, african green monkey, kidney derived fibroblast, adherent	ATCC CRL-651	-
COS-7 sT SNAP-Cldn2 + EYFP-Cldn10a	*Cercopithecidae*, african green monkey, kidney derived fibroblast, adherent	Original strain ATCC CRL-651	Stably expressing SNAP-Cldn2 and EYFP-Cldn10a

COS-7 sT SNAP-Cldn3 + EYFP-Cldn15	*Cercopithecidae*, african green monkey, kidney derived fibroblast, adherent	Original strain ATCC CRL-651	Stably expressing SNAP-Cldn3 and EYFP-Cldn15
COS-7 sT EYFP-Cldn10a	*Cercopithecidae*, african green monkey, kidney derived fibroblast, adherent	Original strain ATCC CRL-651	Stably expressing EYFP-Cldn10a
COS-7 sT EYFP-Cldn15	*Cercopithecidae*, african green monkey, kidney derived fibroblast, adherent	Original strain ATCC CRL-651	Stably expressing EYFP-Cldn15
COS-7 sT SNAP-Cldn2	*Cercopithecidae*, african green monkey, kidney derived fibroblast, adherent	Original strain ATCC CRL-651	Stably expressing SNAP-Cldn2
COS-7 sT SNAP-Cldn3	*Cercopithecidae*, african green monkey, kidney derived fibroblast, adherent	Original strain ATCC CRL-651	Stably expressing SNAP-Cldn3
HEK293	*Homo sapiens*, embryonic kidney, epithelial cells, adherent	ATCC CRL-1573	-
HEK293T	*Homo sapiens*, embryonic kidney, epithelial cells, adherent, contains the SV40 T-antigen	ATCC CRL-3216	-
MDCKC7	*Canis familiaris,* dog, kidney, epithelial-like, adherent	Lorena Suarez Artiles (MDC)	-
MDCKII	*Canis familiaris,* dog, kidney, epithelial-like, adherent	ATCC CRL-2936	-
MDCKII QKO	*Canis familiaris,* dog, kidney, epithelial-like, adherent	Mikio Furuse (Otani et al. 2019)	Quintuple knockout of Cldn1, 2, 3, 4, 7.

MDCKII QKO sT Cldn2	*Canis familiaris,* dog, kidney, epithelial-like, adherent	Original strain Mikio Furuse (Otani et al. 2019)	QKO cells stably expressing Cldn2 (gifted by Mikio Furuse)
MDCKII QKO sT EYFP-/HA-/FLAG-Cldn10a	*Canis familiaris,* dog, kidney, epithelial-like, adherent	Original strain Mikio Furuse (Otani et al. 2019)	QKO cells stably expressing EYFP-/HA-/FLAG-Cldn10a
MDCKII QKO sT EYFP-/HA-/FLAG-Cldn15	*Canis familiaris,* dog, kidney, epithelial-like, adherent	Original strain Mikio Furuse (Otani et al. 2019)	QKO cells stably expressing EYFP-/HA-/FLAG-Cldn15
MDCKII QKO sT SNAP-/HA-/FLAG-Cldn2	*Canis familiaris,* dog, kidney, epithelial-like, adherent	Original strain Mikio Furuse (Otani et al. 2019)	QKO cells stably expressing SNAP-/HA-/FLAG-Cldn2
MDCKII QKO sT SNAP-/HA-/FLAG-Cldn3	*Canis familiaris,* dog, kidney, epithelial-like, adherent	Original strain Mikio Furuse (Otani et al. 2019)	QKO cells stably expressing SNAP-/HA-/FLAG-Cldn3
MDCKII QKO sT FLAG-Cldn2 + FLAG-Cldn10a	*Canis familiaris,* dog, kidney, epithelial-like, adherent	Original strain Mikio Furuse (Otani et al. 2019)	QKO cells stably expressing FLAG-Cldn2 and FLAG-Cldn10a
MDCKII QKO sT FLAG-Cldn3 + FLAG-Cldn15	*Canis familiaris,* dog, kidney, epithelial-like, adherent	Original strain Mikio Furuse (Otani et al. 2019)	QKO cells stably expressing FLAG-Cldn3 and FLAG-Cldn15

3.1.11 Lentiviruses

All lentiviruses were generated by transfection of HEK293T cells as described in 3.2.6. The different generated viruses are equivalent to the used lentiviral plasmids listed in Table 15. Virus containing supernatants were stored at -80°C in 1.5 ml cryo-protectant tubes.

3.1.12 Mouse strains

Mice were housed with food and water available ad libitum and on a 12 hours light/ dark cycle. Breeding of all mouse strains and all experiments were reviewed and approved by the ethics committees of the “Landesamt für Gesundheit und Soziales” (LAGeSo) Berlin and "Ministerium für Landwirtschaft, Umwelt und ländliche Räume" in Schleswig-Holstein (MELUND SH).

Table 22 Mouse strains used for immunohistology experiments.

Mouse strains	Source	Animal experiment number
BL6	Charité Campus Benjamin Franklin, Berlin	LAGeSo (Landesamt für Gesundheit und Soziales) T-025/16
BL6	Forschungsinstitut für Molekulare Pharmakologie (FMP), Berlin Maximilian-Delbrück Centrum (MDC), Berlin	-
C57 Bl/6 J	Carl Albrechts Universität, Kiel	MELUND SH (=Ministerium für Landwirtschaft, Umwelt und ländliche Räume, Schleswig-Holstein) V312-72241.121-2

3.1.13 Software

Table 23 Software.

Program/website	Source	Version	Application
Adobe Acrobat Pro DC	Adobe Systems, USA	20.013.20074.18474	Viewing and editing of pdf-documents
Adobe Illustrator 2021	Adobe Systems, USA	25.1	Illustration of scientific data in figures and schemes
Adobe Photoshop CC 2019	Adobe Systems, USA	20.0.10	Illustration of scientific data in figures and schemes
Clone Manager Professional Suite	Scientific & Educational Software	8.04	*In silico* DNA oligonucleotide design and plasmid cloning

Fiji ImageJ	Wayne Rasband, National Institutes of Health (NIH), USA	1.53a	Processing and analysis of microscopy and Western Blot data
GraphPad PRISM	GraphPad	5.04	Statistical analysis of datasets and generation of plots
Huygens Essential	Scientific Volume Imaging B.V.	16.10.1p4	Software for image deconvolution
Image Lab	Bio-Rad	6.0.1 build 34	Software for HRP signal detection
Image Studio Lite	LI-COR	5.2	Software for LI-COR antibody signal detection and image processing
Leica Application Suite X (LASX)	Leica Microsystems	3.5.223225	Leica SP8 STED microscope software
Mendeley Desktop	Mendeley Ltd.	1.19.6	Collection of scientific articles and reviews
Microsoft Office 365 (Word, Excel, Powerpoint, and OneNote)	Microsoft	2012	Create documents and presentations, analyze scientific data and experimental logbook
NCBI Homepage	www.ncbi.nlm.nih.gov/	2021/01/13	Database for scientific literature, DNA, and protein sequences

NEBiocalculator	https://nebiocalculator.neb.com/#!/ligation	2021/01/13	Calculator for molar ratio for ligation of DNA fragments
NIS-Elements	Nikon Instruments	5.02.01	Nikon microscope software
PubMed	https://pubmed.ncbi.nlm.nih.gov/	2021/01/13	Database for DNA and protein sequences
UniProt	https://www.uniprot.org/	2021/01/13	Database protein sequences and structures
ZEN 2010 B SP1	Carl Zeiss Microscopy	6.0.0.485	Zeiss confocal microscope software

3.1.14 Devices and equipment

A more detailed description of specific instruments can be found in the method part.

Table 24 Devices and equipment.

Devices	Company
Arium advance (Milli Q system)	Sartorius
Bio Photometer Plus	Eppendorf
Bio-Rad ChemiDoc MP	Bio-Rad
Cabsulefuge (PMC-060)	Tomy
Centrifuge 5702	Eppendorf
Flasks 100/250/500/ 1000/2000	Schott
Gel documentation (G:Box)	Syngene
Glass vials (250 ml, 500 ml)	Schott
High-resolution ESI-MS (Waters H-class instrument)	Waters corporation
Hoods in the labs (GAP.185.120)	SAP Umwelttechnologie
Preparative HPLC (Gilson PLC 2020 system)	Gilson Inc
Ice machine	Manitowoc
Incubator (80°C)	Heraeus Instruments
Incubator bacteria (Incu-line)	VWR

Incubator mammalian cell culture (Galaxy 170S)	New Brunswick
Infinite 200 Pro Plate reader	Tecan
K series cryo-storage freezer system	Worthington industries
Leica SP8 STED	Leica Microsystems
LSM 780	Carl Zeiss Microscopy
LSM510-META NLO	Carl Zeiss Microscopy
LSM710	Carl Zeiss Microscopy
Magnetic stirrer (RCT basic)	Kikawerke
Mammalian cell culture Hood	Thermo Fisher Scientific
Micro centrifuge (Micro 22R)	Hettich
Microcentrifuge (Micro Star 17)	VWR
Microm HM560 cryostat	Thermo Fisher Scientific
Millicell ERS2 (Electrical Resistance System)	Merck (Millipore)
Mini Trans-Blot Cell	Bio-Rad
Mini-Spin Plus	Eppendorf
Multifuge (X1R)	Thermo Fisher Scientific
Multipette Plus	Eppendorf
Neubauer improved	Superior Marienfeld
Nikon CSU	Nikon Instruments
Odyssey Fc imaging system	LI-COR
Olympus CKX41 with Olympus U-RFL-T lamp	Olympus
PerfectBlue gel system, Mini L	Peqlab
pH meter	Mettler Toledo
Pipetteboy	Accupipex
Pipettes (Eppendorf research: 0.2 - 10/2 - 20/ 20 - 200/100 - 1000 µl)	Eppendorf
Power Pack P25T	Biometra
S2 hood	BDK
SDS-Page Running chambers	Bio-Rad
Shaker bacteria (Innova-42)	New Brunswick
Shaker bacteria (Innova-44)	New Brunswick
Shaker Duomax1030	Heidolph instruments
Thermocycler, peqSTAR	Peqlab
Thermomixer 5437	Eppendorf
Thermomixer comfort (Typ5)	Eppendorf
UPLC-UV/MS (Water H-class instrument)	Waters corporation
Ussing chambers	Self-build (Clinical physiology at CBF, Berlin)

UV table (UVT-28 LV)	Herolab
VACUSAFE (Vacuum pump mammalian cell culture)	Integra
Vacuum pump (Unit BVC21)	Vacuubrand
Vortex Genie 2	Scientific Industries
Water bath (VWB 26)	VWR
Weight for chemical substances	Sartorius analytic

3.1.15 Suppliers

Table 25 Suppliers.

Supplier	Address
Abcam	Cambridge, UK
Absea Biotechnology Ltd.	Beijing, China
Active Motif	Carlsbad, California, USA
American Type Culture Collection	Manassas, Virginia, USA
Antibodies-online Inc.	Limerick, Pennsylvania, USA
ATTO-TEC	Siegen, Germany
Aviva System Biology	San Diego, California, USA
BD Biosciences	Franklin Lakes, New Jersey, USA
Biometra GmbH	Göttingen, USA
Bio-Rad Laboratories Inc.	Hercules, California, USA
BioTeZ Berlin-Buch GmbH	Berlin, Germany
Biotium	Fremont, California, USA
Carl Roth GmbH	Karlsruhe, Germany
Carl Zeiss	Oberkochen, Germany
Cayman Chemical	Ann Arbor, Michigan, USA
Cellvis	Mountain View, California, USA
ChromoTek GmbH	Planegg-Martinsried, Germany
Corning	New York, USA
Eppendorf AG	Hamburg, Germany
GE Healthcare Life Sciences	Chalfont St. Giles, UK
Gilson Inc	Middleton, USA
Henke-Sass-Wolf	Tuttlingen, Germany
IDYLLE	Paris, France
INTEGRA Biosciences GmbH	Biebertal, Germany
Invitrogen	Carlsbad, USA
Invivogen	San Diego, California, USA

Jackson Immuno Research Ltd.	Cambridge, UK
Janelia Farm Research Campus	Ashburn, Virginia, USA
Leica Microsystems	Wetzlar, Germany
LGC Biosearch Technologies	Berlin, Germany
LI-COR Biosciences	Lincoln, Nebraska, USA
Life Technologies	Carlsbad, California, USA
Macherey-Nagel	Düren, Germany
Merck KGaA	Darmstadt, Germany
Merck Millipore	Burlington, Massachusetts, USA
neoLab Migge GmbH	Heidelberg, Germany
New England Biolabs	Ipswich, Massachusetts, USA
Nikon Instruments	Tokyo, Japan
Paul Marienfeld GmbH & Co. KG	Lauda-Königshofen, Germany
Promega	Madison, Wisconsin, USA
PromoCell GmbH	Heidelberg, Germany
Sakura Finetek	Torrance, California, USA
Sarstedt	Nümbrecht, Germany
Sartorius	Göttingen, Germany
Schott AG	Mainz, Germany
Schreiber Instruments	Schreiber Instruments
Sigma Aldrich	St. Louis, Missouri, USA
Spirochrome Ltd	Stein am Rhein, Suisse
Tecan Group	Männedorf, Suisse
Thermo Fisher Scientific	Waltham, Massachusetts, USA
Tocris Bioscience	Bristol, UK
VWR International	Radnor, Pennsylvania, USA
Waters Corporation	Milford, Massachusetts, USA

3.2 Cell biological methods

3.2.1 Mammalian cell culture

All mammalian cell lines used in this study were cultured in a humidified incubator at 37°C and 5% CO_2. The basic cell culture was carried out in Ø10 cm dishes. COS-7, HEK293, HEK293T, MDCKII, MDCKII QKO, and MDCKC7 (listed in Table 21) were cultivated in Dulbecco's Modified Eagles Medium (DMEM) supplemented with 4.5 g/l glucose, 10% (v/v) heat-inactivated fetal bovine serum (FBS), and 1% (v/v) penicillin/streptomycin (P/S). Caco-2 cells were cultivated in MEM supplemented with 15% (v/v) heat-inactivated FBS, 1% (v/v) P/S and 1% (v/v) non-essential amino acids (NEAA). COS-7 stably expressing (sT) SNAP-, EYFP-tagged claudins or EGFP-C1 as control and MDCKII QKO sT SNAP-, EYFP-, FLAG-, HA-tagged claudins, or EGFP-C1 as control were cultivated in the same cultivation medium as described above with additional 1-2 µg/ml puromycin for single expressing cells and additional 300-500 µg/ml G418 (Geneticin) for double expressing cells. Cells were passaged every 2 to 4 days. The cell density never exceeded 90% confluency. Caco-2, MDCKC7, MDCKII, MDCKII QKO, and MDCKII QKO sT cells were kept at a lower density of 60-80% to guarantee a faster detachment. Cells were washed with PBS and incubated with TrypLE Express (1 ml/Ø10 cm dish; 0.5 ml/Ø6 cm dish; 0.5 ml/well of a 6-well plate) for at least 5 min at 37°C and 5% CO_2. The cell detachment was checked with a brightfield microscope. Detached cells were resuspended in a 10-fold excess of medium. Cells were plated in dilutions of 1:5 to 1:30 in a new cell culture dish. In general, cells were discarded beyond passage 30. COS-7 cells were already discarded after 18 passages. Only MDCKC7 cells were kept in culture for up to 90 passages. For cryo-preservation, cells were cultured to approximately 90% confluency, detached with TrypLE Express, and resuspended in medium containing no FBS and no antibiotics. The cell number was determined by using a Neubauer chamber (described in 3.2.2). Cells were spined down at 800 rpm for 5 min and the pellet was resuspended in cryoprotectant medium (50% (v/v) DMEM and 50% (v/v) (FBS 80% (v/v) and 20% (v/v) DMSO)) to achieve a concentration of $2*10^6$ cells per ml. $2*10^6$ cells per cryo-protectant tube were stored overnight at -20°C and transferred the next day to -80°C. After 24 hours the cells were transferred for long-term storage to the liquid nitrogen vapor phase tank. For re-cultivation, cells were thawed at 37°C and seeded in a Ø10 cm dish containing the cell line specific medium. For live imaging and immunocytochemistry (ICC) experiments, COS-7 cells were seeded on Ø25 mm, Ø18 mm glass coverslips (CS), or in 8-well IBIDI

chambers. The surface of the CS and the wells of the IBIDI chamber were coated with 2% (v/v) Matrigel dissolved in DMEM. Matrigel is a basement membrane preparation enriched with extracellular matrix (ECM) proteins like laminin, collagen IV, proteoglycans, and growth factors. A sufficient coating was achieved by applying a 2% Matrigel solution on the surfaces as a thin layer followed by an incubation for one hour at 37°C. Epithelial cells (Caco-2, MDCKC7, MDCKII, MDCKII QKO and MDCKII QKO sT) were seeded either in a low density (40% confluency) on Ø25 mm glass CS coated with 2% Matrigel or in a higher density (80% confluency) on non-coated Ø25 mm glass CS or non-coated 0.6 cm^2 sized filter insets (0.4 µm pore size, PCF or PET) for immunocytochemistry (ICC) experiments.

3.2.2 Determination of the cell concentration using a Neubauer chamber

Detached cells were resuspended in 10-50 ml of DMEM and transferred to a 15 ml or 50 ml collection tube. 10 µL of the cell suspension were pipetted on the cell counting grid on one side of the Neubauer chamber (Neubauer improved, 0.1 mm depth). Cells were counted in the 64 small squares of the four big squares, including cells on the inner two borders (schematically illustrated in Figure 10), and the cell concentration per ml was calculated by using Equation 1, which results from the depth and area of the big squares of the Neubauer chamber described in Equation 2.

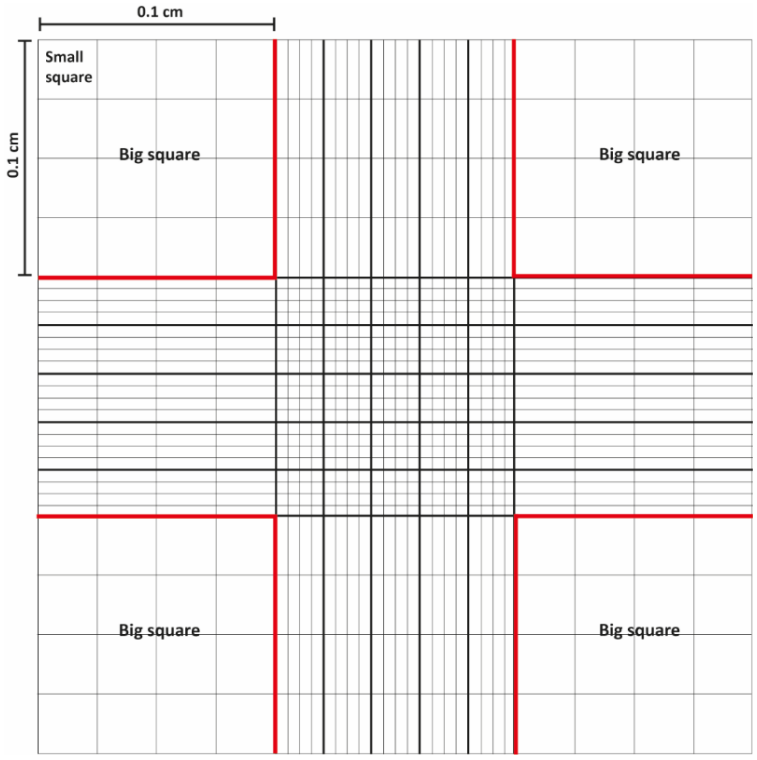

Figure 10 Scheme of the cell counting grid of a Neubauer chamber. The grid consists of four big squares, each covering an area of 0.01 cm^2. The depth of the grid is 0.01 cm, resulting in a volume for one big square of 0.0001 cm^3 which equals 0.1 µl. Every big square contains 16 small squares. Cells were counted in the four big squares, including cells that were on the two red-labeled borders of the big squares.

Equation 1 Simplified calculation of the cell concentrations using a Neubauer chamber.

$$\text{cell concentration in ml} = \frac{\text{counted cells} * 10000}{\text{number of big squares}}$$

Equation 2 Calculation of the cell concentrations using a Neubauer chamber.

$$\text{cell concentration in ml} = \frac{\text{counted cells}}{0.1\ \mu l * \text{number of big squares}} * 1000$$

3.2.3 Transfection of plasmid DNA with Lipofectamine 2000

Lipofectamine 2000 was used to transfect COS-7 or HEK293 cells with plasmid DNA. Lipofectamine is a cationic lipid forming liposomes and complexes with negatively charged DNA, facilitating binding to cell membranes, and thus allowing DNA uptake. Cells were seeded 24 hours before transfection in medium containing FBS and antibiotics. Plasmid DNA and Lipofectamine 2000 were diluted separately in OptiMEM. The specific amounts are

listed in Table 26. Both solutions were briefly mixed and incubated for 5 min at RT. Subsequently, the DNA mix was combined with the Lipofectamine mix and incubated for 20 min at RT. The medium of the cells was changed, and the transfection mix was added dropwise to the cells. The growth medium was exchanged again after 6 hours. After 24 hours, the cells were used for microscopy, ICC, or biochemical experiments.

Table 26 Volume of reagents per well for transfection with Lipofectamine 2000.

One well of a multi-well plate	Total volume (ml)	Medium (ml)	DNA/Lipofectamine-Mix (µl)	DNA (µg)	Lipofectamine 2000 (µl)
10-well (Greiner)	0.1	0.075	2*12.5	0.16	0.2
8-well (Ibidi)	0.2	0.15	2*25	0.32	0.4
12-well	1	0.75	2*125	1.6	2
6-well	2	1.5	2*250	3.2	4

3.2.4 Transfection of plasmid DNA with Lipofectamine 3000

Lipofectamine 3000 was used to transfect Caco-2, MDCKC7 and MDCKII cells with plasmid DNA. Lipofectamine 3000 provides, compared to Lipofectamine 2000, a superior transfection performance and higher transfection yields. It is based on the same biophysical principle as previously described for Lipofectamine 2000. Cells were seeded 24 hours before transfection in medium containing FBS and antibiotics. Plasmid DNA and Lipofectamine 3000 were diluted separately in OptiMEM. Additionally, P3000 was added to the DNA mix. Both solutions were mixed thoroughly. The specific amounts are listed in Table 27. The DNA mix was combined 1:1 with the Lipofectamine 3000 mix and incubated for 15 min at RT. The growth medium was changed, and the transfection mix was added dropwise to the cells. After 24 hours, the cells were used for microscopy, ICC, or biochemical experiments.

Table 27 Volume of reagents per well for transfection with Lipofectamine 3000.

One well of a multi-well plate	Total volume (ml)	Medium (ml)	DNA/Lipofectamine-Mix (µl)	DNA (µg)	Lipofectamine 3000 (µl)	PEG 3000 (µl)
12-well	1	0.875	2*62.5	1.6	2.5	5
6-well	2	1.75	2*125	3.2	5	10

3.2.5 SNAP- and Halo-tag labeling

COS-7 or HEK293 cells transiently expressing SNAP- or Halo-tagged proteins were labeled with the corresponding ligands 24 hours after transfection. COS-7 cells stably expressing SNAP- or Halo-tagged proteins were labeled with the corresponding ligands 24 hours after seeding. SNAP- and Halo-tag ligand stock solutions (1 mM) (listed in Table 19) were thawed slowly at RT. The cell-permeable ligands were diluted in 37°C pre-warmed medium without antibiotics to a final working concentration of 2 µM for SNAP-tag ligands and 1 µM for Halo-tag ligands. Cells were washed once with pre-warmed medium without antibiotics, followed by a complete aspiration of the medium. The ligand solution was carefully added to the cells. When the cells were seeded on glass CS (Ø18 mm; Ø25 mm), the ligand solution was carefully placed as a drop on top of the CS. Cells were incubated for one hour in a humidified incubator at 37°C and 5% CO_2. The labeled cells were washed at least three times with DMEM to reduce the amount of unbound ligand. After 30-60 min post-incubation in a humidified incubator at 37°C and 5% CO_2, the cells were used for microscopy or ICC experiments.

3.2.6 Lentivirus production via calcium phosphate transfection of HEK293T cells

HEK293T cells were used for lentiviral production because of their expression of a mutant version of the SV40 large T antigen. In combination with plasmid DNA which carries the SV40 origin of replication and specific packaging plasmids coding for the viral proteins, a high copy number of virus particles can be achieved. Since lentiviruses are potentially harmful, all steps after the calcium phosphate transfection were performed under strict S2 regulations, and all created viruses were documented in S2 datasheets.

One day before transfection, HEK293T cells were seeded at a confluency of 60-70% in Ø10 cm dishes or wells of a 6-well plate. After 24 hours, the cells were transfected using calcium phosphate. Calcium phosphate transfection is based on the active uptake of DNA-calcium phosphate co-precipitates which adheres to the cell surface of cells. The packaging plasmid DNA pCIG3.NB, the lentiviral envelope plasmid psMD2.G (encodes for a vesicular stomatitis virus glycoprotein (VSV-G)), and the genome plasmid DNA were mixed with 1xTE and 2.5 M $CaCl_2$. After 5 min incubation at RT, the DNA mix was transferred dropwise under swirling into a tube containing HBS (2x). The exact volumes are listed in Table 28. After 20

min incubation at RT, the mixture was added carefully to the cells. After 24 hours, the transfection efficiency was checked with a basic fluorescent microscope. A plasmid coding for EGFP-N1 served in every transfection round as a transfection efficiency control. The medium was changed, and the volume was reduced by 20%. Every 48 hours, the supernatant was collected, and a fresh medium was added. The supernatant was centrifuged for 5 min at 2000 rpm to remove cell debris, filtered (0.45 µm pore sized filter) and transferred in a new 50 ml tube. All supernatants were stored at 4°C for up to 2 weeks or at -80°C for long-term storage. To concentrate the virus, all collected supernatants of one created virus were pooled in Amicon Ultra-15 (100 kDa) tubes and spun down for 20 min at 4,696*g. The concentrated supernatants were collected and stored at -80°C.

Table 28 Volume of reagents per well and dish for calcium phosphate transfection.

One well or dish	Medium (ml)	pCIG3.NB (µg)	psMD2.G (µg)	Plasmid DNA (µg)	TE (1x) (µl)	2.5M $CaCl_2$ (µl)	HBS (2x) (µl)
6-well	2	1.75	0.75	2.5	74	10	84
Ø10 cm dish	10	10.5	4.5	15	440	60	500

3.2.7 Creating stable cell lines with lentivirus

Generating stably expressing cells by lentiviral transduction is based on the random incorporation of viral DNA in the host genome. Depending on the virus's potency and the rounds of infection, one or several copies of viral DNA can be incorporated. The expression of the encoded proteins depends on the used promotor. In this study, the protein expression was under the control of a CMV-promoter.

For the generation of stably expressing cell lines COS-7 or MDCKII QKO were seeded at a confluency of 60-70% in 6-well or 12-well plates containing DMEM supplemented with 10% FBS and 1% P/S. After 24 hours, the medium was reduced to 1 ml for 6-well plates and 0.5 ml for 12-well plates. 0.2-1 ml of non-concentrated or 50-100 µl of the concentrated virus was used to infect the cells. An EGFP-C1 transducing virus served as infection control. After 48-72 hours, the infection efficiency of EGFP-N1 control was checked with a fluorescence microscope. For the selection of successfully infected cells and non-infected cells, 5 µg/ml puromycin and up to 1000 µg/ml G418 were used. The selection was started with 5 µg/ml puromycin and changed after 48 hours to 2 µg/ml puromycin. For double

selection 500-1000 µg/ml G418 was added to the selection medium. The cells were routinely checked for viability and expression level. After one week, the selection pressure was reduced to 2 µg/ml puromycin and 300 µg/ml G418. For long-term culture, 1-2 µg/ml puromycin and 300 µg/ml G418 were used.

3.2.8 Immunocytochemistry (ICC)

COS-7 seeded on CS (Ø18 mm; Ø25 mm) or in 8-well Ibidi chambers with a glass-bottom were washed once with PBS^{++} to remove residual medium and fixed with 4% (w/v) paraformaldehyde (PFA)/sucrose for 15 min at RT. PFA causes covalent cross-links between molecules, that leads to the formation of an insoluble meshwork, fixating the actual close to the native state of the proteins within a cell. Fixated cells were washed once with PBS^{++} and permeabilized with 0.2% (v/v) Triton X-100 for 5 min at RT. Triton X-100 permeabilizes cells and creates non-reversible holes in the plasma membrane by removing cellular membrane lipids. To avoid unspecific antibody binding the cells were incubated in a blocking solution (BS) (6% (v/v) NGS, 1% (w/v) BSA, 0.05% (v/v) Tween 20) for 30 min at RT. The primary antibody was diluted in BS (Table 16) and applied as a 100 µl drop on the cells and incubated for one hour at RT or 24 hours at 4°C in a humidity chamber. Cells were washed three times with PBS^{++} to remove the unbound primary antibody. Directly labeled antibodies (Table 17) were applied together with the normal primary antibodies following the same protocol. The bound primary antibodies were decorated with secondary antibodies (Table 18) by an following incubation for one hour at RT in BS in a humidity chamber. GFP-boosting nanobodies (Table 17) and cell compartment labeling compounds (Table 20) were incubated alone or together with the secondary antibodies for one hour at RT in BS in a humidity chamber. The antibody decorated and cell compartment labeled cells were washed three times with PBS^{++} and stored in PBS^{++} at 4°C until imaging. For long-term storage, the cells were mounted in Immu-Mount on object slides for one hour at 37°C. For STED microscopy, the cells were mounted in ProLong Gold antifade on object slides for at least 48 hours at RT. Cells in 8-well chambers were mounted in ProLong Gold antifade and covered with small Ø6 mm CS.

ICC of Caco-2, MDCKC7, MDCKII, MDCKII QKO and MDCKII QKO sT cells, that were seeded on glass CS or filter insets, was performed as described above. With the exceptions

that the cells were fixed with ice-cold EtOH for 20 min at -20°C. Since EtOH is permeabilizing the cell membranes on its own, no additional permeabilization with Triton X-100 was needed. The immunostaining was directly performed on the filter. The filter inserts were cut out with a scalpel and placed with the filter bottom on object slides. A glass CS (Ø18 mm; Ø25 mm) was placed with a drop of Immu-Mount or ProLong Gold Antifade on top of the filter to seal it.

3.2.9 Cholesterol depletion assay

COS-7 cells were transfected with SNAP-Cldn2 and EYFP-Cldn10a (described in 3.2.3) and treated with 10 µM mevastatin for 24 hours in DMEM with FBS or 20 mM Methyl-β-cyclo-dextrin (MβCD) for two hours in DMEM without FBS. In an additional approach, an equal amount of DMSO or H_2O was used as control. SNAP-Cldn2 was labeled with SNAP-Atto590-BG (described in 3.2.5), and EYFP-Cldn10a was stained with an anti-GFP Atto647N nanovody (described in 3.2.8) and imaged in two-color STED (described in 3.6.3). A Filipin III staining was performed to verify the reduction of intracellular and plasma membrane cholesterol. Cells were fixed with 4% (v/v) PFA/sucrose for 15 min, quenched with 0.1 M glycine in PBS^{++} for 30 min, and incubated for two hours with 25 µg/ml Filipin III in PBS^{++} under light protection. The cells were washed with PBS^{++} and imaged in PBS^{++} with a Leica SP8 TCS microscope. For the excitation of the Filipin III, a UV laser with an excitation wavelength of 405 nm was used.

3.2.10 Cldn2 pore-blocking assay

COS-7 cells were transfected with pEGFP-$Cldn2^{I66C}$ and pSNAP-Cldn10a (described in 3.2.3). Cells were either treated with 1 mM MTSET or an equal volume of DMSO for two hours in DMEM. Cells were labeled with SNAP-Atto590-BG (described in 3.2.5) and immunofluorescent stained with anti-GFP Atto647N (described in 3.2.8) and imaged in two-color STED (described in 3.6.3).

3.2.11 Co-culture

COS-7 cells were seeded in 6-well plates and transfected with 3.2 µg pSNAP-Cldn2$_{ECL10a}$, pEYFP-Cldn10a, or pEYFP-Cldn2 (described in 3.2.3). After 24 hours, the cells were detached and washed thoroughly with PBS. After resuspension in DMEM, the pSNAP-Cldn2$_{ECL10a}$ expressing cells were mixed with pEYFP-Cldn2 or pEYFP-Cldn10a expressing cells in a ratio of 1:1 and seeded on Ø25 mm glass CS and incubated for 24 hours at 37°C and 5% CO_2. For SNAP-tag labeling 2 µM Atto590-BG was used (described in 3.2.5). The EYFP-signal was boosted with the GFP-booster Atto647N (described in 3.2.8). Confocal and STED images were taken with the Leica SP8 TCS STED microscope (described in 3.6.2 and 3.6.3).

3.3 Molecular biology methods

3.3.1 Oligonucleotides

Oligonucleotide design and *in silico* cloning were performed with Clone Manager Professional Suite 8. For the simple amplification of target sequences, primers were designed with an overlap of at least 18 bp. Based on the approach, additional restriction sites and a four base pairs overlap (TATA) for a superior restriction were added at the 5' of the primer. The primer melting temperature (T_M) was kept in between 50°C and 72°C. The GC content was kept in a range of 40-50% to provide high primer stability. A GC clamp was usually included. Regarding potential conceptual errors, including multiple primer binding, frameshifts, dysfunctional restriction sites, and unwanted stop codon insertions, all cloning approaches were first performed *in silico*.

3.3.2 Polymerase chain reaction

The polymerase chain reaction (PCR) was first described by Kary Mullis[181] and described as a method in 1988 by Saiki et al.[184,185]. PCR allows the exponential amplification of a specific DNA sequence which serves in the reaction as a template. It is a multi-cycle reaction repeating mainly three main steps. In the first step, the template DNA gets denatured to create linear DNA strands. In a second step, short, highly specific DNA oligonucleotides known as primers can anneal with their complementary sequence and bind to the linear DNA template. In the last step, a DNA polymerase elongates the primer DNA by

adding free nucleotides (nts). The newly synthesized DNA fragments serve in the following cycles as templates leading to an exponential DNA amplification.

In this study, the PCR method was used to amplify plasmid DNA sequences for subsequent cloning in mammalian expression vectors. The chemicals and volumes used for standard PCR are listed in Table 29. The Phusion DNA polymerase was used due to its high fidelity as a standard amplification enzyme. Depending on the primers' length and their annealing abilities, two different PCR programs were used (described in Table 30). The 2-step protocol was used for long primers (>40 bp) and primers with a high T_M (>72°C).

Table 29 PCR reaction mix for Phusion High-Fidelity DNA polymerase.

Components	Volume	Final concentration
5x Phusion HF buffer	10 µl	1x
10 mM dNTPs	1 µl	200 µM
10 µM forward primer	2.5 µl	0.5 µM
10 µM reverse primer	2.5 µl	0.5 µM
Template DNA	variable	1-10 ng
DMSO (only for 2-step PCR reaction)	(1.5 µl)	(3%)
Phusion High-Fidelity DNA Polymerase	0.5 µl	1 unit
Nuclease-free water	to 50 µl	X
Total volume	50 µl	X

Table 30 PCR programs for Phusion High-Fidelity DNA polymerase.

		Standard	2-step
	Initial denaturation	98°C, 30 s	98°C, 30 s
	Cycle start		
	Denaturation	98°C, 10 s	98°C, 10 s
25-35 cycles	Primer annealing	45-72°C, 30 s	72°C, 30 s per kb
	Elongation	72°C, 30 s per kb	
	Cycle end		
	Final extension	72°C, 10 min	72°C, 10 min
	Storage	8°C, infinite	8°C, infinite

The annealing temperature depended on the used primers and was generally chosen to be equal to the primers' salt-adjusted melting temperature.

3.3.3 Colony PCR using the Taq DNA polymerase

Colony PCR was used to identify bacterial clones that incorporated the desired plasmid after transformation (described in 3.3.12). For each approach, several colonies were picked with sterile pipette tips, dipped in 200 µl LB medium containing the selection antibiotics in a 96-well plate, and cultivated for two hours at 180 rpm at 37°C. The same tips were dipped further on in the PCR reaction mix (described in Table 31) containing the Taq-polymerase and two specific primers (FW and RV) (listed in Table 12). The PCR was performed according to Table 32. The analysis of the PCR was performed with an agarose gel electrophoresis (described in 3.3.6). Positive colonies were taken for cultivation, preparation, and sequencing.

Table 31 PCR reaction for Taq DNA polymerase.

Components	Volume	Final concentration
10x Standard Taq reaction buffer	2.5 µl	1x
$MgCl_2$	2.5 µl	1.5 mM
5 mM dNTPs	1 µl	200 µM
5 U/µl Taq DNA-Polymerase	0.125 µl	0.625 U
10 µM forward primer	0.5 µl	0.2 µM
10 µM reverse primer	0.5 µl	0.2 µM
10x OrangeG loading dye	2.5 µl	1x
Nuclease-free water	to 25 µl	X
Total volume	25 µl	X

Table 32 PCR programs for Taq DNA polymerase.

		Standard	2-step
	Initial denaturation	98°C, 30 s	98°C, 30 s
25-35 cycles	**Cycle start**		
	Denaturation	98°C, 10 s	98°C, 10 s
	Primer annealing	45-68°C, 30 s	68°C, 1 min per kb
	Elongation	68°C, 1 min per kb	
	Cycle end		
	Final extension	68°C, 10 min	68°C, 10 min
	Storage	8°C, infinite	8°C, infinite

The annealing temperature depended on the primers used and was generally chosen to be equal to the primers' salt-adjusted melting temperature.

3.3.4 Site-directed mutagenesis

Site-directed mutagenesis is a PCR-based cloning technique that allows the insertion of point mutations, base pair deletions, or base pair insertions in the region of interest of a plasmid. In the first step, two primers were designed, which annealed back-to-back to the plasmid. One of the primers contained the desired mutation, whereas the other primer was complementary to the plasmid sequence. Primers were either ordered with a 5'-end phosphorylation or were phosphorylated in an additional step using the T4 kinase kit from Thermo Fisher Scientific (described in 3.3.9). Deletions were introduced by designing perfectly matching primers that border the deleted area on both sides. Point mutations were created by designing one or multiple mismatches and short insertions by designing a stretch of mismatches in the mutagenic primer. In general, the primer length was around 25-30 nts, and the mutations were in the middle with at least 10-15 nts on each side. The starting plasmid amount was kept at a low range of 1-5 ng to reduce the unmutated plasmid background. The PCR was performed using the Phusion polymerase following the instructions in 3.3.2 only the number of cycles never exceeded 25 to prevent unwanted secondary mutations induced by the polymerase. The amount and size of DNA fragments of the PCR reaction were checked with gel electrophoresis (described in 3.3.6). To reduce the amount of Dam-methylated parental plasmid DNA, the PCR product was incubated with 1 U DpnI enzyme for 15 min at 37°C. The following ligation and heat-shock transformation were performed as described in 3.3.11 and 3.3.12.

3.3.5 NEBuilder HiFi DNA Assembly cloning

For the assembly of multiple DNA fragments, the NEBuilder HiFi DNA Assembly cloning kit from New England Biolabs was used. In the first step, four primers were designed. Two primers were for the amplification of the plasmid backbone without the region which should be exchanged. These primers were entirely complementary to the plasmid backbone. The other two primers amplified the region of interest, which should be inserted in the generated plasmid backbone. Those primers were complementary to the region of interest and complementary to the ends of the generated plasmid backbone. All shared sequences had a melting temperature of at least 48°C. Both PCR reactions were performed using the Phusion DNA polymerase according to 3.3.2. The success of the PCR reaction was controlled

by gel electrophoresis described in 3.3.6. The assembly reaction of the two PCR products was performed according to the manufacturer's instructions for 15 min at 50°C. The used amounts are listed in Table 33. The DNA concentration of the PCR products was measured with a Nanodrop spectrometer (3.3.16). The amount of PCR fragments was calculated based on Equation 3. A from the manufacturer provided positive control reaction was run in parallel.

Table 33 HiFi assembly reaction mix.

Components	2-3 fragments	4-6 fragments	Positive control
DNA ratio (vector:insert)	1:2	1:1	
Total amounts of fragments	0.1 pmol -X µl	0.5 pmol -X µl	10 µl
NEBuilder HiFi DNA Assembly Master mix	10 µl	10 µl	10 µl
Nuclease free water	to 20 µl	to 20 µl	-
Total volume	20 µl	20 µl	20 µl

Equation 3 Calculation of the molar amounts of fragments for HiFi assembly.

$$\text{pmols} = \frac{(\text{weight in ng}) * 1000)}{\text{basepairs} * 650 \text{ daltons}}$$

For the transformation, 50 µl of commercial DH5α competent cells and 2 µl of the assembled product were used.

3.3.6 Preparative and analytical agarose gel electrophoresis

Agarose gel electrophoresis was used to separate plasmid DNA and DNA fragments based on their size to analyze restriction digest, PCR, colony PCR, and DNA purification. Agarose gels were prepared by dissolving 0.5-2% (w/v) agarose in 1xTAE buffer. For mini gels, 100 ml, and for midi gels, 200 ml of 0.5-2% agarose was used. 5 µl of a 1% concentrated ethidium bromide (EtBr) solution was added to the liquid agarose solution. EtBr intercalates with the DNA and allows the detection and quantification of DNA with UV light. DNA samples were mixed with a 6x Tri-Track loading dye to a 1x final concentration and loaded on the hardened and cooled down agarose gel. As DNA ladder 5-10 µl of GeneRuler 1 kb was

used. The loaded volume depended on the pocket size of the used comb. Subsequently, the gel was run in a Perfect Blue chamber from PeqLab filled with 1x TAE buffer at 160 Volt for 20-30 min. DNA fragments were visualized by UV light on a UV table and imaged with a G-Box gel documenting system. If the DNA fragments were used for further cloning steps, the UV light exposure was kept to a minimum.

3.3.7 Purification of plasmid DNA and PCR products from DNA agarose gels

For the purification of DNA from agarose gels, DNA bands were excised from the gel under UV light and extracted with a NucleoSpin Gel and PCR clean-up kit according to the manufacturer's instructions (Table 10).

3.3.8 Restriction digest

Restriction digests were performed according to the manufacturer's instructions for fast digest enzymes from Thermo Fisher Scientific. The used restriction enzymes are listed in Table 9. The composition of a restriction digest is listed in Table 34. For the digest of 25 µl of PCR product or 1-3 µg of plasmid DNA was used and 1 U of each restriction enzyme. The restriction mix was incubated for one hour at 37°C under constant agitation and stored if needed at 4°C.

Table 34 Composition of the fast digest reaction mix.

Components	1x	6x
10x Fast digest buffer (Green)	3 µl	18 µl
Fast digest enzymes	1 µl (1 U) each enzyme	6 µl (6 U) each enzyme
DNA (PCR product or plasmid DNA)	25 µl PCR or ≤ 2 µg Plasmid	150 µl PCR or ≤ 12 µg Plasmid
Nuclease free water	to 30 µl	to 180 µl
Total volume	30 µl	180 µl

3.3.9 Phosphorylation of primers and PCR products

For the phosphorylation of oligonucleotides and linear double-strand (ds) DNA, the T4 polynucleotide kinase was used. The reaction was performed according to the manufacturer's instructions. The specific amounts of reagents used in this study are listed in

Table 35. A 10 mM ATP solution was prepared by combining 10 µl of 100 mM ATP and 90 µl of nuclease-free H_2O. The reaction took place at 37°C for 20 min. The T4 kinase was heat-inactivated at 75°C for 10 min.

Table 35 Composition of the T4 polynucleotide kinase reaction mix.

Components	Linear double-strand DNA	Oligonucleotide
DNA	10 pmol	30 pmol
10x reaction buffer A	2 µl	2 µl
10 mM ATP	2 µl	2 µl
T4 polynucleotide kinase	1 µl (10 U)	1 µl (10 U)
Water, nuclease-free	to 20 µl	to 20 µl
Total volume	20 µl	20 µl

3.3.10 Dephosphorylation of vector DNA using CIP

Calf-Intestinal-Phosphatase (CIP) was used to dephosphorylate linearized vector DNA. CIP hydrolyzes the 5'-phosphates from linear DNA molecules, thereby preventing spontaneous recircularization of linearized vectors and reducing the number of false-positive colonies after the transformation of ligation reactions. CIP was added directly into the completed restriction digest for an additional incubation of 10 min at 37°C.

3.3.11 Ligation of DNA fragments into linearized plasmid vectors

The concentration of DNA fragment (insert) and the linearized vector after agarose gel purification was photometrically determined with a Nanodrop spectrometer (described in 3.3.16). The insert was used in a molar ratio of 3:1 or 5:1 over the linear vector DNA (100 ng). The corresponding insert mass was calculated with the online tool NEBiocalculator (Table 23). Ligation reactions were performed according to the manufacturer's instruction (Table 36). All reactions were incubated at 16°C overnight in a thermocycler. For the following transformation of chemically competent *E. coli*, 5-10 µl of the ligation mix was used.

Table 36 T4 ligase reaction mix.

Components	Volume
Linear vector DNA	100 ng
Insert DNA	3:1, 5:1 molar ratio over vector
10x T4 DNA ligase buffer	2 µl
T4 DNA ligase	1 U
Nuclease-free water	to 20 µl
Total volume	20 µl

3.3.12 Heat-shock transformation of competent bacteria with plasmid DNA

For the transformation of mammalian plasmid expression vectors, 50 µl chemically ($CaCl_2$) competent *Escherichia coli* (*E. coli*) TOP10 or 10 µl commercially available competent DH5α (New England Biolabs) bacteria were used (described in 3.1.9). For the transformation of lentiviral plasmids, 50 µl of HB101 bacteria was used because of their reduced internal DNA recombination (described in 3.1.9). Competent cells were slowly thawed on ice and incubated with 10 ng/µl plasmid DNA for a re-transformation or 5-10 µl of ligation mix for 20 min on ice. As a transformation control, 10 ng/µl EYFP-N1 or EGFP-N1 were used. The heat-shock was performed by incubation for 45 s at 42°C, followed by a two min incubation on ice. 100-500 µl LB-medium was added, and the mix was incubated for one hour at 37°C under constant agitation. 100-200 µl was plated on pre-warmed LB-agar plates containing the antibiotics corresponding to their selective resistance. The plates were incubated at 37°C overnight or RT for 48 hours until colonies were formed. If necessary, the plates were stored at 4°C for up to 4 weeks. Bacterial colonies were used for colony-PCR and inoculation of overnight cultures for Mini- and Midi DNA preparation (described in 3.3.13).

3.3.13 Overnight cultures

For Mini preparation of plasmid DNA, 5 ml LB-medium with the corresponding antibiotic was inoculated with one colony from a transformation plate or 10 µl of a colony PCR approach and incubated at 37°C and 180 rpm for 18 hours. For Midi preparations, 100-400 ml of LB-medium with the plasmid resistance corresponding antibiotic was inoculated with one picked colony, 100 µl of a colony PCR approach, or 50 µl of a 5 ml pre-culture. A pre-culture was set up as described for a Mini preparation.

3.3.14 Glycerol stocks of bacterial clones

For glycerol stocks of bacterial clones, 500 µl of a bacterial overnight culture were diluted 1:1 with sterile 100% (v/v) glycerol and stored in cryotubes at -80°C.

3.3.15 Mini and Midi purification of DNA from *E. coli*

DNA from *E. coli* was purified either on a small scale by DNA Mini purification using 2 ml of a small overnight culture or on a larger scale by DNA Midi purification of 100-400 ml overnight cultures. The overnight cultures were spun down for 30 min at 4649*g and 4°C. For the DNA Mini purification, the NucleoSpin Plasmid kit from Macherey-Nagel and for DNA Midi purification, the NucleoBond Xtra endotoxin-free (EF) plasmid purification kit from Macherey-Nagel was used according to the manufacturer's instructions (Table 10). Both purification kits are based on the same principle. An alkaline and SDS-containing buffer lyses the bacteria in the first step. The genomic DNA gets removed by centrifugation, as well as proteins and cell debris. The plasmid DNA stays in the supernatant and can be bound in a gravity flow step to a silica column. After intensively washing to remove DNA contaminations, the plasmid DNA is eluted in RNAse-free water or a TE-buffer. The Midi purification includes more washing steps, a column with very high DNA affinity to remove all endotoxins, and final isopropanol precipitation, making the final eluate cleaner compared to the Mini preparation eluate. The final concentration of Midi eluates was set to 1,000 ng/µl. For Mini eluates, no further dilution was applied.

3.3.16 DNA concentration measurement with a NanoDrop spectrometer

DNA concentrations were determined with the spectrometer NanoDrop ND-1000 from Thermo Fisher Scientific. DNA was measured at its specific absorption at 260 nm. The measurement of DNA is based on the Beer-Lamber law:

Equation 4 Beer-Lamber law.

A = absorbance in absorbance units (AU)

ε = extinction coefficient (L*cm/mol)

c = analyte concentration (mol/L)

l = path length (cm)

$$A=\varepsilon*c*l \rightarrow c=\frac{A}{\varepsilon*l}$$

For nucleic acid quantification, the Beer-Lambert equation is modified to use an extinction coefficient (ε') with units of ng*cm/µl:

Equation 5 Modified Beer-Lamber law.

A = absorbance in absorbance units (AU)

ε'= modified extinction coefficient (ng*cm/µl)

c = analyte concentration (ng/µl)

l = path length (cm)

$$c=\frac{A*\varepsilon'}{l}$$

As extinction coefficient (ε') for double-strand DNA, 50 ng*cm/µl was used. The light path within the NanoDrop ND-1000 was l = 1 cm. The quality of DNA preparations, the ratio of DNA extinction at 260 nm and protein extinction at 280 nm, and RNA extinction at 230 nm were determined. A260/A280 values between 1.8-1.9 and A260/A230 values between 2.0-2.2 guaranteed a pure DNA preparation. The linearity for absorbances was guaranteed between an optical density (OD) of 0.1-1 at 260 nm and a DNA concentration of 10 ng/µl and 3,700 ng/µl. Higher DNA concentrations required further dilution.

3.3.17 Sequencing of DNA plasmids

DNA sequences were controlled for correctness by sequencing at LGC Biosearch Technologies. Either custom-designed sequencing primers (Ready2Run) or sequencing primers provided by the LGC Biosearch Technologies (Flexi Run) were used. For a Plasmid Ready2Run approach, 10 µl DNA (100 ng/µl) and 4 µl Primer (5 µM) were needed, and for a Flexi Run approach min. 15 µl DNA (100 ng/µl) was required. For sequencing, the Applied Biosystems ABI 3730 XL Analyzer was used, and per run, a read length of up to 1,100 nts was achieved (PHRED20 quality). Sequencing results were analyzed with the software Clone Manager Professional Suite 8.

3.4 Biochemical methods

3.4.1 Lysate preparation

Cells were placed on ice and washed once with ice-cold PBS. PBS and medium residues were aspirated, ice-cold lysis buffer (500 µl per 10 cm dish; 100 µl per well of a 6-well plate) was added, and the cells were scraped off with a pre-cold plastic cell scraper. The cell lysis solution was gently transferred into a pre-cooled microcentrifuge tube, incubated for 30 min on ice, and centrifuge for 20 min at 12,000 rpm and 4°C. The supernatant was transferred in a fresh microcentrifuge tube and kept on ice. The pellet was discarded.

3.4.2 Bradford assay

For the protein concentration determination 1-10 µl of cell lysate or lysis buffer as control was used and diluted in 500 µl Bradford and 499-490 µL RNAse-free H_2O in a 1.5 ml microcentrifuge tube, mixed and transferred into a 1.5 ml macro cuvette. After 5 min incubation at RT, the protein concentration was determined with the OD of the sample at 595 nm. A monthly pre-done BSA standard curve with known protein concentration was used to calculate the protein concentration of the sample:

Equation 6 Linear function for calculation of protein concentration in cell lysates.

x = protein concentration (µg/ml)

y = optical density (OD)

a = slope of the linear regression

b = intersection with the y-axis

$$y=a*x+b \rightarrow x=\frac{y+b}{a}$$

In a final step, a 6x sample buffer was mixed with the sample in a pre-cooled microcentrifuge tube to reach a final concentration of 1x sample buffer. The ingredients of the sample buffer (listed in Table 5) interact with the proteins in the cell lysate. SDS linearizes the proteins and charges them negatively. DTT disrupts disulfide bridges. Glycerol provides the needed density for loading the sample in a polyacrylamide gel for an SDS-PAGE. The sample was incubated for 5 min at 95°C and stored at -20°C.

3.4.3 Sodium dodecyl sulfate-polyacrylamide gel electrophoresis

A sodium dodecyl sulfate-polyacrylamide gel electrophoresis (SDS-PAGE) was used to separate denatured proteins by size for further detection and quantitative analysis in a Western Blot. This technique is based on the different voltage-dependent traveling speeds of differently sized proteins through a polyacrylamide gel with a specific porosity. To achieve this, the proteins got denatured by incubation in an SDS-containing sample buffer at 95°C (described in 3.4.2). Because of SDS's negative charge, the separation of proteins in a voltage-dependent field is only depending on their size. Smaller proteins travel faster, whereas bigger proteins travel slower. The polyacrylamide gels are formed by an induced copolymerization of acrylamide and *bis*-acrylamide. The initiator of the copolymerization is ammonium persulfate (APS) and tetramethyl ethylenediamine (TEMED). TEMED stabilizes free radicals from persulfates and increases their formation rate, which in turn react on acrylamide monomers and convert them into free radicals to begin the polymerization chain reaction. Randomly crosslinking of the acrylamide polymers by *bis* leads to the formation of

a gel with a characteristic porosity that depends mainly on the polyacrylamide monomer concentration.

For the SDS-PAGE, two differently concentrated polyacrylamide gels, the separating gel, and the stacking gel, were prepared. The stacking gel has the function to concentrate all proteins so that every protein starts into the separating gel simultaneously. This is achieved by a lower pH of 6.8 and a lower acrylamide percentage (3.8%). Depending on the proteins' sizes, the used concentration of acrylamide was adjusted to generate separating gels with different porosity. The ingredients for both solutions except for APS and TEMED were mixed thoroughly in two 50 ml tubes. APS was added first to the separating gel solution and then TEMED (Table 37). The solution was mixed thoroughly and filled in a gel holder from Bio-Rad. A thin layer of 2-propanol was added on top of the gel to prevent the gel from drying out. After 30 min incubation at RT, the 2-propanol was discarded, and the stacking gel was prepared as described above for the separating gel; the different volumes are listed in Table 38. The stacking gel was filled on top of the separating gel. A comb was slide in the stacking gel and the gel polymerized for 30 min at RT. The prepared gel was placed in an SDS-PAGE running tank from Bio-Rad. The tank was filled with SDS-Running buffer, a glycine-containing buffer that concentrated the proteins in the stacking gel. The prepared samples were thawed, and the same amount of sample was loaded (up to 30 µl) in the gel's pockets. As a protein ladder, the Pre-stained PAGE Ruler 170 kDa or Pre-stained PAGE Ruler Plus 250 kDa was used (Figure S1). All empty pockets were filled with 5 µl of loading dye. For the first 10 min, a voltage of 120 Volt was applied, which was kept at 120 Volt or changed to 160 Volt when the loading front reached the separating gel. The gel was stopped when the loading front started to run out of the gel.

Table 37 Separating gel for SDS-PAGE.

Separating gel, for 2 gels (15 ml)	**8%**	**10%**	**12%**
ddH_2O	7 ml	6 ml	5 ml
4x Separating gel buffer	3.75 ml	3.75 ml	3.75 ml
30% Acrylamide/0.8% bis-acrylamide	4 ml	5 ml	6 ml
10% APS	*150 µl*	*150 µl*	*150 µl*
TEMED	*15 µl*	*15 µl*	*15 µl*

Table 38 Stacking gel for SDS-PAGE.

Stacking gel, for 2 gels (7.5 ml)	**3.8%**
ddH_2O	3.25 ml
4x Stacking gel buffer	1.25 ml
30% Acrylamide/0.8% *bis*-acrylamide	0.66 ml
10% APS	*75 µl*
TEMED	*7.5 µl*

3.4.4 Western Blot

Western Blot was used for protein detection and protein quantification in cell lysates. Therefore, the separated proteins in an SDS-PAGE were transferred on a nitrocellulose or a membrane for subsequent antibody labeling and chemiluminescent protein detection. In this study, the Western Blot was performed following the Wet-Blotting method.

An SDS-PAGE was run and washed once with deionized water and placed on a pre-wetted nitrocellulose membrane in a Western Blot sandwich holder from Bio-Rad. The gel and the membrane were in between two layers of filter and sponges. To avoid air bubbles in between gel and membrane, which could lead to incomplete protein transfer, the filter papers and the sponges were flatten on the gel-membrane sandwich with a plastic roller. The whole sandwich was placed in a blotting tank (Mini Trans-Blot Cell) filled with transfer buffer containing 20% methanol (MeOH). The tank was connected to a voltmeter, and the blotting was performed in an ice bucket for 90 min at 110 Volt and 4°C. Ponceau staining of the membrane was used to control the complete protein transfer. Ponceau intercalates reversibly with the positively charged groups of amino acids. The membrane was incubated for 5 min Ponceau staining solution and carefully washed with ddH_2O to remove unbound residues. The washed membrane was imaged with the Bio-Rad ChemiDoc MP in brightfield or manually imaged with a mobile camera. A 1% acetic acid solution was used to de-stain the membrane. The membrane was blocked with 3% BSA and 0.05% Tween 20 in PBST or Intercept (PBS) Blocking Buffer for 30 min at RT. To stain multiple proteins on the membrane, the membrane was cut into smaller pieces. Primary antibodies were applied in 3% BSA and 0.05% Tween 20 in PBST or in 50% PBS-T with 50% Intercept (PBS) Blocking Buffer overnight at 4°C under constant agitation (listed in Table 16). β-actin, GAPDH, Vinculin, or HSP-70 were used as loading controls. Primary antibody solutions were used up

to five times and were stored at -20°C. The membranes were washed with PBST and incubated with secondary antibodies (listed in Table 18) diluted in PBST or in 50% PBS-T with 50% Intercept (PBS) Blocking Buffer for one hour at RT. In this study, secondary antibodies coupled to HRP (horseradish peroxidase) or IRDye 800CW (LI-COR) were used. For HRP detection, the membrane was incubated in Pierce ECL Western Blotting Substrate for 5 min and imaged with the Bio-Rad ChemiDoc MP at different exposure times. For IRDye 800CW the membrane was once more with PBS without Tween 20 and imaged with LI-COR Odyssey Fc imaging system. Colorimetric analysis of the protein bands was performed with Fiji ImageJ or with Image Studio Lite on raw Western Blot images. The loading control was used for the comparison of different samples. Overexposed bands were excluded from this analysis because of the loss of linearity. The brightness and contrast of Western Blot images were only changed for presentational reasons.

3.4.5 Antibody labeling with fluorophores

Directly labeled secondary antibodies were produced by incubating 100 µl donkey anti-rabbit (Jackson Immuno Research Ltd) or 100 µl donkey anti-mouse (Jackson Immuno Research Ltd.) with a 5-fold excess of Atto542-NHS (ATTO-TEC) for 90 min at RT under constant agitation. Directly labeled primary Cldn3 antibody (Thermo Fisher Scientific) was produced by incubating 100 µl of the antibody with a 10-fold excess of Atto590-NHS. The labeled antibodies were purified using Zeba Spin Desalting Columns (7K MWCO, 0.5 ml) according to the manufacturer's instructions for the desalting procedure. The desalting columns separate the unbound fluorophore from the labeled antibody via gel filtration. The purified labeled antibody is collected in a microcentrifuge tube. The degree of antibody labeling (DOL) was determined by absorption spectroscopy masking use of the Beer-Lambert law (Equation 7). The different correction factors were obtained from page.75 in "https://www.atto-tec.com/fileadmin/user_upload/Katalog_Flyer_Support/Catalogue_2009_2010.pdf".

Equation 7 Calculation of the degree of antibody labeling.

DOL = degree of labeling

A_{max} = absorbance at absorbance maximum (λmax) of the dye

ε_{max} = extinction coefficient of the dye at the absorption maximum

A_{prot} = absorption maximum of proteins

ε_{prot} = extinction coefficient of the protein at 280 nm

A_{280} = absorbance of proteins

CF_{280} = correction factor for A_{280} due to the contribution of the dye

$$DOL = \frac{A_{max}/\varepsilon_{max}}{A_{prot}/\varepsilon_{prot}} = \frac{A_{max}*\varepsilon_{prot}}{(A_{280}-A_{max}*CF_{280})*\varepsilon_{max}}$$

Depending on the antibody binding affinity, the labeled antibodies were used in a dilution of 1:20-1:100 in ICC and IHC.

3.4.6 Coupling of SNAP- and Halo-tag ligands to fluorophores

Fluorophore labeled SNAP-tag ligands (Atto590-BG/JF646-BG), and Halo-tag ligands (Atto590-CA/JF646-CA) were chemically synthesized as described in Bottanelli et al. (2016)[186]. Atto590-NHS was obtained from Sigma Aldrich and JF646-NHS was obtained from Tocris Bioscience. SNAP-tag ligand BG-NH2 was obtained from New England Biolabs, and the Halo-tag ligand HaloTag O2-Amine-CA was obtained from Promega (listed in Table 19).

For the fluorophore coupling, SNAP- and Halo-tag ligands were dissolved in water-free DMSO. The fluorophore containing NHS-ester was weighted, and the desired amount was transferred in an amber vial. For the NHS coupling reaction, 1 equivalent of the NHS-Ester was mixed with 1.5 equivalents of the SNAP- or Halo-ligands and 10 equivalents of *N, N*-Diisopropylethylamine (Pr_2Net). Molecular geometries of the different reactions are shown in Figure 11-14. The solution was incubated at RT for 3.5 hours under constant agitation. 3 µl of the reaction mix were diluted in 20 µl of a 0.1% trifluoroacetic acid (TFA) solution and measured with ultra-performance liquid chromatography (UPLC) to check the

reaction turnover indicated by the ratio of the detected mass of the product to the mass of the components. The reaction mix was injected together with 4.5-5 ml of 0.1% TFA in a reverse-phase high-performance liquid chromatography (HPLC). The HPLC was run with acetonitrile as a mobile phase with an increasing concentration starting from 30%. The specific excitation (590 nm for Atto590; 646 nm for JF646) of the fluorophores were used for the fractioning. The eluted fractions were checked for the compound specific mass with high-resolution ESI-MS. All compound containing vials were pooled and transferred in a 15 ml tube. For lyophilization, the vial was put in liquid nitrogen and lyophilized for 24 hours. The lyophilizate was dissolved in 500 µl 0.1% TFA, transferred into a beforehand weighted brown glass vial, freeze in liquid nitrogen, and again lyophilized for 24 hours. The compound was weighed and dissolved in sterile water-free dry DMSO to a final concentration of 1 mM and transferred as 20 µl aliquots into 0.5 ml microcentrifuge tubes. All aliquots were stored at -20°C. The final working concentration of the ligands is described in Table 19.

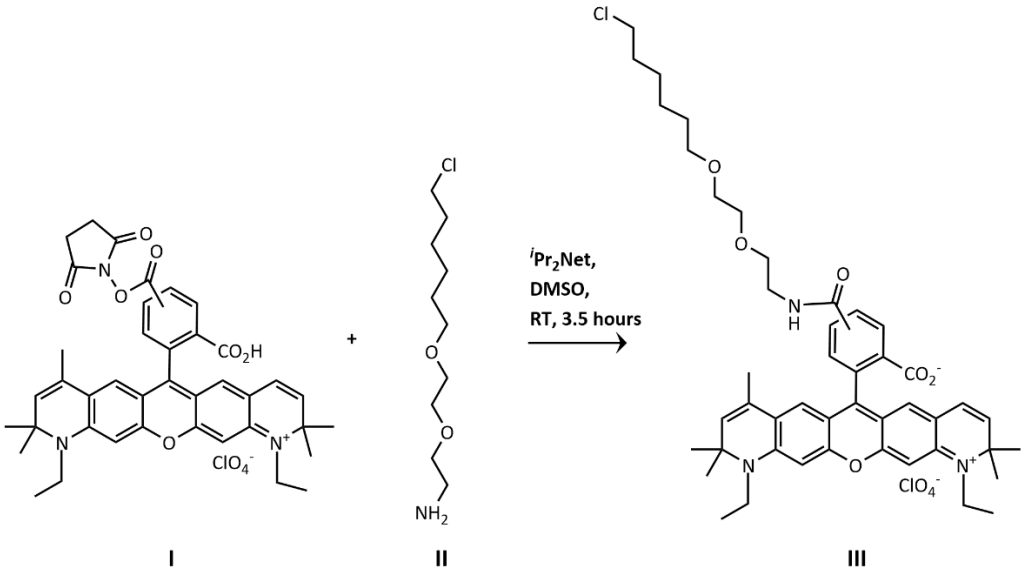

Figure 11 Synthesis of Atto590-CA. Atto590-NHS (I) (1.0 mg, 1.2 µmol, 1.0 eq) was dissolved in water-free dry DMSO, $^{i}Pr_2Net$ (2.1 µl, 12 µmol, 10 eq) and O^6-chloralkane (CA)-NH_2 (II) (0.42 mg, 1.88 µmol, 1.5 eq). The reaction mix was incubated for 3.5 hours at RT under constant agitation and exclusion of light. The reaction turnover was controlled with a UPLC. The final reaction mixture was completely subjected to an RP-HPLC for purification. The fractions were measured with a UPLC/HRMS (ESI) and pooled. The final compound (III) (Atto590-CA) was lyophilized and dissolved in water-free DMSO to a 1 mM stock solution. The stock solution was aliquoted and stored at -20°C.

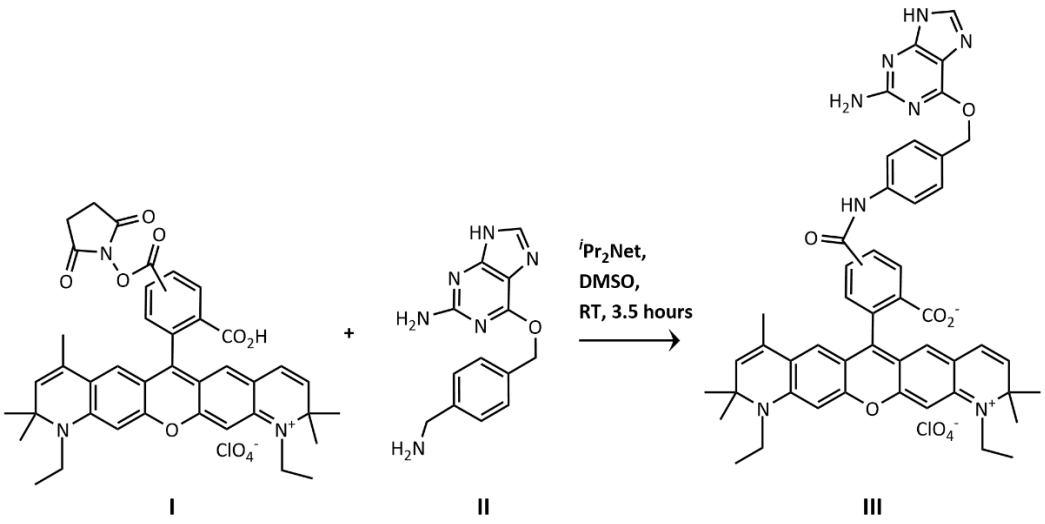

Figure 12 Synthesis of Atto590-BG. Atto590-NHS (I) (1.0 mg, 1.2 µmol, 1.0 eq) was dissolved in water-free dry DMSO, $^{i}Pr_2Net$ (2.1 µl, 12 µmol, 10 eq) and O^6-benzylguanine (BG)-NH2 (II) (0.49 mg, 1.8 µmol, 1.5 eq). The reaction mix was incubated for 3.5 hours at RT under constant agitation and exclusion of light. The reaction turnover was controlled with a UPLC. The final reaction mixture was completely subjected to an RP-HPLC for purification. The fractions were measured with a UPLC/HRMS (ESI) and pooled. The final compound (III) (Atto590-BG) was lyophilized and dissolved in water-free DMSO to a 1 mM stock solution. The stock solution was aliquoted and stored at -20°C.

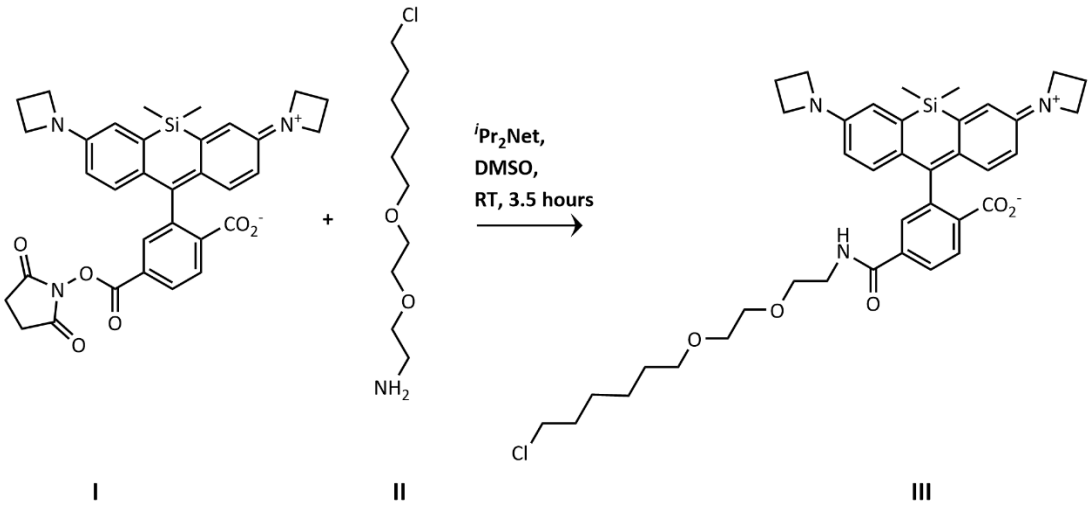

Figure 13 Synthesis of JF646-CA. JF646-NHS (I) (1.0 mg, 1.7 µmol, 1.0 eq) was dissolved in water-free dry DMSO, $^{i}Pr_2Net$ (2.97 µl, 17 µmol, 10 eq) and O^6-chloralkane (CA)-NH_2 (II) (0.7 mg, 2.55 µmol, 1.5 eq). The reaction mix was incubated for 3.5 h at RT under constant agitation and exclusion of light. The reaction turnover was controlled with a UPLC. The final reaction mixture was completely subjected to an RP-HPLC for purification. The fractions were measured with a UPLC/HRMS (ESI) and pooled. The final compound (III) (JF646-CA) was lyophilized and dissolved in water-free DMSO to a 1 mM stock solution. The stock solution was aliquoted and stored at -20°C.

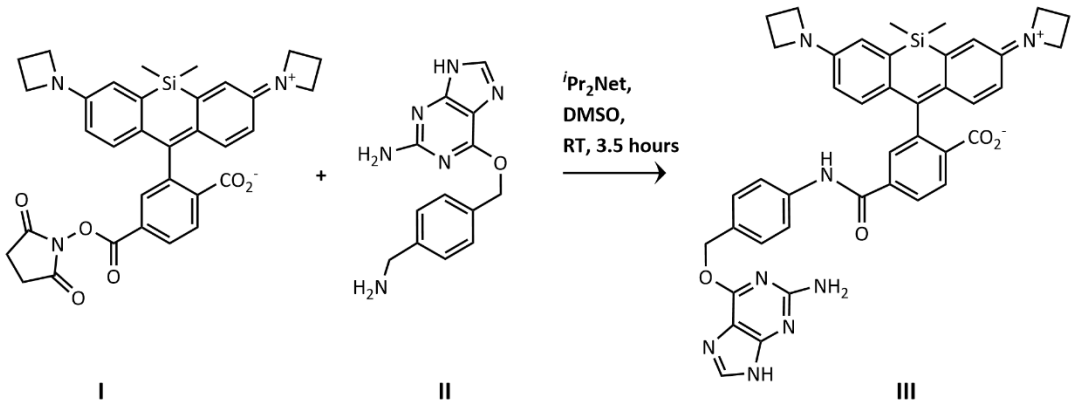

Figure 14 Synthesis of JF646-BG. JF646-NHS (I) (1.0 mg, 1.7 µmol, 1.0 eq) was dissolved in water-free dry DMSO, $^{i}Pr_2Net$ (2.97 µl, 17 µmol, 10 eq) and O^6-benzylguanine (BG)-NH2 (II) (0.57 mg, 2.55 µmol, 1.5 eq). The reaction mix was incubated for 3.5 h at RT under constant agitation and exclusion of light. The reaction turnover was controlled with a UPLC. The final reaction mixture was completely subjected to an RP-HPLC for purification. The fractions were measured with a UPLC/HRMS (ESI) and pooled. The final compound (III) (JF646-BG) was lyophilized and dissolved in water-free DMSO to a 1 mM stock solution. The stock solution was aliquoted and stored at -20°C.

3.5 Histological methods and immunohistochemistry

For immunohistochemistry (IHC) different mouse tissues were obtained from the group of Dr. Dorothee Günzel from the Clinical Physiology at CBF Berlin, the group of Prof. Dr. Thomas Jentsch (FMP/MDC, Berlin), and the group of Prof. Dr. Markus Bleich (CAU, Kiel). The mice species are further described in the following subsections and are listed in Table 22. All mice experiments were performed under the regulations of the LAGeSo and MELUND SH.

3.5.1 Preparation and staining of mouse intestinal tissue

BL6 mice were sacrificed by cervical dislocation. The whole intestine was taken out, washed with a Ringer solution, and separated in ileum, jejunum, and duodenum. The tissue was cut in a lateral direction into multiple 1-2 cm parts. The tissue preparation for cryosections was performed in two different ways. One way was to embed it directly in Tissue-Tek (Sakura Finetek) and immediately freeze it in liquid nitrogen. The second method includes a fixation with 2% PFA in PBS^{++} for one hour at RT. Followed by a 20 min incubation in a 0.1% glycine solution. The tissue was dehydrated over three days using solutions with an

increasing sucrose content (10%, 20%, 30%) at 4°C. The dehydrated tissue was frozen in 2-methyl-butane for 5 min. The tissue was embedded in Tissue Tek in a pre-cooled cryostat. The frozen and embedded tissue was stored in liquid nitrogen until cryo-sectioning. With a cryostat (Microm HM 560 Cryostat, Thermo Fisher Scientific), 10-20 µm thick longitudinal slices were cut and placed on object slides or directly on acid cleaned, and organ silane coated Ø25 mm CS. Tissue sections were stored at -80°C. The tissue sections were post-fixed with cold EtOH for 20 min at -20°C, washed with PBS^{++}, blocked with PBS^{++} containing 6% NGS, 1% BSA, and 0.05% Tween 20 for one hour at RT, and stained with primary antibodies diluted in BS overnight at 4°C. The sections were washed with PBS^{++} and incubated with secondary antibodies diluted in BS for one hour at RT. In the case of using primary antibodies derived from the same host, an over-blocking step was introduced. For over-blocking, the sections were washed thoroughly with PBS^{++} and incubated with a 10-fold excess of a donkey anti-rabbit (Jackson Immuno Research Ltd.) for two hours at RT. The samples were washed thoroughly with PBS^{++}. As over blocking control, one section was incubated with a goat anti-rabbit Alexa Fluor 488 (Thermo Fisher Scientific) for one hour at RT. The samples were washed with PBS^{++} and incubated with a second primary antibody overnight at 4°C. Followed by an incubation with a second secondary antibody for one hour at RT. For confocal imaging, DAPI was added for 15 min to stain the nuclei. The tissue was washed and mounted using ProLong Gold Antifade (Thermo Fisher Scientific) on Ø25 mm CS or directly on object slides when the tissue was attached on CS and incubated for 48 hours at RT. For every over-blocking approach, the control staining with Alexa Fluor 488 was imaged.

3.5.2 Preparation and staining of perfused murine intestinal tissue

BL6 mice were narcotized with Pentobarbital (100-150 mg/kg). The lid and feet reflex tests were performed to validate that the if mice are completely numb. The mice were carefully open, and a needle was placed in the aorta of the heart, and the organs were perfused for two min with PBS and another four min with 1% PFA. The intestinal tissue was removed, sectioned in ileum, jejunum, and duodenum, and washed twice with a Ringer solution. The tissue was incubated in 30% sucrose for two days at 4°C under constant agitation and embedded in TissueTek and stored in liquid nitrogen. The cryo-sectioning and the following IHC staining were performed according to the description in 3.5.1.

3.5.3 Preparation and staining of isolated mouse kidney tubules

C57 Bl/6 J mice were sacrificed by decapitation and kidneys were removed immediately. After de-capsulation, the middle section of each kidney was sliced in a transversal direction in fine (0.2-0.4 mm) sections. The sections were transferred into a pre-warmed incubation solution. Enzymatic digestion was performed at 37°C and 850 rpm in a thermo-shaker for 15 min. Free-floating tubular segments were transferred into ice-cold sorting solution (incubation solution supplemented with albumin 0.5 mg/ml) for washing. Tubular segments were allowed to settle down, and the supernatant was replaced by a fresh, ice-cold sorting solution at least two times to remove erythrocytes and cellular debris. Washed tubular segments were transferred to a dissection microscope, and proximal tubules were identified and sorted. After transfer to poly-L-lysine (PLL) coated object slides and short settlement, tubules were fixed with 4% PFA for 7 min. PFA was subsequently vigorously removed from the slide under visual control and washing with PBS containing 0.3% Triton X-100. The following IHC staining was performed according to the description in 3.5.1.

3.6 Fluorescent microscopy and quantitative image analysis

3.6.1 Fluorescent microscopy

Fluorescence microscopy allows the detection of biomolecules, including proteins, DNA, RNA, and membrane lipids. These biomolecules can be labeled with fluorescent proteins (gene expression) or organic fluorophores (gene expression (SNAP- and Halo-tag system) or via antibody labeling). Excitation of these fluorophores allows the localization of multiple structures within living and fixed cells, tissue, and the whole organism. The fundamental physical principle is explained with a Jablonski diagram in Figure 15.

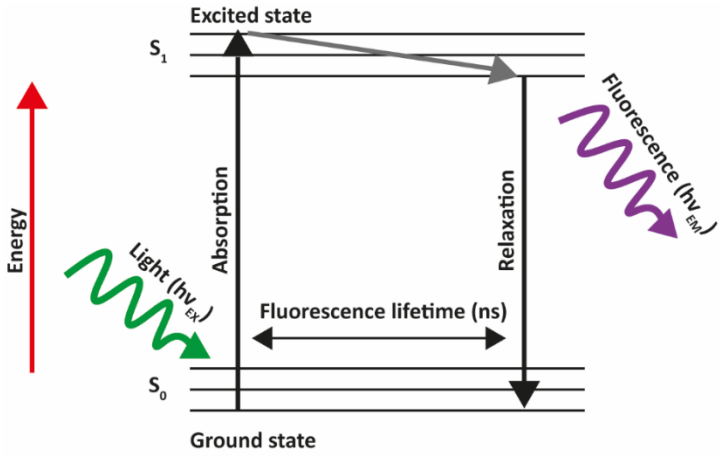

Figure 15 Jablonski diagram of the excitation and emission of a fluorophore. Excitation of a fluorophore with the light of a specific wavelength (hv_{EX}) leads to a transition of its electrons from a ground state (S_0) to a higher energy excited state (S_1). From there, the electrons relax within nanoseconds (ns) back into the electronic ground state by emitting light in form of photons with a longer wavelength (hv_{EM}) and, respectively, lower energy. The time difference between absorption and relaxation is termed as fluorescence lifetime and can be used for separating different fluorophores in one sample. The difference in the excitation and the emission wavelength is termed the Stokes shift.

In a microscope, different physical and mechanical apertures, including dichroic mirrors and spectral emission filters, allow the detection of multiple emission wavelengths by highly photo sensible detectors. Selected excitation wavelengths and emission filters allow the simultaneously detection of different fluorophores. Dependent on the biological question (fixed sample, living sample, nanostructure), different fluorescent microscopy methods and techniques are available. As a general guideline, for comparison of different conditions within independent experiments, the same settings for microscopy and quantitative analysis were used. If not other stated, raw data were analyzed with Fiji/ImageJ and further processed with Excel. All plots and statistical analysis were generated with GraphPad Prism8.

3.6.2 Laser scanning confocal microscopy

In standard wide-field microscopy, the whole sample gets illuminated by the light of a specific wavelength, and the fluorescence gets detected by a camera after passage through different filters. Due to this basic and simple illumination principle, fast image acquisition is possible, which can be of great advantage, for example, in total internal reflection

fluorescence (TIRF) microscopy but, it goes in general hand in hand with a loss of resolution because of very high background from out of focus fluorescence. Laser scanning confocal light microscopy (LSCM) compared to wide-field microscopy offers the possibility of focusing the illumination not on the whole sample but exciting and detecting the emission of molecules in only one z-plane by installing an additional pinhole in the microscopy light path. Out-of-focus light gets rejected, which leads in total to better detection of labeled biomolecules in 2D and 3D and a higher optical lateral and axial resolution. As a disadvantage, the acquisition speed in an LSCM is drastically reduced because of the point-by-point raster scanning of the laser beam across the sample to form a complete image of the focal plane. Confocal images of fixed cells and tissue were acquired with an LSM780 from Carl Zeiss Microscopy ZEISS and with the Leica SP8 TCS STED microscope from Leica Microsystems. For the detection, a photomultiplier (PMT) was used. The basic principle compared to wide-field microscopy is shown in Figure 16. Settings for different fluorophores are listed in Table 39.

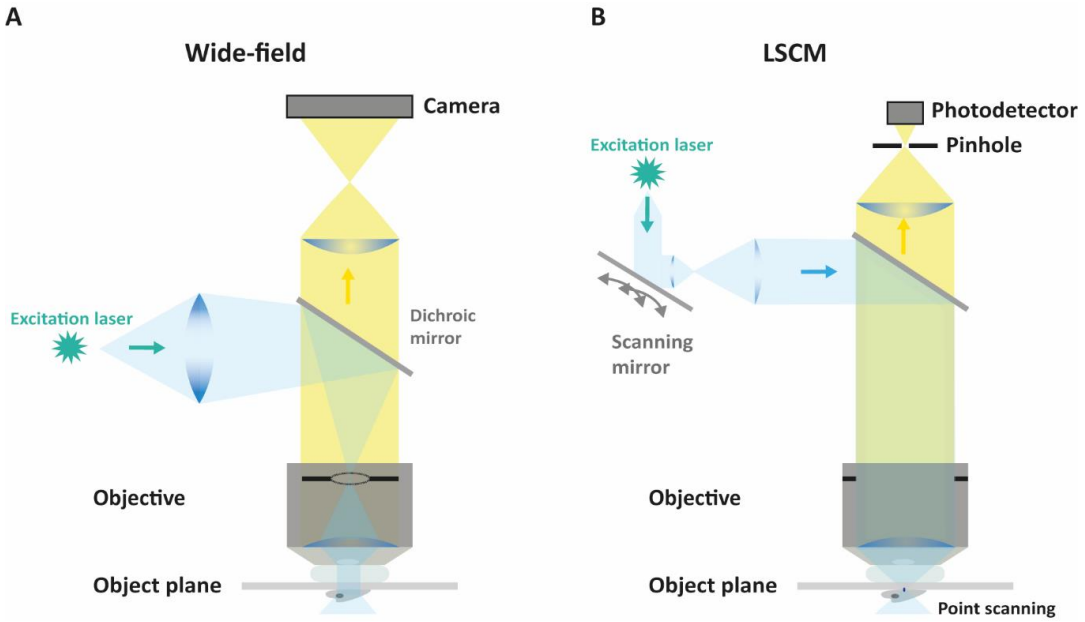

Figure 16 Comparison of wide-field and laser scanning confocal microscopy. (A) In wide-field microscopy, the whole specimen gets illuminated with white light allowing a fast-imaging speed at low resolution. **(B)** Laser scanning microscopy (LSCM) offers the possibility of focusing the illumination not on the whole sample but exciting and detecting the emission of molecules in only one z-plane by installing an additional pinhole in the microscopy light path. The out-of-focus light gets rejected, which leads in total to better subcellular detection of labeled biomolecules in 2D and 3D and a higher optical lateral and axial resolution.

Table 39 Fluorophore settings used for confocal microscopy at LSM780.

Fluorophore	Excitation (in nm)	Detection (in nm)
DAPI	405	415-480
Alexa Fluor 594	561	566-630
Atto647N	633	636-740

3.6.3 Stimulated emission depletion (STED) microscopy

The optical resolution in fluorescence light microscopy is determined by the general diffraction limit of light, which was first described by Abbe in 1873 and defined that the maximum resolution which can be achieved with a light microscope is ~200 nm in lateral and ~500 nm in an axial direction (Equation 8)[187].

Equation 8 Abbe's diffraction limit (1873).

d_{xy} = diameter (nm), lateral

d_z = diameter (nm), axial

λ = wavelength (nm)

NA = numerical aperture of the objective

$$d_{xy}=\frac{\lambda}{2*NA} \rightarrow d_z=\frac{2*\lambda}{NA^2}$$

Super-resolution microscopy (SRM) techniques can overcome this limitation and offers resolution beyond the diffraction limit. Next to SIM (structured illumination microscopy) and SMLM (single molecule localization microscopy), STED (stimulated emission depletion) microscopy gained in the last years more and more attention because of its tunable resolution of down to 40 nm, a better tunable acquisition time, and an artifact-free imaging technique. STED microscopy is based on standard LSCM. It overcomes the diffraction-limited detection of structures by taking advantage of a biophysical process termed stimulated emission. In addition to the excitation laser, a second doughnut-shaped and red-shifted depletion laser is superimposed in a STED microscope. After excitation of the sample with the excitation beam, the STED laser stimulates with a short delay the excited electrons to return from the excited to the ground energy state before it spontaneously

emits a photon and thus “depletes” its fluorescence signal before it reaches the detector. Due to the STED laser's unique shape, which is generated by an implemented phase plate, the emission of excited fluorophores gets suppressed within distance to the center of excitation, and the emission is effectively reduced to a smaller point-spread function (Figure 17).

The resolution limit in STED microscopy can be technically narrowed down by applying more depletion laser power without any physical limitation but it is often limited by the labeling density, photostability, and brightness of the used fluorophores. To further improve the resolution, in gated STED (gSTED) applications, the shortening of fluorescent lifetimes by the depletion laser is used. Only in the center of the STED donut fluorophores exhibit a longer lifetime longer that can be extracted by selecting a fluorescence lifetime gate of 0.5-6 ns after the excitation pulse. STED microscopy can be approximated by a modified Abbe equation (Equation 9) by Stefan Hell (1994), showing that the resolution in STED is directly dependent on the STED laser intensity (I)[188].

Equation 9 Modified Abbe's diffraction limit equation for STED microscopy by Stefan Hell (1994).

d = diameter (nm)

λ = wavelength (nm)

NA = numerical aperture of the objective

I = STED intensity

I_s = threshold intensity

$$d = \frac{\lambda}{2*NA*\sqrt{1+\frac{I}{I_S}}}$$

All multicolor STED images of fixed and living samples were performed with a Leica SP8 TCS STED microscope (Leica Microsystems). The system was equipped with a pulsed white-light excitation laser (WLL; ∼ 80 ps pulse width, 80 MHz repetition rate; NKT Photonics) and two STED lasers for depletion at 592 nm (CW laser) and 775 nm (pulsed laser). The WLL triggered the pulsed 775 nm STED laser. The settings for excitation, emission,

and depletion of used fluorophores are listed in Table 40. For multicolor STED, the fluorophores were depleting in the order starting with the fluorophore with the longest wavelength. The fluorescent signal was detected by two HyDs at corresponding spectra, excluding the STED laser wavelengths keeping a minimum distance of 25 nm to the STED laser excitation wavelength. The time-gate was set to 0.3-6 ns for all dyes. The sample was imaged with an HC PL APO CS2 100x/1.4 N.A. oil objective (Leica Microsystems) and scanned in a 1,024*1,024 px format with eight-bit sampling. The final image was taken with a six-fold zoom resulting in a pixel dimension of 18.9*18.9 nm. The system's maximal resolution was routinely checked with 40 nm beads (Life Technologies) by the FMP imaging facility, and the effective resolution limit of the system of 45 nm was determined with Atto647N coated beads. A heat-able incubator (LIS Life Imaging Services) enclosed the system to reduce thermal drift during imaging in fixed and live. For all quantitatively analyzed experiments, the same settings were used. Only the laser power of excitation and STED laser were adjusted for different experimental set-ups.

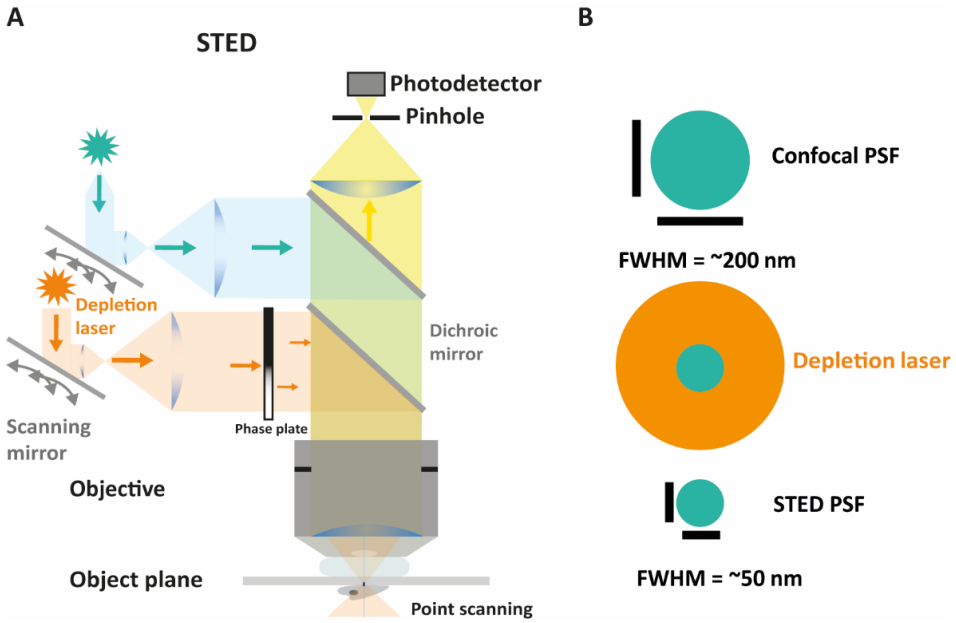

Figure 17 Schematic illustration of stimulated emission depletion (STED) microscopy. (A) STED microscopy is a super-resolution microscopy technique based on confocal microscopy. In addition to the excitation laser, a second laser, termed as STED laser, is installed in the system. **(B)** The STED laser is doughnut-shaped, and it can interfere with the excited electrons in a physical process called stimulated emission depletion, that leads to the reduction of the PSF and a higher lateral and axial resolution as indicated by the lower full-width half-maximum (FWHM).

Table 40 Fluorophore settings used for Leica STED microscopy.

Fluorophore	Excitation (in nm)	Detection (in nm)	Depletion (Depletion laser)	Gate (in ns)
Phalloidin Alexa Fluor 488	488	498-550	6-80% (592 nm)	0.3-6
EYFP	514	524-590	40-60% (592 nm)	0.3-6
Atto542	540	550-590	100% (775 nm)	0.3-6
Alexa Fluor 594	590	600-640	80-100% (775 nm)	0.3-6
Alexa Fluor 594 F(ab')2	590	600-640	80-100% (775 nm)	0.3-6
Alexa Fluor 594 Plus	590	600-640	80-100% (775 nm)	0.3-6
Atto590	590	600-640	50-70% (775 nm)	0.3-6
Atto594	590	600-640	80-100% (775 nm)	0.3-6
Phalloidin Alexa Fluor 594	590	600-640	80-100% (775 nm)	0.3-6
Atto647N	640	650-750	30-45% (775 nm)	0.3-6
JF646	640	650-750	20-40% (775 nm)	0.3-6
Silicon rhodamine (siR)	640	650-750	30-40% (775 nm)	0.3-6

3.6.4 Single- and dual-color live STED imaging

Live STED imaging of COS-7 cells was performed with Ø25 mm glass CS and an ATTOfluor cell chamber (Thermo Fisher Scientific, #A7816) or with µ-Slide 8-well glass-bottom dishes (Ibidi). The cells were transfected with SNAP- or Halo-tagged claudin constructs. A HEPES buffered live imaging solution (Thermo Fisher Scientific) was used. 24 hours before imaging, the heat-able incubation chamber was set to 37°C providing imaging with a stable focus. For single-color live STED imaging, JF646-BG was used. The imaging settings were the same as described above in 3.6.3 except for the reduced scanning format of 512*512, six-fold line averaging, and a 12-fold optical zoom yielding in a pixel dimension of 18.9*18.9 nm. The acquisition time per frame for serial imaging was set to 10 s/frame.

Dual-color Live STED imaging was performed with the JF646-BG as SNAP-tag ligand and Atto590-CA as Halo-tag ligand. The imaging settings were the same as described above 3.6.3 except for the reduced scanning format of 512*512, six-fold line averaging, and a 12-fold optical zoom yielding in a pixel dimension of 18.9*18.9 nm. Imaging was performed with an acquisition speed of 10 s/frame. For faster imaging but at a lower resolution, a resonance scanner at 16,000 MHz was used. Single live images were taken with a scanning format

512*512, 32-fold line averaging, and a 12-fold optical zoom yielding in a pixel dimension of 19*19 nm. Imaging was performed with an acquisition speed of 2.5-19.5 s/frame.

For further imaging processing, Noise2Void[189], a deep learning-based image restoration method, was used to remove noise from images for visualization as specified in the figure legends. We trained the noise model in Fiji ImageJ on a GPU with 150 epochs and 200 steps per epoch on a large set of training data with a batch size of 100 and a dimension of 180*60 px. The neighborhood radius was set to five. After training, the best model was chosen for predicting the image with filtered noise.

3.6.5 Förster resonance energy transfer (FRET)

Förster resonance energy transfer (FRET) describes a physical process of radiation less energy transfer from a donor (excited fluorophore) to an acceptor (second fluorophore) through long-range, dipole-dipole interactions without emission of a photon. It was first described in 1948 by T. Förster[190]. As a basic requirement for FRET to occur, both fluorophores must be in closer proximity of <10 nm, and the emission spectrum of the donor and the excitation spectrum of the acceptor must overlap. Organic fluorophores or fluorescent proteins can be used. If FRET occurs, the donor channel signal will be quenched, and the acceptor channel signal will be increased.

FRET is especially of interest when the resolution of a diffraction-limited fluorescence microscope and super-resolution techniques are insufficient to determine whether an interaction between two biomolecules takes place or not. In general, it is important to take in consideration that the orientation of the fluorophore and the fluorescent protein location within the protein can influence the FRET efficiency. In this study, the well-studied and widely used FRET pair of Turquoise2 and EYFP was used.

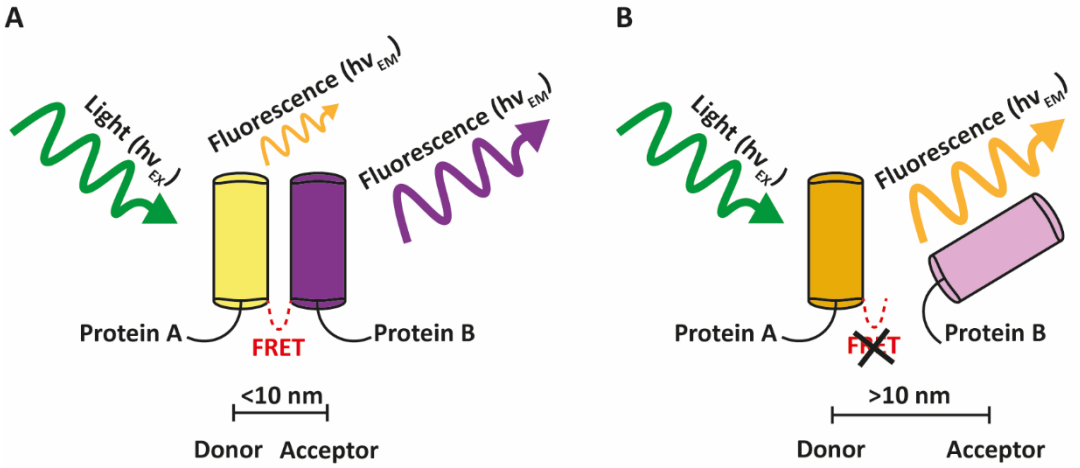

Figure 18 Illustration of the principle of the Förster resonance energy transfer (FRET). FRET describes the radiation less energy transfer from a donor (excited fluorophore) shown in yellow to an acceptor (second fluorophore) shown in magenta without emission of a photon. For FRET, both fluorophores must be in closer proximity of <10 nm. If FRET occurs total donor channel signal will be quenched, and the acceptor channel signal will be increased (**A**). If fluorophores are in a greater distance than 10 nm, no FRET will occur (**B**).

For FRET experiments, HEK293 cells were transfected with pTrq2- and pEYFP-Cldns constructs. A plasmid DNA ratio of 1:1 was used for all Trq2-Cldn3 approaches. For Trq2-Cldn2, the ratio was changed in all approaches to 1:5. The transfected cells were visualized on an LSM510-META NLO inverted microscope (Carl Zeiss Microscopy GmbH) using a 40x/1.3 oil objective. Trq2 fluorescence signals were recorded (IR laser, λexc = 810 nm, two-photon technique, META detector, spectral range 436-650 nm) and split using MBS KP 700. Channel pictures were taken before the recording of spectra to estimate the expression of the Trq2- and EYFP-tagged constructs (Trq2: IR laser λexc 810 nm, two-photon technique, λexc = 430-505 nm, META detector; EYFP: argon laser, λexc = 514 nm, λexc = 560 nm long-pass filter). The fluorescence spectra of Trq2-tagged constructs in the presence and absence of the EYFP-tagged constructs receptor were measured. To calculate the FRET-based fluorescence, a γ-stack with a linear spectral unmixing mode was used to correct any EYFP fluorescence crosstalk into the FRET channel (523-532 nm). The γ-stack is an integral part of the confocal laser system software. EYFP correction was carried out to correct for direct excitation of the acceptor during donor excitation. The effect was expressed by changes in the FRET ratio, which is calculated by dividing the acceptor emission (EYFP, 532 nm) by the donor emission (Trq2, 468 nm). FRET data analysis was performed using the software ZEN2010 (Carl Zeiss Microscopy), Excel, and GraphPad Prism 8, respectively.

3.6.6 Automated meshwork analysis

The automated meshwork analysis was used for a TJ meshwork screen in which COS-7 cells were transfected with all known mammalian claudins and important claudin isoforms (described in 3.2.3). Claudins were N-terminally tagged with EYFP and boosted with an anti-GFP Atto647N nanobody from Chromotek in an additional immunocytochemistry step (described in 3.2.8). Imaging was performed with the Leica SP8 TCS STED microscope (described in 3.6.3). The screen was performed in two independent experiments. For each claudin, at least five images were taken. In the first step of the automated analysis, the texture and meshwork analysis were performed within a single 200*200 px (1 px = 20 nm) region of interest (ROI) per image. Therefore, images were filtered using a 3 px Gaussian filter kernel, and a sigma of 1[191]. Grey level co-occurrence matrices were computed at distances 1, 3, 5, and 10 px and Haralick texture features[192] were extracted from 4 angles and averaged using the python[193] mahotas library[194]. Three texture features (sum average, sum variance, and sum of squares: variance) were selected based on literature[195]. For segmenting, the meshwork images were filtered using Multiscale Oriented-Flux Tubularity filter[196] implemented in the Fiji plugin[197] simple neurite tracer[198]. A threshold was then applied to the filtered image, and the largest connected region[199] comprising the meshwork was kept. Within the ROI, the percent of the segmented area was measured. A skeleton analysis[200] was performed to measure within the ROI the number of branches, average and maximum branch length, number of total junctions as well as triple and quadruple junctions. The binary mask was inverted to measure the mesh size within the ROI, excluding objects touching the edge. The number of meshes, average mesh size, and variance of the mesh size were measured.

For analyzing all claudins, the extracted texture features from each ROI were averaged. Clustering was performed with pheatmap implemented in R (R Core Team 2013), and unit variance scaling was applied. Clustering was computed using euclidean distance, and average linkage, and both the meshwork analysis and texture analysis features were used. ROIs with a segmented area of less than 10% or more than 90% were excluded as well as meshworks with less than 10 branches. The features were then averaged for each ROI. ClustVis server[201] was used for visualizing the clustering with ln(x)-transformation applied to the values, the rows were centered, and unit variance scaling was applied. Clustering was computed using correlation distance and average linkage.

3.6.7 Pearson analysis

Cells were seeded on with Matrigel coated CS and transfected with equal amounts of two or three plasmids coding EYFP-, SNAP- or Halo-tagged claudins (described in 3.2.3). Co-overexpression of the same claudin labeled with a SNAP- and an EYFP-tag served as positive control and as reference value (Cldn2, 3, 19a, $10^{\Delta PDZ}$, $15^{\Delta PDZ}$, $10^{\Delta CT}$, $15^{\Delta CT}$). Cells were labeled with Atto590-BG, Atto590-CA and anti-GFP Atto647N nanobody. For the Pearson analysis of $Cldn2_{ECL10a}$ chimera, the combination of JF646-BG and mouse anti-GFP with anti-mouse Alexa Fluor 594 Plus was used. For every condition at least five independent TJ-like meshworks per experiment over three to four independent experiments were imaged with the same settings (1,024*1,024, 16-fold line averaging, pixel dimension of 18.9*18.9 nm). For every imaged TJ-like meshwork a region of interest (ROI) with a representative signal of the transfected claudins was defined and in this ROI the Pearson above the threshold was measured with a Coloc2 based script in Fiji ImageJ (PSF was set to 2 px = 38.8 nm). The data was further analyzed and plotted with GraphPad Prism8.

Coloc2 script for Pearson analysis:

```
dir1 = getDirectory("Choose Source Directory ");
print(dir1);
list = getFileList(dir1);
print(list.length);
for(i=0;i < list.length;i++)
{
        open(list[i]);
        rename(i+"image.tif");
        selectWindow(i+"image.tif");
        run("Split Channels");
        run("Coloc 2");
        selectWindow("C1-"+i+"image.tif");
        close();
        selectWindow("C2-"+i+"image.tif");
        close();
}
```

For the Pearson analysis of IHC labeled kidney tubules (described in 3.5.3), at least nine STED images of three different isolated proximal tubules were imaged with the same settings (1024*1024, 16-fold line averaging, pixel dimension of 18.9*18.9 nm) (described in 3.6.3). Out of every meshwork, an ROI with a representative signal of the stained claudins was defined, and in this ROI the Pearson above the threshold was measured with a Coloc2 based script in Fiji ImageJ with the PSF set to 2 px = 38.8 nm.

3.6.8 Full-width half-maximum measurements

Full-width half-maximum (FWHM) measurements were performed with pSNAP-Cldn3 transfected COS-7 cells labeled with JF646 (described in 3.2.3 and 3.2.5). The same imaging settings, except for temperature and imaging solution differences (PBS at RT; Live imaging solution at 37°C), were used for fixed and live cell imaging. Line profiles (straight line 0.3 µm length, 10 px = 189 nm width) of 160 strands over 8 meshworks were analyzed using Fiji ImageJ. The FWHM was determined by the multiplication of sigma with the factor 2.35.

Line profile measurement script:

```
n = roiManager("count");
for (i=0; i<n; i++)
{
        roiManager("select", i);
        run("Plot Profile");
        Plot.getValues(xpoints, ypoints);
         Fit.doFit("Gaussian", xpoints, ypoints);
 //print("sigma="+Fit.p(3));
        print(Fit.p(3));
//change 3 to 1 for intensity
//selectWindow("Plot of Composite");
        close();
}
```

3.6.9 Strand length measurements

COS-7 cells were transfected with pSNAP-Cldn2 and pEYFP-Cldn10a in three different ratios (1:1, 3:1, 1:3) with a total plasmid concentration of 3.2 µg/ml (described in 3.2.3). Additionally, a pHalo-C1 was used to normalize the plasmid concentration over the different ratios. For the detection and determination of the protein amount via Western Blot, primary antibodies against SNAP-tag and EGFP-tag were used. As loading control, a primary antibody against HSP70 was used (described in 3.4.4). For the strand length analysis via IHC, the cells were labeled with Atto590-BG (described in 3.2.5) and immunofluorescent stained with anti-GFP Atto647N (described in 3.2.8) and imaged in two-color STED with the same settings (1,024*1,024, 16-fold line averaging, pixel dimension of 18.9*18.9 nm) (described in 3.6.3). For the measurement of each condition, 40 individual strands of 3-4 different TJ meshworks were analyzed using the segmented line function of Fiji ImageJ.

For the strand length measurements of IHC labeled kidney tubules (described in 3.5.3), at least four STED images of three different isolated and immune-stained proximal tubules stained were imaged with the same settings (1,024*1,024, 16-fold line averaging, pixel dimension of 18.9*18.9 nm) (described in 3.6.3). For the measurement, at least 132 individual strands per claudin in each image were analyzed using the segmented line function of Fiji ImageJ.

3.7 Electrophysiological methods

5-7 days before the measurements, MDCKII, MDCKII QKO, and MDCKII QKO sT claudins cells were seeded in DMEM with antibiotics on 0.6 cm^2 big Millipore PCF filter insets (pore size of 0.4 µm) in a 12-well plate (described in 3.2.1). In every experiment, the dilution potential for sodium and chloride and the fluorescein flux of two or three filters per cell type were measured. As blank control an empty filter was measured. For every approach, cells were also seeded in 6-well plates for a following Western Blot (described in 3.4.4) to determine the total claudin expression and on Corning PCF filter insets (0.6 cm^2; 0.4 µm pore size) in an additional 12-well plate for a ICC staining (3.2.8) to determine the homogeneity of the cell monolayer and to measure the claudin amount in the TJ.

3.7.1 Dilution Potential measurements of monovalent ions

For the functional analysis of TJ proteins in epithelial cells, dilution potential measurements were performed at the Institute for Clinical Physiology at the Charité Campus Benjamin Franklin in Berlin. The measurements were carried out with Ussing-Chambers.

An Ussing-Chamber allows the continuous measurement of electrophysiological parameters, including the transepithelial resistance (R) and the voltage (V) of epithelial cell layers. By creating a setup in which two of the passive transport influencing factors (hydrostatic pressure and concentration gradient) get balanced and eliminated, the Ussing-Chamber offers the possibility to measure the ion permeability only depending on the flow along an electrical gradient. The special setup and construction are shown in Figure 19. It consists out of the Ussing-Chamber and two connected identical polyacrylamide compartments only separated by the epithelial cell layer. Both chambers were warmed by surrounding water to 37°C. Each compartment was filled with 5 ml of a Ringer solution which constantly circulated in the chamber due to an applied gas mix of 95% O_2 and 5% CO_2 (speed: 5 ml/min), providing a physiological pH and physiological environment. Each of the chambers also contains one voltage and one current electrode.

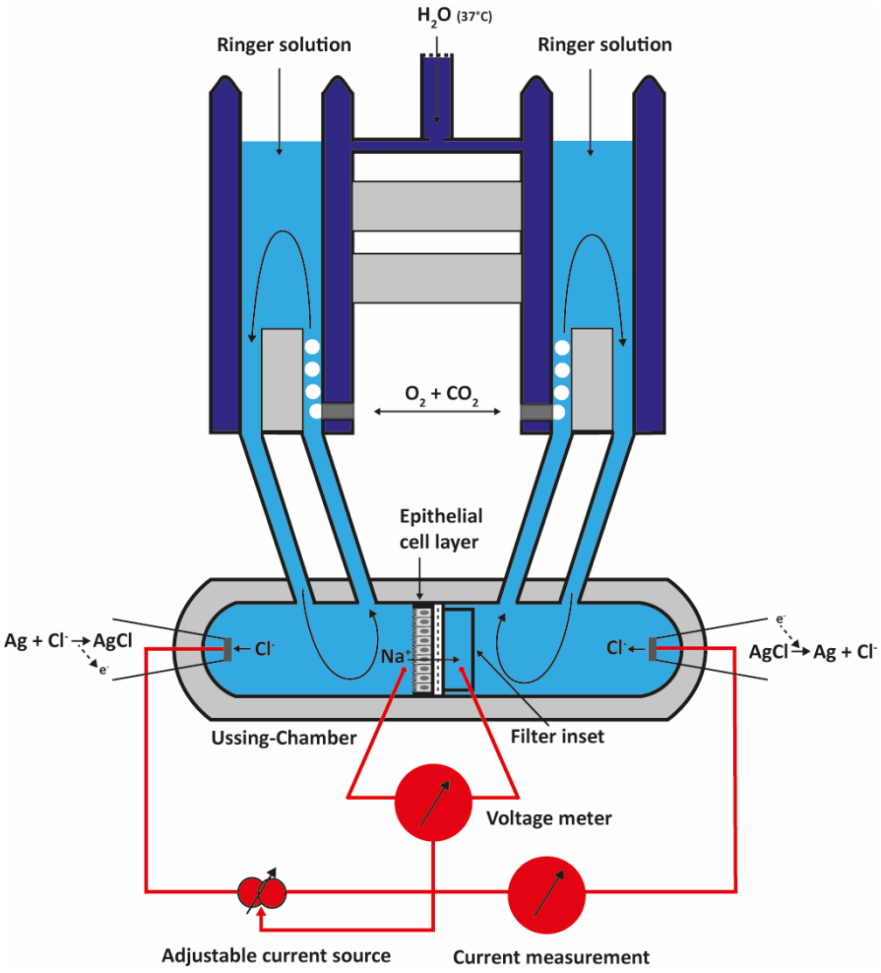

Figure 19 Schematic illustration of an Ussing-Chamber. The classic Ussing-Chamber setup consists out of the actual chamber (Volume: 0.5 ml), which is connected to two reservoirs (Volume: 15 ml each) for applied solutions. The chamber and the reservoirs are both made of polyacrylamide. Two identical compartments can be created by applying a filter in the center of the Ussing-Chamber. Applied solutions are warmed by surrounding water to 37°C and constantly circulated by a gas mix of 95% O_2 and 5% CO_2 (speed: 5 ml/min), providing a physiological pH and physiological environment. Each of the compartments contains one voltage and one current electrode within the part of the Ussing-Chamber, which were used for the induction of current pulses and the recording of the conductance and resistance.

The induction of a recurring current pulse creates the transepithelial potential difference on the epithelial cell layer, which facilitates the calculation of the resistance of the epithelial cell layer and the conductance-based on Ohm's law (Equation 10, Equation 11). A self-developed software (Ing. grad. D. Sorgenfrei, CBF, Berlin) was used for controlling the setup and data acquisition.

Equation 10 Ohm's law.

R = resistance

V = transepithelial potential difference

I = current pulse

$$R=\frac{V}{I}$$

Equation 11 Conductance as reciprocal resistance.

G = conductance

R = resistance

$$G=\frac{1}{R}$$

For measurements, the Ussing-Chamber was pre-warmed to 37°C, washed with ddH_2O, and filled with a Ringer solution. The potential difference and resistance of the empty Ussing-Chamber were measured and subtracted as a blank value from the experimentally acquired values. The chamber was emptied, and a filter with confluently grown epithelial cells was placed in between the two compartments of the Ussing-Chamber. In both compartments, 5 ml of a Ringer solution was carefully applied. After a short equilibration period, the measurement was started, and every 10 s, the transepithelial potential was registered by a voltmeter, and every 0.3 s, 10 µA was applied to measure the resistance. After 10 min, 5 ml of a mannitol solution was applied to the apical side contemporaneously with 5 ml of Ringer solution to the basolateral side, creating an ion concentration difference (solutions are listed in Table 7). This leads to the movement of ions along this gradient to the other compartment side. The transmembrane potential changes, and the dilution potential, the difference in the potential, established over time. After 10 min, the ion concentration difference between the compartments was adjusted by supplementing 5 ml on the basolateral side with 5 ml of mannitol solution. The dilution potential can be determined with the Goldman-Hodkin-Katz-Equation (Equation 12). By solving the equation, the relative ion permeability of Na^+ or Cl^- can be calculated. Because of the solutions' different compositions, a liquid junction potential must be considered ($E_{bl\text{-}ap}$).

Equation 12 Goldman-Hodgkin-Katz-Equation.

$E_{bl\text{-}ap}$ = dilution potential with correction for liquid junction potential

R = gas constant

T = temperature

F = Faraday constant

P_{Na}, P_{Cl} = ion permeability (sodium or chloride)

$[Na]^{ap}$, $[Cl]^{ap}$ = apical concentration of sodium or chloride

$[Na]^{bl}$, $[Cl]^{bl}$ = basolateral concentration of sodium or chloride

$$E_{bl\text{-}ap} = \frac{RT}{F} * \ln \frac{P_{Na}[Na]^{ap} + P_{Cl}[Cl]^{bl}}{P_{Na}[Na]^{bl} + P_{Cl}[Cl]^{ap}}$$

To convert the natural logarithm into the common logarithm, the conversion factor of 2.303 was sum up with R, T, and F to the factor s (Equation 13).

Equation 13 Modified Goldman-Hodgkin-Katz-Equation.

$$s = 2.303 \frac{RT}{F}$$

$$E_{bl\text{-}ap} = s * \log \frac{P_{Na}[Na]^{ap} + P_{Cl}[Cl]^{bl}}{P_{Na}[Na]^{bl} + P_{Cl}[Cl]^{ap}}$$

By solving the equation, the relative ion permeability of sodium or chloride could be calculated (Equation 14).

Equation 14 Solved Goldman-Hodgkin-Katz-Equation for relative ion permeability of sodium and chloride.

$$\frac{P_{Na}}{P_{Cl}} = \frac{[Cl]^{bl} - 10^{\frac{E_{bl\text{-}ap}}{s}}[Cl]^{ap}}{10^{\frac{E_{bl\text{-}ap}}{s}}[Na]^{bl} + [Na]^{ap}}$$

The absolute permeability for sodium (P_{Na}) or chloride (P_{Cl}) was calculated from the TER and the relative permeability ratio P_{Na}/P_{Cl} by using the Kimizuka-Koketsu equation[202]:

Equation 15 Kimizuka-Koketsu equation for determining the absolute chloride and sodium permeabiliy.

$$P_{Cl} = \frac{RT}{F^2} * \frac{G}{[NaCl]*(1+\frac{P_{Na}}{P_{Cl}})}$$

$$P_{Na} = P_{Cl} * \frac{P_{Na}}{P_{Cl}} = \frac{RT}{F^2} * \frac{G}{[NaCl]*(1+\frac{P_{Na}}{P_{Cl}})} * \frac{P_{Na}}{P_{Cl}}$$

3.7.2 Fluorescein flux measurements

Membrane integrity measurements were performed with the same filters directly after the dilution potential measurements (described in 3.7.1). The membrane integrity was analyzed by measuring the flux of fluorescein, a small fluorescent molecule (332.31 Da), over the epithelial cell layer. Since fluorescein is negatively charged, the voltage clamp was turned constantly on during the measurements. 100 µM of fluorescein (Stock: 100 mM) was applied to the basolateral compartment. Every 5 min (0, 5, 10, 15 min), two times 130 µl from the apical side were transferred into a 96-well plate for fluorescence measurements. The volume loss was equalized with 260 µl Ringer solution. The fluorescence intensity of each sample was measured at a wavelength of 520 nm with a plate reader from Tecan. The fluorescein concentration was calculated by using a calibration curve. The fluorescein flux was calculated as described in Equation 16.

Equation 16 Calculation of the fluorescein flux.

Flux (PAPP) = fluorescein flux/paracellular permeability over the epithelial layer

C = concentration at different timepoints or addition

V = volume of chamber or addition

Δt = time interval

A = area of the epithelial cell layer

$$Flux(PAPP) = \frac{(C_2-C_1)*V_{chamber}}{\Delta t * A_{filter} * (\frac{(V_{addition} * C_{addition})}{V_{chamber}})}$$

3.8 Statistical analysis

All data were derived from at least three independent experiments and are presented as means ± standard deviation (SD) unless differently noted in the figure legend. Comparisons among groups were performed using a one-way ANOVA and additional Dunnett's multiple comparison test or Tukey's multiple comparison test. Comparisons between two groups, statistical significance was analyzed with a two-tailed non-parametric Mann-Whitney test in GraphPad Prism Version 5.04. The level of significance is indicated in the figures by asterisks (*P ≤ 0.05, **P ≤ 0.01, ***P ≤ 0.001, ****P ≤ 0.0001). No statistical method was used to pre-determine sample sizes as sample sizes were not chosen based on a prespecified effect size. Instead, multiple independent experiments were carried out using several sample replicates as detailed in the figure legends.

4 Results

4.1 Resolving the TJ meshwork at nanoscale level with STED microscopy

Since its discovery in the early 1960s, the investigation of the TJ's structural organization and formation was part of several research studies. The first obtained FFEM images of the TJ are dated back to the 1970s[8,9] and this discovery was then followed by the identification of individual key components of the TJ, including the cytosolic scaffolding protein ZO1[37], the TAMPs[33–35], and the large group of claudins[31,74] in the 1980s and 1990s. Along with the finding of the ion permeability of specific claudins[203] and the discovery of inherited and pathogen caused diseases that were linked to claudins (e.g., paracellin-1 connected to hypomagnesemia and hypercalciuria with renal failure[69]; foodborne illness caused by *C. perfringens* enterotoxin[204] that disrupts the intestinal TJ), the question about the molecular arrangement of the by now 26 discovered mammalian claudins got more and more into focus. The resolved crystal structure of Cldn15 in 2014[86] was an important step in deciphering the junctional claudin organization as it formed the basis for suggested *cis*- and *trans*-interactions, together forming an antiparallel tetramer as functional unit for claudins[87]. Nevertheless, the arrangement of several different claudin molecules in a fully developed TJ meshwork regarding their intermolecular *cis*- and *trans*-interactions remains unsolved. Other novel methods, especially in the imaging field, are required to overcome the limitations of electron and diffraction-limited fluorescence microscopes to understand the molecular tight junctional protein arrangement.

We propose that super-resolution microscopy (SRM) will enable the nanoscale visualization and localization of multiple tight junctional proteins in the TJ meshwork. The great potential of SRM in discovering fundamental TJ characteristics was already demonstrated on single claudins in fixed cells[23,179–181]. However, most of these studies did not achieve multi-color imaging on a nanoscale level and did not carefully optimize imaging conditions and labeling density. By using new organic fluorophores, a more efficient labeling system, and advanced STED microscopy in fixed and living samples, we wanted to close this gap and connect the nanoscale arrangement of TJ proteins to their described sealing and ion permeability function.

4.1.1 STED microscopy resolves single claudin strands in overexpression in fibroblasts and on endogenous level in tissue

In contrast to previous SRM based studies that focused mainly on SIM and SMLM (dSTORM, PALM), we decided to use STED microscopy for resolving the TJ structure[178]. STED allows imaging below 50 nm resolution and fast multi-color image acquisition at the same time. For getting access to the physiological organization of the TJ structure, we focused on the one hand on antibody labeled claudins in tissue sections (Figure 20A, C) and on the other hand on an artificial claudin overexpression system in TJ-free COS-7 fibroblasts (Figure 20B, D). The fibroblast overexpression system was first described in the late 1990s[57]. It is a common and accepted tool in the TJ research field for studying the interaction of tight junctional proteins. Fibroblasts do not form an endogenous TJ, which enables the study of single TJ structures in a TJ-free background and the usage of fluorescent tags to avoid weakly or potentially unspecific antibody labeling. COS-7 fibroblasts were chosen due to their tendency to form large TJ-like meshwork in the overlap of two claudin expressing cells[98]. Both approaches overcome the previously described imaging problems by converting the TJ from its axial into a lateral direction, allowing imaging of the TJ meshwork at the highest resolution that can be achieved with our STED system. We could successfully visualize single Cldn3 strands in a TJ meshwork in murine duodenum (Figure 20C) as well as in a TJ-like meshwork formed by overexpressed EYFP-Cldn3 in fibroblasts (Figure 20D). The inconsistent appearance of the TJ meshwork structure in the tissue section might reflect the circumstance of labeling only one claudin subtype (here: Cldn3) in an endogenous formed TJ which is in general formed by multiple different claudins[127,205]. In contrast, the TJ-like meshwork formed by one claudin has a much higher strand complexity. Using SNAP-tag labeled Cldn3 and SNAP ligands coupled to a photostable and very bright fluorophore (JF646[206]), we could perform live-STED imaging of TJ-like meshworks and visualize single strand dynamics, including strand breaks and fusion of TJ meshes (Figure 20E). Full-width half-maximum (FWHM) measurements of single strands in fixed cells resulted in an average resolution of 59±11 nm (Figure 20F, G). In contrast, the achieved resolution of strands in living samples was slightly decreased by 10 nm, resulting in an FWHM of 69±14 nm (Figure 20F, G). One possible explanation for the lower resolution in the living samples is the stronger image noise and the combination of dynamics and slow acquisition time.

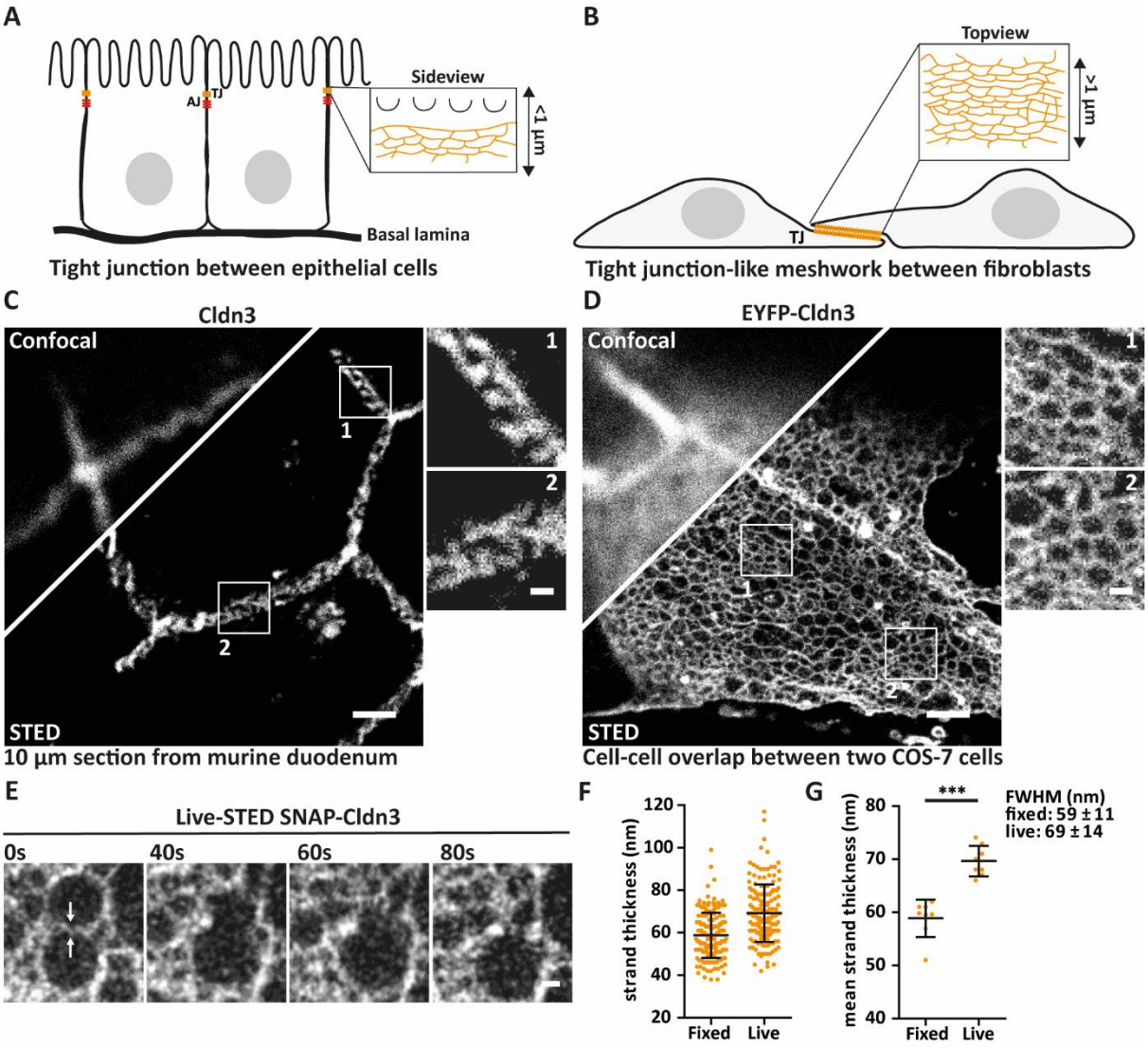

Figure 20 STED microscopy reveals the nanostructure of the TJ meshwork. (A) Scheme is illustrating the endogenous formed TJ meshwork between polarized epithelial cells. Below the TJ at the basolateral cell-cell contact side various other cell-cell junctions are formed one of them is the adherens junction (AJ). **(B)** Scheme is illustrating the TJ-like meshwork formed in the overlap between two claudin overexpressing fibroblasts. **(C)** Confocal and STED image of antibody labeled Cldn3 (Atto647N) in the TJ of murine duodenum. Single strands are visible in the magnifications. **(D)** Confocal and STED image of the TJ-like meshwork in the overlap of two EYFP-Cldn3 overexpressing COS-7. EYFP was enhanced with an anti-EGFP Atto647N nanobody. In the two magnifications, single strands are visible. **(E)** Live-STED sequence over 80 s (1 frame/10 s) of a TJ-like meshwork formed by a SNAP-Cldn3, labeled with JF646-BG in COS-7. A gaussian blur (σ=1) was applied. The two white arrows indicate strand breaks followed by a fusion of two meshes. **(F)** Strand thickness analysis of SNAP-Cldn3 labeled with JF646-BG under fixed and live conditions in COS-7. Every data point represents one strand (160 strands, from 8 TJ-like meshworks). **(G)** Shown are the means of the data from (F) with an FWHM of 59±11 nm (fixed) and of 69±14 nm (live). Every data point represents the mean of 20 measured strands in one meshwork (N=8). Statistics: mean ± SD; Mann-Whitney test, two-tailed, *** p≤0.001. Scale bars: 1 µm (overview images in C and D), 0.2 µm (magnifications in C and D, E).

In summary, we could show that advanced STED microscopy can greatly resolve the nano-details of the endogenous and claudin overexpressed TJ-like meshwork, including single strands and single meshes not only in the periphery but also the center of TJ-like meshworks. In the following experiments, we extensively used the fibroblast system due to its mentioned advantages. When combining it with STED microscopy, we assumed that novel insights into the meshwork structure and the nanoscale interactions of TJ proteins would be resolved.

4.1.2 Validation of the TJ-like meshwork nanostructure formed by fluorescently tagged claudins in COS-7 fibroblasts

Pushed by the rapid developments in the SRM field, the concerns about fixation artifacts and their influence on the nanostructure got more and more in focus[171]. Therefore, we decided to test different fixatives on an EYFP-Cldn19a TJ-like meshwork and compared their TJ nanostructures to the live imaged TJ-like meshwork formed by SNAP-Cldn19a (Figure 21A). Interestingly, only the fixation with 4% PFA/sucrose was able to preserve the meshwork structure completely. Other fixatives led to significant changes in the nanostructure that were not detectable with conventional confocal microscopy. The addition of 0.1% glutaraldehyde (GA) reduced the intensity of the fluorophores, resulting in poorer STED resolution and incomplete visualization of strands. Less concentrated PFA (1% PFA) led to a complete disruption of almost all strand connections, and the addition of ice-cold EtOH/MeOH created more punctual labeling of the TJ strands. Hence, we decided to use 4% PFA/sucrose in the following experiments to fix overexpressed claudins. However, EtOH was used as a fixative for tissue slices and epithelial cells due to the incompatibility of claudin antibodies with PFA fixation in tissue.

Large fluorescent protein labels can influence the properties of tagged proteins, hindering proper protein folding and potential protein-protein interactions. Considering that the TJ meshwork consists of several interconnected strands formed by rows of tightly packed claudin molecules, we wanted to verify that fluorescent tags do not influence the TJ meshwork nanoscale structure. We overexpressed N- and C-terminally EYFP-tagged Cldn3 and compared the formed meshwork structures (Figure 21B). We did not observe any differences regarding their meshwork formation and structure. Additionally, comparison of

overexpressed N- and C-terminally tagged Cldn1 (Figure 21B) also did not reveal any structure differences. Further we compared untagged Cldn3, that was labeled with an Cldn3 antibody, and EYFP-tagged mouse Cldn3 to the in live-STED imaged TJ-like meshworks of a SNAP-Cldn3. All observed meshworks did not indicate any significant changes in their nanoscale meshwork structure regarding meshwork density and mesh structure (Figure 21B, C). In conclusion, we could observe that neither the tag itself nor its N- or C-terminal localization changes the TJ-like meshwork structure. Interestingly, it seems that the TJ-like meshwork identity is conserved among different mammalian species (human and mouse Cldn3) but differs between different claudin subtypes (Cldn1 and Cldn3).

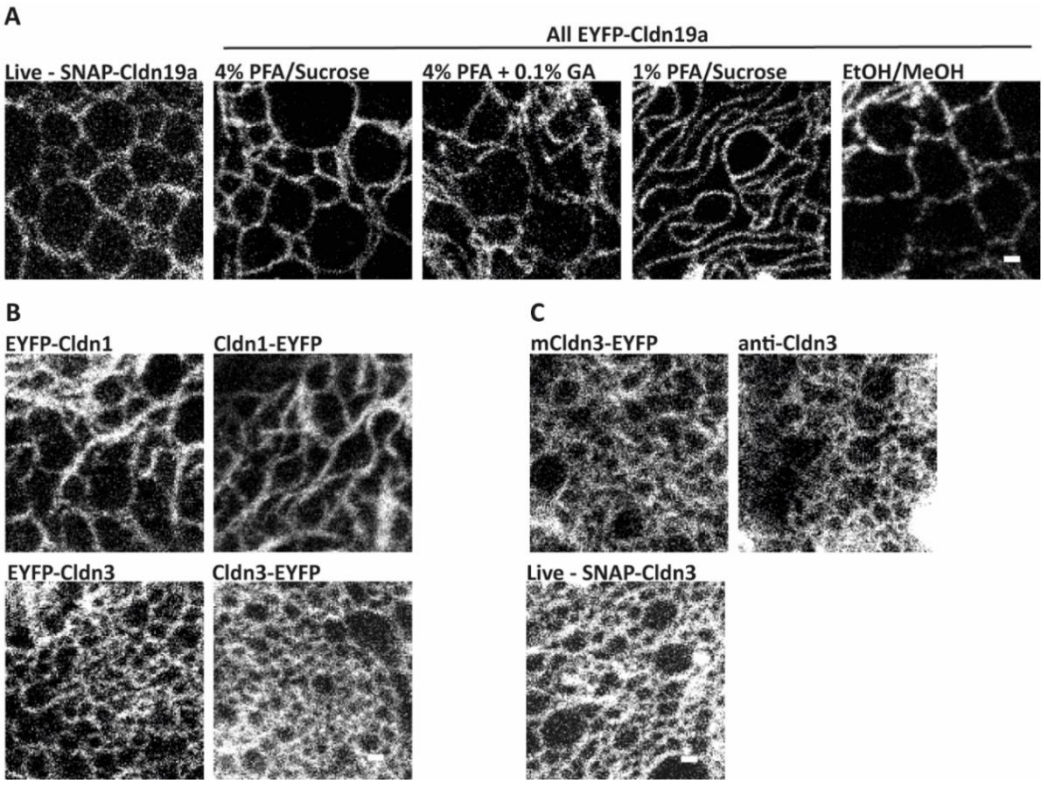

Figure 21 Different fixatives but not the fluorescent-tag have an impact on the meshwork nanostructure. EYFP was enhanced with an anti-GFP Atto647N nanobody. **(A)** Comparison of a live-STED imaged SNAP-Cldn19a labeled with JF646-BG to differently fixed (4% PFA/sucrose, 4% PFA/sucrose + 0.1% glutaraldehyde (GA), 1% PFA/sucrose, ethanol (EtOH) or methanol (MeOH)) EYFP-Cldn19a TJ-like meshworks. Meshworks fixed with 4% PFA/sucrose showed an identical nanostructure compared to live-STED. **(B)** Overexpressed N-terminally EYFP-tagged Cldn1 and Cldn3 show a similar meshwork nanostructure to their C-terminally tagged equivalent. **(C)** mCldn3-EYFP (m=mouse), untagged Cldn3, and SNAP-Cldn3 in live-STED show a similar TJ-like meshwork compared to the EYFP-tagged Cldn3 from (B). Scale bars: 0.2 µm (A, B, C).

4.1.3 Endogenously expressed ZO1 localizes at reconstituted claudin strands in fibroblasts

ZO1 is the major cytosolic adaptor protein for the TJ structure proteins and plays an essential role in the initial formation of the TJ[42,58]. Its PDZ1 domain interacts directly with the PDZ-binding motif at the end of the claudin C-terminus[88] (Figure 22A). One of its main tasks is to partition claudin molecules to the apical-lateral membrane side, creating a starting point for the TJ network formation[42]. Additionally, it links the transmembrane proteins to the actin cytoskeleton via its actin-binding region[154], making it a major regulator of TJ formation and dynamics. The endogenous expression of ZO1 in non-epithelial and non-endothelial cells is usually linked to its role in lamellipodia formation[207]. Nevertheless, it was shown that the binding of endogenous ZO1 to overexpressed claudins in Rat-1 fibroblasts can significantly impact the strand dynamics of the TJ-like meshwork by reducing these dynamics and providing a higher rigidity[23]. We first checked the endogenous ZO1 protein expression in COS-7 cells by Western Blot. Lysates of three different epithelial cell lines (Caco-2, MDCKC7 and MDCKII) served as positive controls. We could detect a clear signal for the endogenous expression of ZO1 in all cell lines, including COS-7 cells (Figure 22B). In ICC staining, we found that endogenous ZO1 partially localizes at claudin strands in the TJ-like meshwork of different overexpressed claudins (Figure 22C, Figure S3A). However, an apparent difference in comparing the ZO1 binding specificity over overexpressed channel-forming or barrier-forming claudins could not be observed. Whether ZO1 is binding the overexpressed claudins only in a partial manner or the partial appearance of ZO1 on claudin strands is related to an insufficient antibody labeling or to the fibroblast background remains unclear. Interestingly, an additional performed actin staining showed no clear localization of actin to the TJ-like meshwork (Figure S3B) going in line with previously published data[23]. Neither a substantial accumulation of actin in the meshwork nor at the meshwork located ZO1 could be observed. The results suggest that actin accumulates more at the borders of the TJ-like meshwork than inside. A clear co-localization of actin with endogenous ZO1 was only detectable in peripherally located cell ruffles (Figure S3B).

It is known that other TJ-associated transmembrane proteins can also accumulate or even directly bind to claudin strands[57] and change the TJ meshwork structure. One protein that is described to be involved is occludin[208]. Occludin is the first tetra span protein TJ protein that was discovered[33]. Its function is still unclear but lately it was shown that it might

be directly involved in the TJ strand arrangement and the TJ tightening[208]. To exclude that occludin is influencing the observed meshwork structure we verify by Western Blot that COS-7 cells are not expressing or at least only a small amount of endogenous occludin (Figure 22B).

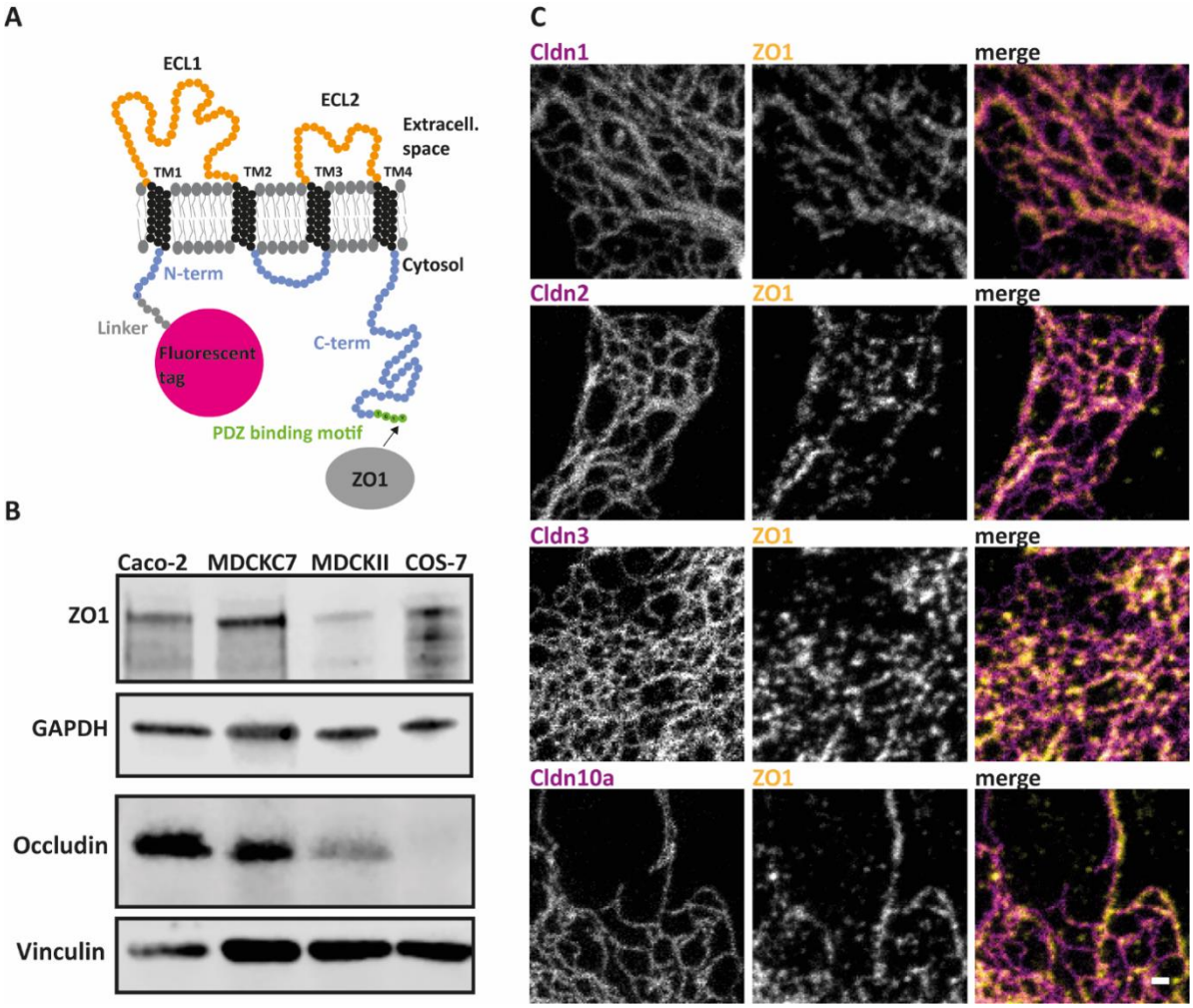

Figure 22 Endogenous ZO1 localizes at reconstituted claudin strands in COS-7 fibroblasts. (A) Scheme is illustrating an N-terminal tagged claudin molecule and with a depiction of the potential binding of the PDZ1 domain of ZO1 to the C-terminally located PDZ binding motif of claudins (green). **(B)** Immunoblotting for endogenous ZO1 (220 kDa) with GAPDH (35 kDa) as loading control and endogenous occludin (65 kDa) with vinculin (125 kDa) as loading control in lysates from different epithelial cell lines Caco-2, MDCKC7, MDCKII and COS-7 fibroblasts. **(C)** Immunostaining of endogenous ZO1 (yellow; Alexa Fluor 594) in TJ-like meshworks formed by overexpressed SNAP-tagged human claudins (Cldn1, Cldn2, Cldn3 and Cldn10a; magenta; JF646-BG) in COS-7 cells. Scale bar: 0.2 µm (C).

4.1.4 Screen over all mammalian claudins revealed structural differences in their formed TJ-like meshworks using an automated computational analysis

After characterizing the claudin overexpression system in COS-7 fibroblasts, we performed a small screening of all mammalian claudins to investigate their polymerization properties. Ideally, an automated analysis could be used to objectively compare the different meshworks and deliver new insights into the meshwork forming properties of claudins. We hypothesized that the observed meshwork structures might correlate with the function of claudins.

Firstly, all 26 mammalian claudins with their important isoforms (21 human claudins; five murine claudins) were cloned with an N-terminal EGFP- or EYFP tag by using the same linker in between fluorescent-tag and protein. Single claudins were overexpressed in COS-7 cells, and the EGFP and EYFP were enhanced with an anti-GFP nanobody conjugated to Atto647N. For each claudin, several cell-cell overlaps were imaged with STED microscopy (Figure 23). The claudins were classified into meshwork forming and non-meshwork forming claudins in an automated analysis based on Haralick texture features[192]. The single features are calculated from a Gray Level Co-occurrence Matrix (GLCM). This matrix helps to classify similar small regions from different images. It is built up by counting the co-occurrence of neighboring gray levels in an image, therefore, describing the spatial distribution of intensities within the image. This automated analysis was performed in collaboration with the FMP Bioimage analyst Dr. Christopher Schmied. The analysis was robust, and only a handful of claudins got misclassified (Figure S4). Resulting misclassifications of the automated analysis could be explained by low signal, very dense, and high-intensity structures, and the misinterpretation of the tubular structure of the ER as claudin strands. Surprisingly, we could detect that only ~50% of the claudins could form TJ-like meshwork (Figure 23A). The other half either only accumulated in the overlaps (Cldn8, 17, 18a, 18b, 24), got stuck in the ER (Cldn11b, 13, 27), showed no accumulation (Cldn4, 12, 22, 23, 25, 26) or accumulated only in the cell borders (Cldn16) (Figure 23B). Importantly, among the meshwork forming and non-meshwork forming claudins, channel- and barrier-forming claudins were equally distributed. Noteworthy, almost all the meshwork forming claudins belong to the group of the classic claudins. The classification in classic and non-classic claudins is based on a sequence alignment of all used claudins in this screening (Figure S2) that corresponds well with sequence alignments from Günzel et al.[80] (Figure 3).

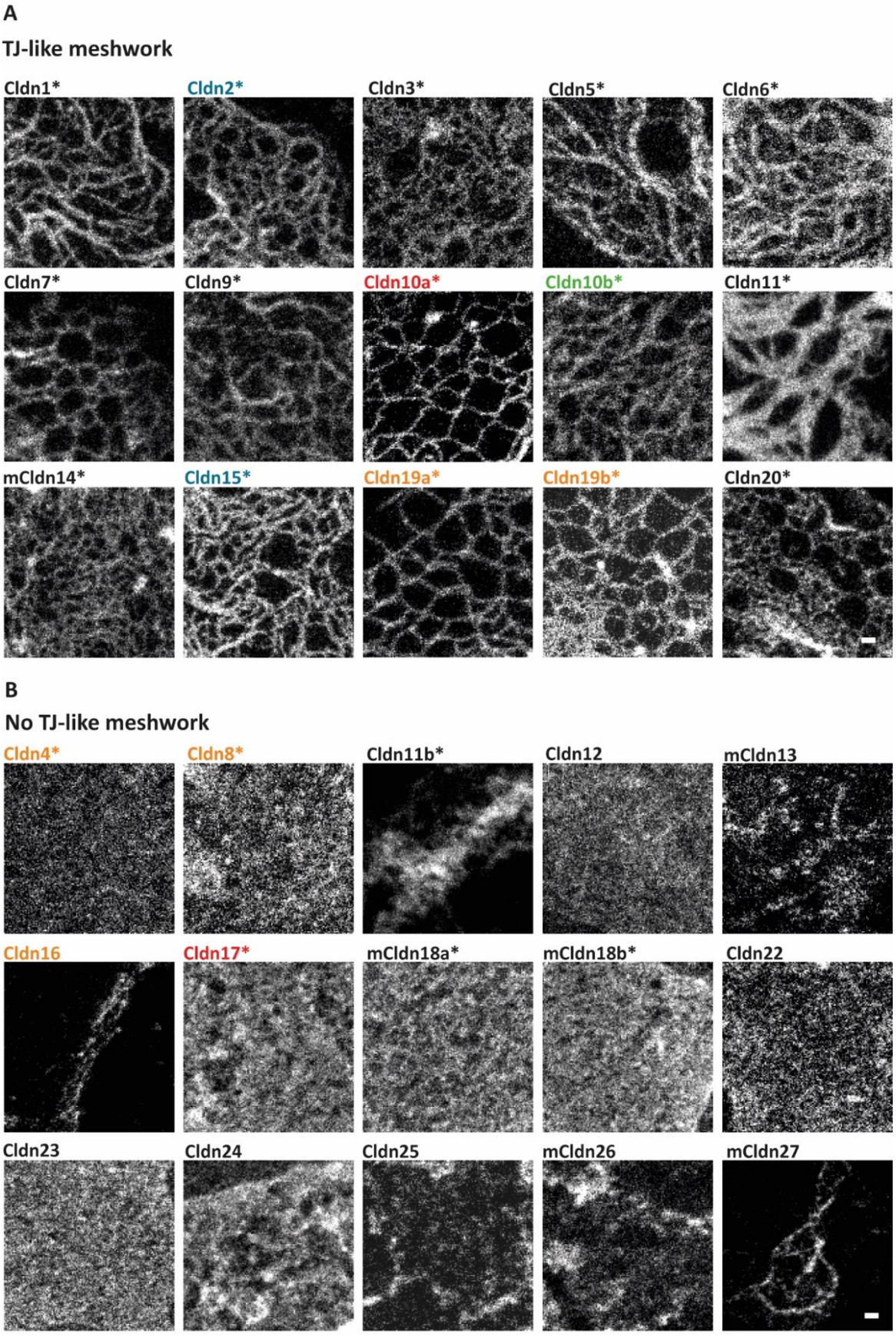
A
TJ-like meshwork
Cldn1*
Cldn2*
Cldn3*
Cldn5*
Cldn6*
Cldn7*
Cldn9*
Cldn10a*
Cldn10b*
Cldn11*
mCldn14*
Cldn15*
Cldn19a*
Cldn19b*
Cldn20*
B
No TJ-like meshwork
Cldn4*
Cldn8*
Cldn11b*
Cldn12
mCldn13
Cldn16
Cldn17*
mCldn18a*
mCldn18b*
Cldn22
Cldn23
Cldn24
Cldn25
mCldn26
mCldn27
* classic claudin
barrier - cation channel - anion channel - cation and water channel - heteromeric ion channel

Figure 23 TJ-like meshwork screening over all mammalian claudins and important isoforms in COS-7 fibroblasts. Claudins are labeled based on their proposed function: barrier (black), cation channel (green), anion channel (red), mixed cation and water channel (blue), and heteromeric ion channel (yellow). The classification in classic and non-classic claudins is based on a performed AA sequence alignment with the Clustal Omega tool from EMBL-EBI (Figure S2) which goes in line with the alignment of all human claudins by Günzel and Fromm in 2012[80] and the alignment of Krause et al in 2008[79]. Classic claudins are additionally labeled with an asterisk. All claudins were N-terminally tagged with an EYFP- or EGFP-tag and enhanced with an anti-GFP Atto647N nanobody. Claudins used were from human origin except for murine Cldn13, 14, 18a, 18b, 26, and 27. **(A)** Shown are overexpressed claudins that form TJ-like meshwork in COS-7 fibroblasts. **(B)** Shown are overexpressed claudins that do not form TJ-like meshwork in COS-7 fibroblasts. Scale bar: 0.2 µm (A, B).

In a second automated meshwork analysis based on strand segmentation (in collaboration with Christopher Schmied), only the meshwork forming claudins were analyzed (Figure 24). This analysis aimed to unravel if the TJ-like meshwork structure correlates with claudin-specific functions. For the analysis, multiple images of TJ-like meshworks from each claudin were used and processed with two different algorithms. Firstly, we again used the Haralick texture features as a first robust analysis tool that delivers information about the meshworks' homogeneity and density. Secondly, we combined it with a classic segmentation approach that provides data about meshwork structure regarding mesh number and size. A more detailed description can be found in chapter 3.6.6 in the method part.

The automated analysis led to the definition of three different classes (Figure 24A, B, and Figure S5) based on TJ-like meshwork values including Haralick texture features (SumAverage and Sum Variance) and meshwork properties (mesh sizes, branch length and number of junctions). Class A covers claudins that form meshwork with large meshes and a low strand density, whereas class B cover claudins with small meshes and a high strand density. The claudins in class C form meshwork with the highest strand density and tend to form multiple strands arranged in parallel indicated by the high signal intensity and most likely structures that were below the resolution of the STED microscope. A clear correlation between claudin function and claudin meshwork could not be observed since, in classes A and B, barrier-and channel-forming claudins were evenly distributed. Class C seemed to correlate with the barrier claudin function, since all members of it are known barrier claudins. This indicates that barrier function might link to very dense meshwork structures.

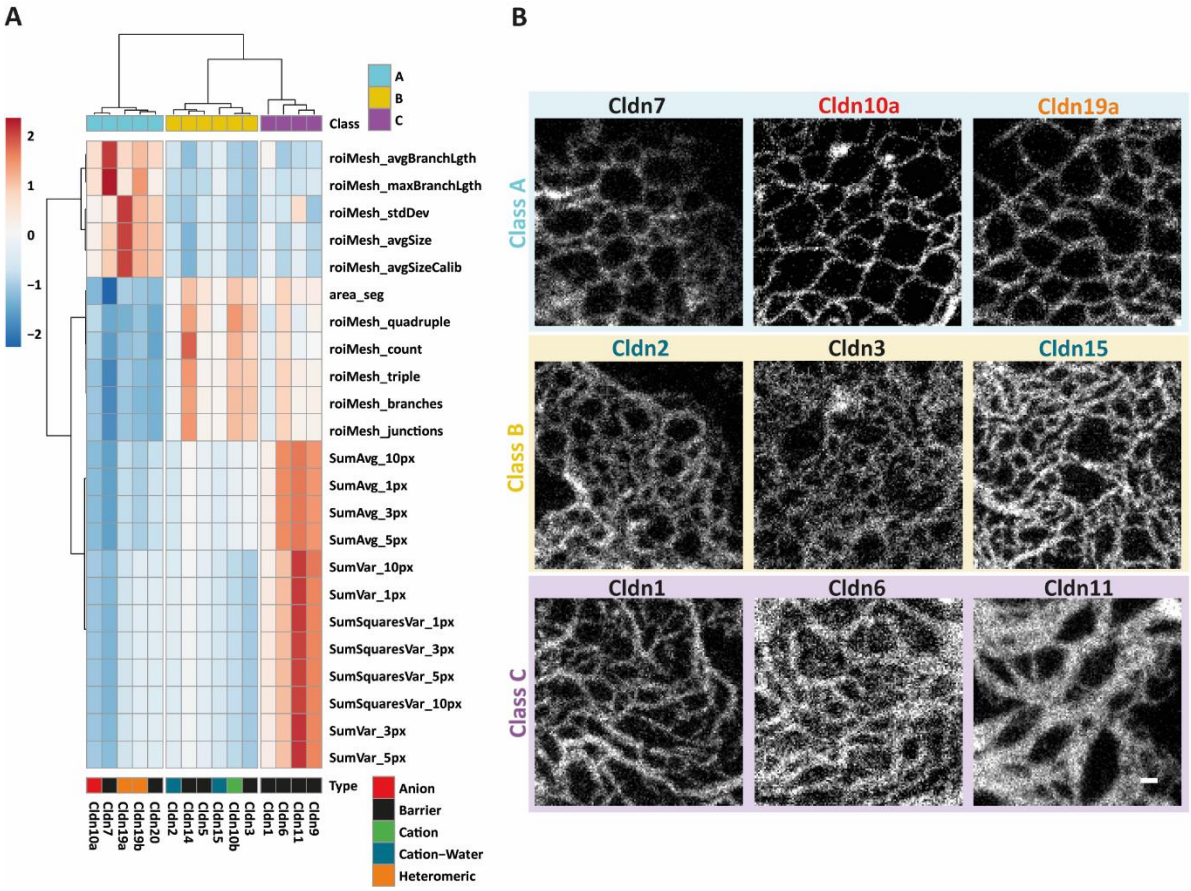

Figure 24 TJ-like meshwork analysis of all meshwork forming claudins. (A) Heat map of the results from the automated meshwork analysis and classification into three classes. The color code indicates from dark blue to dark red the increasing complexity of the analyzed factor. Parameters including roiMesh (maxBranchLgth, stdDev, avgSize, quadruple, count, triple, branches and junctions) and area_seg are derived from segmentation analysis, whereas SumAvg, SumVar and SumSquaresVar are determined by Haralick texture feature analysis[192]. The pixel size was set to 1 px equals 20 nm. The different claudins are labeled in the same color code as described in Figure 23 (barrier (black), cation channel (green), anion channel (red), mixed cation and water channel (blue), and heteromeric ion channel (yellow)). **(B)** Representative STED images of different claudins belonging to the three novel identified meshwork classes A (blue), B (yellow), and C (magenta) in (A). Scale bar: 0.2 µm (B).

4.2 Segregation of the channel-forming claudins Cldn10a, 10b and 15

The mammalian TJ is not only formed by one claudin but primarily by combinations of multiple different claudins. Imaging numerous TJ proteins and with an adequate label-density and at a sufficient resolution to distinguish them, seems to be the key for understanding the TJ meshwork organization formed by multiple different claudins. We addressed this issue by co-overexpressing SNAP-tagged claudins together with EYFP- and Halo-tagged claudins in COS-7 fibroblasts. Based on published data from FRET, co-culture,

and yeast-to-hybrid experiments[97,105,119,130,133,173], we hypothesized that probably most of the in chapter 4.1.4 described non-meshwork forming claudins would be able to integrate themselves in existing TJ meshworks by interacting with specific claudins or other tight junctional transmembrane proteins (Figure 25A). Moreover, based on the Cldn15 crystal structure[87] and the proposed model of an anti-parallel claudin tetramer, we assumed that the channel-forming claudins separate to a certain extent from the barrier-forming claudins to form functional ion channels. We speculated that the separation between two claudins within the TJ meshwork could occur in three different manners: One possibility could be that the channel-forming claudins localize as small functional units (short strands) or as longer strand parts in the TJ. Another way that seems to be also plausible was that the claudins form not only independent strands but larger individual parts (single or multiple meshes) in the TJ meshwork (Figure 25A). To challenge these hypotheses, we focused in co-overexpression experiments on two well-studied claudins, Cldn3 as a representative for the barrier-forming claudins and Cldn2 as representative for the channel-forming claudin group.

4.2.1 Claudins form five different interaction patterns in co-overexpression

In a first experiment, we decided to co-overexpress Cldn3 with several well-described barrier- and channel-forming claudins to investigate their interaction behavior. Cldn3 is described as a strict barrier-forming claudin[105], and it is widely expressed in various human and mammalian tissues[76,80]. Single overexpression in fibroblasts leads to large and dense TJ-like meshwork with multiple small meshes (class B; Figure 24). Next to our analysis of Cldn3, we also analyzed the interactions of Cldn1 and Cldn4 with other claudins in co-overexpression. Similar to Cldn3, they are described to act as sealing and barrier-forming components in the TJ[105,209]. In the previously performed screening we could show that Cldn1 forms very dense TJ-like meshwork with in parallel arranged strands (class C; Figure 24). Interestingly, although Cldn4 shares an almost 70% sequence homology with Cldn3[105], it completely lacks the ability to form meshwork in single overexpression (Figure 23). STED imaging of the different co-overexpression combinations revealed five different interaction patterns that Cldn3 and Cldn4 can participate in (Figure 25B, C, Figure S6, Figure S7):

1. Intermixing – co-overexpressed claudins have a high correlation to each other in the TJ-like meshwork and strongly co-localize.

2. Integration – a non-meshwork forming claudin integrates itself in the TJ-like meshwork of a meshwork forming claudin.
3. Induction – two non-meshwork forming claudins form together a TJ-like meshwork by an induced strand polymerization.
4. Exclusion – co-overexpressed claudins form TJ-like meshworks independently in the same cell-cell overlaps.
5. Segregation – co-overexpressed claudins form a TJ-like meshwork together, but each claudin forms its own separated strands.

The observed intermixing and segregating phenotype are exhibited by multiple different claudins that interestingly share the same functional features. Claudins that formed an intermixing meshwork belonged to the group of barrier-forming claudins, whereas claudins that predominantly segregate were all described as channel-forming claudins[32]. For the quantitative analysis and verification of this observation, the Pearson correlation coefficient was used. The Pearson correlation coefficient measures the correlation between two different variables, in microscopy it is used to determine the range of co-localization of multiple labeled proteins. A Pearson of 1 refers to a high correlation, whereas a Pearson of 0 means no correlation, and a Pearson of -1 indicates anti-correlation. For this analysis, we determined that the Pearson correlation coefficient of two claudins should be higher or equal to 0.25 to count as an intermixing claudin pair, whereas a negative value stands for segregating or excluding claudin pairs. The Pearson analysis revealed that barrier-forming claudins (Cldn1, 5, 6, 7, 9, 14, and 19b) tend to intermix with Cldn3, whereas the channel-forming claudins Cldn10a, 10b, and 15 segregate from Cldn3, indicated by their low Pearson value of -0.22 for Cldn10a, -0.26 for Cldn10b and -0.18 for Cldn15 (Figure 25C). The Pearson analysis for Cldn3 with Cldn2 gave a slightly higher Pearson value of 0.1, indicating a potential different interaction or arrangement of Cldn2 with Cldn3 than Cldn10a, 10b and 15 with Cldn3. This observation goes in line with previously made discoveries that Cldn2 can maybe interact in *trans* with Cldn3[173], which may explain the slightly higher Pearson value and the intermediate phenotype in STED (Figure 25B, C). Importantly, we could detect that the channel-forming claudins not only segregate from Cldn3 but also from the barrier-forming Cldn1 (Figure S6E).

The integration phenotype could be observed for Cldn3 and Cldn4. As mentioned, Cldn4 does not form meshwork in single overexpression (Figure 23). Interestingly, in co-overexpression with Cldn3, Cldn4 seems to integrate partially in the existing Cldn3 meshwork (Figure 25B, Figure S6D). Moreover, we could show that the co-overexpression of Cldn4 with another non-meshwork forming claudin, Cldn8, can induce the formation of claudin strands in the cell-cell overlaps (Figure 25B, Figure S6B). This induced TJ-like meshwork formation by Cldn4 and Cldn8 may indicate a direct interaction between both claudins and can be used as a starting point for understanding the hypothesized and intensely debated anion channel formation of Cldn4 with Cldn8[119].

Exclusion occurred in co-overexpression of Cldn3 with Cldn11. Both claudins form their independent meshworks in the cell-cell overlap without any indication of a connection any connection between their separated strands (Figure 25B, Figure S6C). This interaction pattern seems to be specific for Cldn11 since it shows this behavior also with other claudins in co-overexpression (e.g., with Cldn5, data not shown).

In the following experiments of this study, we focused on the claudin segregation phenotype of the channel-forming claudins due to the novelty of such nanoscale organization. Thus, we hoped to get new insights in the organization principle of these claudins and to understand their individual characteristics and functions for the mammalian TJ.

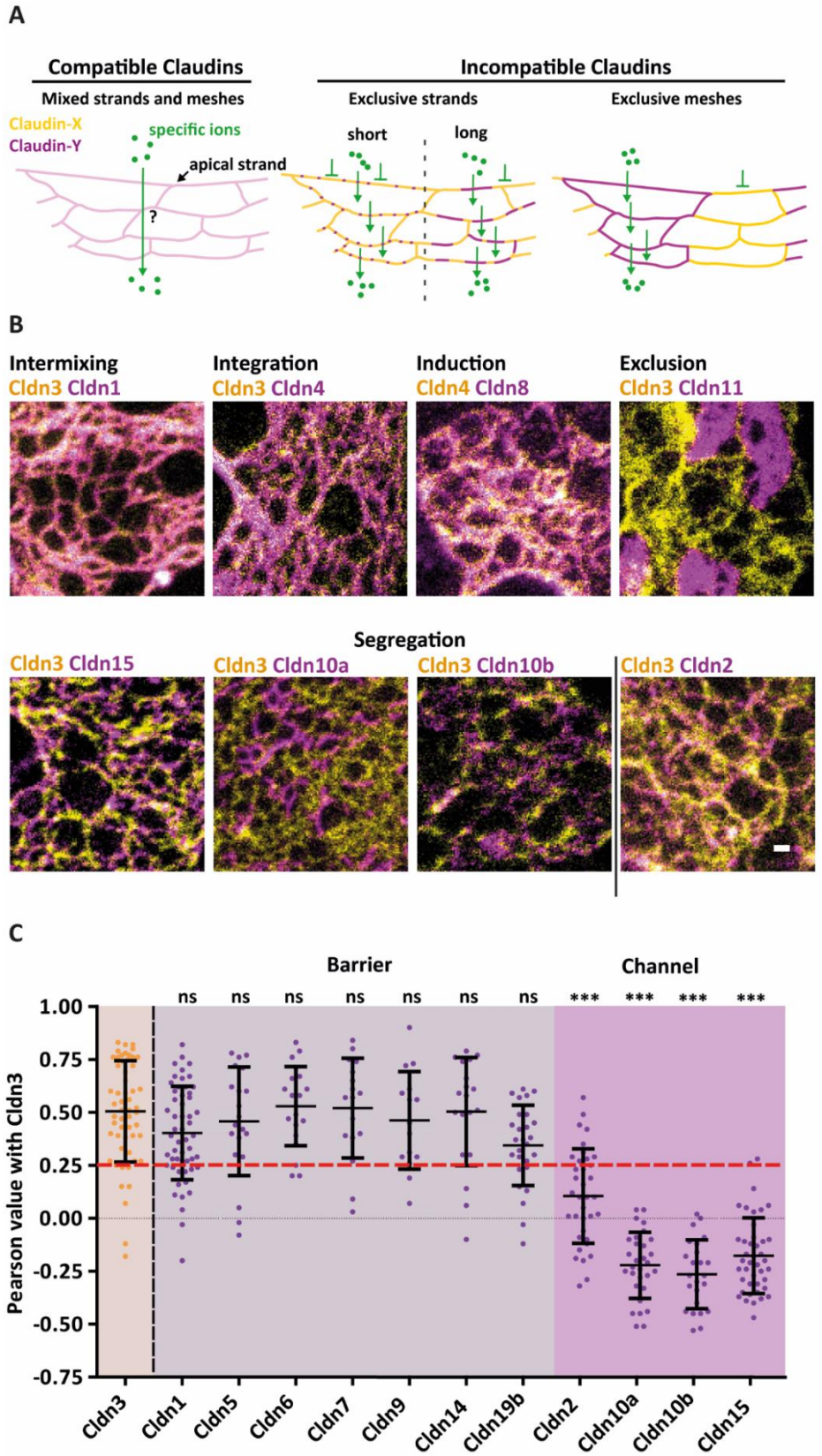
A
Compatible Claudins
Mixed strands and meshes
Claudin-X
Claudin-Y
specific ions
apical strand
?
Incompatible Claudins
Exclusive strands
short
long
Exclusive meshes
B
Intermixing
Cldn3 Cldn1
Integration
Cldn3 Cldn4
Induction
Cldn4 Cldn8
Exclusion
Cldn3 Cldn11
Segregation
Cldn3 Cldn15
Cldn3 Cldn10a
Cldn3 Cldn10b
Cldn3 Cldn2
C
Barrier
Channel
ns
***
Pearson value with Cldn3
1.00
0.75
0.50
0.25
0.00
-0.25
-0.50
-0.75
Cldn3
Cldn1
Cldn5
Cldn6
Cldn7
Cldn9
Cldn14
Cldn19b
Cldn2
Cldn10a
Cldn10b
Cldn15

Figure 25 Claudins exhibit five different interaction patterns in co-overexpression in fibroblasts. The overexpressed claudins in this experiment were based on the human sequence except for murine Cldn14. **(A)** Schematic illustration of the predicted interaction patterns of different claudins in co-overexpression. Compatible claudins should form TJ-like meshwork in an intermixing manner. The prediction for incompatible claudins is that the co-expressed claudins separate from each other in the form of short or longer exclusive strands or larger exclusive meshwork parts including single or multiple meshes. **(B)** Representative STED images of the five discovered interaction patterns (intermixing, integration, induction, exclusion, and segregation) of Cldn3 and Cldn4 in co-overexpression with other claudins in COS-7 fibroblasts. Cldn3 and Cldn4 were N-terminal labeled with a SNAP-tag (yellow) and stained with Atto590-BG, all co-overexpressed claudins were N-terminally tagged with an EYFP-tag (magenta), and the signal was enhanced with an anti-GFP Atto647N nanobody. Single-channel images are shown in Figure S7A. **(C)** Pearson analysis of claudins forming an intermixing meshwork phenotype (grey background; Cldn1, 5, 6, 7, 9, 14, 19) and a segregating meshwork type (magenta background; Cldn2, 10a, 10b and 15). Cldn3, in co-expression with itself, served as control. For each combination, ≥ 15 meshworks were imaged over three independent experiments (N≥15). We defined that intermixing claudins should reach values over 0.25, whereas segregating claudins should not exceed 0. Merged images of the additionally analyzed claudins in (B) and Pearson analysis of the integration, induction, and exclusion type from (B) are shown in Figure S6. Statistics: mean ± SD; one-way ANOVA with Dunnett's multiple comparison test (comparison to Cldn3 with Cldn3); ns (not significant), ***p≤0.001. Scale bar: 0.2 µm (B).

4.2.2 Segregation of Cldn3 and Cldn15

The discovery of the segregation pattern of the channel-forming claudin group Cldn10a, 10b, and 15 with Cldn3 provides novel insights into the claudin based TJ meshwork structure and organization. The claudin segregation is also the first direct hint towards the manner of integration of channel-forming claudins in the complex TJ as selective and functional ion channels. To analyze and verify the observed claudin segregation, we focused first on the combination of Cldn3 and Cldn15. This combination was chosen because of its physiological relevance, as both claudins are expressed in the same cells of the mammalian duodenum[76]. In the small intestine Cldn15 takes on a crucial role for the sodium-based glucose uptake by providing a paracellular channel for sodium transpodrt back into the intestinal lumen[127]. Initially, we wanted to exclude that the observed segregation is based on chemical fixation artifacts. Therefore, we co-overexpressed SNAP-tagged Cldn3 with Halo-tagged Cldn15 and imaged the formed meshworks in living cells using STED microscopy (Figure 26A). For better visualization, the background noise was removed with a Noise2Void[189] approach. The live-STED imaging revealed clearly the segregation of Cldn3 and

Cldn15. Further insight in the segregated meshwork, including the strand dynamics and mesh fusion events, could not be obtained due to the high background noise and severe photobleaching over time.

To further characterize the claudins' proximity to each other in the same membrane (*cis*-interaction), we performed FRET (described in 3.6.5) experiments by co-overexpressing Cldn3 and Cldn15 in HEK293 cells. In the FRET analysis, several contacts where both claudins accumulated were measured (Figure 26B). Single overexpressed Cldn3 served as FRET negative and Cldn3 co-overexpressed with itself as positive control. We could show that the FRET signal of Cldn3 and Cldn15 was significantly lower compared to the positive control, indicating a lack of a potential *cis*-interaction (Figure 26C). FRET was also performed for Cldn2 with Cldn3 to understand the unclear phenotype of their interaction. In comparsion to FRET of Cldn3 and Cldn15 a slightly higher FRET signal could be detected. Nevertheless, it was significantly lower compared to Cldn3 with Cldn3 or Cldn3 with Cldn1 that resulted in an even higher FRET signal indicating that Cldn2 does not interact in *cis* with Cldn3.

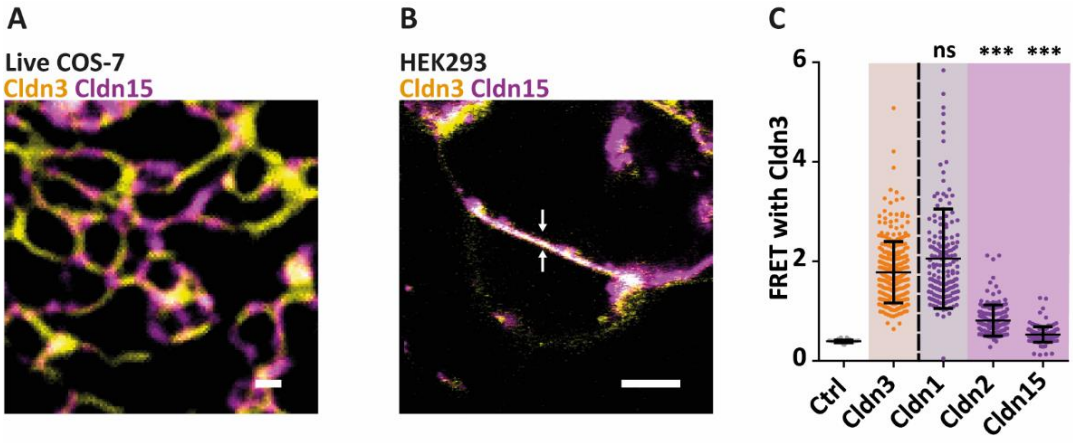

Figure 26 Cldn3 and Cldn15 segregate in living COS-7 cells and show no FRET in HEK293 cells. (A) Representative live-STED image of a TJ-like meshwork formed by SNAP-Cldn3 (yellow; JF646-BG) and Halo-Cldn15 (magenta; Atto590-CA) co-overexpressed in COS-7 cells. The background noise was reduced by using a Noise2Void[189] imaging application. **(B)** Representative confocal image of Trq2-Cldn3 co-overexpressed with EYFP-Cldn15 in HEK293 cells. Two white arrows point on the cell-cell contact site used for FRET measurements. **(C)** FRET analysis of Trq2-Cldn3 in single expression as negative control (grey), in co-overexpression with EYFP-Cldn3 as a positive control (yellow) and with EYFP-Cldn1, 2, and 15 (magenta). For each combination ≥ 20 cell-cell contacts per experiment were imaged in three independent experiments (N≥60). Statistics: mean ± SD; one-way ANOVA with Dunnett's multiple comparison test (comparison to Cldn3 with Cldn3); ns (not significant), ***p≤0.001. Scale bars: 0.2 µm (A) and 5 µm (B).

For a further validation of the segregation's biological relevance, we co-overexpressed Cldn3 with Cldn1 and with Cldn15 in Caco-2 cells. Caco-2 cells are immortalized epithelial cells derived from colorectal adenocarcinoma and are often used as a model for intestinal epithelial cells. When grown at low density and on Matrigel, Caco-2 cells can form flat overlaps. In these overlaps an early lateral located TJ meshwork can be formed (Figure 27A), which allows super resolution imaging of the meshwork structure. We could observe an intermixing of overexpressed Cldn3 with Cldn1 and segregation of Cldn3 with Cldn15 (Figure 27B). This indicates that the segregation also occurs in cells with a TJ background. A Pearson correlation coefficient analysis of multiple meshworks formed by Cldn3 and Cldn15 (Pearson value of -0.06) confirmed the previously obtained results in the fibroblast system (Figure 27C).

Ultimately, we performed IHC staining of Cldn3 and Cldn15 in 10 µm cryosections of the murine duodenum (Figure 27D). The axial to lateral conversion of the TJ in cryo sections of the tissue and STED imaging allowed us to uncover the nano-segregation of Cldn3 and Cldn15 on an endogenous level for the first time. While this was not necessary for the high-quality images of the TJ-like meshworks in fibroblasts, a gaussian blur (σ=1) had to be applied to reduce background noise in the tissue sections. The imaged TJ showed an average thickness of ~500 nm that fits to previously measured FFEM images of the TJ in murine duodenum[205]. The fact that the segregation did not appear in all visible TJ can be explained by the not fully planar and lateral localization of the TJ in the section that results in imaging TJ parts with Cldn3 and Cldn15 that are most likely present in different z-planes.

The observed segregation of barrier-forming claudins Cldn3 and Cldn1, from channel-forming claudins Cldn10a, 10b, 15 and partially from Cldn2, in overexpression and the observed segregation of Cldn3 from Cldn15 on endogenous level, led to the assumption that barrier-forming claudins and channel-forming claudins might be generally incompatible to form TJ strands together. Since it is known that a mammalian TJ can also be formed by multiple channel-forming claudins we raised the question if a channel-forming claudin might also segregate from other channel-forming claudins with the same or with a different described ion specificity.

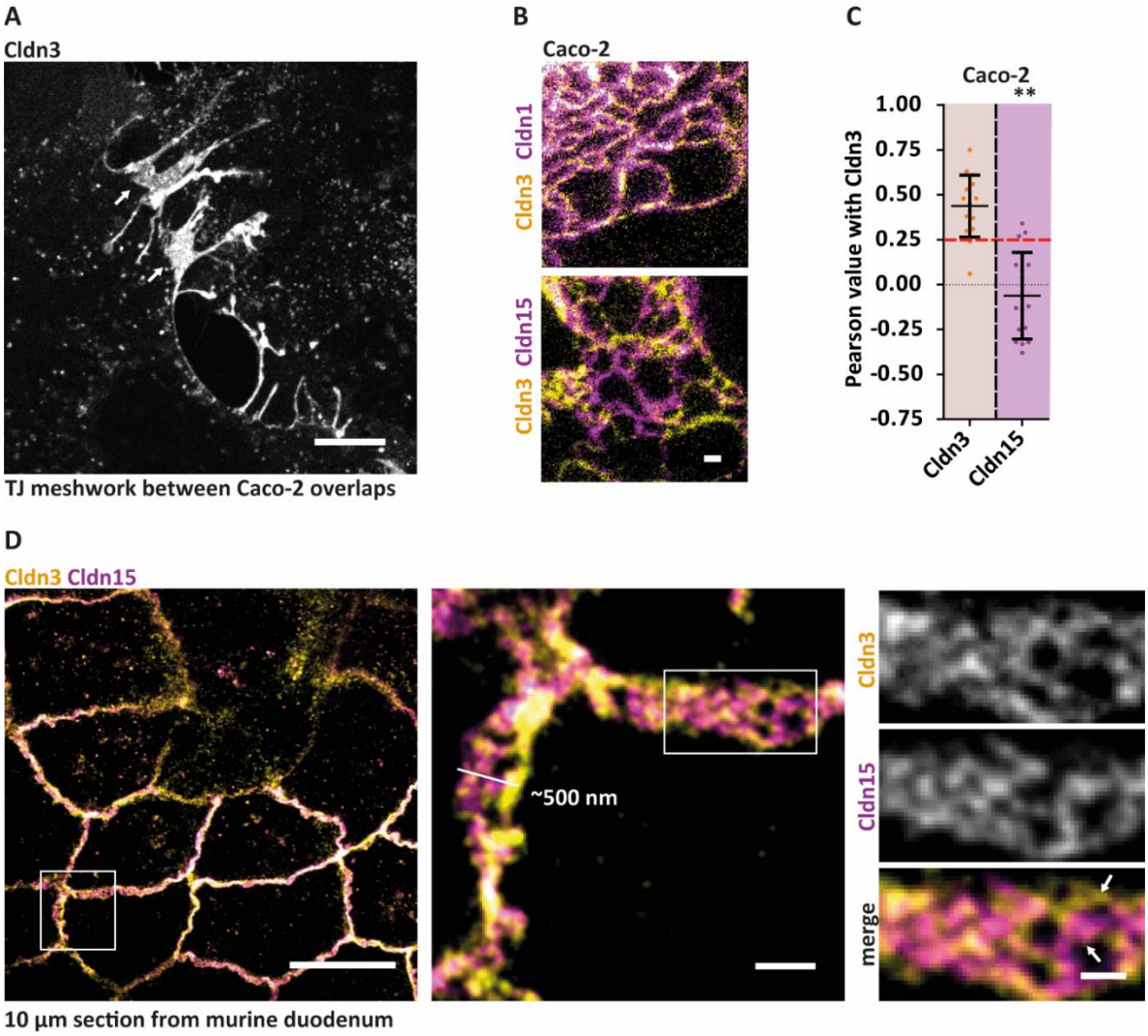

Figure 27 Cldn3 and Cldn15 segregate in co-overexpression in Caco-2 cells and endogenously in murine duodenum. EYFP-tagged claudins were enhanced with an anti-GFP Atto647N nanobody. **(A)** Representative confocal image of two flat growing and overlapping SNAP-Cldn3 (JF646-BG) overexpressing Caco-2 cells. Arrows are pointing at the overlaps with higher signal intensity indicating TJ meshwork formation. **(B)** Representative STED images of Caco-2 co-overexpressing either SNAP-Cldn3 (yellow; Atto590-BG) and EYFP-Cldn1 (magenta) with an intermixing TJ-like meshwork phenotype or SNAP-Cldn3 (yellow) and EYFP-Cldn15 (magenta) with a segregating TJ-like meshwork phenotype. **(C)** Pearson analysis of TJ-like meshworks formed by Cldn3 and Cldn3 as a control for intermixing or by Cldn3 and Cldn15 indicating claudin segregation in Caco-2 cells. For each combination ≥ five TJ meshworks were imaged in three independent experiments (N≥15). **(D)** IHC staining of Cldn3 (yellow) and Cldn15 (magenta) in a cryo-section of murine duodenum. A representative STED image is shown from left to right in increasing magnification. A gaussian blur (σ=1) was applied to reduce background noise in the tissue sections. The diameter of ~500 nm of the TJ fits to previously published data of TJ meshwork thickness in mouse duodenum based on FFEM[205]. Single segregating Cldn3 and Cldn15 strands are pointed out with the white arrows in the highest magnification. Statistics: mean ± SD; Mann-Whitney test, two-tailed; ** p≤0.01. Scale bars: 10 µm (A), 0.2 µm (B), 5 µm, 0.5 µm, 0.2 µm (from left to right in D).

4.2.3 Segregation of channel-forming Cldn2 and Cldn10a

Cldn2 is one of the first discovered and most studied channel-forming claudins. It has a high specificity for small monovalent sodium cations[111,112], and it is described to increase the tight junctional permeability for water[120]. It is usually highly expressed in leaky epithelial cell lines (MDCKII) and leaky epithelium (proximal tubule of the kidney)[32,81,113]. In tissue it is not only expressed with barrier-forming claudins but also with other channel-forming claudins, e.g., it is expressed with Cldn10a in the proximal tubule[81] and with Cldn15 in the murine small intestine[20,127,163]. While Cldn2 and Cldn10a are involved in the PT's bulk reabsorption of ions, filtered solutes and water[81], in the small intestine Cldn2 and Cldn15 enable sufficient soiudm-dependent glucose uptake by facilitating the passive transport of sodium back into the intestinal lumen. Wada et al. showed that this passive transport is of crucial nature since a DKO of Cldn2 and Cldn15 in the murine intestine leads to infant lethality due to glucose malabsorption[20].

In co-overexpression with Cldn3, Cldn2 did not show an obvious segregation phenotype compared to Cldn10a, 10b, and 15 (Figure 25). Interestingly, this result goes in line with the already published controversial FRET and co-culture data that show a potential interaction of Cldn2 with Cldn3 in *trans* and with another barrier-forming claudin, Cldn1, in *cis*[173]. This fact can be considered as a hint that Cldn2 interaction with other claudins or its arrangement in the TJ meshwork is different from the channel group Cldn10a, 10b, and 15. Based on these observations, we decided to co-overexpress Cldn2 with the channel-forming claudins, Cldn10a, 10b, and 15 and with Cldn1 as representative of the barrier claudins. Cldn2 itself served as a positive control (Figure 28A, Figure S7B). Similarly, to Cldn3, we could observe that the co-overexpression of Cldn2 with Cldn10a, 10b, and 15 also led to the formation of a segregating meshwork. In co-overexpression with Cldn1, the segregation phenotype was less clear and comparable to the co-overexpression of Cldn2 with Cldn3. The Pearson analysis confirmed these observations and resulted in low values for Cldn2 with Cldn10a (-0.17), 10b (-0.29), and 15 (-0.18) (Figure 28B). The higher Pearson value of -0.05 for Cldn1 and Cldn2 in co-overexpression indicates an incomplete segregation or different claudin organization (Figure 25B). This result agrees with the published data of Furuse et al. that already pointed out a potential *cis*-interaction between Cldn2 and Cldn1[173]. Another explanation is that the segregation of Cldn2 maybe occurs at a scale below the resolution limit of STED microscopy.

To verify the observed segregation in overexpression, we focused on the combination of Cldn2 and Cldn10a since this combination mimics the nearly exclusive expression in the proximal tubule of the mammalian kidney[81]. Performed FRET experiments resulted in no FRET signal between Cldn2 and Cldn10a, indicating no existing *cis*-interaction (Figure 28C). On the other hand, we could detect a high FRET signal for Cldn2 and Cldn1, which supports the assumption of an existing *cis*-interaction[173] and the formation of shorter and more concise Cldn2 segments. Furthermore, we could observe the segregation of Cldn2 and Cldn10a meshwork in live-STED imaging (Figure 28D) and in the overlaps of a flat grown epithelial kidney cell line (MDCKC7) which co-overexpressed Cldn2 and Cldn10a (Figure 28E). A performed Pearson analysis of the meshworks formed by MDCKC7 cells resulted in low Pearson values of -0.02, indicating a segregation phenotype (Figure 28F).

Additional to the transient single and co-overexpression experiments of Cldn2 and Cldn3, we generated Cldn2, 3, 10a, and 15 stably single expressing COS-7 cells as well as Cldn2 with Cldn10a and Cldn3 with Cldn15 stably double expressing COS-7 cells by lentiviral transduction. These cells not only show similar TJ-like meshwork when compared to transiently expressed claudins, but also the formation of segregation meshwork for Cldn2 and Cldn10a as well as Cldn3 and Cldn15 was identified (Figure S8).

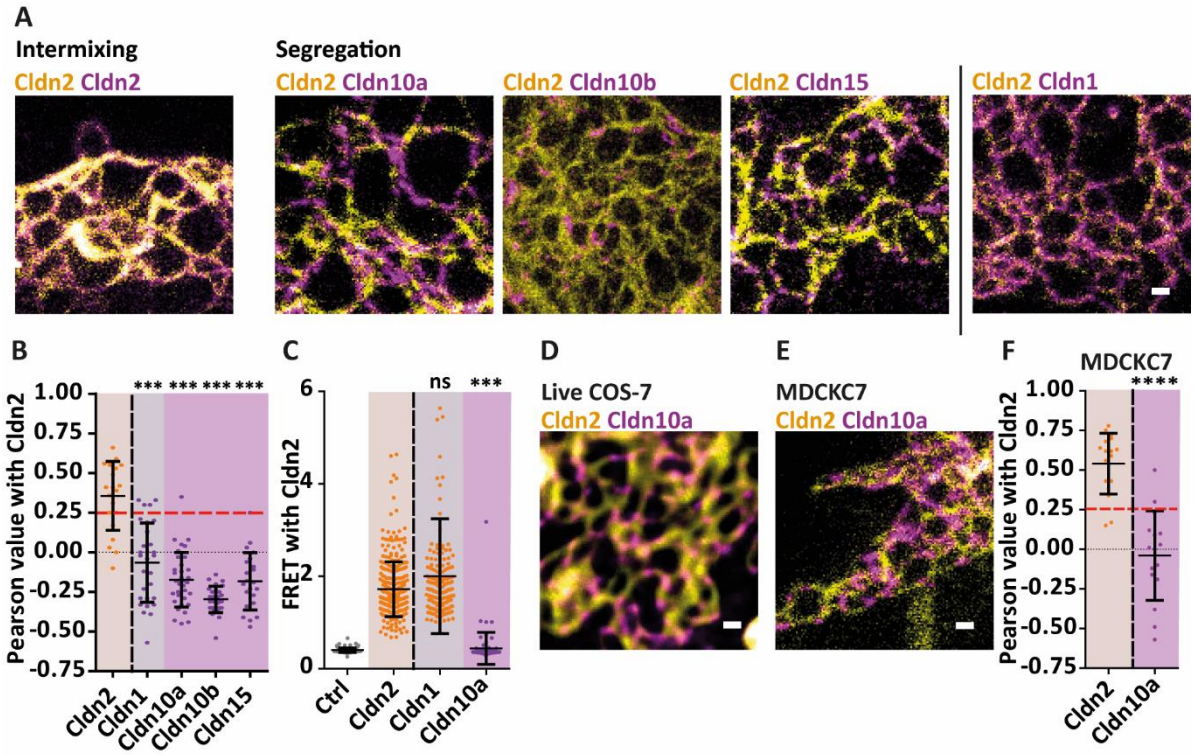

Figure 28 Segregation of channel-forming Cldn2 with the channel-forming claudins, Cldn10a, 10b, and 15. SNAP-tagged claudin were labeled with an Atto590-BG, Halo-tagged claudins were labeled with JF646-CA, and EYFP-tagged claudins were enhanced with an anti-GFP Atto647N nanobody. **(A)** Representative STED images of SNAP-Cldn2 (yellow) in co-overexpression with EYFP-Cldn1, 10a, 10b and 15 (magenta) in fibroblasts. Single-channel images are shown in Figure S7. **(B)** Pearson analysis of Cldn2 co-overexpressed with Cldn1, 2, 10a, 10b, and 15. We defined that intermixing claudins should exceed values over 0.25, whereas segregating claudins should not exceed the value of 0. For each combination, ≥ five TJ meshworks per experiment were imaged in three independent experiments (N≥15). **(C)** FRET analysis of Trq2-Cldn2 with EYFP-Cldn1, 2, and 10a in co-overexpression in HEK293 cells. For each combination ≥ 20 cell-cell contacts per experiment were imaged in three independent experiments (N≥60). **(D)** Representative live-STED image of a TJ-like meshwork formed by co-overexpressed SNAP-Cldn2 (yellow) and Halo-Cldn10a (magenta) in COS-7 cells. The background noise was reduced by using a Noise2Void[189] application. **(E)** Representative STED image of segregating TJ meshwork MDCKC7 cells formed by co-overexpressed SNAP-Cldn2 (yellow) and EYFP-Cldn10a (magenta). **(F)** Pearson analysis of TJ-like meshworks formed by SNAP-Cldn2 and EYFP-Cldn2 (high Pearson value of 0.4) as control or by SNAP-Cldn2 and EYFP-Cldn10a (low Pearson value of -0.05) in MDCKC7 cells. For each combination, ≥ five TJ meshworks were imaged in three independent experiments (N≥15). Statistics: mean ± SD; one-way ANOVA with Dunnett's multiple comparison test (B, C (comparison to Cldn2 with Cldn2)) and Mann-Whitney test, two-tailed (F); ns (not significant), ***p≤0.001, ****p≤0.0001. Scale bars: 0.2 µm (A, D, E).

For an endogenous verification of the segregation of Cldn2 and Cldn10a, whole murine kidney proximal tubules were isolated. The tubules were IHC labeled for Cldn2 and

Cldn10a and imaged with STED microscopy (Figure 29A, B). STED imaging revealed clear segregation of Cldn2 and Cldn10a in the proximal tubule (Figure 29C). The detection of the segregation in this region was easier to achieve since the TJ consists of only 1-2 strands[121] exclusively formed by Cldn2 and Cldn10a[81]. The clear alternating strand pattern was consistent over the whole isolated tubules and between PST and PCT and did not change at any point into an intermixing.

In summary, we could show that not only barrier-forming claudins form with channel-forming claudins a segregating meshwork but also the different channel-forming claudins when expressed together in vitro and in cells of the murine proximal tubule.

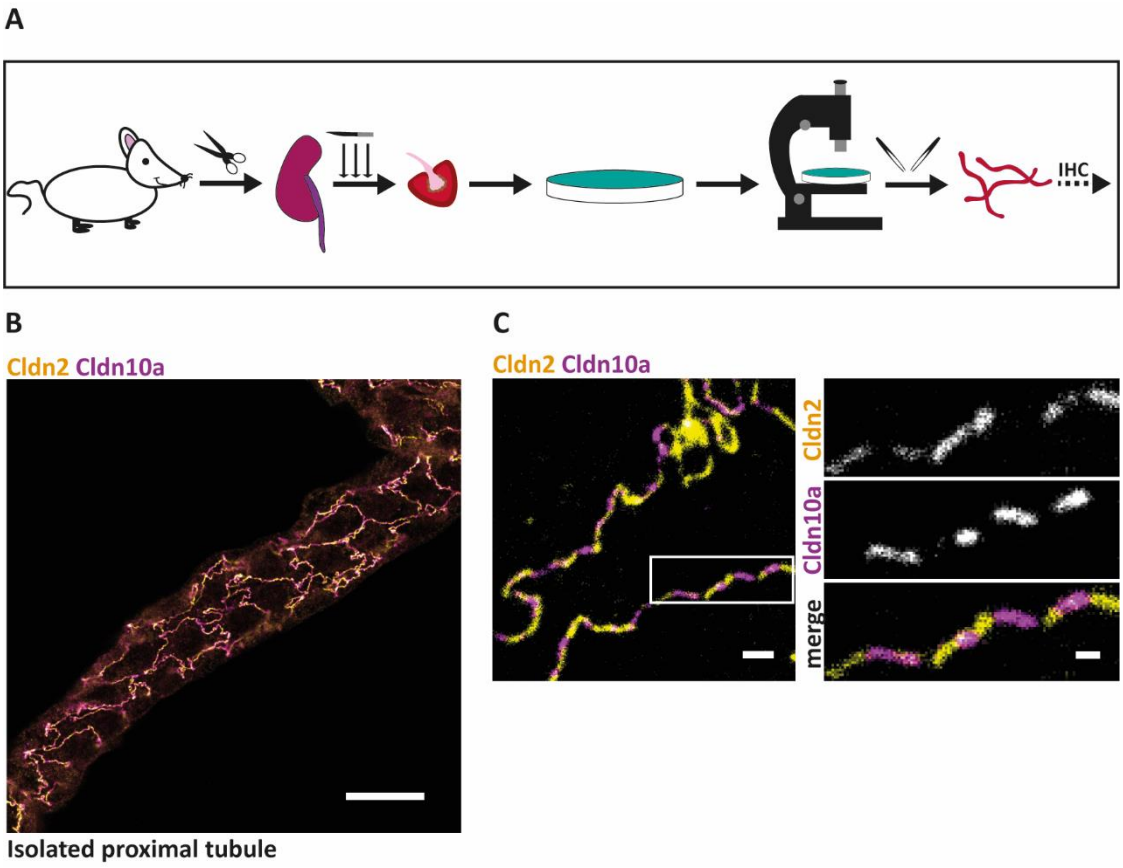

Figure 29 Segregation of Cldn2 and Cldn10a in isolated mouse proximal tubules. (A) Schematic overview of the isolation of whole proximal tubules for STED microscopy imaging. The isolation is described in detail in chapter 3.5.3. **(B)** Representative confocal image of one part of an isolated proximal tubule stained for Cldn2 (yellow) and Cldn10a (magenta). **(C)** Representative STED image and magnifications of the segregating strand parts of Cldn2 (yellow) and Cldn10a (magenta). Scale bars: 20 µm (B), 0.5 µm (overview image in C), 0.2 µm (magnification in C).

4.2.4 Cldn10b interaction patterns correspond to physiological (dys)functions

Within the channel-forming claudin group of Cldn10a, 10b, and 15, we could already show that Cldn10a and Cldn15 segregate from different claudins in overexpression and on endogenous levels in mammalian tissues. For Cldn10b we have only observe its segregation from Cldn2 and Cldn3 in overexpression so far (Figure 25, Figure 28). In contrast to Cldn10a, Cldn10b is not restricted to one specific part of an organ, but it is expressed in several different mammalian tissues and organs[81,113].

Cldn10b and Cldn3 are expressed together in the mammalian sweat glands that play an essential role in balancing the body temperature. It is described that an autosomal recessive mutation of Cldn10b (Cldn10b^{N48K}) causes sweat gland malfunction and results in sweat dysregulation which in the worst cases can lead to anhidrosis[82,210]. Together with other observed Cldn10b related missense and nonsense mutations it is summarized as a novel “claudinopathy” the HELIX (hypohidrosis, electrolyte imbalance, lacrimal gland dysfunction, ichthyosis, xerostomia) syndrome[70,211]. We could show that this mutant cannot form TJ meshwork in overexpression when singly expressed (Figure S9A). Moreover, its interaction with the Cldn10b WT in co-overexpression was also disturbed and it lost its segregating behavior entirely when co-overexpressed with Cldn3 (Figure S9B) probably adding on the fatality of the mutation. These observations are also reflected in the Pearson analysis of the combination of Cldn3 and Cldn10b with Cldn10b^{N48K} resulting in negative Pearson values. Next to its expression in mammalian glands, Cldn10b is also highly expressed in the kidney. Especially its appearance in the thick ascending limb (TAL) of Henle's loop seems to play an essential role in the uptake of monovalent and divalent ions. In 2016 Milatz et al. described that the claudins Cldn10b, and Cldn19 and Cldn16 are expressed in the TAL in a mosaic manner[133]. They showed that the claudins did not segregate within the TJ, but between different cells. Interestingly, we could observe in double and triple overexpression of Cldn10b, Cldn19, and Cldn16 that these three claudins can form three out of the five described claudin-claudin interaction patterns. Cldn10b and Cldn19 form a segregating meshwork in co-overexpression, whereas Cldn19 and Cldn16 form meshwork in an integrative manner, as Cldn16 is unable to form meshwork on its own. Cldn16 and Cldn10b in co-overexpression behaved in an exclusion manner (Figure 30A, B). Triple overexpression resulted in similar interaction types as observed in double overexpression (Figure 30C, D).

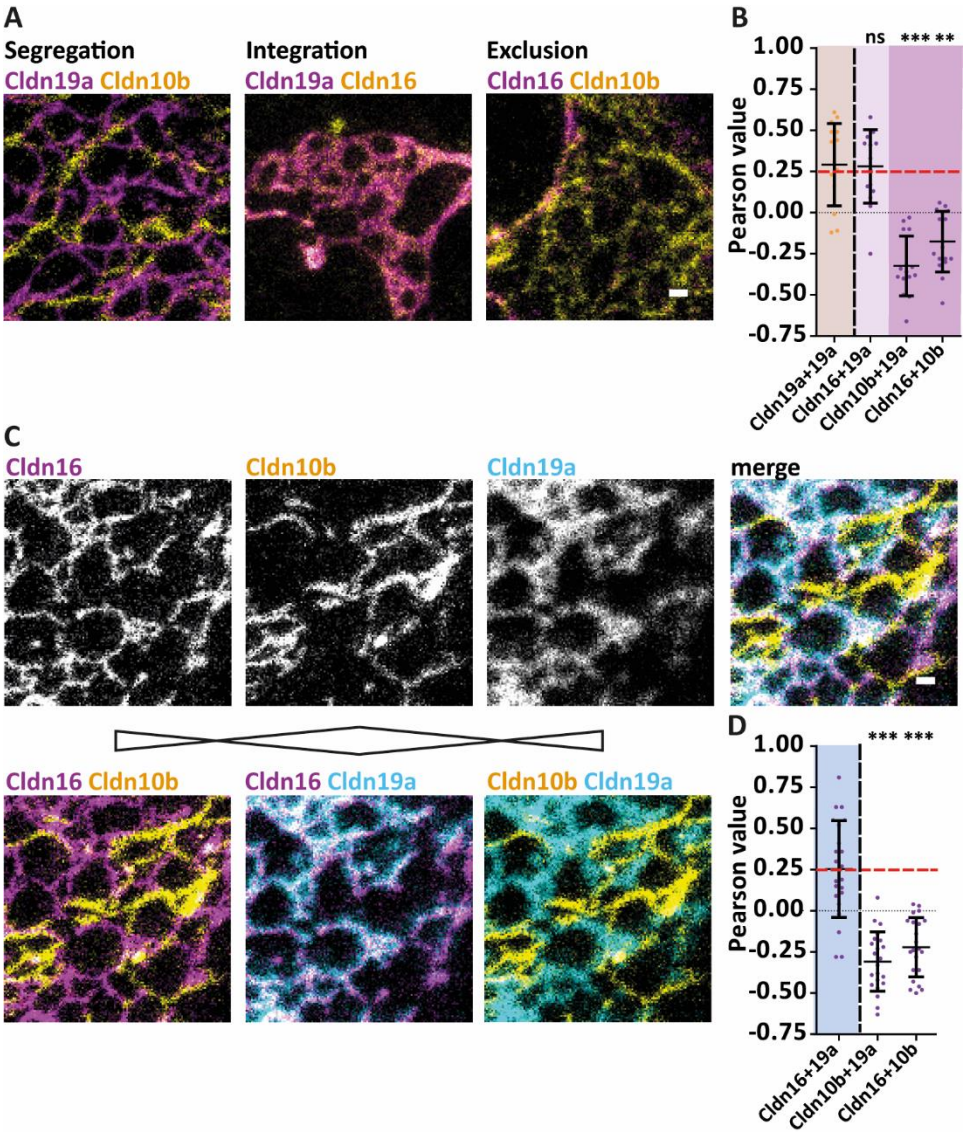

Figure 30 Segregation of Cldn10b from Cldn19 and Cldn16 in triple overexpression in fibroblasts. SNAP- and Halo tagged proteins were labeled with an Atto590-BG and JF646-CA. EYFP-tagged claudins were enhanced with an anti-GFP Atto647N nanobody (A) or labeled with a primary anti-GFP antibody and an Atto542 coupled secondary antibody (C). **(A)** Representative STED images of SNAP-Cldn10b, Halo-Cldn16, and EYFP-Cldn19a in co-overexpression. Cldn19a (magenta) and Cldn10b (yellow) form a segregating meshwork, Cldn19a (magenta) and Cldn16 (yellow) an intermixing meshwork, and Cldn16 (magenta) and Cldn10b (yellow) exclude from each other. **(B)** Pearson analysis of the co-overexpression combinations from (A) (magenta). As positive control served SNAP-Cldn19a in co-overexpression with EYFP-Cldn19a (yellow). For each variety, ≥ five TJ meshworks were imaged in three independent experiments (N≥15). **(C)** Representative STED image of Halo-Cldn16 (magenta), SNAP-Cldn10b (yellow), and EYFP-Cldn19 (cyan) in triple overexpression. **(D)** Pearson analysis of the triple overexpression experiments from (C). For each combination, ≥ five TJ meshworks per experiment were imaged in three independent experiments (N≥15). Statistics: mean ± SD; one-way ANOVA with Dunnett's multiple comparison test (B (comparison to Cldn19a+Cldn19a), D (comparison to Cldn16 with Cldn19a)); ns (not significant), **p≤0.01, ***p≤0.001. Scale bars: 0.2 µm (A, C).

In summary, we were able to determine that the observed interaction pattern of the claudin segregation is most likely a conserved interaction mechanism of the channel-forming group of Cldn10a, 10b, and 15. This is even further substantiated by the fact that all tend to segregate also from each other in co-overexpression experiments (Figure S10), indicating a potential incompatibility for heteromeric claudin interactions.

4.3 Characterization of the claudin segregation

Segregation of Cldn10a, 10b, and 15 seems to be a well-conserved interaction pattern that allows coordinated incorporation of channel-forming claudins into the TJ meshwork. To understand the segregation on the molecular level and determine its functional purpose, we focused in the following experiments on the segregation of cation channel-forming Cldn2 from anion channel-forming Cldn10a and on the segregation of barrier-forming Cldn3 from sodium channel-forming Cldn15.

4.3.1 Strand lengths in a segregating meshwork dependent on claudin's expression level and vary over different kidney tubules

In a first experiment, we asked ourselves whether the observed single strand lengths in a segregating meshwork are specific for one kind of claudin and whether it depends on the stability of a particular strand length or the claudin expression level. To address these hypotheses, we measured first the lengths of Cldn2 and Cldn10a strands over whole isolated kidney proximal tubules. We could show that strand lengths vary drastically between the different tubules without identifying at first sight any correlation (Figure 31A). A subsequent Pearson analysis of these images revealed that the segregation, did not change over the different tubules and not over different parts of the tubules (Figure 31B). Next, we further investigated the strand lengths in a segregating meshwork in fibroblasts. Cldn2 and Cldn10a were co-overexpressed in two different ratios (3:1/1:3) (Figure 31C), and the overall claudin expression was controlled and verified by Western Blot (Figure 31D). STED images of several TJ-like meshwork were taken, and the strand lengths of Cldn2 and Cldn10a were measured over multiple meshworks (Figure 31E). Strand length measurements indicate a clear correlation between claudin strand lengths and claudin expression level. When Cldn2 was co-overexpressed in a ratio of 3:1, the average strand length resulted in 0.35 µm for Cldn2

and 0.18 µm for Cldn10a. Strand lengths changed when Cldn2 and Cldn10a were co-overexpressed in a 1:3 ratio. The average strand length in case of Cldn2 was reduced to 0.26 µm and for Cldn10a increased to 0.30 µm. A final Pearson analysis showed that the different expression levels and different strand lengths do not influence claudins' segregation (Figure 31F). Additional co-overexpression experiments showed that this observation also occurs for the segregating meshwork formed by Cldn3 and Cldn15 (Figure 31G, H). In this experiment, only Cldn15 was gradually (1:1, 1:2, 1:3) increased.

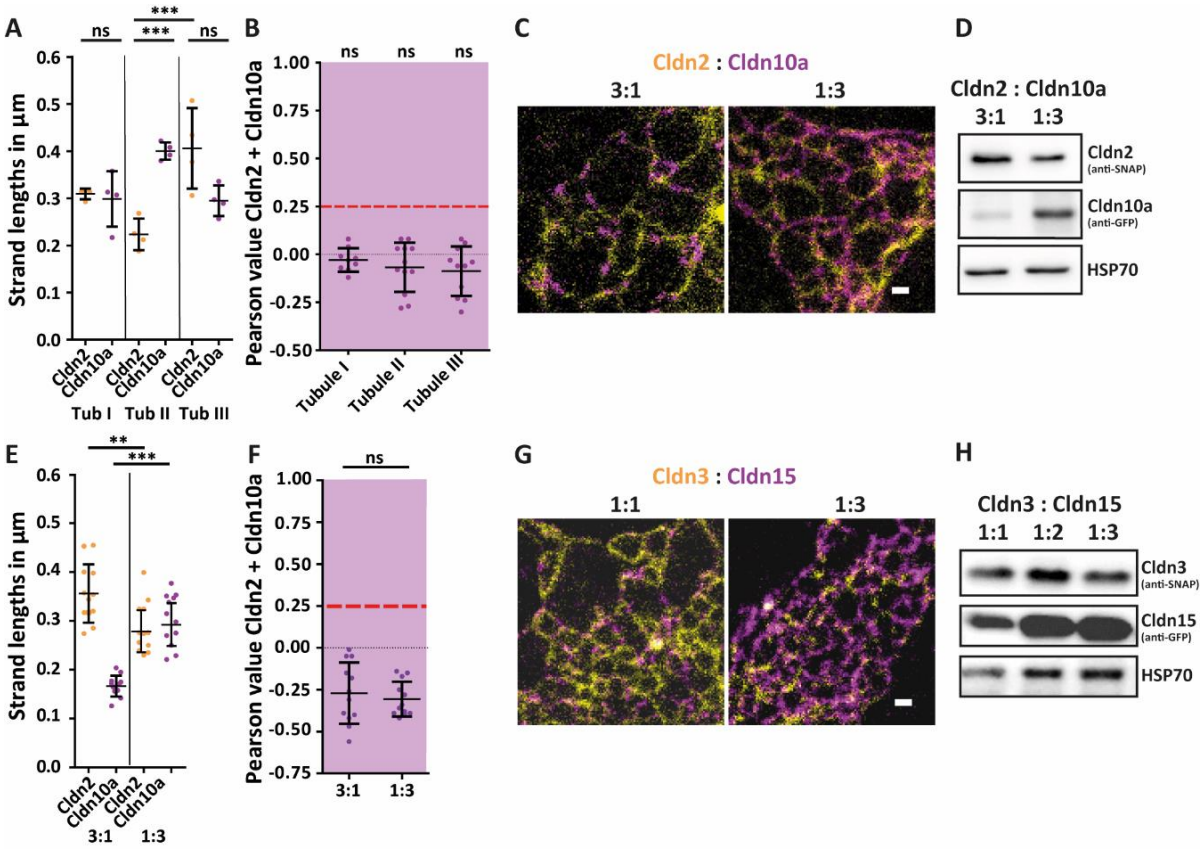

Figure 31 Strand lengths of claudins in segregated meshworks depend on the claudin expression. For STED imaging, all SNAP-tagged proteins were labeled with an Atto590-BG. EYFP-tagged claudins were enhanced with an anti-GFP Atto647N nanobody. **(A)** Strand length measurement of Cldn2 (2; yellow dots) and Cldn10a (10; magenta dots) in isolated proximal tubules. The average strand length is shown in µm. 120 strands per image in four STED images per tubule (three tubules: TubI, TubII and TubIII) were measured (N=4; one N is the averaged strand length in one STED image). **(B)** Pearson analysis of analyzed tubules from (A) (Tub I (N=9), Tub II (N=12), Tub III (N=11); one N is one meshwork). **(C)** Representative STED images of SNAP-Cldn2 (yellow) expressed with EYFP-Cldn10a (magenta) in a plasmid ratio of 3:1 and 1:3. **(D)** Western Blot of lysates from SNAP-Cldn2 and EYFP-Cldn10a co-transfected COS-7 (ratio 3:1 and 1:3). For the detection, an anti-SNAP (SNAP-Cldn2, 45 kDa) and an anti-EGFP (EYFP-Cldn10a, 55 kDa) antibody were used. HSP70 (70 kDa) served as

a loading control. **(E)** Strand length analysis of SNAP-Cldn2 (2; yellow dots) and EYFP-Cldn10a (10; magenta dots) in COS-7 co-transfected in a ratio of 3:1 and 1:3. 40 strands per meshwork (four per experiment) from three independent experiments were measured (N=12; one N is the mean strand length in one meshwork). **(F)** Pearson analysis of the analyzed TJ-like meshworks from (E). 12 meshwork from three independent experiments were measured (N=12). **(G)** Representative STED images of SNAP-Cldn3 (yellow), expressed with EYFP-Cldn15 (magenta) in a plasmid ratio of 1:1 and 1:3. **(H)** Western Blot of lysates from SNAP-Cldn3 (SNAP-Cldn3, 45 kDa) and EYFP-Cldn15 (EYFP-Cldn15, 55 kDa) co-transfected COS-7 (ratio 1:1, 1:2 and 1:3). For the detection, an anti-SNAP and an anti-EGFP antibody were used. HSP70 (70 kDa) served as a loading control. Statistics: mean ± SD; one-way ANOVA with Tukey's multiple comparison test (A, B) and Mann-Whitney test, two-tailed (E, F); ns (not significant), *** p≤0.001, ** p≤0.01. Scale bars: 0.2 µm (C, G).

4.3.2 Extrinsic factors, including the blockage of the Cldn2 pore and depletion of cellular cholesterol, do not influence the segregation of Cldn2 and Cldn10a

To further analyze the claudin segregation, we focused on potential extrinsic factors that might be involved in the segregating meshwork organization. Two extrinsic factors that could play a role are the actual pore function of the channel-forming claudin and cholesterol a lipid that is described to be enriched at TJ[60,61].

For blocking the ion permeability of a claudin channel Weber et al. generated a functional Cldn2 mutant with isoleucine-66 (I66) substituted to cysteine (Cldn2^{I66C}). Then, they showed that MTSET, a cysteine binding compound could block the Cldn2 mutant and impair its ion permeability function[124] (Figure 32A). We assumed that the channel function's loss might influence the segregation by leading to a potential strand and meshwork disruption or re-arrangement. To test this hypothesis, we first generated an EGFP-Cldn2^{I66C} mutant and confirmed that it still could form TJ-like meshwork in single overexpression and that it forms a segregated meshwork in co-overexpression with Cldn10a (Figure S11). Moreover, we excluded in an additional single overexpression experiment that the addition of DMSO or MTSET has any influence on the Cldn2^{I66C} TJ meshwork itself (Figure S11C). In the main experiment, we co-overexpressed Cldn2^{I66C} and Cldn10a, and subsequently incubated the cells for two hours with MTSET (or just DMSO as a control). The cells were then fixed and imaged with STED microscopy. Despite the loss of the channel function, we could not observe any difference in the segregating pattern or behavior (Figure 32B), indicating that the segregation is independent of the claudin's ion permeability function.

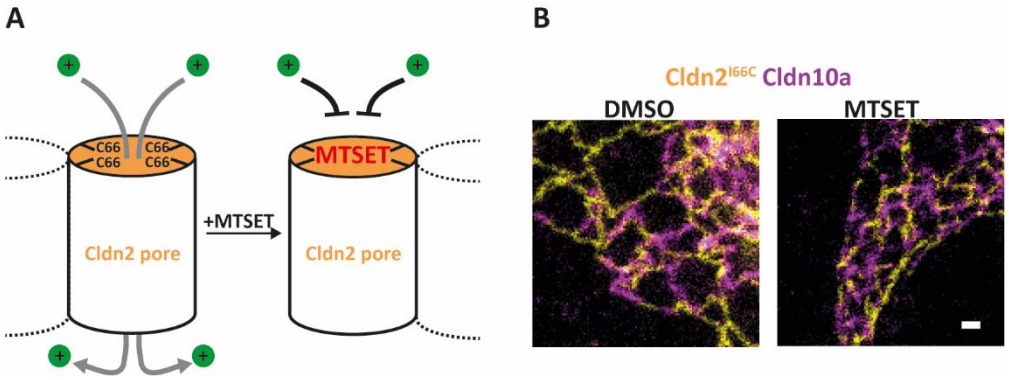

Figure 32 Blockage of the Cldn2 pore has no impact on the claudin segregation. All SNAP-tagged claudins were labeled with Atto590-BG. EGFP-tagged claudins were enhanced with an anti-GFP Atto647N nanobody. **(A)** Schematic illustration of the binding and blocking of the Cldn2^{I66C} pore (yellow) by MTSET (red). MTSET reacts with the free cysteine groups (black) by forming covalent bonds. The binding blocks the Cldn2 channel function. **(B)** Representative STED images of TJ-like meshwork formed by EGFP-Cldn2^{I66C} and SNAP-Cldn10a. 24 hours after transfection, the cells were incubated for two hours with 1 mM MTSET, fixed and ICC stained, and imaged with STED. DMSO was used as control. Scale bar: 0.2 µm.

The membrane lipid composition in and around the TJ meshwork is not yet fully clarified and stays controversially debated in the TJ field[61,212]. One lipid that is supposed to be involved in the TJ formation and organization is cholesterol. Cholesterol is one of the main plasma membrane lipids. It was shown in MDCKII and EpH4 epithelial cells that depletion of cholesterol using methyl-β-cyclodextrin (MβCD) leads to a complete disruption of the TJ and a loss of barrier function[61,213]. Therefore, we wanted to know if the depletion of cholesterol influences the segregating meshwork of Cldn2 and Cldn10a in fibroblasts. We used for the depletion on the one hand MβCD and on the other hand mevastatin. MβCD removes the cholesterol directly from the plasma membrane, whereas mevastatin inhibits the HMG-CoA-reductase and thereby interferes the production of new cholesterol via the mevalonate pathway. MβCD was added to the Cldn2 and Cldn10a expressing COS-7 cells in a concentration of 25 mM for one hour, whilst mevastatin was applied at 10 µM over 24 hours (DMSO was used as control in both approaches). Cholesterol was stained using Filipin III and its depletion was determined based on its intensity decrease. The cholesterol depletion was successful with both chemicals, but it was slightly stronger with MβCD than mevastatin (Figure 33A). In STED, we observed under cholesterol depletion conditions that the meshwork was more disorganized and contained more vesicular claudin enriched structures than the DMSO control. However, the segregation pattern was still intact (Figure 33B).

Taken together the results indicate that the Cldn2 itself as well as the membrane lipid cholesterol probably do not change the claudin segregation of Cldn2 and Cldn10a. If higher concentration of the cholesterol reducing agents might affect the segregation or simply disrupt the TJ meshwork was not further studied.

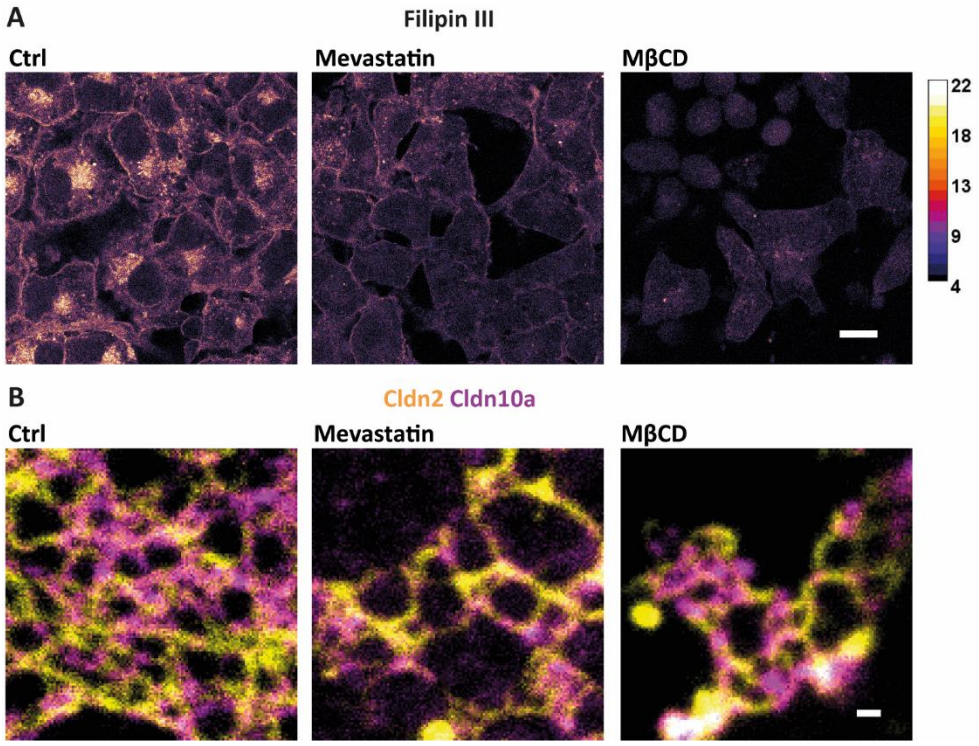

Figure 33 Depletion of cholesterol has no impact on claudin segregation. All SNAP-tagged proteins were labeled with an Atto590-BG, and EYFP-tagged claudins were enhanced with an anti-GFP Atto647N nanobody. **(A)** Control of the cholesterol depletion by staining of endogenous cholesterol with Filipin III. The same imaging settings were used among the different conditions. The intensity is shown in fire color mode. The fire color scale shows the different colors representing the different image intensities. The scale is ranging from white (highest signal) to black (no signal). **(B)** STED images of TJ-like meshwork formed by SNAP-Cldn2 (yellow) and EYFP-Cldn10a (magenta) in COS-7 cells. Shown are example images for DMSO (control), mevastatin (10 µM for 24 hours), and MβCD (25 mM for one hour) treated cells. Scale bars: 0.2 µm (B), 20 µm (A).

4.3.3 Claudin segregation is independent of ZO1 and the claudin C-terminus, but it is mediated by the extracellular loops

Since the so far tested extrinsic factors showed no real impact on the segregating TJ meshwork, we decided to try and identify which part of the claudin structure is involved in

segregation. Therefore, we tested the possibility that the two ECLs, the C-terminally located phosphorylation sites or the domain for binding to ZO1 (important for TJ protein partitioning)[42], influence strand polymerization and claudin segregation.

For ZO1, we could verify that it localizes in the segregated meshwork in proximity to single claudin strands without showing any preference for overexpressed Cldn2 or Cldn10a (Figure 34A). A Pearson analysis supports this observation by showing no apparent correlation to either one of the segregating claudins (Figure 34B).

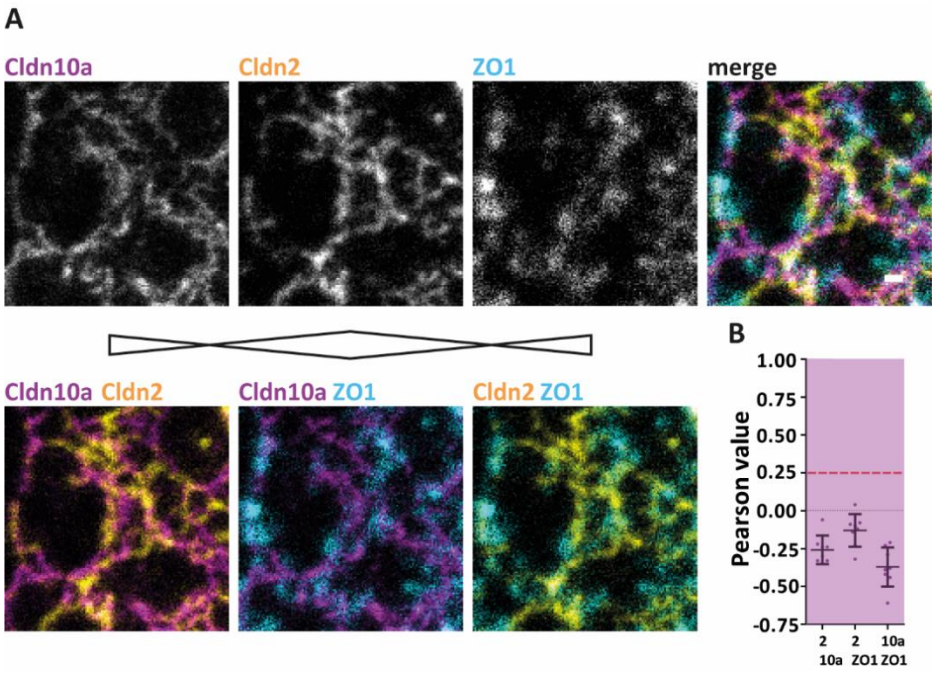

Figure 34 Endogenous ZO1 localizes at single strands in a segregated TJ-like meshwork without any preference for a specific claudin. For STED imaging, SNAP-tagged proteins were labeled with Atto590-BG. EYFP-tagged claudins were enhanced with an anti-GFP Atto647N nanobody. **(A)** Representative STED image of TJ-like meshwork formed by SNAP-Cldn2 (yellow) and EYFP-Cldn10a (magenta) in COS-7 cells. Endogenous ZO1 (cyan) was labeled with an anti-ZO1 antibody and with a secondary antibody coupled to Atto542. **(B)** Pearson analysis of ZO1, Cldn2, or Cldn10a in a segregating TJ-like meshwork (eight different meshworks were analyzed, N=8). Statistical analysis: mean ± SD. Scale bars: 0.2 µm.

By overexpressing Cldn2 and Cldn10a as well as Cldn3 and Cldn15 PDZ-binding motif deletion mutants (ΔPDZ) (Figure 35A) we investigated whether a loss of the linkage of claudin to ZO1 affects the formation and organization of the segregating meshwork. The influence of ZO1 on the TJ-like meshwork was shown by Van Itallie et al. in 2016 by

comparing Cldn2 and a Cldn2 PDZ-binding motif deletion mutant in overexpression in Rat-1 fibroblasts. They could show that a loss of the PDZ-binding motif leads to a more dynamic meshwork behavior[23]. Additionally, we also tested C-terminus deletion mutants (ΔCT; Figure 35A) in co-overexpression. The long C-terminus of claudins contains multiple phosphorylation sites, which play a major role in claudin trafficking[92,93,214]. The deletion of the C-terminus should help to understand whether the phosphorylation sites are essential for claudin segregation. The generated claudin ΔPDZ and ΔCT mutants were co-overexpressed in COS-7 cells, and the formed meshworks were imaged with STED. In comparison to the non-mutated claudins we observed less expanded and more disorganized meshworks for the ΔPDZ and ΔCT mutants. However, claudin segregation was still observable for both deletion mutants (Figure 35B, D). The Pearson correlation coefficient analysis supported this visual impression by resulting in corresponding low Pearson values (Figure 35C, E). The more disorganized meshwork affected the Pearson analysis slightly, but the difference between intermixing control (Cldn10a$^{\Delta PDZ}$ with Cldn10a$^{\Delta PDZ}$; Cldn10a$^{\Delta CT}$ with Cldn10a$^{\Delta CT}$) and segregating claudins was still significant. The STED images and the results of the Pearson analysis let us to conclude that the PDZ-binding motif as well as the C-terminus with its phosphorylation sites are not affecting the claudin segregation.

In a final approach, we generated Cldn2 chimeras that contain the ECLs (Cldn2$_{ECL10a}$) of Cldn10a (Figure 35A). The Cldn2 chimera was able to form contact enrichments and TJ strands, but it was also impaired in its meshwork formation compared to Cldn2 (Figure 23, Figure S12). This chimera should uncover a potential involvement of the ECLs in the claudins segregation. A Cldn3 chimera with the ECLs of Cldn15 was also generated, but it showed no TJ-like meshwork formation and was not used in co-overexpression studies. Interestingly, in contrast to the deletion mutants, the Cldn2$_{ECL10a}$ chimera led in co-overexpression with Cldn10a to a change from its segregating behavior to an intermixing pattern. Moreover, in co-overexpression with Cldn2, a shift from an intermixing into a more segregating phenotype could be observed (Figure 35B). A further performed Pearson correlation analysis supported these observations. In comparison to Cldn2, the Cldn2$_{ECL10a}$ chimera changed the Pearson value significantly when co-overexpressed with Cldn10a towards a higher intermixing value whereas co-overexpression with Cldn2 showed a decreased, more segregating Pearson value (Figure 35C). These results clearly underline the important role of the ECLs in the formation of the segregation.

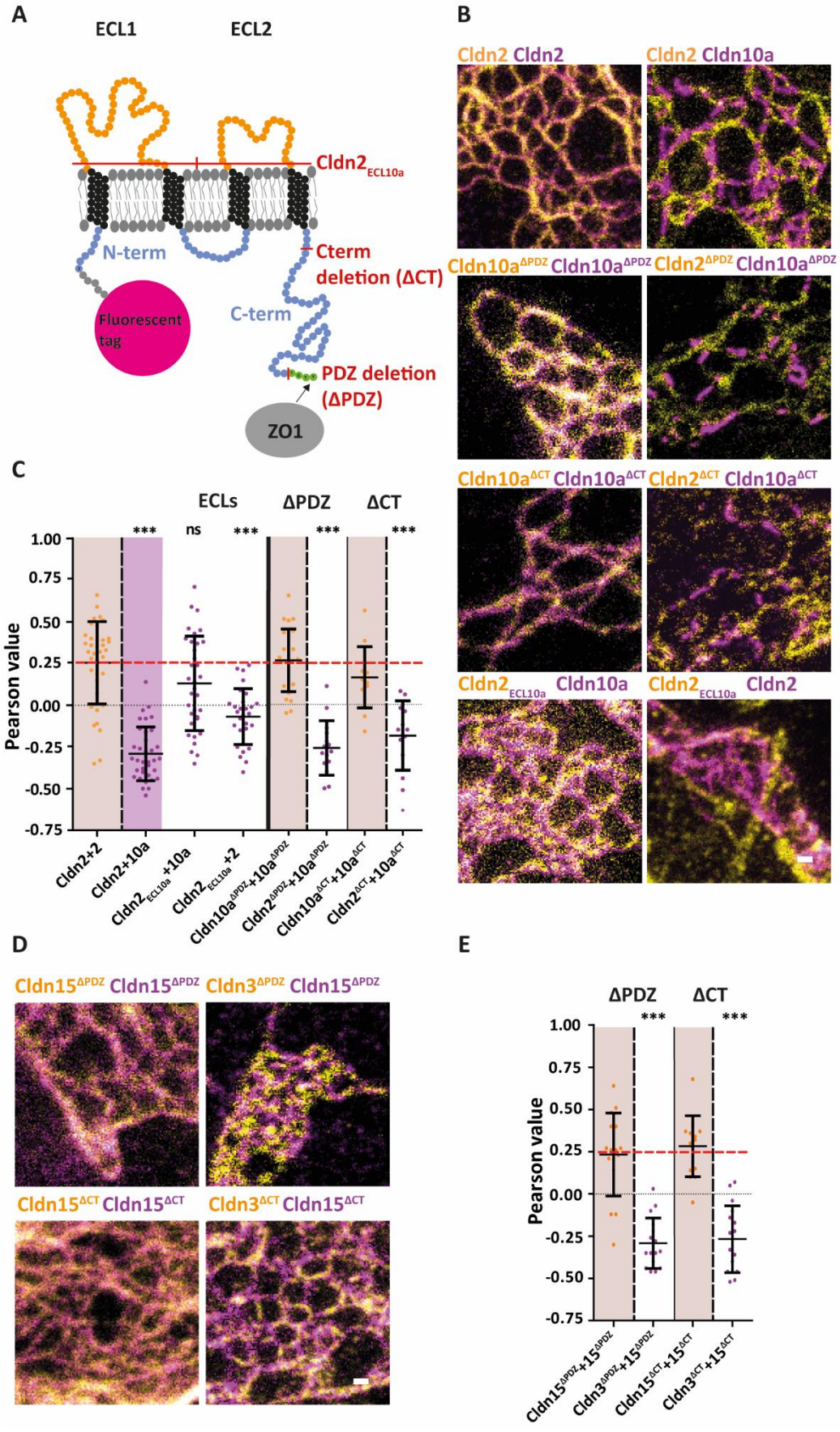
A
ECL1
ECL2
Cldn2ECL10a
N-term
Cterm deletion (ΔCT)
Fluorescent tag
C-term
PDZ deletion (ΔPDZ)
ZO1
B
Cldn2 Cldn2
Cldn2 Cldn10a
Cldn10aΔPDZ Cldn10aΔPDZ
Cldn2ΔPDZ Cldn10aΔPDZ
Cldn10aΔCT Cldn10aΔCT
Cldn2ΔCT Cldn10aΔCT
Cldn2ECL10a Cldn10a
Cldn2ECL10a Cldn2
C
ECLs
ΔPDZ
ΔCT
Pearson value
1.00
0.75
0.50
0.25
0.00
-0.25
-0.50
-0.75
***
ns
***
***
***
Cldn2+2
Cldn2+10a
Cldn2ECL10a+10a
Cldn2ECL10a+2
Cldn10aΔPDZ+10aΔPDZ
Cldn2ΔPDZ+10aΔPDZ
Cldn10aΔCT+10aΔCT
Cldn2ΔCT+10aΔCT
D
Cldn15ΔPDZ Cldn15ΔPDZ
Cldn3ΔPDZ Cldn15ΔPDZ
Cldn15ΔCT Cldn15ΔCT
Cldn3ΔCT Cldn15ΔCT
E
ΔPDZ
ΔCT
Pearson value
1.00
0.75
0.50
0.25
0.00
-0.25
-0.50
-0.75
***
***
Cldn15ΔPDZ+15ΔPDZ
Cldn3ΔPDZ+15ΔPDZ
Cldn15ΔCT+15ΔCT
Cldn3ΔCT+15ΔCT

Figure 35 Claudin segregation is conserved in the claudin extracellular loops, and it is unaffected by ZO1 binding or claudin C-terminal phosphorylation sites. For STED imaging, SNAP-tagged proteins were labeled with JF646-BG. EYFP-tagged claudins were labeled with an anti-GFP primary antibody and secondary antibody coupled to an AF594. **(A)** Scheme is illustrating the Cldn2, 3, 10a, and 15 PDZ-binding motif (ΔPDZ) and C-terminus deletion (ΔCT) mutants and the generated $Cldn2_{ECL10a}$ chimera. The mutations and the chimera sites are labeled in red. **(B)** Representative STED images of the TJ-like meshwork of SNAP-Cldn2 (yellow) with EYFP-Cldn2 (magenta) or with EYFP-Cldn10a (magenta), EYFP-$Cldn10a^{\Delta PDZ}$ (magenta) with SNAP-$Cldn2^{\Delta PDZ}$ (yellow) or with SNAP-$Cldn10a^{\Delta PDZ}$ (yellow), EYFP-$Cldn10a^{\Delta CT}$ (magenta) with SNAP-$Cldn2^{\Delta CT}$ (yellow) or with SNAP-$Cldn10a^{\Delta CT}$ (yellow) and $Cldn2_{ECL10a}$ (yellow) with EYFP-Cldn2 (magenta) or with EYFP-Cldn10a (magenta). **(C)** Pearson analysis of the combinations and some additional controls shown in (B). For the chimeras ≥ five TJ meshworks per experiment were imaged in four independent experiments, for the mutants ≥ five TJ meshworks per experiment were imaged in three independent experiments (chimeras: N≥20; mutants: N≥15). **(D)** Representative STED images of the TJ-like meshwork of EYFP-$Cldn15^{\Delta PDZ}$ (magenta) with SNAP-$Cldn15^{\Delta PDZ}$ (yellow) or SNAP-$Cldn3^{\Delta PDZ}$ (yellow) and of EYFP-$Cldn15^{\Delta CT}$ (magenta) with SNAP-$Cldn15^{\Delta CT}$ (yellow) or SNAP-$Cldn3^{\Delta CT}$ (yellow). **(E)** Pearson analysis of the combinations and controls shown in (D). For each combination, ≥ five TJ meshworks per experiment were imaged in three independent experiments (N≥15). Statistical analysis: mean ± SD; one-way ANOVA with Dunnett's multiple comparison test (C (ECLs: comparison to Cldn2 with Cldn2)) and Mann-Whitney test, two-tailed (C (ΔPDZ, ΔCT); E (ΔPDZ, ΔCT)); ns (not significant), *** p≤0.001%. Scale bars: 0.2 µm (B), (D).

Interestingly, acquired FRET data indicates a more complex situation since the chimera showed a slightly increased FRET signal in co-overexpression with Cldn2 and with Cldn10a compared to the intermixing Pearson of Cldn2 with Cldn2. Whether increased FRET signal is based on a potential interaction in *cis* mediated by the transmembrane domains must be figured out in further studies (Figure 36A). Additionally, performed co-culture experiments uncover that the $Cldn2_{ECL10a}$ chimera interacted with Cldn10a in *trans*, indicating that the chimera's ECLs are properly formed and can provide a functional *trans*-interaction (Figure 36B).

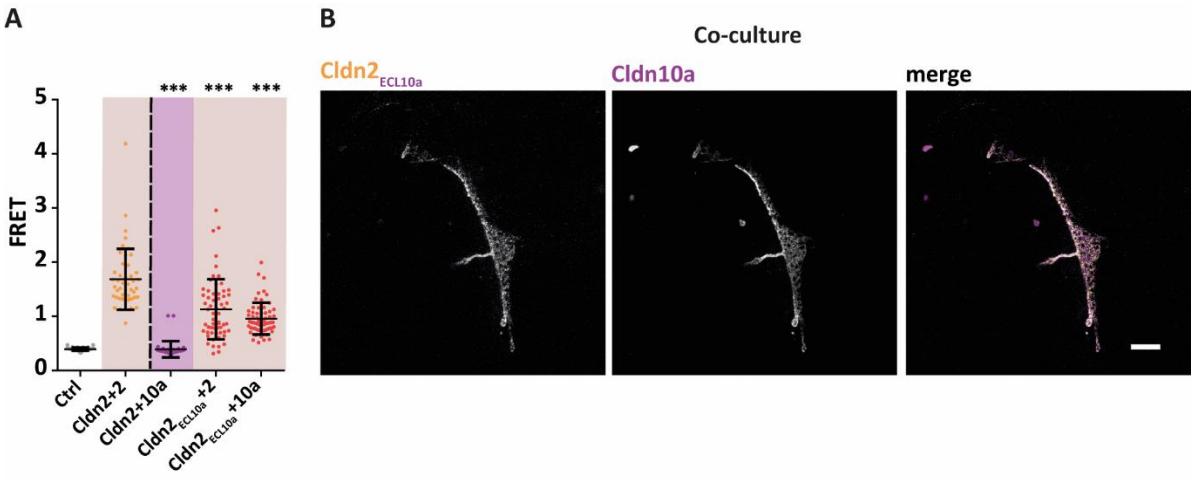

Figure 36 Cldn2$_{ECL10a}$ chimera interacts in *trans* and partially in *cis* with Cldn10a. (A) FRET analysis of co-expression of Trq2-Cldn2 with EYFP-Cldn2 (positive control) and EYFP-Cldn10a (negative control) and Trq2-Cldn2$_{ECL10a}$ with EYFP-Cldn2 and EYFP-Cldn10a in HEK293 cells. Single overexpression of Trq2-Cldn2 served as a negative control. For each combination ≥ 20 cell-cell contacts per experiment were imaged in three independent experiments (N≥60). **(B)** Co-culture of SNAP-Cldn2$_{ECL10a}$ (yellow; labeled with Atto590-BG) with EYFP-Cldn10a (magenta; enhanced with Atto647N) expressing COS-7 cells. Statistical analysis: mean ± SD; one-way ANOVA with Dunnett's multiple comparison test (comparison to Cldn2 with Cldn2); *** p≤0.001%. Scale bar: 0.5 µm.

4.4 Claudin segregation enables specific paracellular ion permeability

The manner of integration and the precise localization of channel-forming claudins in the TJ meshwork was unknown for a long time. Up to now, most of the proposed models were based on the solved crystal structure of Cldn15 and suppose that channel-forming claudins form several single ion specific pores in the TJ to equip it with ion permeability. We could show that the channel-forming claudins Cldn10a, 10b, and 15 integrate in the TJ meshwork by forming longer continuous strand parts that segregate from other claudins. The specific arrangement and organization of the segregation raised the question for its functional purpose. One very plausible explanation for the segregation is the necessity of forming a functional tetrameric channel as previously described and assumed by Suzuki et al.[87]. This functional channel cannot be formed when other claudins would incorporate into and disturb the organization of the channel claudin homo-tetramer. Additional to this hypothesis segregation could also increase the possibility for the channel-forming claudins to integrate into the TJ meshwork. Moreover, following the theory of the antiparallel claudin tetramer, we also raised the question whether segregation allows a more efficient ion flow

over the TJ by allowing ions of opposite charge to pass separately and simultaneously. A last and less conservative idea is that the segregation mediates the ion permeability directly at segregation points where strands from two different claudins are in contact challenging the proposed antiparallel tetramer as a functional channel unit.

In all so far performed studies, the influence of claudins on the TJ was investigated under KO, KD, mutagenesis, and overexpression conditions in epithelial cell lines that express several different claudins since the TJ research field was lacking a claudin-free epithelial cell line. In 2019 Otani et al. introduced a generated MDCKII quintuple claudin KO (MDCKII QKO) cell line which lacks the five claudins (Cldn1, 2, 3, 4, 7) that are usually most expressed in MDCKII[58]. The claudins were chosen based on an RNA seq data set of MDCKII cells from Shukla et al. in 2015[215]. Otani et al. demonstrate in FFEM that the MDCKII QKO cells did not form any TJ strands and that the paracellular ion permeability and macromolecule barrier were deregulated[58]. We wanted to use this so far unique claudin-free epithelial cell line to study the functional impact of single claudins and the segregated claudins pairs, Cldn2 and Cldn10a, as well as Cldn3 and Cldn15, on the paracellular permeability. First, we verified the complete KO of the five claudins by comparing ICC stainings of MDCKII QKO cells with wildtype MDCKII cells (Figure S13). We could not detect any specific localization of the five silenced claudins to the cell-cell contacts of MDCKII QKO cells. In contrast, the MDCKII control cells showed for each labeled claudin a clear signal at the apical contact side of the TJ. Next, we generated MDCKII QKO cells that stably expressed single FLAG-tagged claudins (FLAG-Cldn2, 3, 10a, 15) and combinations of FLAG-tagged segregating claudins (FLAG-Cldn2+Cldn10a and FLAG-Cldn3+Cldn15) by lentiviral transduction. We validated the infection's success, the claudin expression and correct localization by ICC staining of the stably claudin expressing MDCKII QKO cells (Figure 37A, B). All generated stable cell lines showed a precise apical-localization of the expressed FLAG-tagged claudin at the TJ in a homogeneously grown and polarized cell layer. As a side observation, we were able to observe an evident change in the membrane structure from a straighter cell-cell contact (MDCKII QKO) to a wrinkly cell-cell contact when a claudin was expressed (Figure 37C, D). Interestingly, in the confocal images of the FLAG-Cldn2+Cldn10a double expressing cells, claudin segregation seems to be already observable (Figure 37E). Moreover, it seems that Cldn10a is localized less continuously throughout the TJ than Cldn2 (Figure 37A, E).

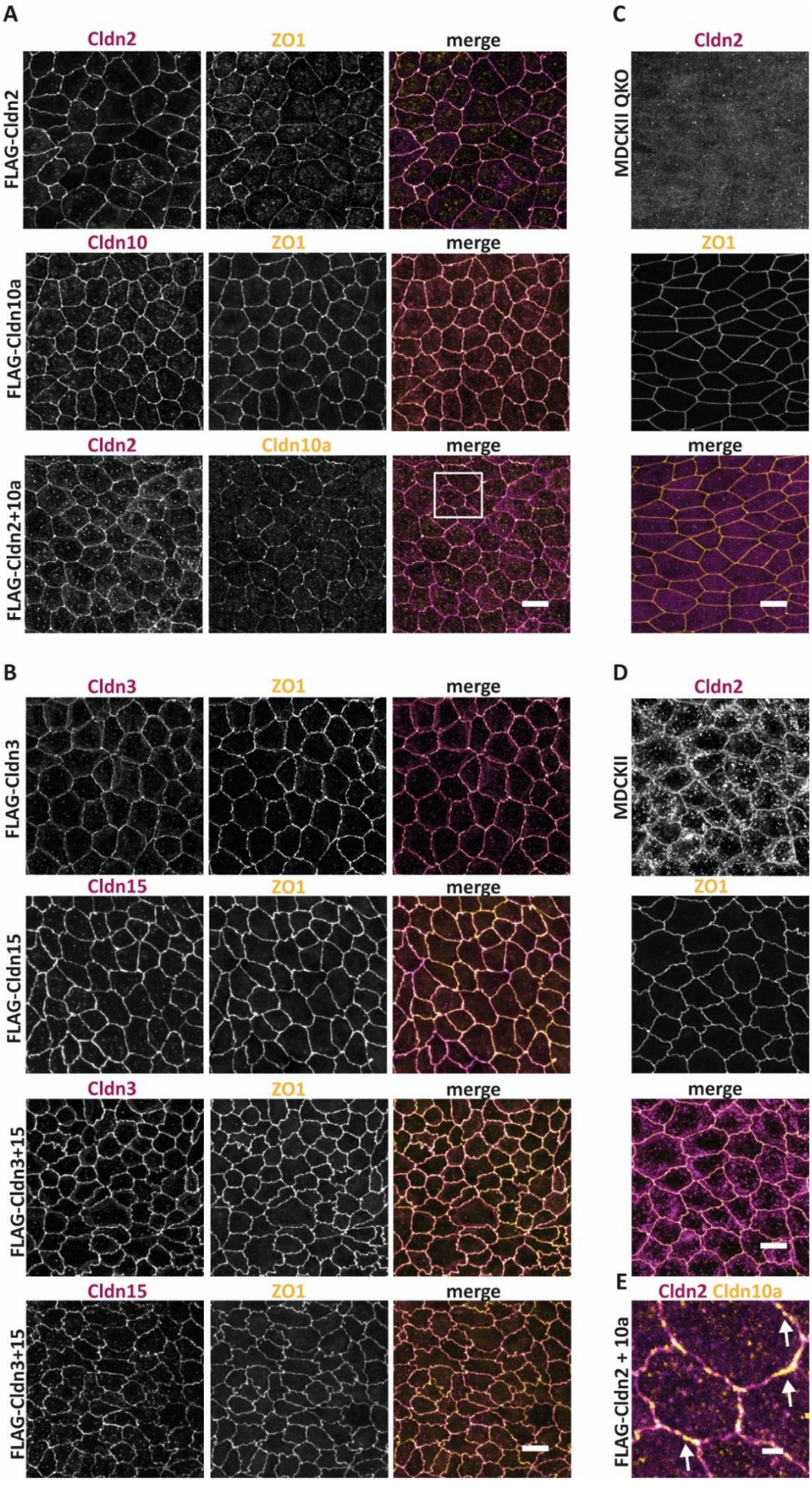
A
Cldn2
ZO1
merge
FLAG-Cldn2
Cldn10
ZO1
merge
FLAG-Cldn10a
Cldn2
Cldn10a
merge
FLAG-Cldn2+10a
C
Cldn2
MDCKII QKO
ZO1
merge
B
Cldn3
ZO1
merge
FLAG-Cldn3
Cldn15
ZO1
merge
FLAG-Cldn15
Cldn3
ZO1
merge
FLAG-Cldn3+15
Cldn15
ZO1
merge
FLAG-Cldn3+15
D
Cldn2
MDCKII
ZO1
merge
E
Cldn2 Cldn10a
FLAG-Cldn2 + 10a

Figure 37 Verification of the single and double claudins stably expressing MDCKII QKO cells. Secondary antibodies coupled to AF594 and Atto647N were used. **(A)** Confocal images of ICC labeled MDCKII QKO cells stably expressing FLAG-Cldn2, FLAG-Cldn10a and FLAG-Cldn2+10a. FLAG-Cldn2 expressing cells were stained with an anti-Cldn2 (magenta) primary antibody, FLAG-Cldn10a (magenta) expressing cells were stained with an anti-Cldn10 primary antibody. All single claudins expressing cells were additionally labeled for ZO1 (yellow) with an anti-ZO1 primary antibody. FLAG-Cldn2+Cldn10a expressing cells were stained with an anti-Cldn2 (magenta) and an anti-Cldn10 (yellow) primary antibody. **(B)** Confocal images of ICC labeled MDCKII QKO cells stably expressing FLAG-Cldn3, FLAG-Cldn15 and FLAG-Cldn3+Cldn15. FLAG-Cldn3 expressing cells were stained with an anti-Cldn3 (magenta) primary antibody, FLAG-Cldn15 (magenta) expressing cells were stained with an anti-Cldn15 primary antibody. FLAG-Cldn3+Cldn15 expressing cells were stained either with an anti-Cldn3 (magenta) or an anti-Cldn15 (magenta) primary antibody. All FLAG-Cldn3 and/or FLAG-Cldn15 expressing cells were additionally labeled for ZO1 (yellow) with an anti-ZO1 primary antibody. **(C)** Confocal images of ICC labeled MDCKII QKO cells. Cells were stained with an anti-Cldn2 (magenta) and an anti-ZO1 (yellow) primary antibody. **(D)** Confocal images of ICC labeled MDCKII cells. Cells were stained with an anti-Cldn2 (magenta) and an anti-ZO1 (yellow) primary antibody. **(E)** Magnification from FLAG-Cldn2+Cldn10a expressing MDCKII QKO cells from (A), discontinuous Cldn10a TJ parts are pointed out by white arrows. Scale bars: 10 µm (A-D), 2 µm (magnification in E).

To investigate the impact of single claudins and segregating claudins on the TJ ion permeability and its integrity, we measured the electrophysiological properties including the transepithelial resistance (TER), the dilution potential for estimating the relative permeability of the epithelial monolayer for sodium and chloride and the fluorescein flux for the generated stable cell lines with an Ussing-chamber application (detailed description in 3.7). MDCKII cells that endogenously highly express the predicted sodium channel-forming Cldn2 and MDCKII QKO cells served as controls. For every measurement, immunostainings were used to check the cell homogeneity. Whole-cell lysates served as control for claudins' total expression level (Figure S14A-D). Noteworthy, the total expression level of Cldn2 in FLAG-Cldn2 expressing cells and in FLAG-Cldn2 and FLAG-Cldn10a double expressing cells was similar or even slightly increased to Cldn2 levels in MDCKII cells (Figure S14A). In contrast, the amount of Cldn2 in the TJ was decreased by 30-50% when comparing the intensity of Cldn2 in stably FLAG-Cldn2 expressing cells with MDCKII cells (Figure S14E, F). FLAG-Cldn3 expressing cells showed a higher total expression compared to MDCKII cells (Figure S14B). The total expression level of Cldn10 seemed to stay constant among single FLAG-Cldn10a expressing cells and FLAG-Cldn2 and FLAG-Cldn10a double expressing cells

(Figure S14C). Similar levels could be also observed for singly expressed FLAG-CLdn15 and when co-expressed with FLAG-Cldn3 (Figure S14D).

The electrophysiological measurements revealed that the expression of Cldn3 in the MDCKII QKO increases the TER of the epithelial cell layer drastically and significantly (350 Ohm*cm^2) when compared to MDCKII QKO cells (15 Ohm*cm^2) and MDCKII cells (38 Ohm*cm^2). However, MDCKII QKO cells expressing FLAG-Cldn2 (28 Ohm*cm^2), FLAG-Cldn10a (25 Ohm*cm^2), FLAG-Cldn15 (28 Ohm*cm^2), FLAG-Cldn2+Cldn10a (26 Ohm*cm^2) and FLAG-Cldn3+Cldn15 (41 Ohm*cm^2) showed only a slightly, but significantly increased TER compared to MDCKII QKO cells (Figure 38A, B).

The dilution potential measurements showed that the FLAG-Cldn2 and FLAG-Cldn15 expressing cells have a significantly increased permeability for sodium ions (Figure 38C) and FLAG-Cldn10a expressing cells for chloride ions (Figure 38D) confirming published data that propose their ion specific channel functions. Nevertheless, the permeability for sodium seems to be less specific compared to MDCKII cells which showed a higher Na/Cl ratio compared to MDCKII QKO sT FLAG-Cldn2 or FLAG-Cldn15 cells. FLAG-Cldn3 expressing cells showed no permeability for ions neither for sodium nor for chloride (Figure 38C, D), supporting the assumption that Cldn3 is a predominantly barrier-forming claudin. Cells that co-express FLAG-Cldn2+Cldn10a showed lower dilution potential values and intermediate permeability for sodium or chloride (Figure 38C, D). Whereas FLAG-Cldn3+Cldn15 expressing cells have a highly increased permeability for sodium ions (Figure 38C, D), clearly higher compared to single FLAG-Cldn15 expressing cells.

Additional performed fluorescein (332.31 Da) flux measurements showed that FLAG-Cldn2, FLAG-Cldn10a, FLAG-Cldn15 as well as FLAG-Cldn2+Cldn10a co-expressing cells have a higher macromolecule flux compared to the MDCKII cells indicating a potential difference in the TJ integrity. Nevertheless, all cell lines showed a significant lower flux than MDCKII QKO cells. This increased fluorescein flux could not be observed for FLAG-Cldn3 expressing cells as well as not for FLAG-Cldn3+Cldn15 co-expressing cells (Figure 38E, F). Both cell lines show a permeability for fluorescein that was comparable to MDCKII cells indicating a potential influence of Cldn3 on the whole TJ integrity and considering the higher sodium permeability of FLAG-Cldn3+Cldn15 cells on the specificity of the ion permeability.

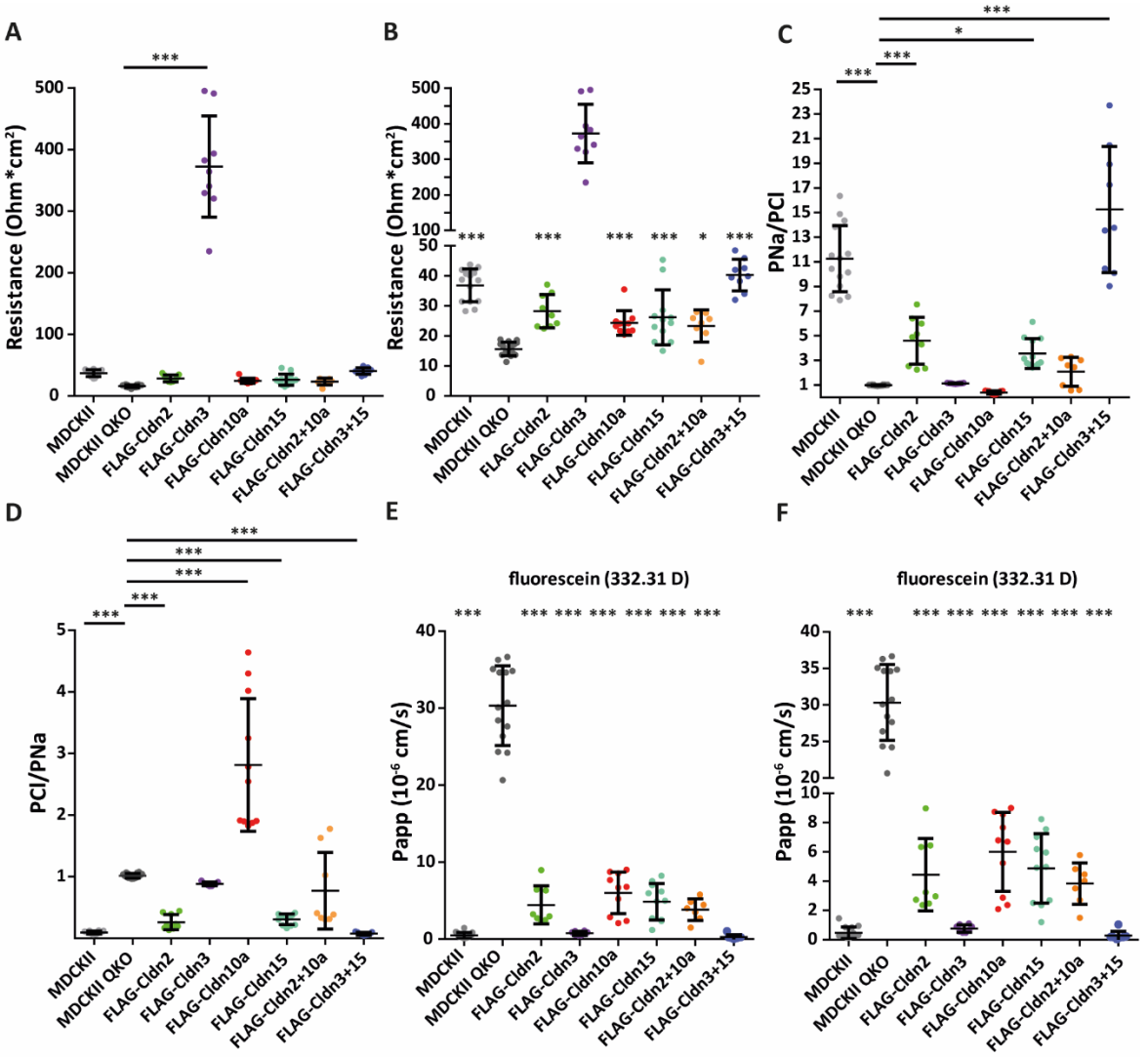

Figure 38 Dilution potential measurements of MDCKII QKO cells expressing single claudins and segregating claudin pairs revealed a compensatory and an enhanced effect on the ion permeability. The different cell lines are labeled as following: MDCKII (grey), MDCKII QKO (dark grey), MDCKII QKO stably expressing (sT) FLAG-Cldn2 (green), MDCKII QKO sT FLAG-Cldn3 (magenta), MDCKII QKO sT FLAG-Cldn10a (red), MDCKII QKO sT FLAG-Cldn15 (mint green), MDCKII QKO sT FLAG-Cldn2+Cldn10a (orange) and MDCKII QKO sT FLAG-Cldn3+Cldn15 (blue). The electrophysiological measurements were performed with an Ussing-chamber. In every experiment, firstly the TER was measured, secondly the dilution potential and lastly the fluorescein flux. In (A-F) each dot represents one filter. **(A)** Shown are the results of the transepithelial resistance (TER) measurements in Ohm/cm^2. **(B)** Shown are the same results from (A) with a separation of the y-axis into two segments. **(C)** Shown are the results of the dilution potential measurement plotted for Na/Cl. **(D)** Shown are the results for the dilution potential measurement plotted for Cl/Na. **(E)** Shown are the fluorescein (332.31 Da) flux measurements. The paracellular permeability (Papp) is plotted in the unit of 10^{-6} cm/s. **(F)** Shown are the same results from (E) with a separation of the y-axis into two segments. For all measurements, at least eight filters from three independent experiments were measured (N≥8). Statistics: mean ± SD; one-way ANOVA with Dunnett's multiple comparison test (A-F (comparison to MDCKII QKO); ns (not significant), * p≤0.05%, ** p≤0.01%, *** p≤0.001%.

The obtained results from the electrophysiological measurements get even more clear when comparing the calculated absolute ion permeabilities of the different cell lines (Figure 39). The absolute permeabilities show very conclusively that the described channel-forming claudins Cldn2, 10a and 15 form functional ion channels when expressed alone in epithelial cells indicated by their higher permeability for sodium or chloride ions. Whereas Cldn3 acts as a barrier-forming claudin by sealing the paracellular cleft against sodium and chloride ions. Moreover, we could observe that the segregating Cldn2 and Cldn10a in co-overexpression keep their ion specificity and compensated each other's ion permeability in the measurement potentially by forming independent functional channels in the TJ meshwork. The MDCKII QKO cells gives comparable values for the absolute permeability for sodium and chloride but in this case, it is not because of the formation of specific ion channels but more the circumstance that these cells lack the TJ resulting in an uncontrolled flux of sodium and chloride ions through the paracellular cleft. In contrast, the co-overexpression of Cldn3 with Cldn15 resulted in a higher specificity in sodium permeability compared to single expressed sodium-forming channel claudins Cldn2 and Cldn15. The measured levels were comparable to the values of the MDCKII cells indicating that the expression of a barrier-forming claudin and the formed segregating meshwork potentially provides a higher ion specificity. This is also partially reflected by the higher fluorescein flux of Cldn2 or Cldn15 compared to co-expressed Cldn3 and Cldn15 (Figure 38E, F).

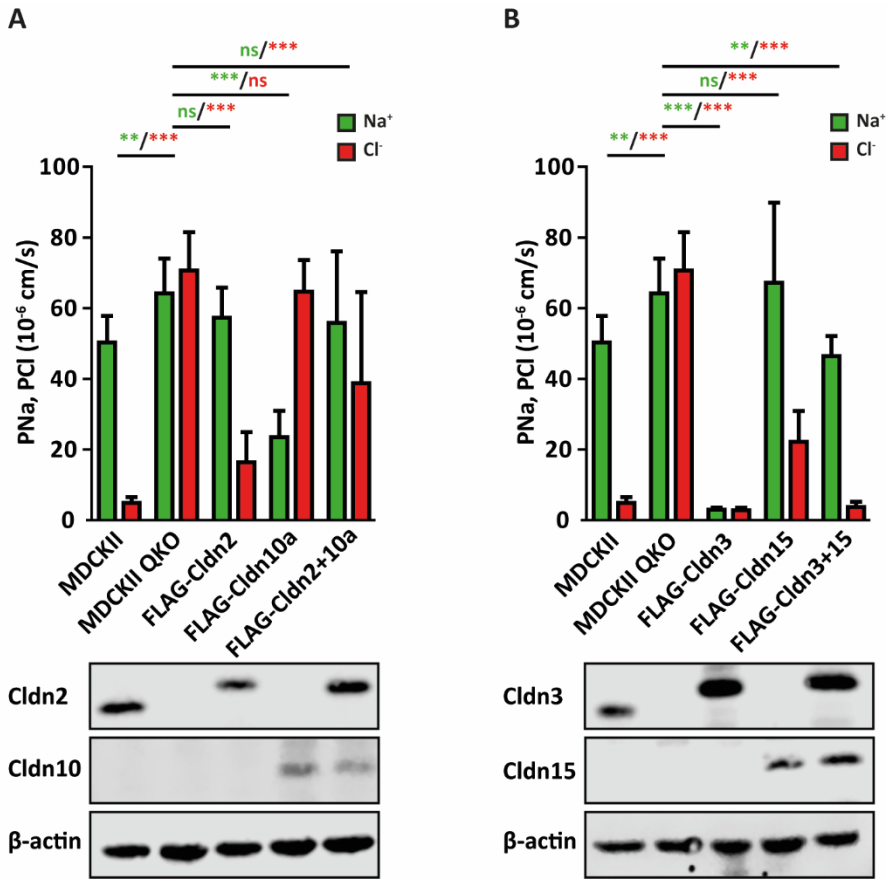

Figure 39 Absolute permeability measurements of MDCKII QKO cells expressing single claudins and segregating claudin pairs. The absolute permeability was calculated from the relative permeability Na/Cl, Cl/Na and the TER shown in Figure 38. For the calculation the Kimizuka-Koketsu equation (Equation 15) was used (described in 3.7.1). Shown are the calculated absolute permeabilities (Papp is plotted in the unit of 10^{-6} cm/s) for sodium (green bars) or chloride (red bars) in **(A)** for MDCKII, MDCKII QKO, MDCKII QKO sT FLAG-Cldn2, MDCKII QKO sT FLAG-Cldn10a and MDCKII QKO sT FLAG Cldn2+Cldn10a and in **(B)** for MDCKII, MDCKII QKO, MDCKII QKO sT FLAG-Cldn3, MDCKII QKO sT FLAG-Cldn15 and MDCKII QKO sT FLAG Cldn3+Cldn15. The expression of the reconstituted claudins was validated by immunoblotting and is representatively shown in (A) and (B). The different claudins were labeled with anti-Cldn2 and anti-Cldn10 antibodies in (A) and anti-Cldn3 and anti-Cldn15 antibodies in (B) and detected at ~22-25 kDa. Lysates from MDCKII and MDCKII QKO were used as controls. Endogenous expression levels for Cldn10 and Cldn15 in MDCKII could not be detected since MDCKII cells do not expressed them endogenously at high levels. β-actin (42 kDa) was used as loading control. For all measurements, at least eight filters from three independent experiments were measured (N≥8). Statistics: mean ± SD; one-way ANOVA with Dunnett's multiple comparison test (A, B (comparison to MDCKII QKO); ns (not significant), * p≤0.05%, ** p≤0.01%, *** p≤0.001%.

5 Discussion

In the present work, we demonstrate the significant impact of STED microscopy on the TJ research by resolving the TJ meshwork structure and revealing novel insights in the claudin nanoscale organization. We identified with an automated analysis over all mammalian claudins significant differences in their meshwork forming ability and their meshwork nanostructure, resulting in the definition of three different distinct classes. Furthermore, we unraveled five different interaction patterns that claudins can undergo when co-overexpressed in fibroblasts: intermixing, integration, induction, segregation, and exclusion. We could verify the claudin segregation as a novel interaction pattern for the channel-forming claudins Cldn10a, 10b, and 15 on endogenous levels and determine at least partially its structural foundation in the extracellular loops. Functional analysis of the segregating claudins in genome-engineered claudin-free epithelial cells led us to conclude that nano-segregation is a conserved and indispensable mechanism to provide functional ion channels providing the possibility of a constant ion permeability over the TJ meshwork independent of the TJ meshwork complexity.

5.1 Nanoscale imaging of the TJ meshwork

Over the last fifty years, the tight junctional nanostructure was the subject of several research studies. These studies were insightful, but still left many open questions regarding the organization and dynamic within the TJ meshwork[3,29,216]. After discovering the claudins[31,74] and their ability to form fibril-like structures in fibroblasts[57] it was clarified that mainly proteins and not lipids form the TJ strands[3]. In the following years, understanding the differences among claudins and their functional purpose for different tissue, organs, and the whole organism was the main focus[69,76,132,217]. With the discovery of paracellular channel properties of a specific subset of claudins and their involvement in the tissue specific ion homeostasis[20,210], and the following identification of specific sites in their ECLs that are responsible for the channel specificity[19,218], the organization of the claudins in the TJ got more into focus[87,98,107]. Labeling problems and diffraction-limited fluorescence microscopy made it so far very challenging to study single or multiple claudins on the nanoscale within the TJ meshwork. Performed SRM of the TJ on endogenous level by antibody labeling[180] and overexpression of single claudins in fibroblasts[23,179] indicated its great potential for the TJ

research field. However, these studies were mainly unable to reveal the complex nano-organization of the TJ.

5.1.1 STED resolves the TJ meshwork structure in fixed and living samples

We demonstrate that advanced STED microscopy can solve the described imaging limitations of electron microscopy (no multi-protein labeling, low throughput, weak antibody labeling) and conventional fluorescence light microscopy (diffraction limited resolution). Combined with systems in which we were able to change the TJ orientation from an axial direction with a lower z-resolution to a lateral with a higher xy-resolution (Figure 20A, B) this enabled us to image the TJ meshwork in tissue (Figure 20C) and in overexpression (Figure 20D) at the nanoscale. The potential to study the nanostructure of a TJ meshwork formed by overexpressed claudin was already shown by Kaufmann et al. in 2012 (SMLM)[179] and Van Itallie et al. in 2016 (SIM)[23]. SIM and SMLM rely both on additional image processing that increases the probability of creating post-imaging artifacts due to noise amplification, blowing up of structures and loss of information because of excessive smoothening. In our study, we showed that STED microscopy can resolve the TJ meshwork structure in an artifact-free and raw manner without further imaging processing needed. Compared to SIM, which offers a resolution in biological samples of ~100 nm, STED allows imaging at a higher resolution of below 50 nm[177,178]. It resolves single strands and meshes not only in the isolated meshwork periphery as previously shown[22,23] but also in the meshwork center (Figure 20D). Moreover, STED microscopy provides the possibility to investigate the TJ meshwork structure in a higher throughput than SMLM[177,178], giving a direct verification of labeling efficiency and sample quality which allows a fast optimization of labeling and imaging conditions. Enhancing of the fluorescent tags with organic fluorophores coupled to small nanobodies and the SNAP- and Halo-tag system resulted in a STED resolution of 60 nm in fixed and 70 nm in living samples (Figure 20 F,G) similar to Bottanelli et al. in 2016[186]. The resolution difference between fixed and live derives from increased background noise and the TJ meshwork dynamic.

On endogenous level, we could resolve the nanostructure of the TJ meshwork in murine tissue with fluorescence microscopy for the first time. Schlingmann et al. in 2016 were able to image endogenous Cldn5 and ZO1 in alveolar endothelial cells with dSTORM.

Nevertheless, the staining showed a very punctual pattern[180] which was not comparable to the in STED observed strands. To determine if this observation shows the real nano-organization or the punctual pattern results from a labeling problem, it needs further verification with an optimized staining protocol or endogenous labeling. In our example, the labeled Cldn3 in the murine duodenum appeared more as single strands than a complete meshwork. This observation was not surprising since, in the duodenum, mainly Cldn2, Cldn3, and Cldn15 are expressed[76] which we found to be segregated from each other in the later experiments (Figure 27). The seemingly lower resolution compared to the imaged TJ meshworks in overexpression could be due to the greater distance between the CS and the TJ in the 10-20 µm thick tissue sections.

The achieved resolution of ~70 nm in live imaging gave us the possibility to image dynamics (Figure 20E) and importantly to test the influence of fixatives on the TJ meshwork nanostructure (Figure 21A). The dynamics of single strands in TJ meshwork were already investigated in a couple of studies[22,23]. However, in these studies the analyzed strands were always located at the more peripheral areas of the TJ meshwork. Since it was shown that newly synthesized claudins are attached to the TJ's peripheral areas[182] it is at least debatable that the dynamic of peripheral claudin strands is similar to those in the more central areas of the meshwork. In this study, we could demonstrate that STED can resolve meshwork structure also in the denser regions in living samples. We could observe dynamic events, including mesh fusions and strand disruptions (Figure 20E), indicating that dynamics also occur in the inner TJ meshwork. Yet, the slower image acquisition compared to SIM, photobleaching, and loss of z-focus did not enable us to analyze these observations more quantitatively and must be improved to be fully capable of resolving different dynamics among claudins and the dynamics of multiple claudins in a TJ meshwork. One possibility to solve this problem might be the use of another STED system. The STEDYCon from Abberior Instruments, which is equipped with photosensitive ABDs and can be used together with hardware auto-focus systems which are currently not compatible with the in this study used Leica SP8 TCS STED system. Additionally, brighter fluorophores (e.g., SiR-D12[219]) could provide the needed photostability and brightness for more prolonged live imaging in single. With a suitable second fluorophore (e.g., JF552[220] or Atto590[186]) that can also be depleted with the 775 nm laser, dual color might even be possible.

5.1.2 Automated TJ-like meshwork analysis of all meshwork forming claudins revealed different claudin specific properties

The fibroblast overexpression system for reconstituting TJ-like meshwork is a tool that is commonly used since its first discovery in 1998[57]. The significant advantage of the fibroblast system is the TJ-free and claudin-free background. Moreover, claudin overexpression leads to extensive TJ-like meshwork formation in the lateral direction between the overlapping cells. It allows the investigation of interactions between claudins or other TJ proteins in FRET, co-culture, and FFEM[66,97,98,133,173,175]. So far, nobody systematically compared the nanostructure of the TJ-like meshwork of all claudins. A first step in this direction was done by Kaufmann et al. in 2012. They identified with SMLM that two claudins, Cldn3 and Cldn5, form different meshworks with two distinct mesh sizes in HEK cells[179]. One major disadvantage of HEK cells is the high expression of endogenous occludin, a TAMP known to influence the TJ meshwork structure of claudins[66]. Moreover, only fixed samples were imaged without further verifying the potential fixative's impact on the TJ meshwork nanostructure.

For our screen, we used COS-7 fibroblasts that do not contain endogenously expressed TJ structure proteins. SNAP-tagged claudins labeled with novel organic fluorophores (JF646)[206] allowed us to validate the influence of different fixatives[171] and the fluorescent-tag on the TJ nanostructure (Figure 21). We could show that only the fixation with 4% PFA/sucrose preserved the TJ nanostructure completely (Figure 21A). Regarding the fluorescent tag's potential influence, we could not observe any difference when comparing N-terminally, C-terminally tagged, and untagged human Cldn3 in fixed samples with SNAP-tagged Cldn3 in live-STED imaging. Even the TJ meshwork of a murine Cldn3 showed a similar meshwork structure, indicating that the nanostructure might be conserved over different species (Figure 21B, C). But still, it cannot be excluded that this might be different for other claudins. Nevertheless, N-terminally, and C-terminally tagged human Cldn1 also showed no difference in their nanostructure.

It was surprising that the N-terminally and C-terminally tagged claudins did not reveal any difference since it was shown that endogenous ZO1, which is expressed in COS-7 fibroblasts (Figure 22B, C), can bind the last amino acids of their C-terminus and that this link can change the TJ meshwork dynamic when compared to claudin mutants that lack the

ability to bind to ZO1[23]. Our results lead to the assumption that the binding to ZO1 in fibroblasts is most likely of minor importance for the meshwork structure itself. Endogenous ZO1 staining for different N-terminally tagged claudins revealed no specificity of ZO1 for a certain claudin. Also, a specific localization of ZO1 along the TJ strands was not observable (Figure 22C). If this was due to insufficient antibody labeling or the different fibroblast background cannot be excluded and must be investigated. An additional actin staining showed no accumulation of the endogenous actin at the TJ meshwork located ZO1. Only around the meshwork actin could be detected (Figure S3). This observation goes in line with Van Itallie et al. 2016 but speaks against the general assumption of the function of ZO proteins as a direct linker between TJ and actin. It might be that ZO1, when it is bound to claudins, does not interact that strongly with actin anymore, supporting the recently submitted paper in bioRxiv showing that the actin-belt is primarily anchored to nectins at the AJ so below the TJ[54]. Lastly, claudin ΔPDZ mutants that lack the ability to bind to endogenously expressed ZO1 were able to form TJ-like meshwork (Figure 35). One very plausible explanation is also that ZO1 is not needed for the formation of TJ-like meshwork by claudins in our overexpression system and the high expression of claudins is sufficient to for strands and meshwork without the need of ZO1 for portioning and localization at the site of the TJ.

For the TJ-like meshwork analysis in the claudin screen, we focused in the first step on the general meshwork features and not on the exact numbers regarding mesh size and diameters. The exciting discovery that not all claudins can form strands indicates that some claudins contain structural features that allow them to create strands. In contrast, claudins that do not form meshwork potentially need an already preformed structure or other TJ proteins to incorporate in the TJ or start initial strand formation (Figure 23). Remarkably all non-classic claudins (Figure S2) cannot form TJ-like meshwork, providing a hint towards a structurally conserved pattern that enables the strand formation. Although, we used for every claudin the same amount of plasmid DNA for transfection, the same CMV-promoter and same linker between fluorescent protein and claudin, we cannot fully exclude that not all claudins were expressed at the same level and that these differences might influence single claudins regarding their ability to accumulate and polymerize. Among the tested claudins, six were murine derived and not human-based (Cldn13, 14, 18a, 18b, 26, 27). It

cannot be excluded that this might affect meshwork formation, but this is highly unlikely as claudin structures are highly conserved across species.

In several FFEM images of different claudins from previous studies, it appeared to us that channel-forming claudins tended to create more dot-wise strand patterns. In contrast, the barrier-forming claudins form straight strands without any gaps[173,175]. We asked ourselves if this difference might be visible in the TJ meshwork structure in STED. Comparing the channel-forming claudins with barrier-forming claudins, a difference in their meshwork forming ability was not detectable. In general, this goes in line with a study by Inai et al. in 2010 that claimed that there is no correlation between claudin channel function and the pattern of the protoplasmic and exoplasmic face in FFEM[175].

The automated analysis based on Haralick Texture Features[192] led to some false classification regarding meshwork forming (Cldn3 and Cldn10b) and non-meshwork forming claudins (Cldn12, 18a, 22, and 27) (Figure S4). Reasons for these incorrect classifications were misinterpreted ER tubule patterns and dense claudin accumulations that did not form strands between the overlaps. Since the Haralick Texture Features compare the homogeneity and difference among different imaged meshworks, it might be not specific enough to differentiate between very similar structures in terms of intensity-based gradients. In these unclear cases, a visual interpretation and already published data about the meshwork forming abilities of single claudins[175,179] were considered to distinguish between meshwork forming and non-meshwork forming claudins. Whether these false classifications can be avoided by fine-tuning the analysis, e.g., by increasing the training sample size must be tested.

By analyzing all TJ-like meshworks with a combination of Haralick Texture Features and basic image segmentation, we could reveal that there are mainly three different classes of meshworks (Figure 24). A clear structure-function correlation between the claudins in the first class (A) and second class (B) could not be observed. Both types contain channel-forming and barrier-forming claudins. Interestingly, the described class C contains exclusively barrier-forming claudins[32] that show a common characteristic: creating a very dense meshwork structure indicating the formation of multiple in parallel arranged strands with a distance below the resolution limit of the used STED microscope. In general, the appearance of parallel strands with less branching points is in the literature already connected to the

formation of a tightly sealing TJ[110,183]. For Cldn11, it could be already shown that it forms parallel strands in Sertoli cells, CNS myelin, and cells of the cochlea, generating a paracellular barrier essential for spermatogenesis[110,221], normal CNS function[222], and hearing[223].

With the performed screen of the mammalian claudin meshwork nano-organization, we provide not only for the first time a general overview over the 26 mammalian claudins regarding their abilities to form TJ-like meshwork but also automated classification of claudins based on their meshwork structure. We identified that some claudins lack the capability of forming meshwork and that most of these belong to the non-classic claudins. Nevertheless, since this analysis was based on meshwork structures up to the resolution limit of STED microscopy, it might be possible that specific patterns of certain claudins were still “invisible” and below the resolution of STED microscopy and that the classification must be refined with SRM techniques that deliver sub-STED resolution.

Overall, the analysis delivers several new insights that might be very useful for further studies focusing on the differences among the claudins to uncover the structural regions that might be important for claudin strand formation. The automated analysis could be a valuable tool for further studies to analyze changes in the TJ meshwork structure due to claudin mutants or the implementation of other factors and proteins to the environmental system.

5.1.3 Five different claudin-claudin interaction patterns

Multiple different claudins build the TJ meshwork *in vivo*. The composition differs between different cell types, tissues, and organs. Only in a few exceptions is it assumed that single claudins form the TJ (e.g., Cldn11 in CNS myelin[110]). The interaction of different claudins in the TJ was part of several studies (Figure 41)[66,107]. Often overexpression in fibroblast cell lines or HEK cells was used, and the grade of interaction was measured by FRET[66,97], co-culture approaches[173], or yeast-to-hybrid experiments[119,130]. A systematic investigation of claudin-claudin interactions on the nanoscale level in the TJ meshwork was not done yet. Gold labeling of claudins in FFEM sections only allows a rough determination of the different claudins' localization in the TJ meshwork.

To investigate the claudin-claudin interaction at the nanoscale, we co-overexpressed different claudins in fibroblasts and analyzed the formed TJ-like meshworks. Based on the current knowledge of 26 mammalian claudins and four more physiological relevant isoforms (Cldn10a/b, 11a/b, 18a/b, 19a/b) there are in total 435 binary combinations possible. To narrow down our investigation, we focused mainly on the well-studied and widely expressed, Cldn3, a classic barrier-forming claudin, and Cldn2, a cation channel-forming claudin. In combination with the discussed data on the ability of single claudins to form TJ-like meshwork, we could define in claudin co-overexpression five different interaction types: intermixing, integration, induction, segregation, and exclusion (Figure 25, Figure 40). The interaction types of integration, induction, and exclusion seem to be patterns of specific claudins. Still, it might be possible that other claudins can also undergo these interaction types. On the other hand, intermixing/segregation seems to correlate with barrier-/channel-forming properties. However, some exceptional claudins show the other three interaction types.

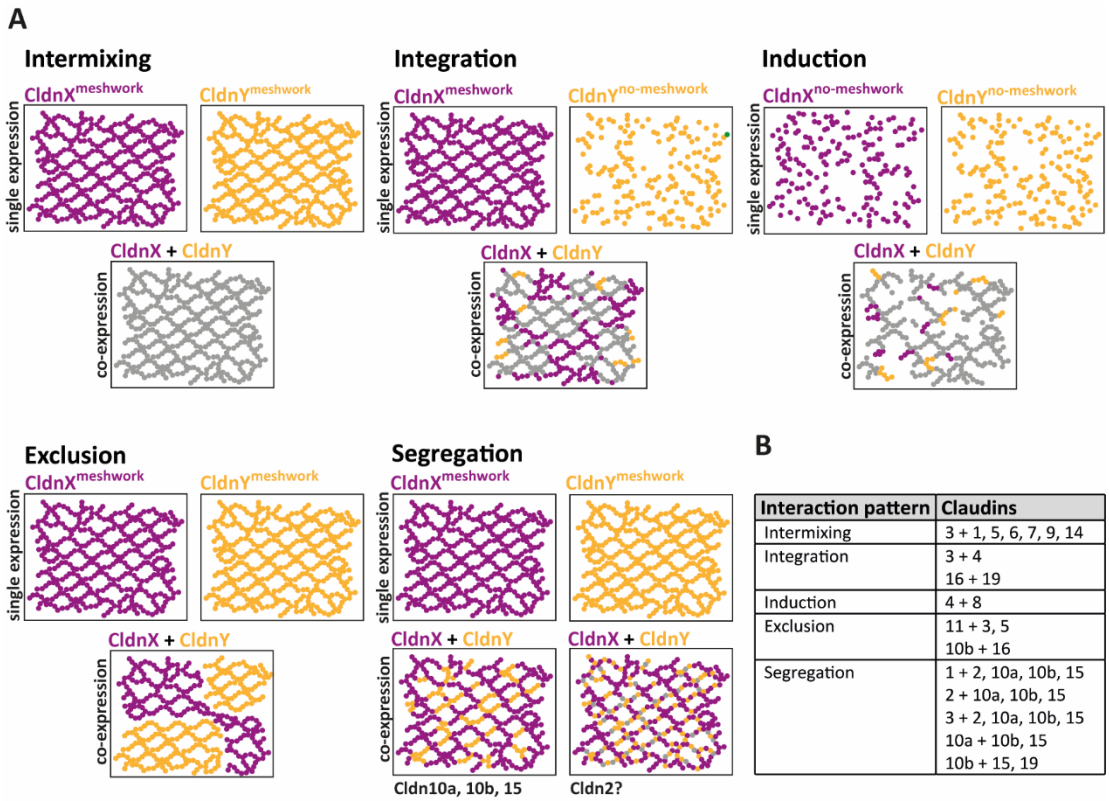

B

Interaction pattern	Claudins
Intermixing	3 + 1, 5, 6, 7, 9, 14
Integration	3 + 4 16 + 19
Induction	4 + 8
Exclusion	11 + 3, 5 10b + 16
Segregation	1 + 2, 10a, 10b, 15 2 + 10a, 10b, 15 3 + 2, 10a, 10b, 15 10a + 10b, 15 10b + 15, 19

Figure 40 Overview of the observed claudin-claudin organization patterns in co-overexpression in fibroblasts. (A) Schematic illustration of the five organization patterns: intermixing, integration, induction, exclusion, and segregation. For each pattern, the meshwork forming abilities of the expressed claudins are shown in magenta and yellow. Intermixing of claudins is labeled in grey. Segregation of Cldn2 with barrier-forming Cldn1 and Cldn3 seems to differ from the channel-forming Cldn10a, 10b and 15 and is potentially segregating on a smaller scale. **(B)** Classification of all in this study observed claudin combinations into the five defined claudin-claudin organization patterns.

Cldn3 and Cldn4 form the integration type. Both claudins are classified as predominantly barrier-forming claudins[32]. Although these two claudins share around 67% of their AA sequence (ECL1: 94%; ECL2: 68%)[105], we could detect that only Cldn3 and not Cldn4 can form TJ-like meshwork in a single expression (Figure 23). Interestingly, in co-overexpression, Cldn4 starts to form meshwork with Cldn3 by integrating itself in the Cldn3 meshwork (Figure 25). Cldn4 does not completely intermix with the Cldn3 meshwork as indicated by the lower Pearson value (Figure S6) and forms in co-overexpression also small independent strand parts. FRET and co-culture data suggest that the interaction of Cldn3 and Cldn4 is most likely based on a compatibility in *cis* (Figure 41)[107]. Potentially, this *cis*-interaction site allows Cldn4 to integrate in the Cldn3 TJ-like meshwork. That Cldn3 and Cldn4 differ in their function for the TJ could be already described. It was shown that Cldn4 has, compared to other claudins, a higher dynamic at the TJ and that the treatment of epithelial cells with IFN-γ or TNF-α can displace Cldn4 partially from the TJ into a highly mobile lateral located sub-pool. It could be shown that this displacement is the result of an increased expression of claudins incompatible with Cldn4 (e.g., Cldn2)[224,225]. Our observation combined with the described higher dynamic of Cldn4 and its competitive behavior to other claudins[224,225] points in the direction of a different and more dynamically regulated interaction compared to Cldn3. It is known that the ECLs play a vital role in the TJ strand formation[98]. Due to the high sequence similarity of Cldn3 and Cldn4 in both ECLs the amino acids responsible for the significant difference in their strand polymerization should be possible to determine in a site-directed mutagenesis approach. Such an approach can be highly valuable for identifying the structural properties that are needed for strand polymerization.

Supporting the different interaction types of Cldn4, we could show that co-overexpressed Cldn4 and Cldn8 form together TJ-like meshwork. In this case, two non-meshwork but individual barrier-forming claudins (Figure 23) start to form a meshwork together in an inductive manner (Figure 25). This observation provides new insights to the described and controversially debated anion channel formation by Cldn4 and Cldn8, supporting their by yeast-to-hybrid experiments demonstrated interaction[119]. One idea to clarify the Cldn4 and Cldn8 anion channel debate is to stably co-overexpress Cldn4 and Cldn8 in MDCKII QKO cells and measure their dilution potential and compare it to single Cldn4 or Cldn8 expressing MDCKII QKO cells. Furthermore, any physiological relevance of Cldn4 and 8 interaction should be demonstrated by staining both claudins in relevant tissues (e.g., distal tubule and collecting duct in the adult mammalian renal tubule)[81].

Another interesting discussion in this context are the proposed anion channel-forming properties of Cldn17. Cldn17 is described to localize within the TJ in the murine nephron in regions that are known for a high paracellular permeability (PCT and TAL). Further, it was shown that overexpression of Cldn17 in MDCKC7 cells resulted in a significantly decreased TER and an increased relative permeability for chloride ions whereas a knockdown of endogenous Cldn17 in LLC-PK_1 cells led to a lowered preference for chloride ions[117,118]. Cldn17 is phylogenetically very close to Cldn8 (Figure S2). Like Cldn8, it cannot form meshwork when it is expressed alone in fibroblasts and stands thereby in contrast to the other channel-forming claudins (Figure 23). It might be that Cldn17, comparable to Cldn4 and Cldn8, needs another yet unidentified claudin or TAMP protein for its TJ localization and strand formation. In preliminary experiments, we could not find another claudin that induces strand formation of Cldn17 (data not shown). Similarly, also Cldn16 shows no meshwork formation in the overexpression screening. It is proposed that Cldn16 needs the interaction with Cldn19 to form a paracellular cation channel[130]. We could confirm that Cldn16 and Cldn19 can form TJ-like meshwork (Figure 30) in an integrative manner. It might be possible that the integration and induction pattern displays another way to form paracellular ion channels which differs from the homomeric Cldn2 and the group of Cldn10a, 10b, and 15. The advantage of selective heteromeric channel formation should be investigated in further details. One hypothesis to start with could be that such a mechanism provides higher flexibility to react rapidly to environmental changes due to a more dynamically regulated and inducible channel formation.

The exclusion pattern is defined by a complete lack of interaction of the co-overexpressed claudins. We could show that exclusion occurred in co-overexpression of Cldn11 with Cldn3 (Figure 25). Cldn11 is expressed in the human body in three specific areas that are known to tightly regulate the ion homeostasis: Sertoli cells in the testis, basal cells in the cochlea, and myelin-forming cells in the brain[32]. It was shown that a KO of Cldn11 leads to congenital infertility and deafness in mice[108,223,226,227]. It is also described to be expressed in the endothelial cells of the blood-brain barrier (BBB) where it, based on confocal images, seems to exclude itself from Cldn5[228]. FFEM images of the TJ in these specific areas show the formation of multiple parallel strands in close distance to each other (~10 nm) below the resolution limit of STED. In overexpression, Cldn11 shows very dense structures with single strands in the peripheral areas (Figure 23). These observed structures are most likely consisting of multiple Cldn11 strands comparable to the FFEM images in tissue. Whether Cldn11 excludes from other claudins because of a potentially strong self-association reflecting its crucial function in forming a tight seal or whether it is based on a structural incompatibility with other claudins due to its exclusive expression in specific tissue regions must be investigated. Additional to Cldn11, a sort of claudin exclusion could also be observed for Cldn16 and Cldn10b in co-overexpression (Figure 30). The exclusion of these both claudins differs from the Cldn11 exclusion since Cldn16 does not form meshwork in single overexpression. This incompatibility of Cldn10b and Cldn16 could be already observed in FRET and co-culture experiments nicely correlates with the observed mosaic expression of Cldn16 and Cldn19 on the one hand, and Cldn10b on the other hand in the TAL of the kidney where the exclusive expression plays an essential role for the ion homeostasis[133] (Figure 30).

The intermixing phenotype could be observed primarily for Cldn3 together with other barrier-forming claudins. The interaction of Cldn3 in *cis* and *trans* with other barrier-forming claudins was already demonstrated in several publications[105,107,173]. A generalization that barrier-forming claudins (with exception of Cldn11) intermix with other barrier-forming claudins cannot be made yet since it was shown in FFEM that the barrier-forming Cldn14 separates from the barrier claudins Cldn6 and Cldn9 in the endogenous TJ of the inner hair cells. Nevertheless, it was proposed that other junctional factors (β-catenin and $p120^{ctn}$) and not the claudin itself provoke this local separation[183]. The intermixing of Cldn6, 9 and 14 with Cldn3 supports this and speaks for at least comparable *cis*- and *trans*-interactions. A simple co-overexpression approach in fibroblasts could enlighten the interaction pattern of Cldn14

with Cldn6 and Cldn9 in the absence of other TJ factors. Alternatively, it could be possible that Cldn14 has a so far uncharacterized ion channel function as it is evolutionary close to Cldn2 (Figure S2). Stable expression of Cldn14 in MDCKII QKO cells should be considered as an approach to understand the function of Cldn14 alone and in combination with Cldn6 and Cldn9.

5.2 Segregation of Cldn10a, 10b, and 15 as a fundamental ion channel organization principle

One of the TJ's essential functions is the specific paracellular ion permeability that keeps different tissues in homeostasis[2,3,29]. A loss of this function can have a severe outcome for the tissue and the whole organism, e.g., anhidrosis, familial hypomagnesemia, hypercalciuria, nephrocalcinosis, non-syndromic deafness[76,81,229,230]. To further understand how channel-forming claudins provide this ion-specific permeability to the TJ, previous studies focused on the role of the different structural parts of the claudins. Especially the ECLs, the TMs, and the C-terminus were investigated. Mutagenesis and claudin pore-blocking studies revealed that the ECL1 plays a crucial role in forming a specific ion pore[123,124]. The crystal structure of Cldn15[86] and a successive polymer model that proposes an anti-parallel double-row Cldn15 arrangement[87,101], support these studies. Homology modeling suggests that this arrangement also counts for other claudins, but the paracellular center differs between barrier and channel claudins[176]. Considering the different grades of complexity of the TJ-meshwork[231] the question arises how channel-forming claudins are arranged in this multi-protein meshwork. Do channel-forming claudins interact with specific TJ proteins to get incorporated in the TJ or do they integrate themselves as single pores in the TJ meshwork? So far acquired data on *cis*- and *trans*-interactions is mainly based on FRET, and co-culture experiments performed in many different cell lines and spread over several individual studies (Figure 41). Also, considering the already mentioned 435 possibilities for claudin-claudin interactions the amount of data is very limited (Figure 41)[107].

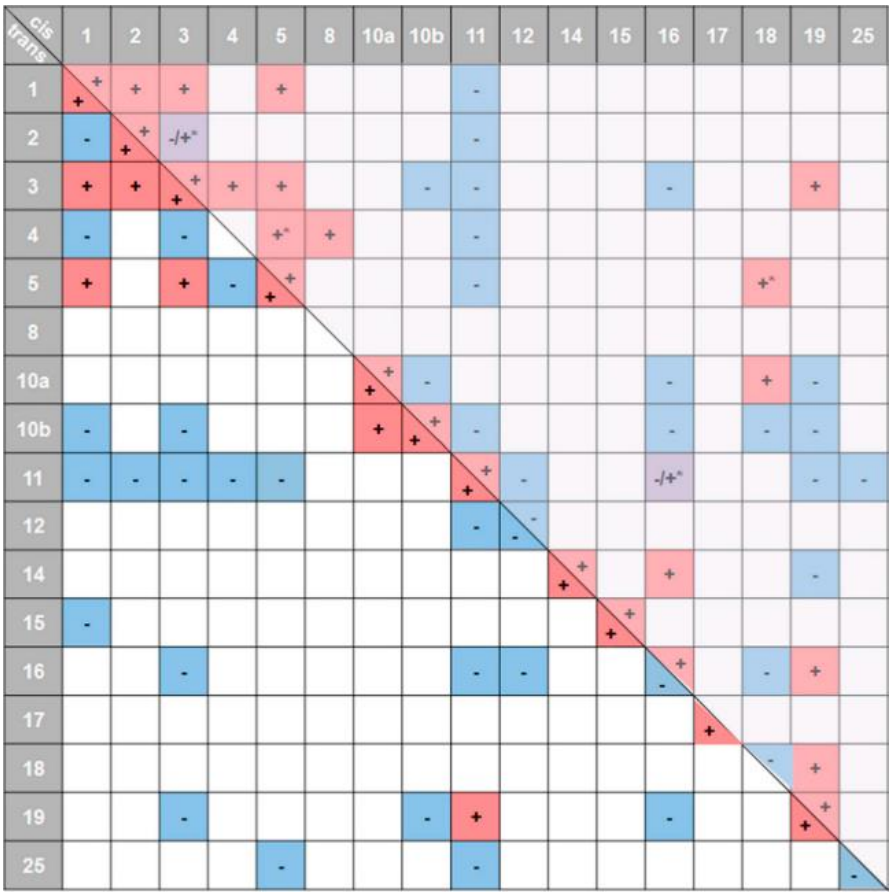

Figure 41 Overview of the in literature described *cis*- and *trans*-interactions between mammalian claudins. The illustration was taken from Piontek et al. (2020). The different claudins are labeled with their numbers. "+" indicates that an interaction was observed. "-" indicates that an interaction could not be observed. "*" indicates ambiguous results[107].

For the channel-forming claudins it could be shown that Cldn10a and Cldn10b show only in *trans* heterophilic compatibility and in *cis* incompatibility[97] and Cldn10b is incompatible with Cldn3[176] and Cldn19[133]. For Cldn15, only an incompatibility with Cldn1 in *trans* could be observed[175]. Interestingly, compatibility studies of Cldn2 showed a distinct *cis*-interaction with Cldn1 and *trans* with Cldn3[173] pointing out a potential difference in their heterophilic interaction ability and channel formation compared to Cldn10a, 10b and 15. We could show that Cldn10a, 10b, and 15 segregate from Cldn3 and Cldn1 in co-overexpression (Figure 25). Cldn2 also seems to segregate from Cldn1 and Cldn3, but the typical alternating strand pattern could not be observed, indicating a potential difference in its interaction behavior (Figure 25). Interestingly, Cldn2 segregates also from Cldn10a, 10b, and 15 in co-overexpression (Figure 28). Moreover, the co-overexpression of Cldn10a, 10b, and 15 with each other led in every combination to claudin segregation (Figure S7). These results indicate

that segregation seems to be a specific organizational pattern for channel-forming claudins. Additional FRET data of Cldn10a with Cldn2 (Figure 28) and Cldn15 with Cldn3 (Figure 26) did not show any FRET signal supporting a missing interaction between the segregating claudins. On the other hand, Cldn2 shows a strong FRET signal with Cldn1 (Figure 28) and a slightly increased FRET with Cldn3 compared to FRET of Cldn15 with Cldn3 (Figure 26). Whether the interaction of Cldn2 with Cldn3 in *trans* and Cldn1 in *cis* leads to another kind of segregation that might be below our STED resolution must be investigated in further experiments. Potentially, MINFLUX microscopy with a lateral resolution down to 5 nm[232] could solve this question. The difference of Cldn2 compared to the segregation pattern of Cldn10a, 10b, and 15 might be explainable due to the high sequence similarity between the latter three (Figure S2). They may share a feature in their sequence that allows them to arrange themselves in different ways. A comparison of the AA sequences, computational modelling and site-directed mutagenesis could help to understand how these different interactions of Cldn2 to Cldn1 and Cldn3 compared to Cldn10a, 10b and 15 can occur on molecular and structural level.

On endogenous level we could confirm the segregation for Cldn2 and Cldn10a, and for Cldn3 and Cldn15 in regions where paracellular ion permeability is of high importance, the murine proximal tubule of the kidney and the murine duodenum. Segregation of Cldn2 and Cldn10a in the proximal tubule was easier to resolve because of the less complex TJ[121] (Figure 29). Besides this, Cldn2 and Cldn10a are also exclusively expressed in this part of the kidney[81]. Some reports also claim the appearance of Cldn17 in the proximal tubule[117], but this must be further investigated and the antibody specificity should be verified. Interestingly, the observed segregation of Cldn2 and Cldn10a in the proximal tubule is very much comparable to the observation in the fibroblasts. In both systems Cldn2 and Cldn10a form alternating extended strand parts. The segregation of Cldn3 and Cldn15 was more challenging to visualize since the intestinal TJ is formed by multiple claudins and show a higher degree of strand complexity in a very dense area (~500 nm in vertical diameter)[205]. Nevertheless, in the areas of the cryo-sections where the TJ was oriented in the lateral direction, the segregation could be clearly detected.

For Cldn10b, an endogenous verification of the segregation was not performed. A potential region to look for Cldn10b segregation would be the TAL in the kidney. In the TAL

the TJ meshwork is more complex compared to the TJ in the proximal tubule[231], and next to Cldn10b, other claudins including Cldn3, Cldn16, and Cldn19 are expressed[81]. The TAL in the mammalian kidney tubules drives the paracellular Na^+, $Ca^{2+,}$ and Mg^{2+} reabsorption. It is described that Cldn10b is essential for the reabsorption of monovalent ions, whereas Cldn16 and Cldn19 form a channel for divalent ions. Milatz et al. demonstrated in 2017 that Cldn3, Cldn16 and Cldn19 separate from Cldn10b in a mosaic expression manner[133]. In our co-overexpression experiments, Cldn10b forms either meshwork in a segregating (with Cldn3, Cldn19) or more exclusive way (with Cldn16) going in line with the described mosaic expression in the TAL[133]. Potentially, the exclusion and not segregation of Cldn10b and Cldn16 reflects the inability of Cldn16 to form meshwork in single overexpression. This assumption would also explain the observed segregation of Cldn10b from Cldn16 and Cldn19 in triple overexpression where Cldn16 can form strands with Cldn19.

It was demonstrated that Cldn3 and Cldn10b are also expressed together in sweat glands cells. Interestingly, a recently discovered Cldn10b inherited autosomal recessive mutation ($10b^{N48K}$) causes a disbalanced ion homeostasis in the sweat glands that leads to severe heat tolerance problems [70,82,210]. Co-expression of $Cldn10b^{N48K}$ with Cldn3 shows a loss of segregation, and with Cldn10b, a loss of self-association (Figure S9). This lack of interaction is also reflected in its complete inability to form meshwork in single expression. The findings suggest that these claudin-claudin interactions are indispensable for the needed paracellular ion permeability to regulate the ion homeostasis in the sweat glands.

Hence, we could describe nano-segregation as a novel organization principle for channel-forming claudins in the TJ meshwork, providing new insights to the claudin channel formation; we decided to investigate the segregation on structural and functional level in more detail focusing on different described extrinsic and intrinsic factors that are known to influence claudin localization to the TJ and claudin function.

5.2.1 Not extrinsic factors but intrinsic elements of the claudin extracellular loops determine claudin segregation

The TJ's initial formation between epithelial cells and the continuous addition of new claudin strands depends on different extrinsic factors. It was recently shown that the cytosolic scaffolding protein ZO1 can partition claudins via a phase separation-based

mechanism and facilitates claudin polymerization at the apical side of epithelial cells[42]. Still, it is unclear whether ZO1 partitions all claudins in the same manner or whether it prefers specific claudin subtypes. Our data on the localization of ZO1 at single expressed claudins in fibroblasts (Figure 22) suggests an equal binding of ZO1 to barrier- and channel-forming claudins. Moreover, ZO1 also localizes in the segregating claudin meshwork without demonstrating a clear preference for a claudin subtype (Figure 34). In epithelial cells, the deletion of the PDZ-binding motif of claudins leads to a loss of the connection between claudins and ZO1[23] thereby causing claudin mislocalization[214]. Moreover, the deletion of the PDZ-binding motif leads to an increased meshwork dynamic in fibroblasts[23], identifying the linkage to ZO1 as a stabilizing factor for the TJ meshwork. Co-expression of the segregating claudin pairs (Cldn2 and Cldn10a, Cldn3 and Cldn15) as PDZ-binding motifs deletion mutants (ΔPDZ) does not affect the segregation (Figure 35). But as a general impression, less meshwork formation was observable, indicating an effect of ZO1 on the claudin polymerization abilities but not directly on the structure of the segregating meshwork. Since ZO1 is described to enhance the TJ meshwork dynamic it might be interesting to compare the strand dynamics of a segregating meshwork between WT claudins and the ΔPDZ mutants.

Phosphorylation at the claudin C-terminus is known to control claudin localization, endocytosis and function[64,93]. Besides, phosphorylation at the C-terminus (S408) of occludin, another transmembrane protein, showed changes in its interaction behavior with ZO1 and specific claudins (Cldn1, Cldn2)[233]. By co-overexpressing segregating claudins that lacked their C-terminus (ΔCT) we could show that C-terminal phosphorylation is not essential for claudin segregation (Figure 35). Nevertheless, it might be possible that comparable to a missing PDZ-binding motif the C-terminal phosphorylation influences the dynamic of the single claudin strands.

Another extrinsic factor that is described to affect the claudin organization is cholesterol. A recently published study by Shigetomi et al. shows that KO of α-catenin leads to a loss of AJs in an epithelial cell line[61]. This loss causes a change in the plasma membrane lipid composition and leads to an increased endocytosis of claudins. The addition of cholesterol to the KO cells restored the TJ formation indicating that cholesterol has a vital role in the TJ formation and for claudins. We could show that neither the depletion of

plasma membrane cholesterol with 25 mM methyl-β-cyclodextrin (MβCD) nor the reduction of cholesterol with statins changed the claudin segregation (Figure 33). On the other hand, we could observe an increased appearance of claudin containing vesicles at the TJ meshwork potentially reflecting increased endocytosis of claudins. Shigetomi et al. demonstrated that 25 mM MβCD leads to a reduction of claudin-3 from the TJ. This reduction got even stronger when a higher concentration of MβCD was applied (up to 75 mM). In our hands, the fibroblast cells suffered with concentrations over 25 mM and showed increased cell death, making it impossible to test how the TJ was affected by stronger cholesterol depletion. Another reason for the still intact TJ-like meshwork could also be the fibroblast system itself and its different membrane orientation, the absence of polarity and the unphysiological high claudin expression. Nevertheless, a strikingly increased endocytosis of one of the segregating claudins or a change of its segregation pattern could not be observed, eliminating the potential role of cholesterol in the organization of claudin segregation.

By using a point mutated Cldn2 (Cldn2^{I66C}) combined with a reactive cysteine reagent (MTSET) it could be demonstrated that the Cldn2 channel function for paracellular flux of sodium ions can be rapidly blocked[123,124]. To test whether the inhibition of ion flux through the claudin channel affects the segregation, we overexpressed Cldn2^{I66C} alone and in combination with Cldn10a and blocked the Cldn2 pore by applying MTSET. In conclusion, we could not observe any differences compared to the unmutated Cldn2 in single expression nor regarding segregation (Figure 32, Figure S11). Moreover, recently published data of a Cldn2 and Cldn10a inducible MDCKI cell line suggest that a functional block of the Cldn2 pore by MTSET has no impact on the channel function of co-expressed Cldn10a supporting the functional independence of their ion channels[234], which may be the results of the maintained segregation.

Extrinsic factors play essential roles in the localization and function of claudins. However, we could show that the in this study tested extrinsic factors did not affect the claudin segregation, indicating a structurally encoded mechanism that leads to the segregating strands. In the first place, we wondered if the observed alternating strand pattern underlies a specific strand stability for each of the segregating claudins. Using different plasmid ratios, we could confirm a correlation between claudin strand length and their expression levels (Figure 31). These results indicate that the claudin strand lengths in a

segregating meshwork are not based on inherent stability but most likely depend on the total claudin expression level. The strand length measurements over whole proximal tubules also showed a high variability without indicating a specific strand length for Cldn2 or Cldn10a. Whether this observation is a result of different expression levels or whether other cellular or extracellular factors in the kidney are responsible must be clearified. Notably, the segregation itself was not changed over the different expression ratios pointing out that the segregation itself is not expression level dependent.

While the C-terminus including the PDZ-binding motif mediates intracellular interactions and signaling, the ECLs of claudins have been described as important structures for the *trans*-interaction, the *cis*-interaction, and the formation of the ion-specific channel[107]. Even single point mutations in the ECLs can affect claudin interactions[235] (Figure S9) and lead to mis-localization and malfunction (e.g., Cldn10b^{N48K} in the sweat glands of HELIX syndrome patients[82]). The ECLs of Cldn10a, 10b, and 15 differ in multiple regions from Cldn2 or Cldn3[79,107]. The exchange of the ECLs among different claudins can change their interaction specificity without losing the ability to integrate in the TJ meshwork (e.g., Cldn10a and Cldn10b)[97]. Reflecting the importance of the ECLs we could demonstrate that a Cldn2 chimera consisting of the N-terminus, internal loop, C-terminus, and TMs from Cldn2 and the ECLs of Cldn10a can form strand-like structures (Figure S12), indicating a functional *trans*-interaction and partially functional *cis*-interaction. However, the claudin chimera could not form extended TJ-like meshwork reflecting a structural problem to form multiple strand interconnections. One explanation could be the previously described importance of the first transmembrane domain (TM_1) of claudins in the *cis*-interaction between claudins[97,98]. Remarkably, when co-overexpressed with Cldn2 a change from its previous intermixing pattern to a more segregating pattern could be observed, whereas co-overexpression with Cldn10a lead to a switch from segregation to an intermixing meshwork (Figure 35). A reason for the less strong phenotype lays probably in the observed disability of the chimera to form extended TJ meshworks and in the most likely not fully functional *cis*-interaction. Also, the imaged meshwork structure appeared more unstructured (Figure 35). Nevertheless, co-culture data supports the interaction of the chimera with Cldn10a in *trans*. Additional acquired FRET data indicates that not only the ECLs but also the TMs seem to play a role in the interaction (Figure 36). Whether the interaction is based on the TM1 which is proposed to be involved in the *cis*-interaction[97,98] or on another TM, must be investigated in further

studies on the claudin structure. Such an approach will be a very tedious task due to the three-dimensional arrangement and the indicated more complex interplay of several different structural elements. From our results we can conclude that the ECLs are the most important regions for claudin segregation but for an optimal claudin arrangement the TMs might be also required.

An interesting topic to follow would be to investigate the connection site between the segregating strands. Novel insights would help to understand the dynamics at this connection site and its potential involvement in the paracellular permeability. One hypothesis might be that the claudins are held close together or even enriched at these points of extreme membrane curvature due to the tension and the membrane proximity. It might be also possible that claudin polymerization produces membrane proximity that could lead to a positive feedback for more polymerization, independent of claudin compatibility. Since the role of lipids at the TJ is not fully clear yet, and it is assumed that the lipid environment plays a role in the TJ function, a potential involvement of lipids by creating local lipid imbalances or high curvature at these contact points should be considered. Another TJ protein's involvement seems concerning the TJ-free fibroblast system unlikely. The latter point would also go in line with our data that suggest no *cis*- or *trans*-interaction between the segregating claudins. One possibility to understand the dynamics at these contact points is live imaging of the segregated meshworks in super-resolution and carefully analyzing strand dynamics, membrane tension and local lipid accumulation.

5.2.2 Nanoscale claudin segregation is an indispensable nanoscale organization principle for constant ion permeability over the TJ

For a long time, the TJ research field was lacking an *in vitro* cell system that allows the investigation of the function and properties of single claudins. Until 2019 all acquired data regarding claudin channel specificity and organization was based on the expression or deletion of claudins in cell lines that endogenously express several other claudins. Our data suggest that claudins can interact in many ways with each other. How these interactions play a role in the claudin function and how this can influence the TJ properties is unclear. The problem of unknown claudin interactions affecting functional data was solved by Otani et al. in 2019[58]. Otani et al. created a genetically modified MDCKII cell line (MDCKII QKO)[58] lacking

five claudins that are usually most expressed in these cells[215] leading to a complete loss of the formation of a TJ meshwork[58]. We used the MDCKII QKO cells (Figure S13) and reconstituted single claudin and segregating claudin pairs to examine to what extent the segregation influences the specific ion permeability by measuring their electrophysiological properties.

Performed ICC staining of the stably expressing cells suggested that the single expressed FLAG-Cldn2, 3, 10a, 15 and the co-expressed FLAG-Cldn2 and FLAG-Cldn10a as well as FLAG-Cldn3 and FLAG-Cldn15 are all localizing at the apical contact of adjacent cells and form a TJ (Figure 37). For Cldn2 and Cldn10a expressing cells, the segregation was already partially visible in confocal microscopy images. Interestingly, the strands of Cldn2 looked in the co-expression along the TJ more homogeneously distributed than Cldn10a, which showed a less prominent TJ localization indicating already a potential claudin incompatibility. Noteworthy, all stably expressing cell lines showed an increase in wrinkles at the cell-cell contact compared to the MDCKII QKO cells, that appeared to have a straighter TJ (Figure 37C, D). The same phenotype could be already observed in MDCKII cells lacking TOCA-1, an F-BAR protein that localizes via its binding to ZO1 at the TJ and provides tight junctional membrane tension[236]. The missing linkage of ZO1 and TOCA-1 to the TJ due to the lack of claudins might explain these two very similar phenotypes whereas the reconstitution of single claudins and TJ meshwork formation led again to an increased membrane tension.

The performed dilution potential measurements revealed that the single claudin expressing cells behaved according to their literature described barrier or channel function. The MDCKII and the MDCKII QKO cells also delivered comparable results to the already shown data by Otani et al. in 2019. Regarding the TER, Cldn3 expressing cells showed a substantial increase to ~350 $\Omega*cm^2$ demonstrating its tightening properties (Figure 38A, B). The TER of Cldn2 (28 $\Omega*cm^2$), Cldn10a (26 $\Omega*cm^2$), Cldn15 (28 $\Omega*cm^2$) as well as of Cldn2 and Cldn10a (25 $\Omega*cm^2$) expressing cells was in between TER values of the MDCKII (38 $\Omega*cm^2$) and the QKO (~15 $\Omega*cm^2$) cells (Figure 38A, B) confirming that channel claudins in general decrease the TER[125]. The higher TER of the MDCKII cells (compared to the channel-expressing cells) is probably a result of the endogenous expression of tightening claudins (e.g., Cldn1, 3, 4, 7). This assumption could be partially confirmed by MDCKII QKO cells co-expressing Cldn15 and Cldn3 that result in a higher TER (41 Ω*cm2) comparable to MDCKII

cells. Nevertheless, compared to Cldn3 expressing cells the lower TER reflects the strong effect of Cldn2 in MDCKII and Cldn15 in the co-expressing cells on the TJ barrier, providing it with leaky properties[125]. If the total claudin expression and the ratio might influence the TER was not tested in this study. But it might be possible that a higher expression of Cldn3 in the Cldn3 and Cldn15 expressing cells compared to the Cldn15 expression is the main reason for the higher TER. That Cldn3 expression leads to a higher TER was already shown by Milatz et al. in 2010 in Cldn3 overexpression studies in MDCKII cells[105].

The leaky properties of the channel-forming claudins are also reflected in the fluorescein flux measurements. Cells expressing channel-forming claudins show a significantly higher flux compared to MDCKII and Cldn3 expressing cells. Nevertheless, it was significantly lower compared to MDCKII QKO cells (Figure 38). The reason for the higher fluorescein flux of the channel-expressing MDCKII QKO cells compared to MDCKII cells is most likely linked to the endogenous expression of barrier-forming claudins in MDCKII cells. Still, it could be also possible that the higher total expression of all expressed claudins (Cldn1, 2, 3, 4, 7) in MDCKII cells compared to the single channel-forming claudin expressing MDCKII QKO cells leads to a tighter and less leaky TJ. On the other hand, going in line with the live imaging data of the high dynamic of Cldn2 that shows several strand breaks, annealing and re-annealing processes[23] it might be also possible that lower TJ integrity is a consequence from a higher strand dynamic of channel-forming claudins. The reduced tight junctional appearance of Cldn2 in FLAG-Cldn2 expressing MDCKII QKO cells compared to endogenously Cldn2 expressing MDCKII cells (Figure S14) supports this hypothesis of a less stable TJ meshwork when it is only formed by Cldn2. Live-STED imaging of different barrier- and channel-forming claudins could be used as an approach to clarify this hypothesis.

The dilution potential measurements and the results for the relative (Figure 38C, D) and absolute ion permeability (Figure 39A, B) clearly revealed that the proposed channel claudins Cldn2 and Cldn15 can form in single expression sodium channels, whereas Cldn10a forms an anion channel. Barrier-forming Cldn3 showed, as described in the literature, no selective ion permeability[105]. The combinatorial expression of Cldn2 and Cldn10a gave ion flux across the TJ, but without any charge-specificity (Figure 39A) suggesting that both ion-channels are functional in a TJ with segregating Cldn2 and Cldn10a. Our results align with the findings of Muto et al. in 2010. They could observe that the S2 segment of the proximal

tubule from Cldn2 KO mice has a distinct paracellular anion permeability[121] that was attributed to the remaining Cldn10a. A complementary measurement was performed by Curry et al. in 2020 in MDCKI cells, a very tight epithelial cell line (high endogenous expression of Cldn1, Cldn3, and Cldn4) lacking endogenous Cldn2 and Cldn10a. By controlling the expression of Cldn2 with doxycycline (Tet-Off) and Cldn10a with cumate, they were also able to measure respective cation and anion specificity[234]. The presence of endogenous barrier claudins had in this approach no substantial effect on selective ion permeability, indicating that the channel-forming claudins can also form their ion channels in presence of abundant barrier claudins. This goes in line with the dilution potential measurements of Cldn3 and Cldn15 co-expressing MDCKII QKO cells. In comparison to the neutral charge-specificity when Cldn2 and Cldn10a were co-expressed, a specific permeability for sodium could be detected. The relative permeability of Na/Cl was even higher compared to MDCKII QKO cells expressing Cldn2 or Cldn15 and resulted in values comparable to MDCKII cells that express endogenously Cldn2. A potential explanation is that the presence of Cldn3 in the TJ provides the TJ with a higher integrity and maybe also with a more stable TJ meshwork compared to singly expressed channel-forming claudins. Such a stable TJ would allow then the channel-forming claudins to incorporate in the TJ strands and to provide the TJ with a highly selective ion permeability. Another possible explanation might be the beforehand mentioned expression level of the claudins. A higher expression leads to a more stable TJ that prevent unspecific ion flux over the meshwork.

In summary, we propose that the segregation of the channel-forming claudins Cldn10a, 10b, and 15 facilitates the formation and incorporation of a functional channel in the TJ meshwork by avoiding the direct structural interaction with other claudins (Figure 42A). This incompatibility of the channel-forming claudins to interact with other barrier- and channel-forming claudins is conserved in the structure of the two extracellular loops and facilitates the channel-forming claudins to form its “functional” unit exclusively with itself. Additionally, we postulate that the claudin segregation enables channel-forming claudins to incorporate into complex TJ meshworks creating an "ion-maze" (Figure 42B), providing the TJ of tissues that rely on a critical ion-dependent absorptive process with an indispensable ion permeability.

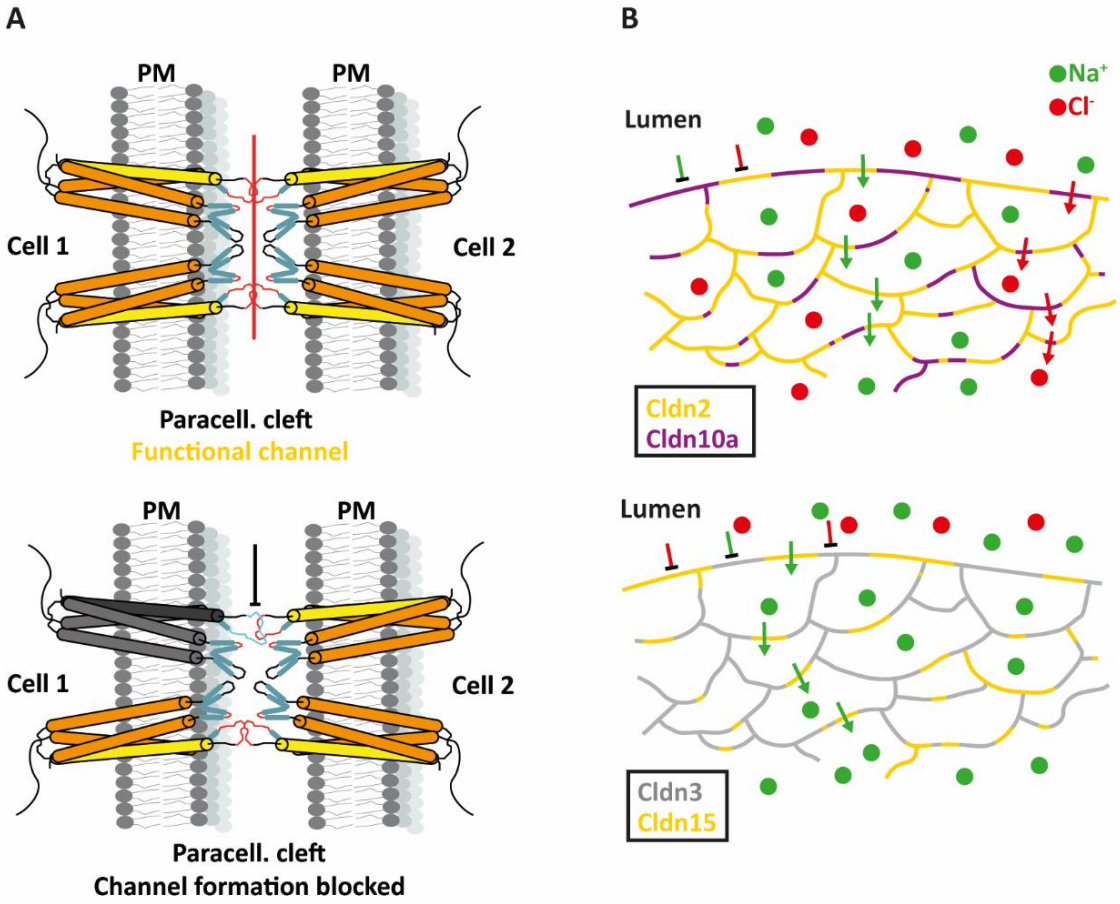

Figure 42 The importance of claudin segregation for ion flux across the TJ. (A) Channel-forming claudins Cldn10a, 10b, and 15 (illustrated as yellow claudin protomers) interact exclusively with their own claudin subtype to form a functional ion channel in the TJ meshwork. A "false" interaction with a barrier- or another channel-forming claudin (illustrated as grey claudin protomers) would lead to a loss of function of the ion channel and could have severe consequences on the passive ion exchange through the paracellular cleft of epithelial cells. **(B)** To provide a constant ion flow over complex TJ meshworks that contain multiple rows of strands and meshes with different sizes, the channel-forming claudins must segregate from other barrier-forming claudins (e.g., Cldn15 (yellow) from Cldn3 (grey)) and other channel-forming claudins (e.g., Cldn2 (yellow) from Cldn10a (magenta)) but also need to incorporate in every mesh to provide a constant and unstopped ion flux in an "ion maze" manner over the TJ meshwork (green dots represent sodium ions and green arrows represent the flow of sodium ions through specific sodium channels formed by sodium channel-forming claudins over the TJ meshwork; red dots represent chloride ions and red arrows represent the flow of chloride ions through specific sodium channels formed by sodium channel-forming claudins over the TJ meshwork).

6 Outlook

The novel discovery of the different nanoscale organization principles of claudins with STED microscopy and the detailed investigation on the segregation of channel-forming claudins contributes significantly to the understanding of the paracellular ion permeability and barrier function of the TJ. The functional studies of claudins in a claudin-free epithelial cell line support previously published data and clarify the specific channel and barrier function of single claudins. The gained novel insights of claudins' meshwork-forming abilities and the identified claudin interaction patterns can be used as starting points to solve fundamental open questions regarding claudins and other structural TJ proteins, including TAMPs and JAMs.

From the technical point of view, we could show that STED microscopy will be one of the critical techniques in understanding the nano-arrangement of TJ proteins. Its fast acquisition, artifact-free, and live imaging possibility also make it very suitable for larger screens and quantitative measurements. Depending on the development of new organic fluorophores and better labeling systems to tip the scales of super-resolution microscopy techniques beyond the resolution limit of STED (MINFLUX[232]), it will be only a matter of time until the tight junctional nano-organization will be completely uncovered and understood.

From the biological side, it will be one of the future tasks to understand the different described meshwork forming properties and claudin organization patterns on a structural level and to put them in a functional and *in vivo* context. Especially the dynamic behind the different interaction patterns and dynamics among the channel-forming claudins should be addressed to answer the question whether Cldn2 belongs also to the segregating channel-forming claudins and to what extend the proposed combinatorial channel-forming claudins Cldn4/Cldn8 and Cldn16/Cldn19 as well as Cldn17 can be classified into a different channel-forming claudin class. Multicolor live imaging of the TJ meshwork on a super-resolution level will offer the possibility of studying the dynamics of and between the claudins and might provide the answer for the nature of the contact points between the segregating claudins. It might also offer novel insights into the TJ's fence function and the diffusion dynamic of lipids over the TJ meshwork that are not fully characterized. In the same context, the interaction of claudins with TAMPs, especially with the first identified tight junctional transmembrane protein, occludin, is of great interest to the TJ field. Recent studies proposed that occludin

acts as a stabilizer for the TJ meshwork, supporting cross-links in TJ strands, strengthening the barrier function, and reducing the flux of small macromolecule[23,208]. Moreover, it is still entirely unknown if the macromolecule flux has any physiological role for the tissue and the organism or whether it is only the consequence of TJ remodeling or the less tight organization of the tTJ. How the tTJ is initially formed and what keeps the claudins tightly restricted to the most apical region of the intercellular junction is not fully understood and should be part of future research studies.

The critical biological system that will be of great importance in the future is the MDCKII QKO system. The possibility of studying claudins and other TJ proteins in a claudin-free background make the system to an indispensable tool for understanding the TJ components. We could show how powerful this system is regarding the functional studies of the claudin-specific ion permeability properties. Additionally, the group around Mikio Furuse already used it to reveal novel functions for JAM-A in cell polarity and barrier function regarding macromolecule flux[58]. It could help solve controversial debated studies, e.g., the anion channel formation by Cldn4 and Cldn8[119] or the proposed anion channel formation of Cldn17[117]. In combination with a by Maraspini et al. published protocol for imaging junctions in an epithelial cysts system with STED microscopy[181], it can be used as a powerful system to study the TJ meshwork between epithelial cells at nanoscale. The MDCKII QKO cells would offer the possibility to study meshworks formed by single claudins and the localization of endogenous TJ proteins, like occludin, along the TJ meshwork. This combination would overcome elegantly the still unsuccessful approaches of imaging the epithelial TJ in 3D-STED.

Lastly, to overcome the commonly used epithelial cell lines derived from different mammalian species and carcinomas, epithelial cells derived from human iPSC will take an essential role in studying the TJ. First steps in this direction were already made by generating human iPSC–derived intestinal epithelial cells[237] and human iPSC-derived alveolar and airway epithelial cells[238] indicating its great potential for a better and more precise understanding of the function and organization of the well-orchestrated TJ.

7 Bibliography

1. Sadava, D., Hillis, D. M., Heller, H. C. & Hacker, S. D. *Purves Biologie, 10th Edition*. *Purves Biologie* (2019).

2. Hamilton, K. L. *Ion Transport Across Epithelial Tissues and Disease*. **2**, (2020).

3. Zihni, C., Mills, C., Matter, K. & Balda, M. S. Tight junctions: From simple barriers to multifunctional molecular gates. *Nat. Rev. Mol. Cell Biol.* **17**, 564–580 (2016).

4. Meldolesi, J., CastiGlioni, G., Parma, R., Nassivera, N. & Camilli, P. D. Ca++-dependent disassembly and reassembly of occluding junctions in guinea pig pancreatic acinar cells. *J. Phys. A Math. Theor.* **79**, 156–172 (1978).

5. Pitelka, D. R., Taggart, B. N. & Hamamoto, S. T. Effects of extracellular calcium depletion on membrane topography and occluding junctions of mammary epithelial cells in culture. *J. Cell Biol.* **96**, 613–624 (1983).

6. Muir, A. R. & Peters, A. Quintuple-layered membrane junctions at terminal bars between endothelial cells. *J. Cell Biol.* **12**, 443–448 (1962).

7. Bazzoni, G. & Dejana, E. Endothelial cell-to-cell junctions: Molecular organization and role in vascular homeostasis. *Physiol. Rev.* **84**, 869–901 (2004).

8. Farquahr, M. G. & Palade, G. E. Junctional complexes in various epithelia. *J. Cell Biol.* **17**, 375–412 (1963).

9. Staehelin, L. A., Mukherjee, T. M. & Williams, A. W. Freeze-etch appearance of the tight junctions in the epithelium of small and large intestine of mice. *Protoplasma* **67**, 165–184 (1969).

10. Staehelin L.A. Further observations on the fine structure of freeze-cleaved tight junctions. *J. Cell Sci.* **13**, 763–786 (1973).

11. Goodenough, D. A. & Revel, J. P. A fine structural analysis of intercellular junctions in the mouse liver. *J Cell Biol* **45**, 272–290 (1970).

12. Claude, P. & Goodenough, D. A. Fracture faces of zonulae occludentes from 'tight' and 'leaky' epithelia. *J. Cell Biol.* **58**, 390–400 (1973).

13. Lu, R. Y., Yang, W. X. & Hu, Y. J. The role of epithelial tight junctions involved in pathogen infections. *Mol. Biol. Rep.* **41**, 6591–6610 (2014).

14. Frömter, E. & Diamond, J. Route of Passive Ion Permeation in Epithelia. *J. Gen . Physiol .* **235**, 9–13 (1972).

15. Dragsten, P. R., Blumenthal, R. & Handler, J. S. Membrane asymmetry in epithelia: Is the tight junction a barrier to diffusion in the plasma membrane? *Nature* **294**, 718–722 (1981).

16. Van Meer, G., Gumbiner, B. & Simons, K. The tight junction does not allow lipid molecules to diffuse from one epithelial cell to the next. *Nature* **322**, 639–641 (1986).

17. Moreno, J. H. & Diamond, J. M. Discrimination of Monovalent Inorganic Cations by " Tight " Junctions of Gallbladder Epithelium. *J. Membr. Biol.* **15**, 277–318 (1974).

18. Yu, A. S. L. *et al.* Molecular basis for cation selectivity in claudin-2-based paracellular pores: Identifi cation of an electrostatic interaction site. *J. Gen. Physiol.* **133**, 111–127 (2009).

19. Angelow, S. & Yu, A. S. L. Structure-function studies of claudin extracellular domains by cysteine-scanning mutagenesis. *J. Biol. Chem.* **284**, 29205–29217 (2009).

20. Wada, M., Tamura, A., Takahashi, N. & Tsukita, S. Loss of claudins 2 and 15 from mice causes defects in paracellular Na+ flow and nutrient transport in gut and leads to death from malnutrition. *Gastroenterology* **144**, 369–380 (2013).

21. Lingarajua, A., Longa, T. M., Wanga, Y., Austin II, J. R. & Turner, J. R. Conceptual barriers to understanding physical barriers. *Semin. Cell Dev. Biol.* **42**, 13–21 (2015).

22. Sasaki, H. *et al.* Dynamic behavior of paired claudin strands within apposing plasma membranes. *Proc. Natl. Acad. Sci. U. S. A.* **100**, 3971–3976 (2003).

23. Van Itallie, C. M., Tietgens, A. J. & Anderson, J. M. Visualizing the dynamic coupling of claudin strands to the actin cytoskeleton through ZO-1. *Mol. Biol. Cell* **28**, 524–534 (2016).

24. Steed, E., Balda, M. S. & Matter, K. Dynamics and functions of tight junctions. *Trends Cell Biol.* **20**, 142–149 (2010).

25. Van Genderen, I. L., Van Meer, G., Slot, J. W., Geuze, H. J. & Voorhout, W. F. Subcellular localization of forssman glycolipid in epithelial MDCK cells by immuno-electronmicroscopy after freeze-substitution. *J. Cell Biol.* **115**, 1009–1019 (1991).

26. Diamond, J. M. Twenty-first Bowditch lecture. The epithelial junction: bridge, gate, and fence. *Physiologist* **20**, 10–18 (1977).

27. Rodriguez-Boulan, E. & Nelson, W. J. Morphogenesis of the polarized epithelial cell phenotype. *Science* **245**, 718–725 (1989).

28. van Meer, G. & Simons, K. The function of tight junctions in maintaining differences in lipid composition between the apical and the basolateral cell surface domains of MDCK cells. *EMBO J.* **5**, 1455–1464 (1986).

29. Otani, T. & Furuse, M. Tight Junction Structure and Function Revisited. *Trends Cell Biol.* **30**, 805–817 (2020).

30. Anderson, J. M., Van Itallie, C. M. & Fanning, A. S. Setting up a selective barrier at the apical junction complex. *Curr. Opin. Cell Biol.* **16**, 140–145 (2004).

31. Furuse, M., Fujita, K., Hiiragi, T., Fujimoto, K. & Tsukita, S. Claudin-1 and -2: Novel integral membrane proteins localizing at tight junctions with no sequence similarity to occludin. *J. Cell Biol.* **141**, 1539–1550 (1998).

32. Günzel, D. & Yu, A. S. L. Claudins and the Modulation of Tight Junction Permeability. *Physiol Rev* **93**, 525–569 (2013).

33. Furuse, M. *et al.* Occludin: A novel integral membrane protein localizing at tight junctions. *J. Cell Biol.* **123**, 1777–1788 (1993).

34. Ikenouchi, J. *et al.* Tricellulin constitutes a novel barrier at tricellular contacts of epithelial cells. *J. Cell Biol.* **171**, 939–945 (2005).

35. Steed, E., Rodrigues, N. T. L., Balda, M. S. & Matter, K. Identification of MarvelD3 as a tight junction-associated transmembrane protein of the occludin family. *BMC Cell Biol.* **10**, 1–14 (2009).

36. Martìn-Padura, I. *et al.* Junctional adhesion molecule, a novel member of the immunoglobulin superfamily that distributes at intercellular junctions and modulates monocyte transmigration. *J. Cell Biol.* **142**, 117–127 (1998).

37. Stevenson, B. R., Siliciano, J. D., Mooseker, M. S. & Goodenough, D. A. Identification of ZO-1: A high molecular weight polypeptide associated with the tight junction (Zonula Occludens) in a variety of epithelia. *J. Cell Biol.* **103**, 755–766 (1986).

38. Gumbiner, B., Lowenkopf, T. & Apatira, D. Identification of a 160-kDa polypeptide that binds to the tight junction protein ZO-1. *Proc. Natl. Acad. Sci. U. S. A.* **88**, 3460–3464 (1991).

39. Jesaitis, L. A. & Goodenough, D. A. Molecular characterization and tissue distribution of ZO-2, a tight junction protein homologous to ZO-1 and the Drosophila discs-large tumor suppressor protein. *J. Cell Biol.* **124**, 949–961 (1994).

40. Balda, M. S. & Anderson, J. M. Two classes of tight junctions are revealed by ZO-1 isoforms. *Am. J. Physiol. - Cell Physiol.* **264**, (1993).

41. Haskins, J., Gu, L., Wittchen, E. S., Hibbard, J. & Stevenson, B. R. ZO-3, a novel member of the MAGUK protein family found at the tight junction, interacts with ZO-1 and occludin. *J. Cell Biol.* **141**, 199–208 (1998).

42. Beutel, O., Maraspini, R., Pombo-García, K., Martin-Lemaitre, C. & Honigmann, A. Phase Separation of Zonula Occludens Proteins Drives Formation of Tight Junctions. *Cell* **179**, 923-936.e11 (2019).

43. Hamazaki, Y., Itoh, M., Sasaki, H., Furuse, M. & Tsukita, S. Multi-PDZ domain protein 1 (MUPP1) is concentrated at tight junctions through its possible interaction with claudin-1 and junctional adhesion molecule. *J. Biol. Chem.* **277**, 455–461 (2002).

44. Ide, N. *et al.* Localization of membrane-associated guanylate kinase (MAGI)-1/BAI-associated protein (BAP) 1 at tight junctions of epithelial cells. *Oncogene* **18**, 7810–7815 (1999).

45. Laura, R. P., Ross, S., Koeppen, H. & Lasky, L. A. MAGI-1: A widely expressed, alternatively spliced tight junction protein. *Exp. Cell Res.* **275**, 155–170 (2002).

46. Stevenson, B. R., Heintzelman, M. B., Anderson, J. M., Citi, S. & Mooseker, M. S. ZO-1 and cingulin: tight junction proteins with distsinct identities and localizations. *Am. J. Physiol. - Cell Physiol.* **257**, (1989).

47. Cordenonsi, M. *et al.* Cingulin contains globular and coiled-coil domains and interacts with ZO-1, ZO-2, ZO-3, and myosin. *J. Cell Biol.* **147**, 1569–1581 (1999).

48. Yano, T., Matsui, T., Tamura, A., Uji, M. & Tsukita, S. The association of microtubules with tight junctions is promoted by cingulin phosphorylation by AMPK. *J. Cell Biol.* **203**, 605–614 (2013).

49. Vasileva, E. *et al.* Cingulin unfolds ZO-1 and organizes myosin-2B and g-actin to mechanoregulate apical and tight junction membranes. *bioRxiv* (2020). doi:10.1101/2020.05.14.095364

50. Balda, M. S. & Matter, K. The tight junction protein ZO-1 and an interacting transcription factor regulate ErbB-2 expression. *EMBO J.* **19**, 2024–2033 (2000).

51. Balda, M. S., Garrett, M. D. & Matter, K. The ZO-1 – associated Y-box factor ZONAB regulates epithelial cell proliferation and cell density. **160**, 423–432 (2003).

52. Nie, M. *et al.* The Y-box factor ZONAB/DbpA associates with GEF-H1/Lfc and mediates Rho-stimulated transcription. *EMBO Rep.* **10**, 1125–1131 (2009).

53. Frankel, P. *et al.* Ra1A interacts with ZONAB in a cell density-dependent manner and regulates its transcriptional activity. *EMBO J.* **24**, 54–62 (2005).

54. Mangeol, P., Massey-Harroche, D., Bivic, A. Le & Lenne, P. F. Nectins rather than E-cadherin anchor the actin belts at cell-cell junctions of epithelia. *bioRxiv* (2019). doi:10.1101/809343

55. Tan, B. *et al.* The Mammalian Crumbs Complex Defines a Distinct Polarity Domain Apical of Epithelial Tight Junctions. *Curr. Biol.* **30**, 2791-2804.e6 (2020).

56. Kan, F. W. K. Cytochemical evidence for the presence of phospholipids in epithelial tight junction strands. *J. Histochem. Cytochem.* **41**, 649–656 (1993).

57. Furuse, M., Sasaki, H., Fujimoto, K. & Tsukita, S. A single gene product, claudin-1 or -2, reconstitutes tight junction strands and recruits occludin in fibroblasts. *J. Cell Biol.* **143**, 391–401 (1998).

58. Otani, T. *et al.* Claudins and JAM-A coordinately regulate tight junction formation and epithelial polarity. *J. Cell Biol.* **218**, 3372–3396 (2019).

59. Nusrat, A. *et al.* The coiled-coil domain of occludin can act to organize structural and functional elements of the epithelial tight junction. *J. Biol. Chem.* **275**, 29816–29822 (2000).

60. Lambert, D., O'Neill, C. A. & Padfield, P. J. Depletion of Caco-2 cell cholesterol disrupts barrier function by altering the detergent solubility and distribution of specific tight-junction proteins. *Biochem. J.* **387**, 553–560 (2005).

61. Shigetomi, K., Ono, Y., Inai, T. & Ikenouchi, J. Adherens junctions influence tight junction formation via changes in membrane lipid composition. *J. Cell Biol.* **217**, 2373–2381 (2018).

62. Ando-Akatsuka, Y., Yonemura, S., Itoh, M., Furuse, M. & Tsukita, S. Differential behavior of E-cadherin and occludin in their colocalization with ZO-1 during the establishment of epithelial cell polarity. *J. Cell. Physiol.* **179**, 115–125 (1999).

63. Suzuki, A. *et al.* aPKC kinase activity is required for the asymmetric differentiation of the premature junctional complex during epithelial cell polarization. *J. Cell Sci.* **115**, 3565–3573 (2002).

64. González-Mariscal, L., Garay, E. & Quirós, M. Regulation of Claudins by Posttranslational Modifications and Cell-Signaling Cascades. *Curr. Top. Membr.* **65**, 113–150 (2010).

65. Shen, L., Weber, C. R. & Turner, J. R. The tight junction protein complex undergoes rapid and continuous molecular remodeling at steady state. *J. Cell Biol.* **181**, 683–695 (2008).

66. Cording, J. *et al.* In tight junctions, claudins regulate the interactions between occludin, tricellulin and marvelD3, which, inversely, modulate claudin oligomerization. *J. Cell Sci.* **126**, 554–564 (2013).

67. Wilcox, E. R. *et al.* Mutations in the gene encoding tight junction claudin-14 cause autosomal recessive deafness DFNB29. *Cell* **104**, 165–172 (2001).

68. Lee, K. *et al.* Novel CLDN14 Mutations in Pakistani Families With Autosomal Recessive Non-Syndromic Hearing Loss. *Am J Med Genet A.* 315–321 (2012).

69. Simon, D. B. *et al.* Paracellin-1, a renal tight junction protein required for paracellular Mg2+ resorption. *Science* **285**, 103–106 (1999).

70. Hadj-rabia, S. *et al.* Multiplex epithelium dysfunction due to CLDN10 mutation: the HELIX syndrome. *Genet. Med.* **20**, 190–201 (2018).

71. Grosse, B., Cassio, D., Yousef, N., Jacquemin, E. & Gonzales, E. Claudin-1 Involved in Neonatal Ichthyosis Sclerosing Cholangitis Syndrome Regulates Hepatic Paracellular Permeability. *Hepatology* **55**, 1249–1259 (2012).

72. Evans, M. J. *et al.* Claudin-1 is a hepatitis C virus co-receptor required for a late step in entry. *Nat. Lett.* **446**, 801–805 (2007).

73. Katahira, J. *et al.* Clostridium perfringens Enterotoxin Utilizes Two Structurally Related Membrane Proteins as Functional Receptors in Vivo *. *J. Biol. Chem.* **272**, 26652–26658 (1997).

74. Morita, K., Furuse, M., Fujimoto, K. & Tsukita, S. Claudin multigene family encoding four-transmembrane domain. *Cell* **96**, 511–516 (1999).

75. Wu, Z., Nybom, P. & Magnusson, K. Distinct effects of Vibrio cholerae haemagglutinin / protease on the structure and localization of the tight junction-associated proteins occludin and ZO-1. *Cell. Microbiol.* **2**, 11–17 (2000).

76. Lu, Z., Ding, L., Lu, Q. & Chen, Y.-H. Claudins in intestines. *Tissue Barriers* **1**, e24978 (2013).

77. Krug, S. M., Schulzke, J. D. & Fromm, M. Tight junction, selective permeability, and related diseases. *Semin. Cell Dev. Biol.* **36**, 166–176 (2014).

78. Mineta, K. *et al.* Predicted expansion of the claudin multigene family. *FEBS Lett.* **585**, 606–612 (2011).

79. Krause, G. *et al.* Structure and function of claudins. *Biochim. Biophys. Acta - Biomembr.* **1778**, 631–645 (2008).

80. Günzel, D. & Fromm, M. Claudins and other tight junction proteins. *Compr. Physiol.* **2**, 1819–1852 (2012).

81. Yu, A. S. L. Claudins and the kidney. *J. Am. Soc. Nephrol.* **26**, 11–19 (2015).

82. Klar, J. *et al.* Altered paracellular cation permeability due to a rare CLDN10B variant causes anhidrosis and kidney damage. *PLoS Genet.* **13**, 1–22 (2017).

83. Furuse, M. *et al.* Claudin-based tight junctions are crucial for the mammalian epidermal barrier: A lesson from claudin-1-deficient mice. *J. Cell Biol.* **156**, 1099–1111 (2002).

84. Tabariès, S. & Siegel, P. M. The role of claudins in cancer metastasis. *Oncogene* **36**, 1176–1190 (2017).

85. Bhat, A. A. *et al.* Tight junction proteins and signaling pathways in cancer and inflammation: A functional crosstalk. *Front. Physiol.* **10**, 1–19 (2019).

86. Suzuki, H. *et al.* Crystal structure of a claudin provides insight into the architecture of tight junctions. *Science* **344**, 304–307 (2014).

87. Suzuki, H., Tani, K., Tamura, A., Tsukita, S. & Fujiyoshi, Y. Model for the architecture of claudin-based paracellular ion channels through tight junctions. *J. Mol. Biol.* **427**, 291–297 (2015).

88. Itoh, M. *et al.* Direct binding of three tight junction-associated MAGUKs, ZO-1, ZO-2, and ZO-3, with the COOH termini of claudins. *J. Cell Biol.* **147**, 1351–1363 (1999).

89. Souza, T. D., Agarwal, R. & Morin, P. J. Phosphorylation of Claudin-3 at Threonine 192 by cAMP-dependent Protein Kinase Regulates Tight Junction Barrier Function in Ovarian Cancer Cells *. *J. Biol. Chem.* **280**, 26233–26240 (2008).

90. Tanaka, M., Kamata, R. & Sakai, R. EphA2 phosphorylates the cytoplasmic tail of claudin-4 and mediates paracellular permeability. *J. Biol. Chem.* **280**, 42375–42382 (2005).

91. Ikari, A. *et al.* Phosphorylation of paracellin-1 at Ser217 by protein kinase A is essential for localization in tight junctions. *J. Cell Sci.* **119**, 1781–1789 (2006).

92. Findley, M. K. & Koval, M. Regulation and roles for claudin-family tight junction proteins. *IUBMB Life* **61**, 431–437 (2009).

93. Van Itallie, C. M. *et al.* Phosphorylation of claudin-2 on serine 208 promotes membrane retention and reduces trafficking to lysosomes. *J. Cell Sci.* **125**, 4902–4912 (2012).

94. Van Itallie, C. M., Gambling, T. M., Carson, J. L. & Anderson, J. M. Palmitoylation of claudins is required for efficient tight-junction localization. *J. Cell Sci.* **118**, 1427–1436 (2005).

95. Wen, H., Watry, D. D., Marcondes, M. C. G. & Fox, H. S. Selective Decrease in Paracellular Conductance of Tight Junctions: Role of the First Extracellular Domain of Claudin-5. *Mol. Cell. Biol.* **24**, 8408–8417 (2004).

96. Rossa, J. *et al.* Claudin-3 and Claudin-5 Protein Folding and Assembly into the Tight Junction Are Controlled by Non-conserved Residues in the Transmembrane 3 (TM3) and Extracellular Loop 2(ECL2) Segments. *J. Biol. Chem.* **289**, 7641–7653 (2014).

97. Milatz, S. *et al.* Tight junction strand formation by claudin-10 isoforms and claudin-10a/-10b chimeras. *Ann. N. Y. Acad. Sci.* **1405**, 102–115 (2017).

98. Zhao, J. *et al.* Multiple claudin–claudin cis interfaces are required for tight junction strand formation and inherent flexibility. *Commun. Biol.* **1**, (2018).

99. Krause, G., Winkler, L., Piehl, C., Blasig, I. & Sebastian, L. M. Structure and Function of Extracellular Claudin Domains. **43**, 34–43 (2009).

100. Piontek, A. *et al.* Polar and charged extracellular residues conserved among barrier-forming claudins contribute to tight junction strand formation. *Ann. N. Y. Acad. Sci.* 143–156 (2017).

101. Samanta, P. *et al.* Molecular determination of claudin-15 organization and channel selectivity. *J. Gen. Physiol.* **150**, 949–968 (2018).

102. Colegio, O. R., Van Itallie, C. M., McCrea, H. J., Rahner, C. & Anderson, J. M. Claudins create charge-selective channels in the paracellular pathway between epithelial cells. *Am. J. Physiol. - Cell Physiol.* **283**, 142–147 (2002).

103. Colegio, O. R., Van Itallie, C., Rahner, C. & Anderson, J. M. Claudin extracellular domains determine paracellular charge selectivity and resistance but not tight junction fibril architecture. *Am. J. Physiol. - Cell Physiol.* **284**, 1346–1354 (2003).

104. Krystofiak, E. S., Heymann, J. B. & Kachar, B. Carbon replicas reveal double stranded structure of tight junctions in phase-contrast electron microscopy. *Commun. Biol.* **2**, 1–6 (2019).

105. Milatz, S. *et al.* Claudin-3 acts as a sealing component of the tight junction for ions of either charge and uncharged solutes. *Biochim. Biophys. Acta - Biomembr.* **1798**, 2048–2057 (2010).

106. Castro Dias, M. *et al.* Claudin-3-deficient C57BL/6J mice display intact brain barriers. *Sci. Rep.* **9**, 1–16 (2019).

107. Piontek, J., Krug, S. M., Protze, J., Krause, G. & Fromm, M. Molecular architecture and assembly of the tight junction backbone. *Biochim. Biophys. Acta - Biomembr.* **1862**, 183279 (2020).

108. Mazaud-Guittot, S. *et al.* Claudin 11 deficiency in mice results in loss of the sertoli cell epithelial phenotype in the testis. *Biol. Reprod.* **82**, 202–213 (2010).

109. Gow, A. *et al.* Deafness in Claudin 11-null mice reveals the critical contribution of basal cell tight junctions to stria vascularis function. *J. Neurosci.* **24**, 7051–7062 (2004).

110. Gow, A. *et al.* CNS Myelin and sertoli cell tight junction strands are absent in OSP/claudin-11 null mice. *Cell* **99**, 649–659 (1999).

111. Furuse, M., Furuse, K., Sasaki, H. & Tsukita, S. Conversion of zonulae occludentes from tight to leaky strand type by introducing claudin-2 into Madin-Darby canine kidney I cells. *J. Cell Biol.* **153**, 263–272 (2001).

112. Amasheh, S. *et al.* Claudin-2 expression induces cation-selective channels in tight junctions of epithelial cells. *J. Cell Sci.* **115**, 4969–4976 (2002).

113. Van Itallie, C. M. *et al.* Two splice variants of claudin-10 in the kidney create paracellular pores with different ion selectivities. *Am. J. Physiol. Renal Physiol.* **291**, F1288–F1299 (2006).

114. Günzel, D. *et al.* Claudin-10 exists in six alternatively spliced isoforms that exhibit distinct localization and function. *J. Cell Sci.* **122**, 1507–1517 (2009).

115. Van Itallie, C. M., Fanning, A. S. & Anderson, J. M. Reversal of charge selectivity in cation or anion-selective epithelial lines by expression of different claudins. *Am. J. Physiol. - Ren. Physiol.* **285**, 1078–1084 (2003).

116. Hou, J. *et al.* Claudin-16 and claudin-19 interaction is required for their assembly into tight junctions and for renal reabsorption of magnesium. *Proc. Natl. Acad. Sci.* **106**, 15350–15355 (2009).

117. Krug, S. M. *et al.* Claudin-17 forms tight junction channels with distinct anion selectivity. *Cell. Mol. Life Sci.* **69**, 2765–2778 (2012).

118. Conrad, M. P., Piontek, J., Günzel, D., Fromm, M. & Krug, S. M. Molecular basis of claudin-17 anion selectivity. *Cell. Mol. Life Sci.* **73**, 185–200 (2016).

119. Hou, J., Renigunta, A., Yang, J. & Waldegger, S. Claudin-4 forms paracellular chloride channel in the kidney and requires claudin-8 for tight junction localization. *Proc. Natl. Acad. Sci.* **107**, 18010–18015 (2010).

120. Rosenthal, R. *et al.* Claudin-2, a component of the tight junction, forms a paracellular water channel. *J. Cell Sci.* **123**, 1913–1921 (2010).

121. Muto, S. *et al.* Claudin-2-deficient mice are defective in the leaky and cation-selective paracellular permeability properties of renal proximal tubules. *Proc. Natl. Acad. Sci. U. S. A.* **107**, 8011–8016 (2010).

122. Rosenthal, R. *et al.* Claudin-15 forms a water channel through the tight junction with distinct function compared to claudin-2. *Acta Physiol.* 1–15 (2019).

123. Li, J., Zhuo, M., Pei, L., Rajagopal, M. & Yu, A. S. L. Comprehensive cysteine-scanning mutagenesis reveals claudin-2 pore-lining residues with different intrapore locations. *J. Biol. Chem.* **289**, 6475–6484 (2014).

124. Weber, C. R. *et al.* Claudin-2-dependent paracellular channels are dynamically gated. *Elife* **4**, 1–20 (2015).

125. Tokuda, S. & Furuse, M. Claudin-2 knockout by TALEN-mediated gene targeting in MDCK cells: Claudin-2 independently determines the leaky property of tight junctions in MDCK cells. *PLoS One* **10**, 1–22 (2015).

126. Holmes, J. L., Van Itallie, C. M., Rasmussen, J. E. & Anderson, J. M. Claudin profiling in the mouse during postnatal intestinal development and along the gastrointestinal tract reveals complex expression patterns. *Gene Expr. Patterns* **6**, 581–588 (2006).

127. Tamura, A. *et al.* Loss of claudin-15, but not claudin-2, causes Na+ deficiency and glucose malabsorption in mouse small intestine. *Gastroenterology* **140**, 913–923 (2011).

128. Milatz, S. & Breiderhoff, T. One gene, two paracellular ion channels—claudin-10 in the kidney. *Pflugers Arch. Eur. J. Physiol.* **469**, 115–121 (2017).

129. Breiderhoff, T. *et al.* Deletion of claudin-10 (Cldn10) in the thick ascending limb impairs paracellular sodium permeability and leads to hypermagnesemia and nephrocalcinosis. *Proc. Natl. Acad. Sci. U. S. A.* **109**, 15072 (2012).

130. Hou, J. *et al.* Claudin-16 and claudin-19 interact and form a cation-selective tight junction complex. *J. Clin. Invest.* **118**, 619–628 (2008).

131. Gong, Y. *et al.* Biochemical and biophysical analyses of tight junction permeability made of claudin-16 and claudin-19 dimerization. *Mol. Biol. Cell* **26**, 4333–4346 (2015).

132. Jaya Kausalya, P. *et al.* Disease-associated mutations affect intracellular traffic and paracellular Mg2+ transport function of Claudin-16. *J. Clin. Invest.* **116**, 878–891 (2006).

133. Milatz, S. *et al.* Mosaic expression of claudins in thick ascending limbs of Henle results in spatial separation of paracellular Na+ and Mg2+ transport. *Proc. Natl. Acad. Sci.* **114**, E219–E227 (2016).

134. Raleigh, D. R. *et al.* Tight Junction–associated MARVEL Proteins MarvelD3, Tricellulin, and Occludin Have Distinct but Overlapping Functions. *Mol. Biol. Cell* **21**, 1200–1213 (2010).

135. Sánchez-Pulido, L., Martín-Belmonte, F., Valencia, A. & Alonso, M. A. MARVEL : a conserved domain involved in membrane apposition events. *TRENDSin Biochem. Sci.* **27**, 599–601 (2002).

136. McCarthy, K. M. *et al.* Occludin is a functional component of the tight junction. *J. Cell Sci.* **109**, 2287–2298 (1996).

137. Buschmann, M. M. *et al.* Occludin OCEL-domain interactions are required for maintenance and regulation of the tight junction barrier to macromolecular flux. *Mol. Biol. Cell* **24**, 3056–3068 (2013).

138. Saitou, M. *et al.* Complex phenotype of mice lacking occludin, a component of tight junction strands. *Mol. Biol. Cell* **11**, 4131–4142 (2000).

139. Schulzke, J. D. *et al.* Epithelial transport and barrier function in occludin-deficient mice. *Biochim. Biophys. Acta - Biomembr.* **1669**, 34–42 (2005).

140. Kitajiri, S. I. *et al.* Deafness in occludin-deficient mice with dislocation of tricellulin and progressive apoptosis of the hair cells. *Biol. Open* **3**, 759–766 (2014).

141. O'Driscoll, M. C. *et al.* Recessive mutations in the gene encoding the tight junction protein occludin cause band-like calcification with simplified gyration and polymicrogyria. *Am. J. Hum. Genet.* **87**, 354–364 (2010).

142. Leblanc, M. A. *et al.* A novel rearrangement of occludin causes brain calcification and renal dysfunction. *Hum. Genet.* **132**, 1223–1234 (2013).

143. Elsaid, M. F. *et al.* Whole genome sequencing identifies a novel occludin mutation in microcephaly with band-like calcification and polymicrogyria that extends the phenotypic spectrum. *Am. J. Med. Genet. Part A* **164**, 1614–1617 (2014).

144. Jenkinson, E. M. *et al.* Comprehensive molecular screening strategy of OCLN in band-like calcification with simplified gyration and polymicrogyria. *Clin. Genet.* **93**, 228–234 (2018).

145. Ekinci, F., Yildizdas, R. D., Horoz, O. O., Herguner, O. & Bisgin, A. A homozygote frameshift mutation in OCLN gene result in Pseudo-TORCH syndrome type I: A case report extending the phenotype with central diabetes insipidus and renal dysfunction. *Eur. J. Med. Genet.* **63**, 103923 (2020).

146. Wade, J. B. & Karnovsky, M. J. The structure of the zonula occludens: A single fibril model based on freeze-fracture. *J. Cell Biol.* **60**, 168–180 (1974).

147. Friend, D. S. & Gilula, N. B. Variations in tight and gap-junctions in mammalian tissues. *J. Cell Biol.* **53**, 758–776 (1972).

148. Sugawara, T., Furuse, K., Otani, T. & Furuse, M. Angulin-1 seals tricellular contacts independently of tricellulin and claudins. *bioRxiv* (2020).

149. Ikenouchi, J., Sasaki, H., Tsukita, S., Furuse, M. & Tsukita*, S. Loss of Occludin Affects Tricellular Localization of Tricellulin. *Mol. Biol. Cell* **19**, 4687–4693 (2008).

150. Williams, L. A., Martin-Padura, I., Dejana, E., Hogg, N. & Simmons, D. L. Identification and characterization of human junctional adhesion molecule (JAM). *Mol. Immunol.* **36**, 1175–1188 (1999).

151. Liu, Y. *et al.* Human junction adhesion molecule regulates tight junction resealing in epithelia. *J. Cell Sci.* **113**, 2363–2374 (2000).

152. Ebnet, K., Suzuki, A., Ohno, S. & Vestweber, D. Junctional adhesion molecules (JAMs): More molecules with dual functions? *J. Cell Sci.* **117**, 19–29 (2004).

153. Adachi, M. *et al.* Normal Establishment of Epithelial Tight Junctions in Mice and Cultured Cells Lacking Expression of ZO-3, a Tight-Junction MAGUK Protein. *Mol. Cell. Biol.* **26**, 9003–9015 (2006).

154. Fanning, A. S., Ma, T. Y. & Anderson, J. M. Isolation and functional characterization of the actin binding region in the tight junction protein ZO-1. *FASEB J.* **16**, 1835–1837 (2002).

155. Umeda, K. *et al.* ZO-1 and ZO-2 Independently Determine Where Claudins Are Polymerized in Tight-Junction Strand Formation. *Cell* **126**, 741–754 (2006).

156. Ye, F., Zeng, M. & Zhang, M. Mechanisms of MAGUK-mediated cellular junctional complex organization. *Curr. Opin. Struct. Biol.* **48**, 6–15 (2018).

157. Xu, J. *et al.* Early Embryonic Lethality of Mice Lacking ZO-2, but Not ZO-3, Reveals Critical and Nonredundant Roles for Individual Zonula Occludens Proteins in Mammalian Development. *Mol. Cell. Biol.* **28**, 1669–1678 (2008).

158. Katsuno, T. *et al.* Deficiency of Zonula Occludens-1 Causes Embryonic Lethal Phenotype Associated with Defected Yolk Sac Angiogenesis and Apoptosis of Embryonic Cells. *Mol. Biol. Cell* **19**, 2465–2475 (2008).

159. Itoh, M., Tsukita, S., Yamazaki, Y. & Sugimoto, H. Rho GTP exchange factor ARHGEF11 regulates the integrity of epithelial junctions by connecting ZO-1 and RhoA-Myosin II signaling. *Proc. Natl. Acad. Sci. U. S. A.* **109**, 9905–9910 (2012).

160. Ito, S. *et al.* Induced cortical tension restores functional junctions in adhesion-defective carcinoma cells. *Nat. Commun.* **8**, 1–16 (2017).

161. Zenker, J. *et al.* Expanding Actin Rings Zipper the Mouse Embryo for Blastocyst Formation. *Cell* **173**, 776–791 (2018).

162. Belardi, B. *et al.* A Weak Link with Actin Organizes Tight Junctions to Control Epithelial Permeability. *Dev. Cell* **54**, 792–804 (2020).

163. Garcia-Hernandez, V., Quiros, M. & Nusrat, A. Intestinal epithelial claudins: Expression and regulation in homeostasis and inflammation. *Ann. N. Y. Acad. Sci.* **1397**, 66–79 (2017).

164. Spadaro, D. *et al.* Tension-Dependent Stretching Activates ZO-1 to Control the Junctional Localization of Its Interactors. *Curr. Biol.* **27**, 3783–3795 (2017).

165. Schwayer, C. *et al.* Mechanosensation of Tight Junctions Depends on ZO-1 Phase Separation and Flow. *Cell* **179**, 937–952 (2019).

166. Odenwald, M. A. *et al.* ZO-1 interactions with F-actin and occludin direct epithelial polarization and single lumen specification in 3D culture. *J. Cell Sci.* **130**, 243–259 (2016).

167. Odenwald, M. A. *et al.* The scaffolding protein ZO-1 coordinates actomyosin and epithelial apical specializations in vitro and in vivo. *J. Biol. Chem.* **293**, 17317–17335 (2018).

168. Haas, A. J. *et al.* Interplay between Extracellular Matrix Stiffness and JAM-A Regulates Mechanical Load on ZO-1 and Tight Junction Assembly. *Cell Rep.* **32**, 107924 (2020).

169. Stephenson, R. E. *et al.* Rho Flares Repair Local Tight Junction Leaks. *Dev. Cell* **48**, 445-459.e5 (2019).

170. Steere, R. L. Electron microscopy of structural detail in frozen biological specimens. *J. Biophys. Biochem. Cytol.* **3**, 45–60 (1957).

171. Schnell, U., Dijk, F., Sjollema, K. A. & Giepmans, B. N. G. Immunolabeling artifacts and the need for live-cell imaging. *Nat. Methods* **9**, 152–158 (2012).

172. Gonzalez-Mariscal, L., Maria Del Carmen Namorado, D. M., Sierra, G. & Reyes, J. L. The tight junction proteins claudin-7 and -8 display a different subcellularlocalization at Henle's loops and collecting ducts of rabbit kidney. *Nephrol Dial Transpl. (* **21**, 2391–2398 (2006).

173. Furuse, M., Sasaki, H. & Tsukita, S. Manner of Interaction of Heterogeneous Claudin Species Within and Between Tight Junction Strands. *J. Cell Biol.* **147**, 891–903 (1999).

174. Inai, T., Sengoku, A., Hirose, E., Iida, H. & Shibata, Y. Freeze-fracture electron microscopic study of tight junction strands in HEK293 cells and MDCK II cells expressing claudin-1 mutants in the second extracellular loop. *Histochem. Cell Biol.* **131**, 681–690 (2009).

175. Inai, T., Kamimura, T., Hirose, E., Iida, H. & Shibata, Y. The protoplasmic or exoplasmic face association of tight junction particles cannot predict paracellular permeability or heterotypic claudin compatibility. *Eur. J. Cell Biol.* **89**, 547–556 (2010).

176. Hempel, C. *et al.* Assembly of Tight Junction Strands: Claudin-10b and Claudin-3 Form Homo-Tetrameric Building Blocks that Polymerise in a Channel-Independent Manner. *J. Mol. Biol.* **432**, 2405–2427 (2020).

177. Schermelleh, L. *et al.* Super-resolution microscopy demystified. *Nat. Cell Biol.* **21**, 72–84 (2019).

178. Gonschior, H., Haucke, V. & Lehmann, M. Super-resolution imaging of tight and adherens junctions: Challenges and open questions. *Int. J. Mol. Sci.* **21**, 1–15 (2020).

179. Kaufmann, R. *et al.* Visualization and Quantitative Analysis of Reconstituted Tight Junctions Using Localization Microscopy. *PLoS One* **7**, 1–9 (2012).

180. Schlingmann, B. *et al.* Regulation of claudin/zonula occludens-1 complexes by hetero-claudin interactions. *Nat. Commun.* **7**, 1–14 (2016).

181. Maraspini, R., Wang, C.-H. & Honigmann, A. Optimization of 2D and 3D cell culture to study membrane organization with STED microscopy. *J. Phys. D. Appl. Phys.* **53**, 014001 (2020).

182. Van Itallie, C. M., Lidman, K. F., Tietgens, A. J. & Anderson, J. M. Newly synthesized claudins but not occludin are added to the basal side of the tight junction. *Mol. Biol. Cell* **30**, 1406–1424 (2019).

183. Nunes, F. D. *et al.* Distinct subdomain organization and molecular composition of a tight junction with adherens junction features. *J. Cell Sci.* **119**, 4819–4827 (2006).

184. Mullis, K. *et al.* Specific enzymatic amplification of DNA in vitro: the polymerase chain reaction. 1986. *Cold Spring Harb. Symp. Quant. Biolcgy,* **24**, 17–27 (1986).

185. Saiki, R. *et al.* Primer-Directed Enzymatic Amplification of DNA with a Thermostable DNA Polymerase. *Science* **239**, 487–491 (1988).

186. Bottanelli, F. *et al.* Two-colour live-cell nanoscale imaging of intracellular targets. *Nat. Commun.* **7**, 1–5 (2016).

187. Abbe, E. Beiträge zur Theorie des Mikroskops und der mikroskopischen Wahrnehmung. *Arch. für Mikroskopische Anat. 9* 413–418 (1873).

188. Hell, S. W. & Wichmann, J. Breaking the diffraction resolution limit by stimulated emission: stimulated-emission-depletion fluorescence microscopy. *Opt. Lett.* **19**, 780 (1994).

189. Krull, A., Vicar, T. & Jug, F. Probabilistic noise2Void: Unsupervised content-aware denoising. *Front. Comput. Sci.* **2**, 1–9 (2020).

190. Förster, T. Zwischenmolekulare Energiewander und Fluorezenz. *Ann. Phys.* **2**, (1948).

191. Gary Bradski. The OpenCV Library. (2000).

192. Haralick, Robert M., Shanmugam. K, A. & Dinstein, I. Textural Features for Image Classification. *IEEE Trans. Syst. Man Cybern.* **SMC-3,** 610–621 (1973).

193. Van Rossum, G., Drake Jr, F. L. & Centrum voor Wiskunde en Informatica Amsterdam. Python reference manual. (1995).

194. Coelho, L. P. *et al.* Determining the subcellular location of new proteins from microscope images using local features. *Bioinformatics* **29**, 2343–2349 (2013).

195. Hall-Beyer, M. Practical guidelines for choosing GLCM textures to use in landscape classification tasks over a range of moderate spatial scales. *Int. J. Remote Sens.* **38**, 1312–1338 (2017).

196. Law, M. W. K. & Chung, A. C. S. Three dimensional curvilinear structure detection using optimally oriented flux. *Lect. Notes Comput. Sci.* 368–382 (2008).

197. Schindelin, J. *et al.* Fiji: An open-source platform for biological-image analysis. *Nat. Methods* **9**, 676–682 (2012).

198. Longair, M. H., Baker, D. A. & Armstrong, J. D. Simple neurite tracer: Open source software for reconstruction, visualization and analysis of neuronal processes. *Bioinformatics* **27**, 2453–2454 (2011).

199. Legland, D., Arganda-Carreras, I. & Andrey, P. MorphoLibJ: Integrated library and plugins for mathematical morphology with ImageJ. *Bioinformatics* **32**, 3532–3534 (2016).

200. Arganda-Carreras, I., Fernández-González, R., Muñoz-Barrutia, A. & Ortiz-De-Solorzano, C. 3D reconstruction of histological sections: Application to mammary gland tissue. *Microsc. Res. Tech.* **73**, 1019–1029 (2010).

201. Metsalu, T. & Vilo, J. ClustVis: A web tool for visualizing clustering of multivariate data using Principal Component Analysis and heatmap. *Nucleic Acids Res.* **43**, W566–W570 (2015).

202. Kimizuka, H. & Koketsu, K. Ion transport through cell membrane. *J. Theor. Biol.* **6**, 290–305 (1964).

203. Krug, S. M. *et al.* Charge-selective claudin channels. *Ann. N. Y. Acad. Sci.* **1257**, 20–28 (2012).

204. Sonoda, N. *et al.* Clostridium perfringens Enterotoxin Fragment Removes Specific Claudins from Tight Junction Strands : Evidence for Direct Involvement of Claudins in Tight Junction Barrier. **147**, 195–204 (1999).

205. Furuse, M. Molecular basis of the core structure of tight junctions. *Cold Spring Harb. Perspect. Biol.* **2**, 1–14 (2010).

206. Gramm, J. B. *et al.* A general method to fine-tune fluorophores for live-cell and in vivo imaging. *Nat. Methods* (2017).

207. Taliana, L., Benezra, M., Greenberg, R. S., Masur, S. K. & Bernstein, A. M. ZO-1: Lamellipodial localization in a corneal fibroblast wound model. *Investig. Ophthalmol. Vis. Sci.* **46**, 96–103 (2005).

208. Saito, A. C. *et al.* Occludin and tricellulin facilitate formation of anastomosing tight-junction strand network to improve barrier function. *Mol. Biol. Cell* (2021).

209. Van Itallie, C., Rahner, C. & Anderson, J. M. Regulated expression of claudin-4 decreases paracellular conductance through a selective decrease in sodium permeability. *J. Clin. Invest.* **107**, 1319–1327 (2001).

210. Milatz, S. A novel claudinopathy based on claudin-10 mutations. *Int. J. Mol. Sci.* **20**, 1–15 (2019).

211. Prot-Bertoye, C. & Houillier, P. Claudins in renal physiology and pathology. *Genes (Basel).* **11**, (2020).

212. Ikenouchi, J. Roles of membrane lipids in the organization of epithelial cells: Old and new problems. *Tissue Barriers* **6**, 1–8 (2018).

213. Francis, S. A. *et al.* Rapid reduction of MDCK cell cholesterol by methyl-β-cyclodextrin alters steady state transepithelial electrical resistance. *Eur. J. Cell Biol.* **78**, 473–484 (1999).

214. Nomme, J. *et al.* Structural basis of a key factor regulating the affinity between the zonula occludens first PDZ domain and claudins. *J. Biol. Chem.* **290**, 16595–16606 (2015).

215. Shukla, P. *et al.* High-throughput mRNA and miRNA profiling of epithelial-mesenchymal transition in MDCK cells. *BMC Genomics* **16**, 1–19 (2015).

216. Claude, P. Morphological factors influencing transepithelial permeability: A model for the resistance of the Zonula Occludens. *J. Membr. Biol.* **39**, 219–232 (1978).

217. Förster, C. Tight junctions and the modulation of barrier function in disease. *Histochem. Cell Biol.* **130**, 55–70 (2008).

218. Samanta, P. *et al.* Molecular determination of claudin-15 organization and channel selectivity. *J. Gen. Physiol.* **150**, 949–968 (2018).

219. Roßmann, K. *et al.* Deuterated rhodamines for protein labelling in nanoscopy. *bioRxiv* 1–14 (2020). doi:10.1101/2020.08.17.253880

220. Grimm, J. B. *et al.* A general method to optimize and functionalize red-shifted rhodamine dyes. *Nat. Methods* **17**, 815–821 (2020).

221. McCabe, M., Foo, C., Dinger, M., Smooker, P. & Stanton, P. Claudin-11 and occludin are major contributors to Sertoli cell tight junction function, in vitro. *Asian J. Androl.* **18**, 620–626 (2016).

222. Denninger, A. R. *et al.* Claudin-11 Tight Junctions in Myelin Are a Barrier to Diffusion and Lack Strong Adhesive Properties. *Biophys. J.* **109**, 1387–1397 (2015).

223. Liu, W., Schrott-Fischer, A., Glueckert, R., Benav, H. & Rask-Andersen, H. The Human "Cochlear Battery" – Claudin-11 Barrier and Ion Transport Proteins in the Lateral Wall of the Cochlea. *Front. Mol. Neurosci.* **10**, 1–16 (2017).

224. Capaldo, C. T. *et al.* Proinflammatory cytokine-induced tight junction remodeling through dynamic self-assembly of claudins. *Mol. Biol. Cell* **25**, 2710–2719 (2014).

225. Turner, J. R., Buschmann, M. M., Romero-Calvo, I., Sailer, A. & Shen, L. The role of molecular remodeling in differential regulation of tight junction permeability. *Semin. Cell Dev. Biol.* **36**, 204–212 (2014).

226. Kitajiri, S. I. *et al.* Expression patterns of claudins, tight junction adhesion molecules, in the inner ear. *Hear. Res.* **187**, 25–34 (2004).

227. Kitajiri, S.-I. *et al.* Compartmentalization established by claudin-11-based tight junctions in stria vascularis is required for hearing through generation of endocochlear potential. *J. Cell Sci.* **117**, 5087–5096 (2004).

228. Berndt, P. *et al.* Tight junction proteins at the blood–brain barrier: far more than claudin-5. *Cell. Mol. Life Sci.* **76**, 1987–2002 (2019).

229. Ong, M. L. D. M., Yeruva, S., Sailer, A., Nilsen, S. P. & Turner, J. R. Differential regulation of claudin-2 and claudin-15 expression in children and adults with malabsorptive disease. *Lab. Investig.* **100**, 483–490 (2020).

230. France, M. M. & Turner, J. R. The mucosal barrier at a glance. *J. Cell Sci.* **130**, 307–314 (2017).

231. Kühn, K. & Reale, E. Junctional complexes of the tubular cells in the human kidney as revealed with freeze-fracture. *Cell Tissue Res.* **160**, 193–205 (1975).

232. Balzarotti, F. *et al.* Nanometer resolution imaging and tracking of fluorescent molecules with minimal photon fluxes. *Science* (2017).

233. Raleigh, D. R. *et al.* Occludin S408 phosphorylation regulates tight junction protein interactions and barrier function. **193**, 565–582 (2011).

234. Curry, J. N., Tokuda, S., McAnulty, P. & Yu, A. S. L. Combinatorial expression of claudins in the proximal renal tubule and its functional 2 consequences. *Amercian J. Physiol.* **318**, 49–52 (2020).

235. Piontek, J. *et al.* Formation of tight junction: determinants of homophilic interaction between classic claudins. doi:10.1096/fj.07-8319com

236. Van Itallie, C. M., Tietgens, A. J., Krystofiak, E., Kachar, B. & Anderson, J. M. A complex of ZO-1 and the BAR-domain protein TOCA-1 regulates actin assembly at the tight junction. *Mol. Biol. Cell* **26**, 2769–2787 (2015).

237. Takayama, K. *et al.* Generation of Human iPSC–Derived Intestinal Epithelial Cell Monolayers by CDX2 Transduction. *Cmgh* **8**, 513–526 (2019).

238. Abo, K. M. *et al.* Human iPSC-derived alveolar and airway epithelial cells can be cultured at air-liquid interface and express SARS-CoV-2 host factors. *bioRxiv* (2020).

8 Appendix

8.1 Abbreviations

Table 41 Abbreviations.

µl	microliter
µm	micrometer
µM	micromolar
µm	micrometer
A	area
AA	amino acid
ABR	actin binding region
AF	alexa fluor
AJ	adherens junction
AJC	Apical junctional complex
aPKC	atypical protein kinase C
APS	ammonium persulfate
APS	ammonium persulfate
area_seg	Area segmentation
ATP	adenosin triphosphate
AU	absorbance units
avg	average
BG	O^6-benzylguanine
bp	basepair
BS	blocking solution
BSA	bovine serum albumine
C	concentration
C. perfringens	*Clostridium perfringens*
CA	O^6-chloralkane
CDK4	cyclin-dependent kinase 4
CF280	correction factor for A280
CIP	calf-intestinal-phosphatase
Cldn	claudin
cm	centimeter
CMV promoter	human cytomegalovirus *promoter*
CNS	central nervous system
CO_2	carbon dioxide
COS	*Chlorocebus aethiops*
CPE	*Clostridium perfringens* enterotoxin
CS	coverslip
C-term	C-terminus
Da	dalton
DAPI	4',6-diamidino-2-phenylindole
ddH_2O	double-distilled water
DKO	double knockout
DM	desmosome
DMEM	dulbecco's minimal essential medium
DOL	degree of labeling
dsDNA	double-stranded desoxyribonucleic acid
dSTORM	direct stochastic optical reconstruction microscopy
DTT	dithiothreitol
E. coli	*Escherichia coli*
$E_{bl\text{-}ap}$	dilution potential with correction for liquid junction potential

ECL	extra cellular loop
ECM	extra cellular matrix
EDTA	ethylene diamine tetraacetic acid
E-face	exoplasmic face
EGFP	enhanced green fluorescent proteins
EM	electron microscopy
EtBr	ethidium bromide
EtOH	ethanol
EYFP	enhanced yellow fluorescent proteins
F	Faraday constant
FBS	fetal bovine serum
FFEM	freeze-fracture electron microscopy
FRET	Förster resonance energy transfer
FW	forward
FWHM	full-width half-maximum
G	conductance
GA	glutaraldehyde
GAA	glacial acetic acid
GAPDH	glyceraldehyde 3-phosphate dehydrogenase
GJ	gap junction
GTP	guanosine triphosphate
GUK	guanylate kinases
h	hour
HA	hemagglutinin
HCl	hydrochloric acid
HDM	hemi desmosome
HEK cells	human embryonic kidney cells
HeLa	Henrietta Lacks
HMG-CoA	3-hydroxy-3-methylglutaryl-CoA
HPLC	high-performance liquid chromatography
HSP70	heat-shock protein 70
HyD	hybrid detector
I	current
I66C	isoleucine exchange at AA position 66 to cysteine
ICC	immunocytochemistry
IFN-γ	interferon γ
IgG	immunoglobulin G
IHC	immunohistochemistry
IRES	internal ribosome entry site
JAM	junctional adhesion molecule
JF	Janelia Fluor
kb	kilobase
KD	knockdown
kDa	Kilodalton
KO	knockout
L	liter
LB	lysogeny broth
LSCM	laser scanning microscopy
M	molar
MAGI	membrane-associated guanylate kinase inverted
MARVEL	MAL and related proteins for vesicle trafficking and membrane link
maxBranchLgth	maximal branch length
mCldn	mouse claudin
MCS	multiple cloning site
MDCK cells	Madin-Darby canine kidney cells

MEM	minimal essential medium
MeOH	methanol
Mhz	mega hertz
ml	milliliter
mM	millimolar
mm	millimeter
MTSES	sodium (2-sulfonatoethyl)methane-thiosulfonate, 2-[(methylsulfonyl)thio]-ethanesulfonic acid, monosodium salt
MTSET	N,N,N-trimethyl-2-[(methylsulfonyl)thio]-ethanaminium, monochloride
MUPP-1	multi-PDZ domain protein 1
MβCD	methyl-β-cyclodextrin
N48K	glutamine exchange at AA position 48 to Lysine
NA	numerical aperture
NaOH	sodium hydroxide
NEAA	non-essential amino acids
Neo	neomycin
NGS	normal goat serum
nm	nanometer
nM	nanomolar
nm	nanometer
N-term	N-terminus
nts	nucleotides
OD	optical density
PAGE	polyacrylamide gel electrophoresis
Pals1	proteins associated with Lin Seven 1
PAPP	paracellular permeability
PAR-3	partitioning defective 3
PATJ	PALS1-associated tight junction
PBS	phosphate buffered saline
PCA	principle component analysis
PCF	polycarbonate filter
PCR	polymerase chain reaction
PCT	proximal convoluted tubule
PDZ domain	PSD95, Dlg1 and ZO1 domain
P/S	penicillin-streptomycin
PET	polyethylene terephthalate
PFA	paraformaldehyde
P-face	protoplasmic face
Pierce ECL	Pierce chemiluminescence
PLL	poly-L-lysine
PM	plasma membrane
PMT	photomultiplier
Pr_2Net	N,N-diisopropylethylamine
PSF	point spread function
PST	proximal straight tubule
PT	proximal tubule
Puro	puromycin
P_x	permeability ion x
pxl	pixel
QKO	quintuple knockout
R	resistance
RNA	ribonucleic acid
ROI	region of interest
RT	room temperature
RV	reverse

s	second
stdDev	standard deviation
SDS	sodium dodecyl sulfate
SDS-PAGE	sodium dodecyl sulfate-polyacrylamide gel electrophoresis
SH3	SRC Homology 3
SIM	structured illumination microscopy
siR	silicon rhodamine
SMLM	single-molecule localization microscopy
SRC	sarcoma
SRM	super-resolution microscopy
sT	stable
STED	stimulated emission depletion
t	time
T	temperature
TAL	thick ascending limb
TAMP	TJ associated MARVEL proteins
TC-treated	tissue culture treated
TEMED	N,N,N′,N′-tetramethylethylenediamine
TER	transepithelial resistance
TFA	trifluoroacetic acid
TIRF	total internal reflection fluorescence
TJ	tight junction
tTJ	tricellular tight junction
TM	transmembrane
T_M	primer melting temperature
TNF-α	tumor necrosis factor α
TRIS	tris(hydroxymethyl)aminomethane
tTJ	tricellular Tight junction
U	unit
UPLC	ultra-performance liquid chromatography
V	volume
Var	variance
V_HH	single variable domain on a heavy chain
WB	Western Blot
WT	wildtype
ZO	zonula occludens
ZONAB	ZO-1–associated nucleic acid binding protein
ΔCT	deletion of C-terminus
ΔPDZ	deletion of PDZ-binding motif
ε	extinction coefficient
ε'	modified extinction coefficient
λ	wavelength
λexc	excitation wavelength

8.2 Supplementary figures

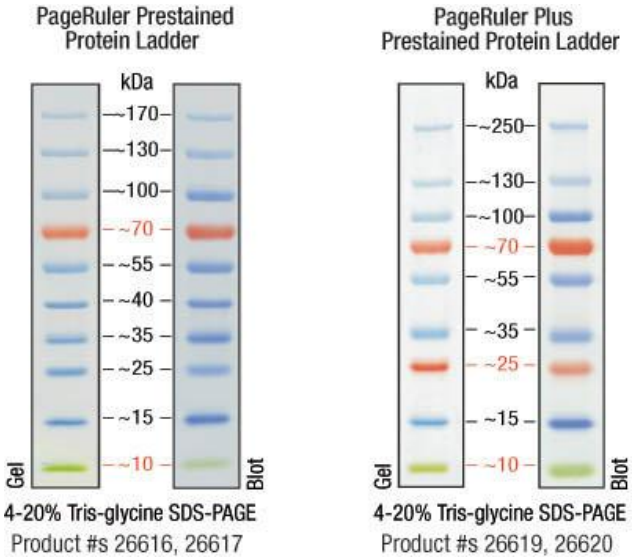

Figure S1 PageRuler Prestained Protein Ladder 10-170 kDa and PageRuler Prestained Plus Protein Ladder 10-250 kDa (Thermo Fisher Scientific).

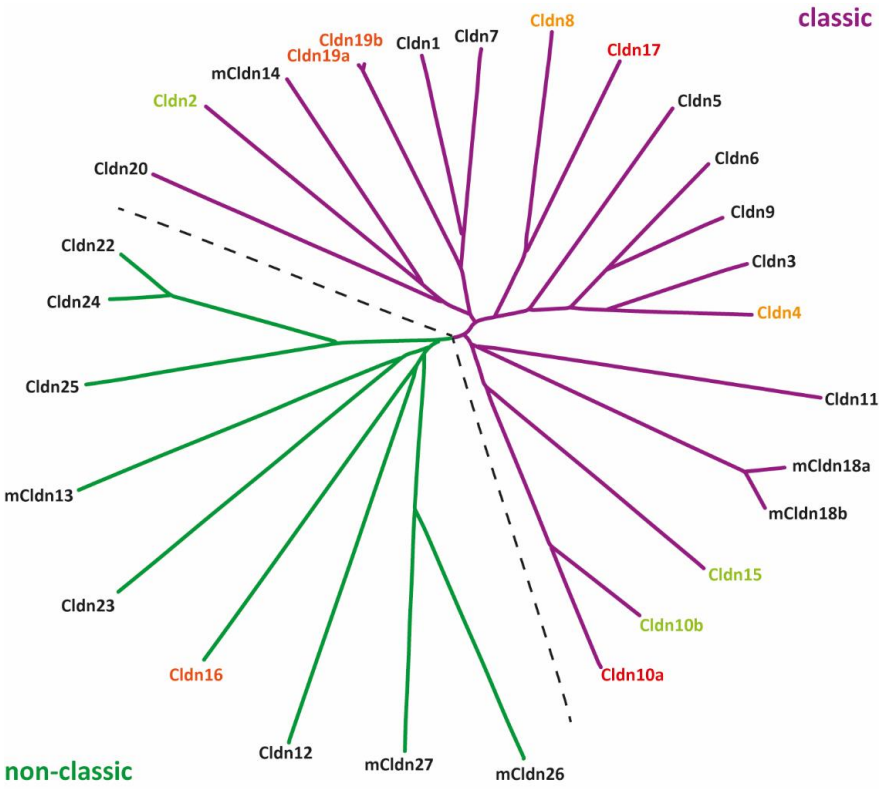

Figure S2 Phylogenetic tree of all 26 mammalian claudins with specific isoforms that were used in this study. In this study, all claudins were based on the human sequence except for the following mouse claudins: mCldn13, 14, 18a, 18b, 26, 27. The phylogenetical calculation was performed with Clustal Omega (https://www.ebi.ac.uk/Tools/msa/clustalo/), an online alignment tool based on the publication of Sievers et al. in 2011. For the alignment, the full-length amino acid sequences of the single claudins were taken from UniProt. Classic claudins are labeled with magenta lines and non-classic with green lines. Barrier-forming claudins are colored in black, cation channel-forming claudins in light green, anion channel in red, predicted heteromeric channel in orange. The terms classic and non-classic are adapted from the sequence alignment in Krause et al. (2008)[79].

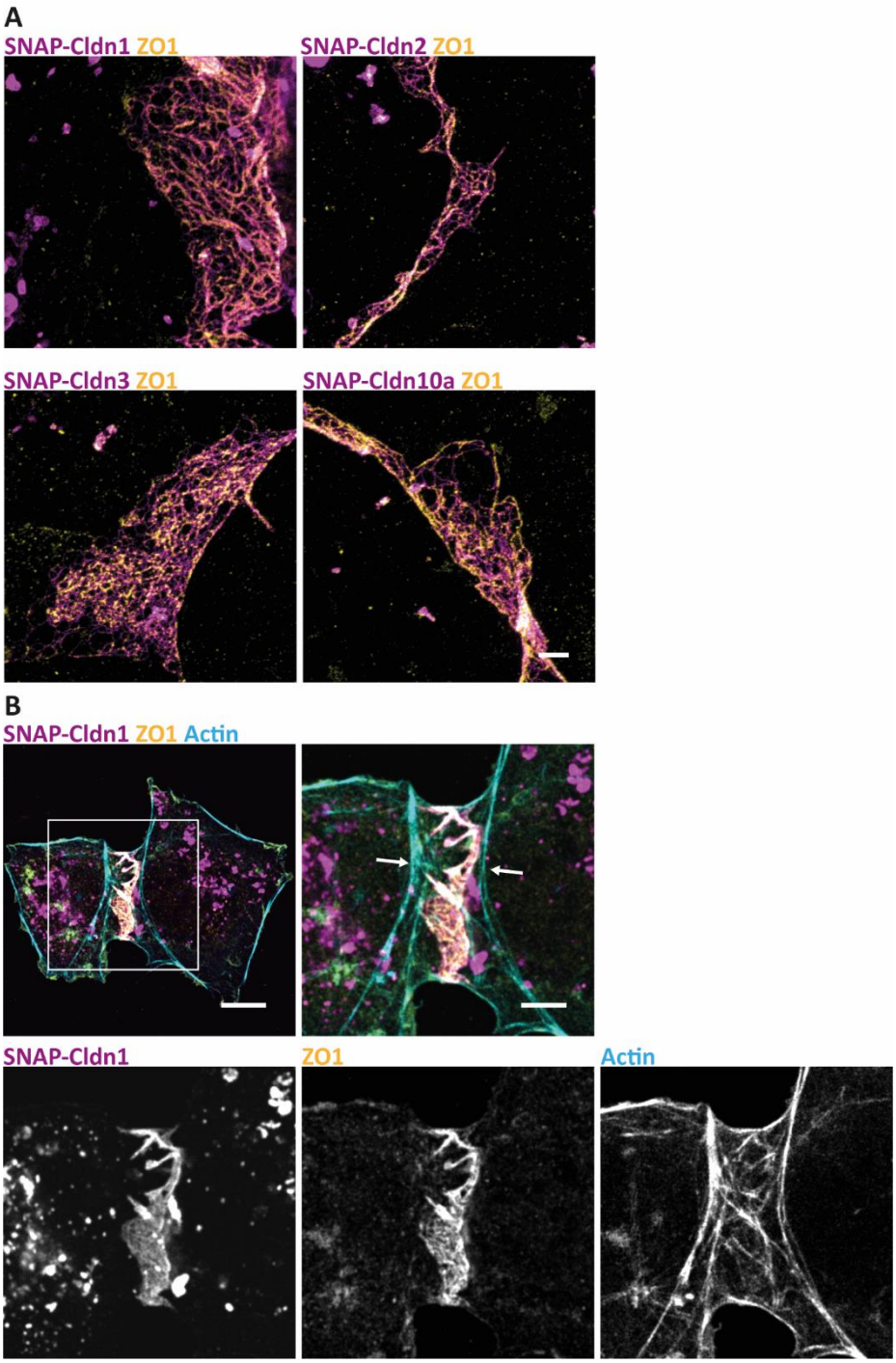

Figure S3 Endogenous ZO1 localizes at the TJ-like meshwork in fibroblasts without leading to an accumulation of actin along the meshwork. SNAP-tagged claudins were labeled with JF646-BG. ZO1 was decorated with antibodies and labeled with AF594. Actin was stained with Phalloidin AF488. **(A)** Overview STED images of the magnifications shown in Figure 22. ZO1 (yellow) localizes at the formed TJ-like meshworks of SNAP-Cldn1, 2, 3, and 10a (magenta). **(B)** Confocal image of SNAP-Cldn1 (magenta), endogenous ZO1 (yellow), and actin (cyan). White arrows point at the actin accumulation formed at the border of the TJ-like meshwork. Scale bars: 1 µm (A), 10 µm, 5 µm (B).

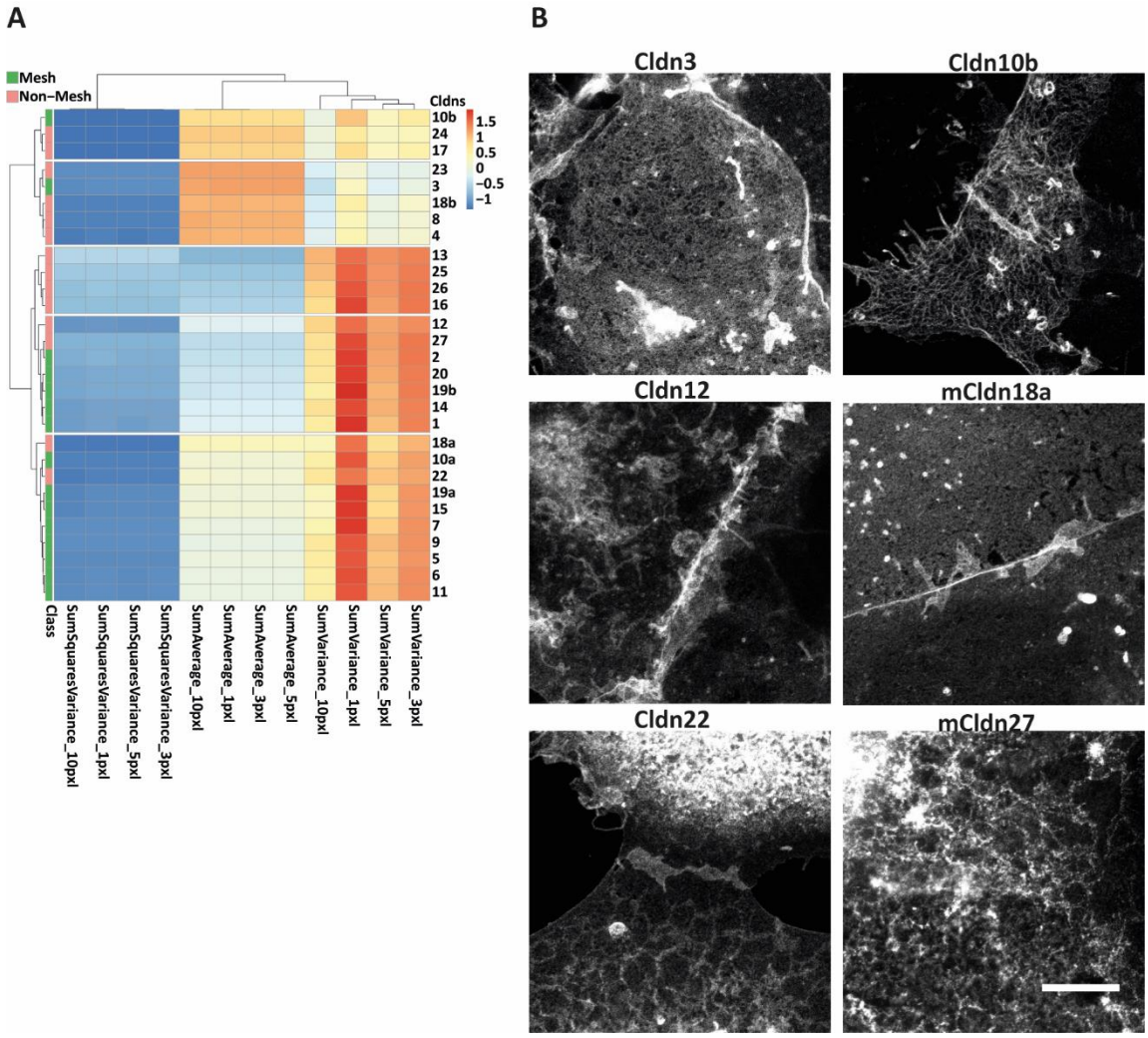

Figure S4 Automated analysis of TJ-like meshwork forming and non-meshwork forming claudins by using an automated analysis based on Haralick texture features. All used images were derived from overexpression of N-terminally EYFP- or EGFP-tagged claudins. The signal was enhanced with an anti-GFP Atto647N nanobody. Human claudins were used except for murine Cldn13, 14, 18a, 18b, 26, and 27. **(A)** Heatmap of the Haralick texture features analysis. Claudins, which made the visual impression of forming meshwork, are labeled in green, and non-meshwork forming claudins are labeled in red. The range of complexity of a certain parameter is shown with the colorized range indicator from -1 (dark blue) to 1.5 (red). The different texture parameters (SumVariance, SumAverage, SumSquareVariance) were analyzed for each pixel and its surrounding 1, 3, 5, or 10 px (1px = 20 nm). **(B)** Representative STED images of the misclassified claudins. The meshwork forming claudins, Cldn3 and Cldn10b, were misclassified due to low signal intensity and high meshwork density. The non-meshwork forming claudins, Cldn12, 18a, 22, and 27, were misclassified because of tubular structures derived from a strong localization in the ER. Scale bars: 5 µm (B).

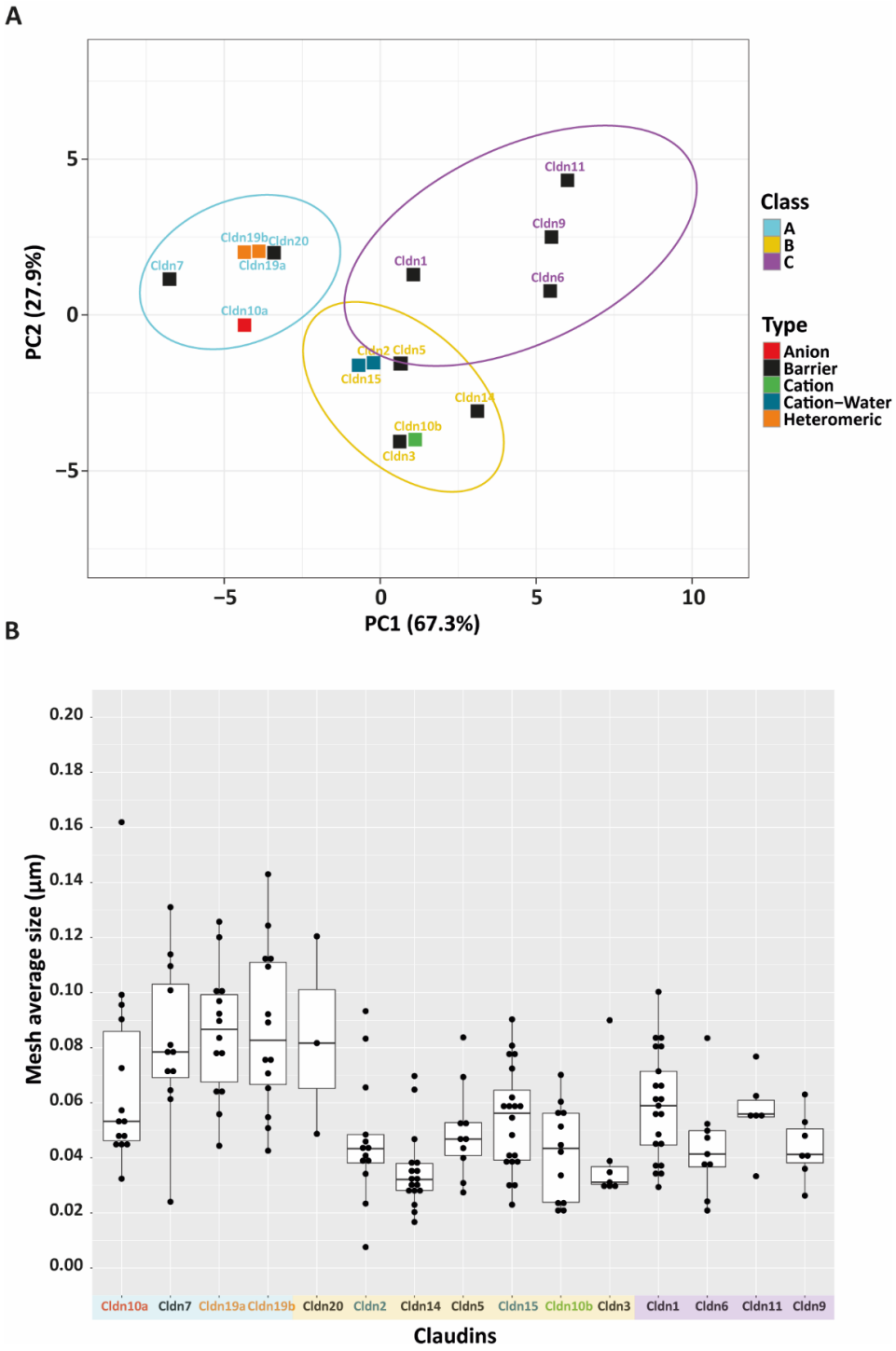

Figure S5 Principal components analysis and average mesh sizes of TJ-like meshworks derived from the computational automated analysis. Claudins are colorized based on their proposed function: barrier (black), cation channel (green), anion channel (red), mixed cation and water channel (blue), and heteromeric ion channel (yellow). The three different meshwork classes are labeled with a differently colored background in blue for class A, yellow for class B, and magenta for class C. **(A)** Principal component analysis of the claudin-based TJ meshworks. Three different and distinct clusters could be detected. **(B)** Shown are the average mesh sizes in µm of all analyzed claudin meshworks in this analysis. Every dot represents one TJ-like meshwork. Statistics: median interquartile range.

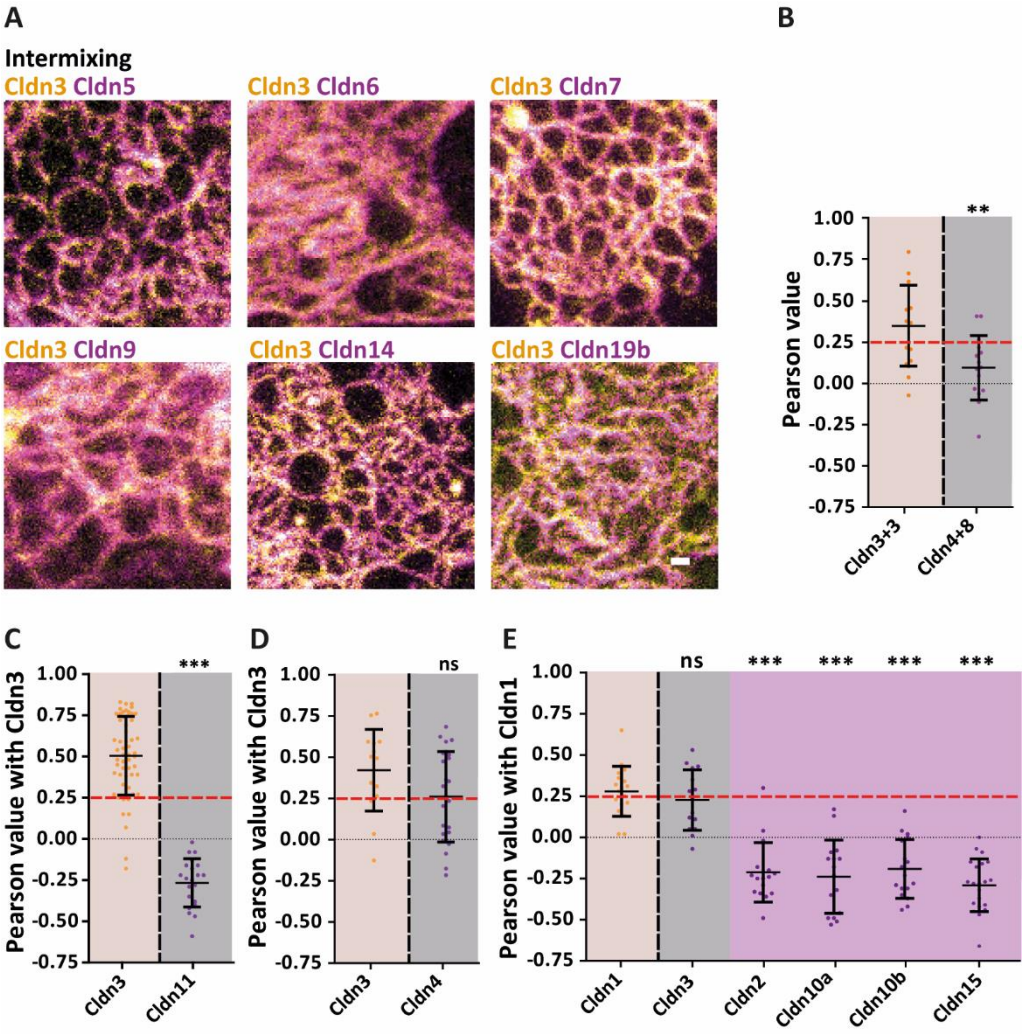

Figure S6 STED images of intermixing barrier-forming claudins, Pearson analysis of the different organization patterns and Pearson of Cldn1 in co-overexpression with channel-forming claudins. (A) Representative STED images of intermixing TJ-like meshworks formed by SNAP-tagged Cldn3 labeled with Atto590-BG in co-overexpression with EYFP-tagged Cldn5, 6, 7, 9, 14, 19b enhanced with an anti-GFP Atto647N nanobody. **(B)** Pearson analysis of the induction meshwork pattern formed by Cldn4 and Cldn8, **(C)** the exclusion meshwork pattern formed by Cldn3 and Cldn11, **(D)** the integrating meshwork pattern formed by Cldn3 and Cldn4. **(E)** Pearson analysis of Cldn1 with Cldn3, 2, 10a, 10b and 15 in co-expression. For each combination, ≥ five meshworks per experiment were imaged in three independent experiments (N≥15). We defined that intermixing claudins should reach values over 0.25, whereas segregating claudins should not exceed 0. Statistics: mean ± SD; Mann-Whitney test, two-tailed (B-D); one-way ANOVA with Dunnett's multiple comparison test (E; comparison to Cldn1 with Cldn1); ns (not significant), ** p≤0.01%, *** p≤0.001%. Scale bar: 0.2 µm (A).

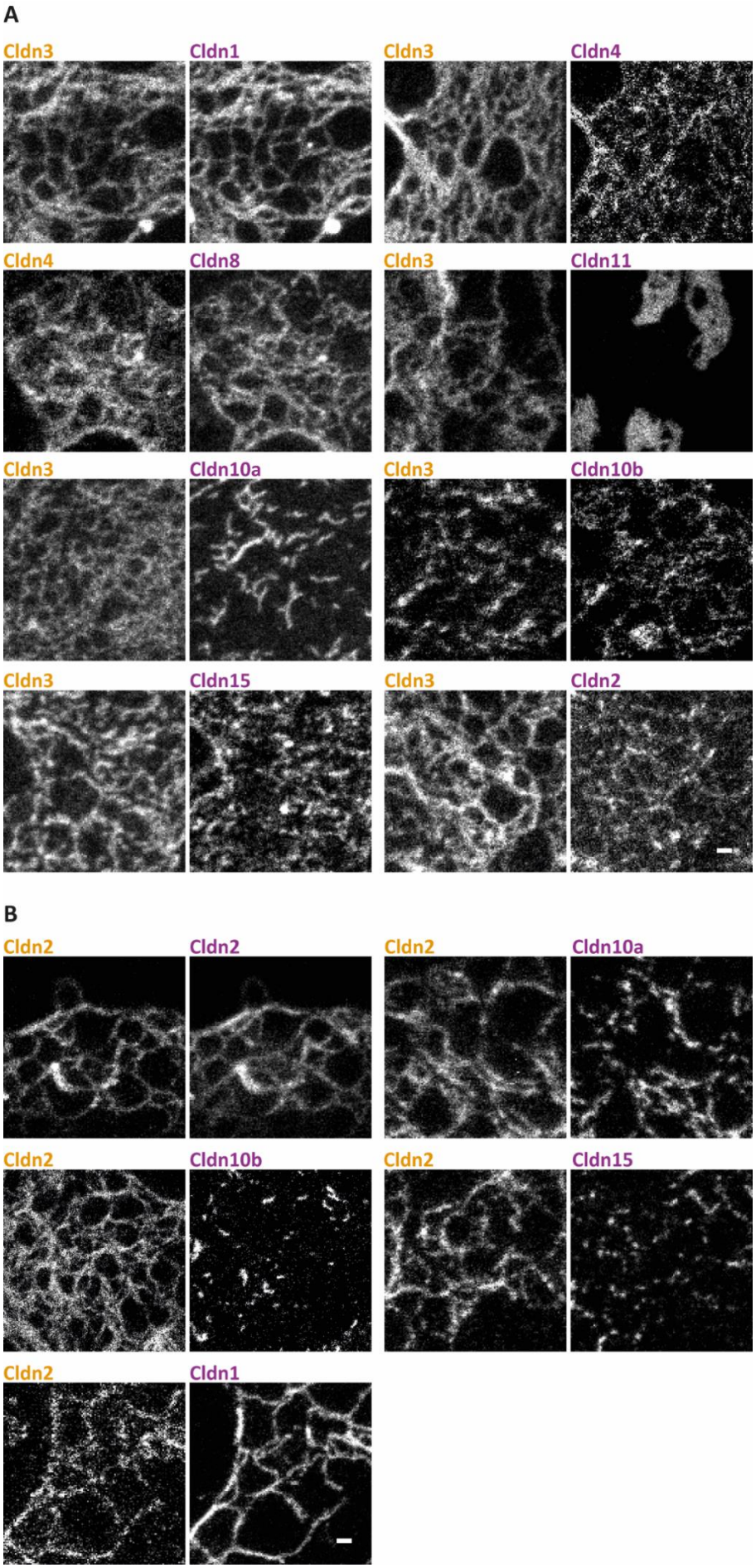

Figure S7 Single channels of the STED images from the overexpression experiments of Cldn3, Cldn4 and Cldn2 with other claudins. (A) Single channels from the STED images shown in Figure 25 of TJ-like meshworks formed by SNAP-tagged Cldn3 or Cldn4 labeled with Atto590-BG in co-overexpression with EYFP-tagged Cldn1, 2, 4, 8, 10a, 10b, 11 and 15 enhanced with an anti-GFP Atto647N nanobody. **(B)** Single channels from the STED images shown in Figure 28 of TJ-like meshworks formed by SNAP-tagged Cldn2 labeled with Atto590-BG in co-overexpression with EYFP-tagged Cldn1, 2, 10a, 10b, and 15 enhanced with an anti-GFP Atto647N nanobody. Scale bars: 0.2 µm (A, B).

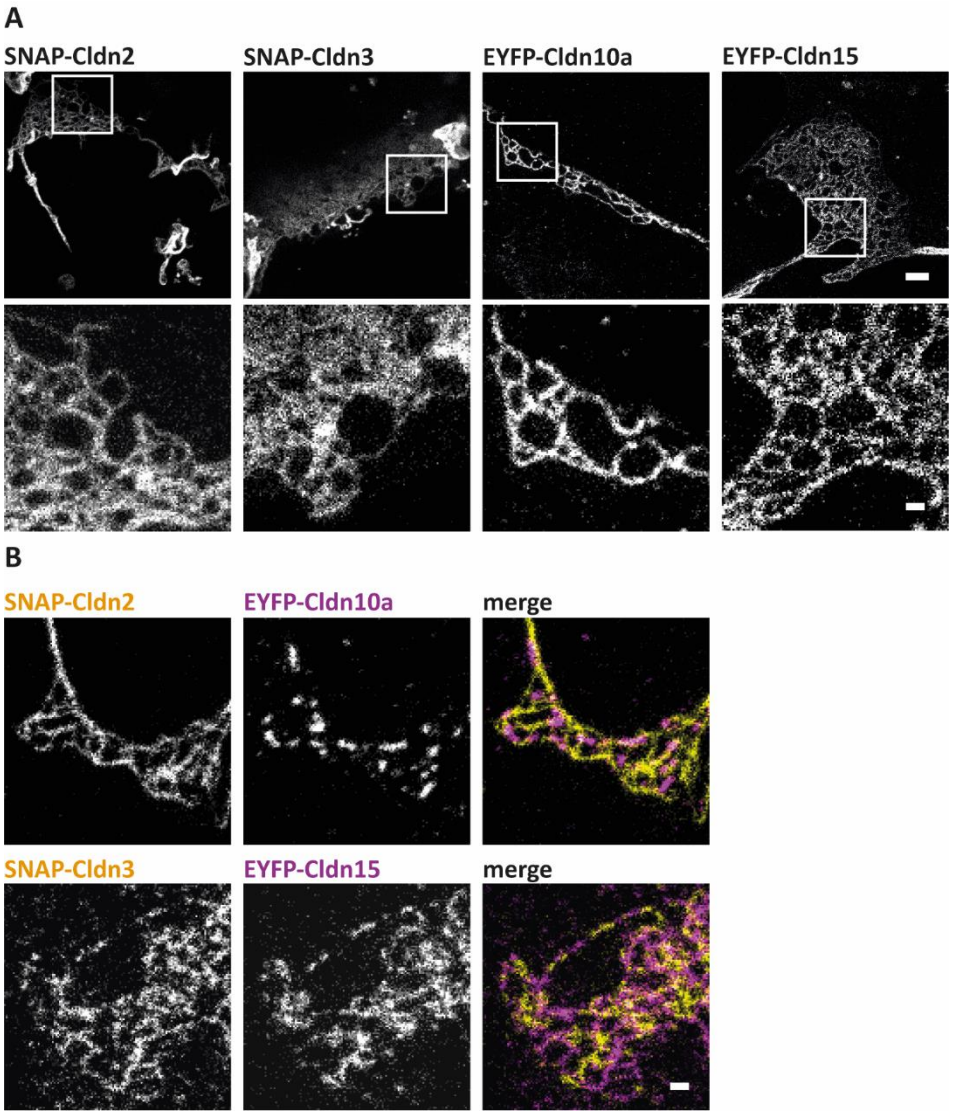

Figure S8 COS-7 fibroblasts stably expressing Cldn2, 3, 10a, 15 form characteristic TJ-like meshwork and segregates in co-expression. SNAP-tagged claudins were labeled with Atto590-BG, and EYFP-tagged claudins were enhanced with an anti-GFP Atto647N nanobody. **(A)** Representative STED images of SNAP-Cldn2, 3 and EYFP-Cldn10a, 15 stably expressing COS-7 cells. **(B)** COS-7 cells stably co-expressing SNAP-Cldn2 with EYFP-Cldn10a and SNAP-Cldn3 with EYFP-Cldn15. Scale bars: 1 µm (overview in A) and 0.2 µm (magnification in A and B).

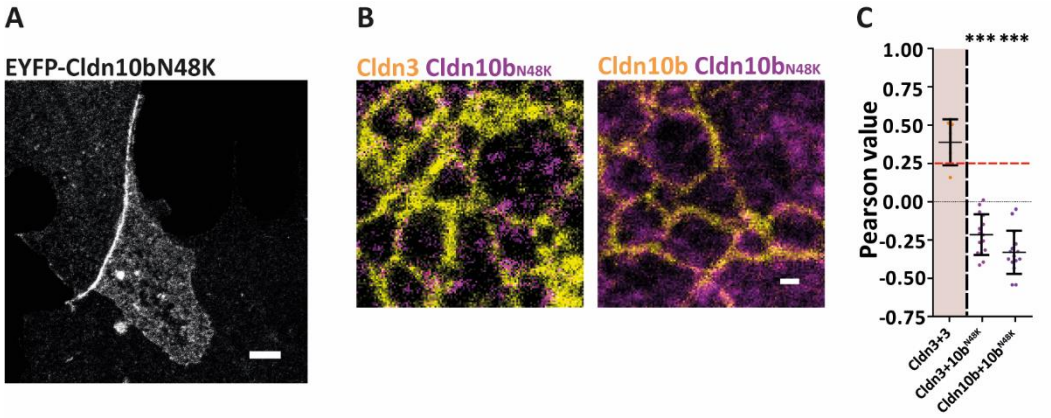

Figure S9 HELIX-syndrome disease mutant Cldn10b^{N48K} loses its meshwork properties and its segregation phenotype. SNAP-tagged claudins were labeled with an Atto590-BG, and EYFP-tagged claudins were enhanced with an anti-GFP Atto647N nanobody. **(A)** Representative STED image of EYFP-Cldn10b^{N48K} overexpressed in COS-7 cells. **(B)** SNAP-Cldn3 and SNAP-Cldn10b were co-overexpressed with EYFP-Cldn10b^{N48K} in COS-7 cells. **(C)** Pearson analysis of the claudin-claudin combinations in (B). Cldn3 in co-expression with itself served as an intermixing control. For Cldn3 with itself five meshworks were measured (N≥5). For the Cldn3 and Cldn10b with Cldn10b^{N48K}, ≥ five meshworks per experiment were imaged in three independent experiments (N≥15). We defined that intermixing claudins should reach values over 0.25, whereas segregating claudins should not exceed 0. Statistics: mean ± SD; one-way ANOVA with Dunnett's multiple comparison test (E; comparison to Cldn3 with Cldn3); *** p≤0.001%. Scale bar: 0.5 µm (A), 0.2 µm (B).

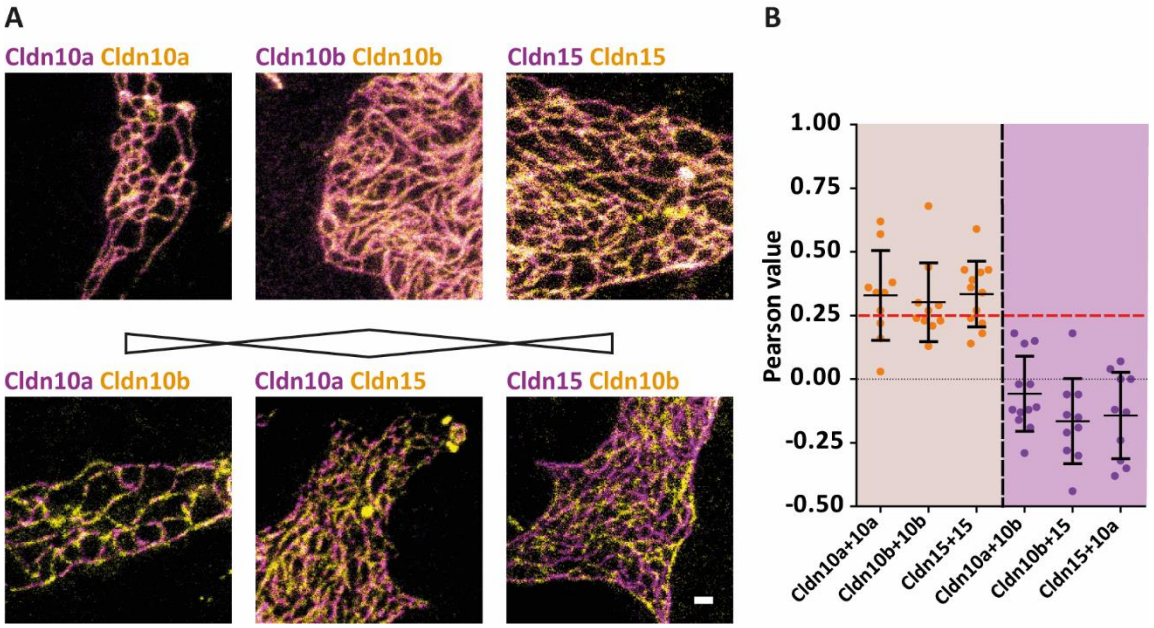

Figure S10 STED images and Pearson analysis of the channel-forming claudins Cldn10a, 10b and 15 in co-expression. (A) Representative STED images of SNAP-Cldn10a, 10b and 15 co-overexpressed with and EYFP-Cldn10a, 10b, and 15 in COS-7 cells. SNAP-tagged claudins were labeled with a Atto590-BG, and EYFP-tagged claudins were enhanced with an anti-GFP Atto647N nanobody. **(B)** Pearson analysis of the claudin-claudin combinations in (A). Claudins in co-expression with itself served in all approaches as an intermixing control. For each combination, ≥ five meshworks per experiment were imaged in two independent experiments (N≥10). We defined that intermixing claudins should reach values over 0.25, whereas segregating claudins should not exceed 0. Statistics: mean ± SD. Scale bar: 0.2 µm (A).

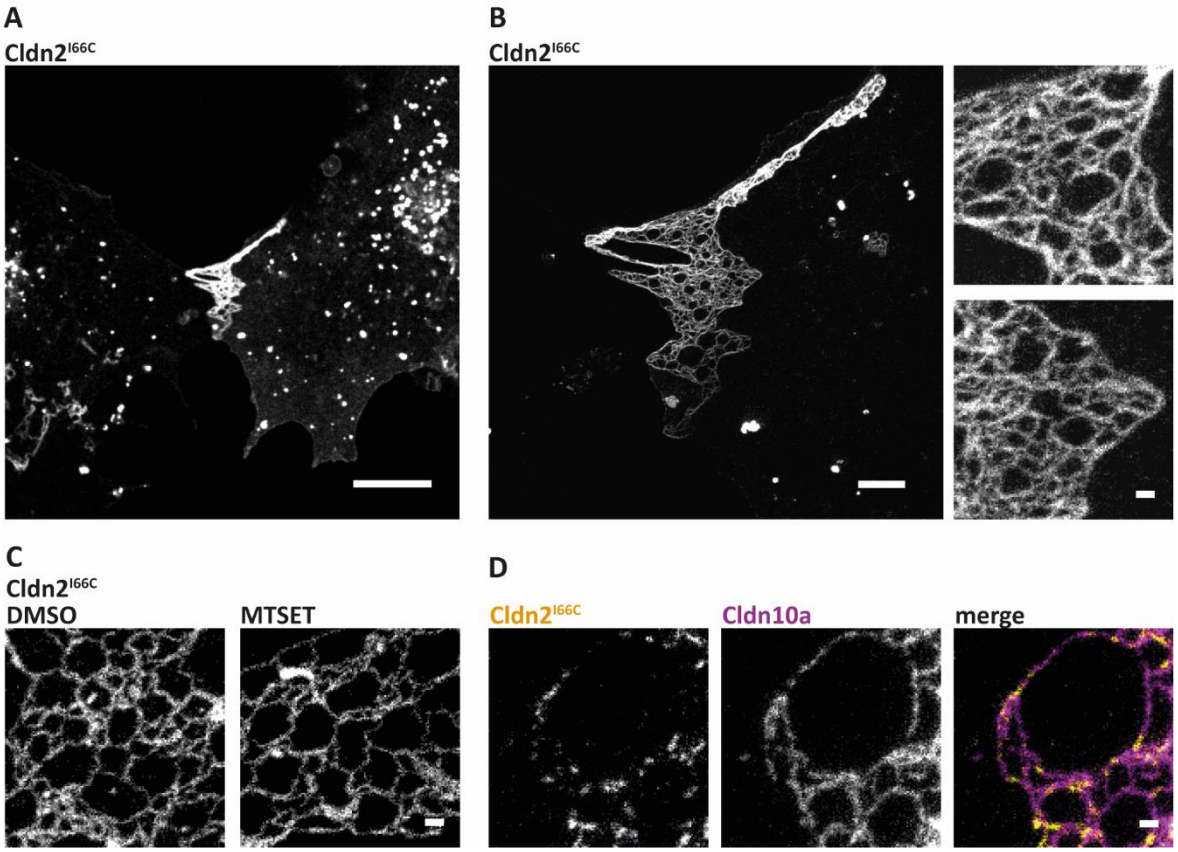

Figure S11 Cldn2^{I66C} forms TJ-like meshwork and segregates from Cldn10a in COS-7 fibroblasts. SNAP-tagged claudins were labeled with an Atto590-BG, and EGFP-tagged claudins were enhanced with an anti-GFP Atto647N nanobody. **(A)** Representative confocal image of a cell-cell overlap between two EGFP-Cldn2^{I66C} expressing COS-7 cells. **(B)** Representative STED image of a TJ-like meshwork formed by EGFP-Cldn2^{I66C}. **(C)** Representative STED image of a TJ-like meshwork of EGFP-Cldn2^{I66C} after two hours incubation with DMSO or 1 mM MTSET. **(D)** Representative STED image of a segregating TJ-like meshwork formed by EGFP-Cldn2^{I66C} (yellow) with SNAP-Cldn10a (magenta). Scale bars: 10 µm (A), 2 µm (overview, B), 0.2 µm (magnification in B, C, D).

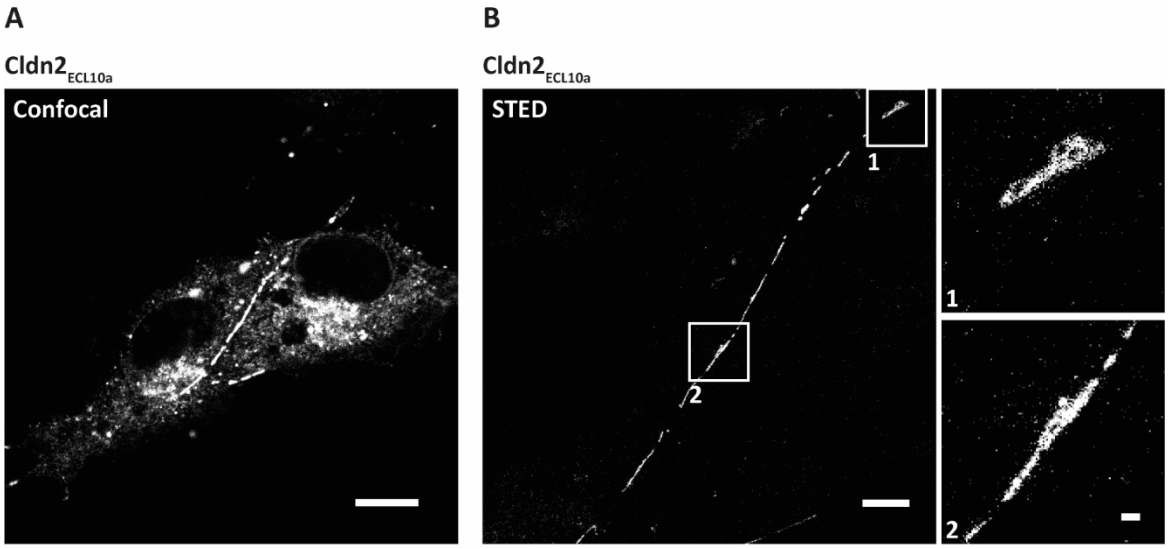

Figure S12 Cldn2$_{ECL10a}$ chimera forms strands in overexpression in fibroblasts. SNAP-tagged claudins were labeled with a JF646-BG. **(A)** Representative confocal image of a cell-cell overlap between two SNAP-Cldn2$_{ECL10a}$ expressing COS-7 cells. **(B)** Representative STED image of a TJ-like meshwork formed by SNAP-Cldn2$_{ECL10a}$. Scale bars: 10 µm (A), 2 µm (overview in B), 0.2 µm (magnifications in B).

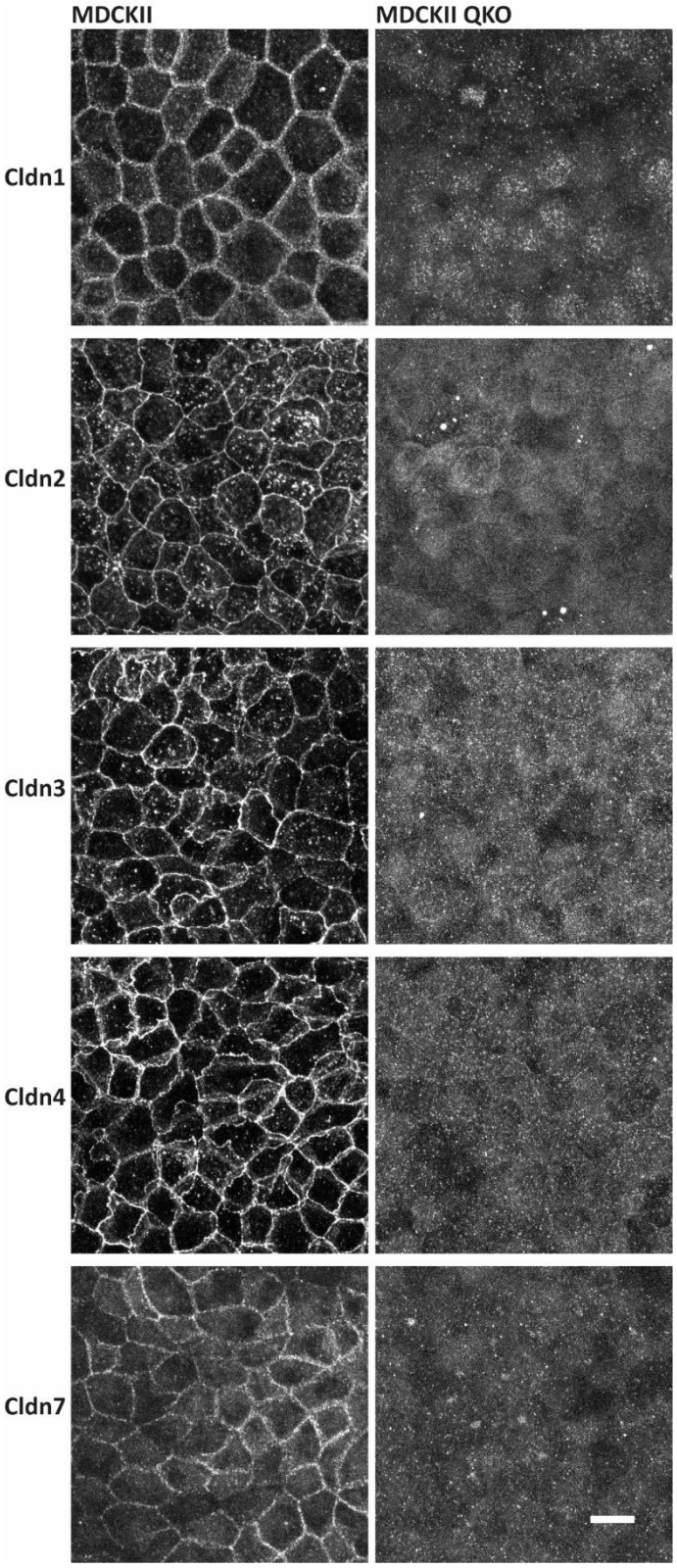

Figure S13 Validation of the claudin quintuple knockout in MDCKII QKO cells. Representative confocal images of immunocytochemistry labeled MDCKII cells and MDCKII QKO cells. MDCKII and MDCKII QKO cells were decorated with antibodies for Cldn1, 2, 3, 4, or 7 (all grey). Scale bar: 10 µm.

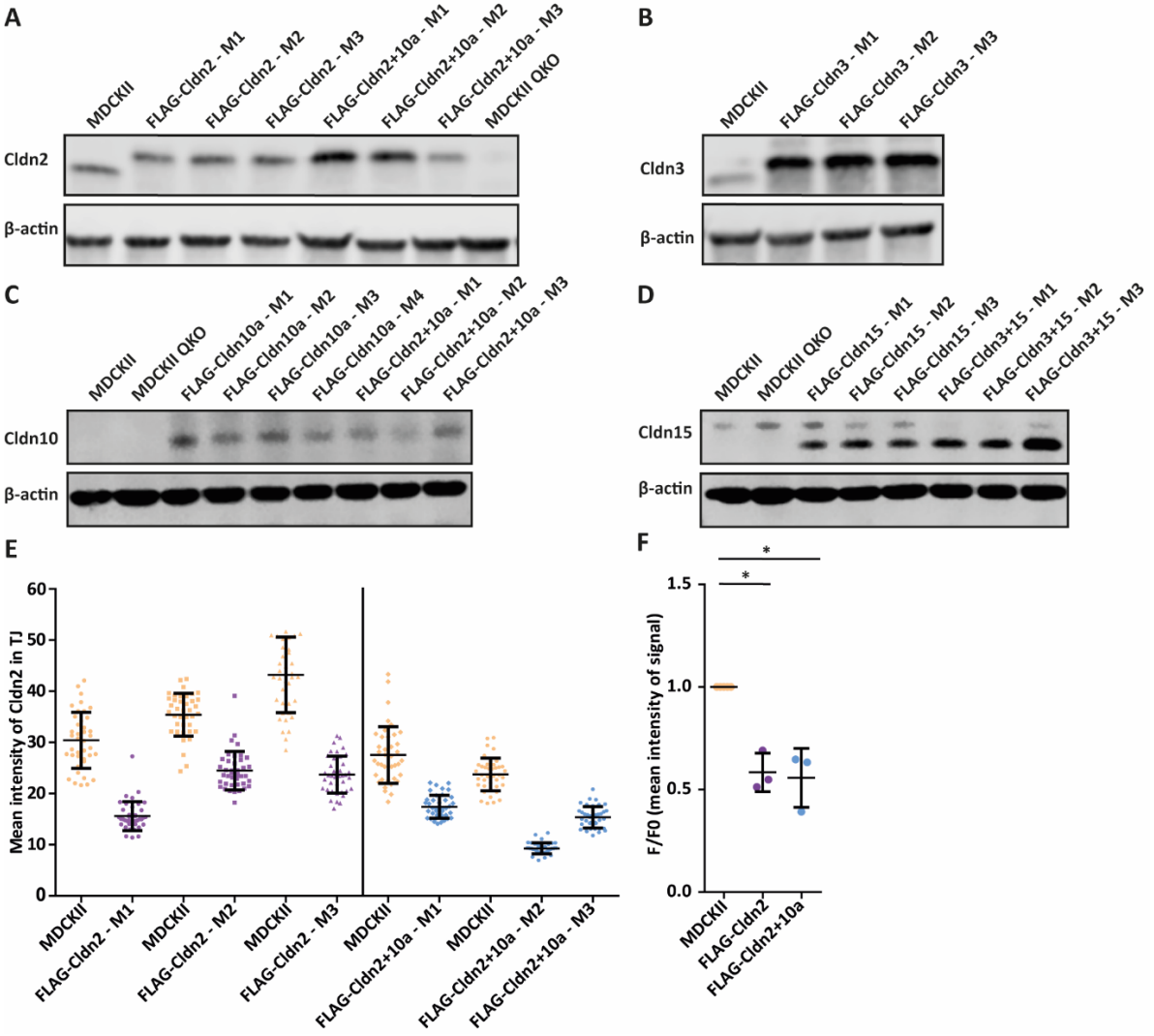

Figure S14 Western Blot of the total claudin expression level of stably claudin expressing cells and analysis of the Cldn2 localization in the TJ comparing MDCKII and MDCKII QKO cells stably expressing Cldn2 or co-expressing Cldn2 and Cldn10a. The additional labeling of the stably claudin expressing MDCKII QKO cells with "M" indicates the different dilution potential measurements. **(A)** Western Blot of the cell lysates of MDCKII, MDCKII QKO, MDCKII QKO cells stably expressing FLAG-Cldn2, and FLAG-Cldn2+Cldn10a from three different measurements. It was immunoblotted for Cldn2 (22 kDa; with FLAG-tag 24 kDa) and for β-actin (42 kDa) as loading control. **(B)** Western Blot of the cell lysates of MDCKII, MDCKII QKO cells stably expressing FLAG-Cldn3 from three different measurements. It was immunoblotted for Cldn3 (22 kDa; with FLAG-tag 24 kDa) and for β-actin (42 kDa) as loading control. **(C)** Western Blot of the cell lysates of MDCKII, MDCKII QKO, MDCKII QKO cells stably expressing FLAG-Cldn10a from four different measurements, and FLAG-Cldn2+Cldn10a from three different measurements. It was immunoblotted for Cldn10 (22 kDa; with FLAG-tag 24 kDa) and for β-actin (42 kDa) as loading control. **(D)** Western Blot of the cell lysates of MDCKII, MDCKII QKO, MDCKII QKO cells stably expressing FLAG-Cldn15 and FLAG-Cldn3+Cldn15 from three different measurements. It was immunoblotted for Cldn15 (22 kDa; with FLAG-tag 24 kDa) and for β-actin (42 kDa) as loading control. **(E)** Mean intensity measurement of Cldn2 in the TJ of ICC labeled MDCKII (magenta), MDCKII QKO cells stably expressing FLAG-Cldn2 (yellow), and FLAG-Cldn2+Cldn10a (blue). The measurement

was performed for the cells that were used in every dilution potential measurement (M1-M3). MDCKII cells from each individual measurement served as control. For each cell line the intensity for Cldn2 in 40 individual TJ was measured (N=40). **(F)** Normalized mean intensity of the MDCKII QKO cells stably expressing FLAG-Cldn2 and FLAG-Cldn2+Cldn10a. The mean intensity was normalized to mean intensity of the MDCKII from the corresponding experiment shown in (E). Statistics: mean ± SD; Mann-Whitney test, two-tailed (F; comparison to MDCKII); * p≤0.01%.

8.3 Tables and figures

8.3.1 List of tables

8.3.2 List of figures

8.3.3 List of supplementary figures

8.3.4 List of equations

8.4 Publications

Klose M, Salloum J, Gonschior H, Linder S. *SNX3 drives maturation of Borrelia phagosomes by forming a hub for PI(3)P, Rab5a, and galectin-9*. J. Cell. Biol. (2019) 218 (9): 3039–3059.

Gonschior H, Haucke V, Lehmann M. *Super-resolution imaging of tight and adherens junctions: Challenges and open questions.* Int. J. Mol. Sci. (2020), 21, 74.

Mecklenburg N, Kowalczyk I, Witter F, Hammes A. *Identification of novel disease relevant genetic modifiers affecting the SHH pathway in the developing brain.* bioRxiv 2020.11.03.366302; doi: https://doi.org/10.1101/2020.11.03.366302